



The
University
Of
Sheffield.

**Strain balancing of self-assembled InAs/GaAs quantum dots grown by
metal-organic vapour phase epitaxy**

By:

Timothy Stephen Lewis-Roberts

A thesis submitted in partial fulfilment of the requirements for the degree of
Doctor of Philosophy

The University of Sheffield
Faculty of Engineering
Department of Electronic and Electrical Engineering

Submission Date: May 2018

Intentionally Blank

Abstract

In this thesis, the strain balancing of self-assembled InAs/GaAs quantum dots (QDs), grown by metal-organic vapour phase epitaxy (MOVPE) is investigated. Initially, the optimisation of the important QD growth parameters, InAs coverage, growth rate, V/III ratio during the QD growth and the V/III ratio during the capping layer growth is explored. Incorporation of a strain-balancing layer will allow the close vertical stacking of QD layers, giving the potential for increased volumetric QD density and hence increased optical gain. Strain balancing can only be achieved practically using a $\text{GaAs}_z\text{P}_{1-z}$ layer. Therefore, modelling is performed of different phosphorus concentrations to understand the effects of placing a large potential barrier between QD layers on the electrical characteristics and the lasing threshold current density. In addition, X-ray diffraction (XRD) spectra are modelled to estimate the thickness of $\text{GaAs}_{0.8}\text{P}_{0.2}$ required to strain balance a QD layer. Based on this modelling, the implementation of a strain-balancing layer, which does not adversely affect the electrical characteristics and threshold current density, was attempted for three different QD layer separations: 50, 30 and 20 nm. Incorporation of this layer is shown to improve the performance of a device with a 30 nm spacing between QD layers, although performance is still inferior to that of a 50 nm device without strain balancing. Successful laser fabrication of the 50 and 30 nm structures with strain balancing gave laser operation up to 240 and 200 K, respectively. Further optimisation of the QD growth resulted in a room temperature laser with a layer separation of 50 nm, however, this was without the strain-balancing layer.

Modelling of a relatively new type of semiconductor laser structure, a photonic crystal surface emitting laser (PCSEL) is performed to develop the incorporation of QDs. Three material systems for the photonic crystal are considered: void/GaAs, InGaP/GaAs and AlAs/GaAs, where the potential performance of each material system is discussed and compared. Preliminary investigations of the effect of the overgrowth temperature on the QD emission and the effect of incorporating an AlAs layer on the electrical characteristics were performed.

For my loving wife and parents who have supported me throughout my Ph. D.

Acknowledgements

First and foremost, I would like to thank my loving wife, Amber, for putting up with me in my pursuit of a Ph. D., she has given me amazing support for the past four and a half years as well as my parents, who have supported me in everything I wanted to do.

I would also like to thank Professor Richard Hogg, who sparked my interest into semiconductors and in particular, photonics back in 2009 in my first year as an undergraduate. If it were not for his projects during the summer months, I would never have pursued a Ph. D. and a career in semiconductors. I would also like to thank my current Ph. D. supervisor Professor David Mowbray for agreeing to take me on when Richard left and for the amazing support and guidance, he has given me over the past two and a half years.

This work could not have been completed solely by myself; I would like to thank Doctor Benjamin Stevens for teaching and guidance on how to use the MOVPE reactor. I would especially like to thank, Doctor Edmund Clarke for stepping in as my second supervisor when Ben left. He supported me throughout my time as a student and has always helped with my understanding of QDs and epitaxial growth. Special thanks to Doctor Nasser Babazadeh, Doctor Kenneth Kennedy and Mr Saurabh Kumar who all supported me with their knowledge of fabrication and Doctor David Childs with his support and knowledge of device testing.

I would like to thank all those who have contributed towards my Ph. D., Mr Brett Harrison, Mr David Morris, Mr Ian Tooley, Doctor Ian Farrer, Professor Nobuhiko Ozaki, Doctor Negin Peyvast, Miss Charlotte Ovenden, Doctor Kristian Groom, Doctor David Williams, Doctor Richard Taylor, Doctor Pavlo Ivanov and Doctor John Roberts, who sadly passed away last year.

Special thanks to the EPSRC for the funding, without this, I would not have been able to complete a PhD.

List of Publications

Journal Papers:

1. Timothy S. Roberts, Benjamin J. Stevens, Edmund Clarke, Ian Tooley, Jonathan Orchard, Ian Farrer, David T.D Childs, Nasser Babazadeh, Nobuhiko Ozaki, David Mowbray, Richard A. Hogg, “*Strain Balancing Of Metal-Organic Vapour Phase Epitaxy InAs/GaAs Quantum Dot Lasers*” *IEEE J. Sel. Top. Quantum Electron.*, vol. 23, no. 6, pp. 1–8, Nov. 2017.
2. R. J. E. Taylor, Guangrui Li, Pavlo Ivanov, David T. D. Childs, Timothy S. Roberts, Benjamin J. Stevens, Brett Harrison, Jayanta Sarma, Nasser Babazadeh, Gary Terrnent, Richard A. Hogg, “Mode Control in Photonic Crystal Surface Emitting Lasers Through External Reflection,” *IEEE J. Sel. Top. Quantum Electron.*, vol. 23, no. 6, pp. 1–8, Nov. 2017.
3. Nobuhiko Ozaki, David T. D. Childs, Jayanta Sarma, Timothy S. Roberts, Takuma Yasuda, Hiroshi Shibata, Hirotaka Ohsato, Eiichiro Watanabe, Naoki Ikeda, Yoshimasa Sugimoto, Richard A. Hogg, “*Superluminescent diode with a broadband gain based on self-assembled InAs quantum dots and segmented contacts for an optical coherence tomography light source,*” *J. Appl. Phys.*, vol. 119, no. 8, p. 83107, Feb. 2016.

Oral Presentations:

1. Timothy S. Roberts, Benjamin J. Stevens, Edmund Clarke, Ian Tooley, Jonathan Orchard, Ian Farrer, David T. D. Childs, Nasser Babazadeh, Nobuhiko Ozaki, David Mowbray, Richard A. Hogg, “*Opto-electronic Properties of Strain Compensated InAs/GaAs Quantum Dot Devices Grown by MOVPE*” UK Semiconductors Conference, Sheffield, July 2016.
2. Timothy S. Roberts, Benjamin J. Stevens, David T. D. Childs, Edmund Clarke, Richard A. Hogg, “*Development of Metal-Organic Vapour*

List of Publications

Phase Epitaxy of InAs/GaAs Quantum Dots” Sixth International conference on Optical, Optoelectronic and Photonic Materials and Applications, Leeds, July 2014.

Poster Presentations:

1. Timothy S. Roberts, Benjamin J. Stevens, Edmund Clarke, Ian Tooley, Jonathan Orchard, Ian Farrer, David T. D. Childs, Nasser Babazadeh, Nobuhiko Ozaki, David Mowbray, Richard A. Hogg, “*Characterisation of MOVPE InAs/GaAs QDs grown by MOVPE with and without strain balancing*” SPIE Photonics West, San Francisco, January 2017.
2. Timothy S. Roberts, Benjamin J. Stevens, Edmund Clarke, Ian Tooley, Jonathan Orchard, Ian Farrer, David T. D. Childs, Nasser Babazadeh, Nobuhiko Ozaki, David Mowbray, Richard A. Hogg, “*Strain balancing of MOVPE InAs/GaAs quantum dots using GaAs_{0.8}P_{0.2}*” 25th International Semiconductor Laser Conference, Kobe, September 2016.
3. Timothy S. Roberts, Benjamin J. Stevens, David T. D. Childs, Nasser Babazadeh, Edmund Clarke, Nobuhiko Ozaki, Richard A. Hogg, “*Long Wavelength & High Areal Density InAs/GaAs QDs Grown by MOVPE*” UK Semiconductors Conference, Sheffield, July 2015
4. Timothy S. Roberts, Benjamin J. Stevens, David T. D. Childs, Nasser Babazadeh, Edmund Clarke, Nobuhiko Ozaki, Richard A. Hogg, “*Long Wavelength & High Areal Density InAs/GaAs QDs Grown by MOVPE*” 16th European Workshop on Metalorganic Vapour Phase Epitaxy, Lund, June 2015.
5. Timothy S. Roberts, Benjamin J. Stevens, David T. D. Childs, Edmund Clarke, Richard A. Hogg, “*InAs/GaAs Quantum Dots By Metal-Organic Vapour Phase Epitaxy*” UK Semiconductors Conference, Sheffield, July 2014.

Glossary

Al	Aluminium
AlAs	Aluminium Arsenide
AlGaAs	Aluminium Gallium Arsenide
A	Amps
Å	Angstrom
Å/s	Angstrom per second
a.u	Arbitrary Units
As	Arsenic
AsH ₃	Arsine
AFM	Atomic Force Microscopy
E _g	Bandgap
C-V	Capacitance-Voltage
CCl ₄	Carbon tetrachloride
°C	Celcius
cm	Centimetre
CB	Conduction Band
CW	Continuous Wave
CuKα	Copper Kappa Alpha
IV	Current-Voltage
DMZn	Dimethylzinc
EME	Eigenmode expansion
eCV	Electrochemical Capacitance Voltage
EL	Electroluminescence
e-beam	electron beam

Glossary

eV	Electron Volts
E	Energy
epi-layer	Epitaxial Layer
EpiTT	Epitaxial True Temperature
C ₂ H ₆	Ethyl
ES 1	Excited State 1
ES 2	Excited State 2
EQE	External Quantum Efficiency
FM Growth	Frank Van Der Merwe Growth
Ga	Gallium
GaAs	Gallium Arsenide
GaAsP	Gallium Arsenide Phosphide
GaInP	Gallium Indium Phosphide
GaP	Gallium Phosphide
Ge	Germanium
Gb	Gigabits
Gb/s	Gigabits per second
g/mm	gratings per millimetre
GID	Grazing Incidence diffraction
GS	Ground State
III	Group III Element
IV	Group IV Element
V	Group V Element
VI	Group VI Element
Hz	Hertz
HMDS	Hexamethyldisilazane
ΔE_{hom}	Homogeneous Linewidth

Glossary

HF	Hydrofloric
In	Indium
InAs	Indium Arsenide
InGaAs	Indium Gallium Arsenide
InGaP	Indium Gallium Phosphide
InP	Indium Phosphide
IR	Infrared
ΔE_{inhom}	Inhomogeneous linewidth
K	Kelvin
kV	Kilovolt
LED	Light Emitting Diode
MOCVD	Metal-Organic Chemical Vapour Deposition
MOVPE	Metal-Organic Vapour Phase Epitaxy
CH ₃	Methyl
μeV	microelectron Volts
μm	micrometre
μs	Microsecond
Mid-IR	Mid-Infrared
mA	Milliamps
meV	Millielectron Volts
mW	Milliwatts
MBE	Molecular Beam Epitaxy
ML	Monolayer
ML/s	Monolayer per second
MQW	Multiple Quantum Well
nm	nanometre
Near-IR	Near-Infrared

Glossary

n-type	Negative Type doping
Nd:YAG	Neodymium-doped Yttrium Aluminium Garnet
ND	Neutral Density
1D	One-Dimension
O-band	Original Band
P	Phosphorous
PH ₃	Phosphine
PL	Photoluminescence
PC	Photonic Crystal
PCSEL	Photonic Crystal Surface Emitting Laser
PMGI	Polymethylglutarimide
p-type	Positive type doping
PID	Proportional–Integral–Derivative
QD	Quantum Dot
QD-PCSEL	Quantum Dot Photonic Crystal Surface Emitting Laser
QW	Quantum Well
QW-PCSEL	Quantum Well Photonic Crystal Laser
QWR	Quantum Wire
RHEED	Reflection High-Energy Electron Diffraction
RPM	Revolutions per minute
SEM	Scanning Electron Microscopy
s	Seconds
SiH ₄	Silane
Si	Silicon
SiO ₂	Silicon Dioxide
sccm	Standard Cubic Centimetre per minute
SRL	Strain reducing layer

Glossary

S-K	Stranski-Krastanov
SLED	Superluminescent Light Emitting Diode
TBAs	Tertiarybutylarsine
3D	Three-Dimensional
J_{th}	Threshold current density
g_{th}	Threshold gain
TEM	Transmission Electron Microscopy
TE	Transverse electric
TEGa	Triethyl-Gallium
TMAI	Trimethyl-Aluminium
TMAAs	Trimethylarsine
TMGa	Trimethyl-Gallium
TMIn	Trimethyl-Indium
2D	Two-Dimensional
UHV	Ultra High Vacuum
UV	Ultra Violet
VB	Valance Band
VCSEL	Vertical cavity surface emitting laser
VW	Volmer-Weber
V	Volts
W	Watts
λ	Wavelength
XRD	X-ray Diffraction
XRR	X-ray Reflectivity
Z_0	Zeroth order peak (Strain peak)

Intentionally Blank

Contents

Abstract	ii
Acknowledgements	iv
List of Publications	v
Glossary	vii
1. Introduction & Thesis Outline	3
1.1. Introduction	3
1.2. Chapter Two Outline	6
1.3. Chapter Three Outline	8
1.4. Chapter Four Outline	10
1.5. References	12
2. Epitaxial Growth & Quantum Dot Optimisation	15
2.1. Epitaxial Growth Techniques	15
2.2. Epitaxial Growth Modes	24
2.3. Material Characterisation	28
2.4. Low-Dimensional Structures	37
2.5. Literature Review	40
2.6. Quantum Dot Growth Optimisation	46
2.7. Removal of the Indium Diffusion Layer	65
2.8. Further Quantum Dot Optimisation	69
2.9. Conclusions	71
2.10. References	72
3. Strain Balancing of Quantum Dot Layers	81
3.1. Introduction	81
3.2. Background and Literature Review	84
3.3. LaserMod Modelling	89
3.4. LEPTOS Modelling	93
3.5. Growth Calibration	107
3.6. X-Ray Diffraction Studies of Device Structures	109
3.7. Preliminary Electrical and Optical Characterisation	117
3.8. Further Work	122
3.9. Conclusions	124

Contents

3.10. References	126
4. Optoelectronic Device Fabrication, Measurement and Modelling ...	132
4.1. Introduction	132
4.2. Background and Literature Review	134
4.3. Device Fabrication	140
4.4. Electroluminescent Mesa Diodes	145
4.5. Broad Area Fabry-Perot Lasers	149
4.6. Further Quantum Dot Laser Development	156
4.7. Photonic Crystal Laser Modelling	159
4.8. Epitaxial Overgrowth of Planar Structures	183
4.9. Further Work	186
4.10. Conclusions	187
4.11. References	189
5. Conclusions and Further Work	199

Chapter 1:

Introduction and Thesis Outline

1.1 Introduction

In this thesis, the focus will be to study the epitaxial growth of III/V compound semiconductor materials. In particular, it describes a study of the growth and development of strain-balanced InAs/GaAs quantum dot (QD) structures and laser devices by metal-organic vapour phase epitaxy (MOVPE). QDs have been of considerable interest over the past 35 years since the prediction of Arakawa and Sakaki of their potential benefits for injection lasers. [1] There are many III/V compounds including both binary e.g. GaAs, InP etc., and ternary, e.g. InGaAs, AlGaAs etc. but a very limited number of substrates; almost all epitaxial growth is on GaAs or InP. Figure 1.1 shows the energy bandgap versus the unstrained lattice constant for the most common III/V semiconductors as well as the two elemental semiconductors Si and Ge. [2] For III/V compound semiconductors grown on a GaAs substrate, a similar lattice constant (5.65 \AA) is required for pseudomorphic growth. However, for the formation of self-

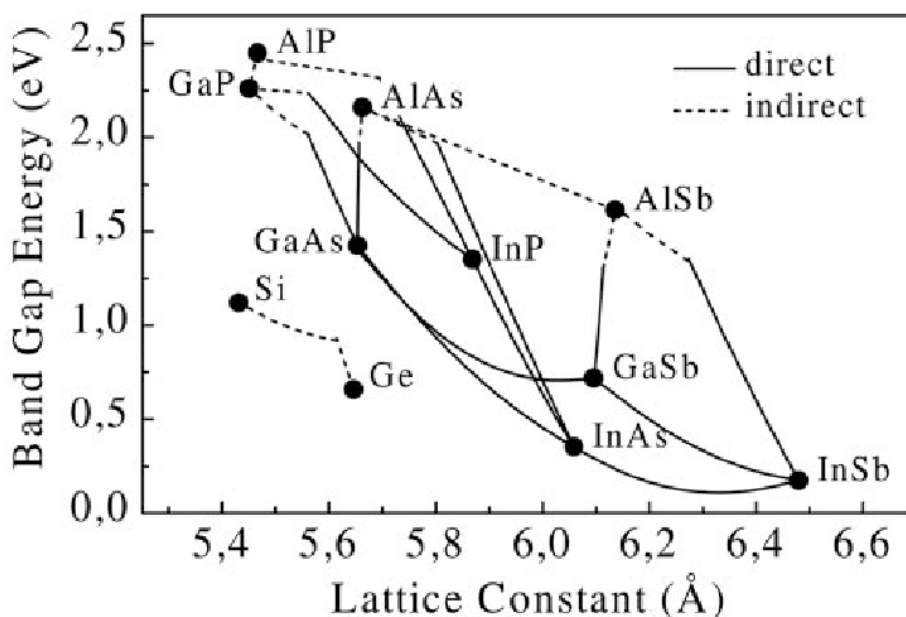


Figure 1.1: Energy bandgap versus the unstrained lattice constant for the most common III/V semiconductors. [2]

assembled QDs using the Stranski-Krastanov growth mode, a large difference in lattice constant is required. For the present study InAs is used, with a 7% difference in lattice constant compared to GaAs. Self-assembled InAs QDs grown on GaAs emit in the near infrared region between 1.1 and 1.3 μm . Although the majority of studies have used Molecular Beam Epitaxy (MBE), a relatively small number of research groups have studied the growth of self-assembled QDs by MOVPE, including reports of ground state lasing at room temperature. [3]–[11]

InAs/GaAs self-assembled QD lasers have applications in telecommunication systems operating within the O-band. In addition, QDs have potential in a number of other different applications. These include semiconductor optical amplifiers, with fast gain recovery allowing high bit rate (>40 Gb/s) pattern-free signal amplification [12], solar cells, where InAs/GaAs QDs can extend the absorption band of GaAs-based cells [13] [14], superluminescent light emitting diodes (SLEDs) with a broad emission bandwidth suitable for optical coherence tomography [15], saturable absorber mirrors with low saturation fluence and fast absorption recovery [16], mid- and far-IR photodetectors with normal incidence operation [17], and single photon sources with fast on demand operation and on-chip integration for quantum information applications. [18]

MOVPE is the growth technique of choice for this thesis as it lends itself to large-scale manufacturing, due to the high uptime and volume scalability. In addition, epitaxial regrowth is significantly more mature in MOVPE, with polycrystalline-free selective area regrowth being highly challenging for molecular beam epitaxy (MBE). However, MBE is the preferred method of choice for QD growth for most research groups and industry, partly due to the availability of in situ characterisation techniques, such as reflection high-energy electron diffraction (RHEED) that allows direct and real-time observation of QD formation.

InAs/GaAs QD structures and devices contain a large amount of strain and this can easily result in the formation of dislocations, which relieve the strain but significantly degrade the optical efficiency. This is a particular problem in structures with multiple QD layers with a relatively small inter-layer separation,

Chapter 1: Introduction and Thesis Outline

as may be required in a laser device. This thesis describes the design and implementation of a strain-balancing layer, placed between the QD layers, which compensates the strain produced by the QDs. With the introduction of a suitable strain-balancing layer, the total internal strain can be reduced close to zero. Achieving a net strain of zero for each period of a QD structure allows the total number of QD layers to be increased and the layers to be placed closer together. The latter property is of particular importance for a laser where it is necessary to place a small number of QD layers close to the maximum of the optical cavity mode, hence achieving a higher total gain.

Following the development of strain balanced InAs/GaAs self-assembled QDs for standard edge emitting Fabry-Perot laser structures; integration into a relatively new type of semiconductor laser, a photonic crystal surface emitting laser (PCSEL) is discussed. The modelling of the PCSEL waveguide is developed and initial investigations of sample overgrowth during PCSEL fabrication described. Such lasers offer the possibility of vertical emission, very low beam divergences, as low as 1 degree, beam steering, high power single mode operation and wavelength selectivity. [19]–[27]

1.2 Chapter 2 Outline

Chapter 2 provides relevant background and describes the development of single and five stacked layers of InAs/GaAs QDs for the active regions of lasers.

Section 2.1 discusses both molecular beam epitaxy (MBE) and MOVPE growth technologies. MBE is the usual growth technique used in the fabrication of QDs and therefore the basic principles behind MBE growth are discussed. However, the growth technology used in this thesis is MOVPE and hence this technique is discussed in more detail. Topics covered include the precursors available for the group III's and group V's, metal-organics and metal-hydrides, and the pyrolysis process that both types of precursors undergo to enable epitaxial growth. The precursors used in MOVPE can create unintentional doping within the structure, which is discussed as well as intentional doping. Both n-type and p-type doping is described along with the materials and precursors that can be used. Section 2.1 is completed with an outline of the differences between MBE and MOVPE.

Section 2.2 discusses the two fundamental epitaxial growth modes, homoepitaxy and heteroepitaxy, including the consequences of strain in heteroepitaxy. In addition, the three growth modes pseudomorphic, Stranski-Krastanov (S-K) and Volmer-Weber (VW) are described with particular emphasis on pseudomorphic and S-K growth as these are the ones most relevant to this thesis.

Section 2.3 describes the sample and device characterisation techniques used in this work. Nomarski microscopy is used to characterise the surface morphology. In addition, atomic force microscopy (AFM) can also be used to characterise the surface morphology and determine the density of surface QDs. Electron microscopy techniques, scanning electron microscopy (SEM) and transmission electron microscopy (TEM), are discussed. SEM is used to study the etch profiles during device fabrication and TEM is used to determine epitaxial layer thicknesses and QD densities. Two doping level characterisation techniques, electrochemical capacitance voltage (eCV) and Hall measurements are introduced and their differences discussed. Electroluminescence (EL) and

Chapter 1: Introduction and Thesis Outline

photoluminescence (PL) are used to study the optical properties of the semiconductors. These techniques provide information on QD uniformity, optical efficiency and confinement potentials. Section 2.4 describes how the electronic and optical properties of a semiconductor are changed by altering its dimensionality.

Section 2.5 is a literature review where the growth parameters for optimum QD growth are discussed for both MOVPE and MBE. Section 2.5 describes the optimisation process for the growth of InAs/GaAs QDs by MOVPE. The first parameter optimised is the InAs coverage with initial studies identifying the point at which the S-K transition occurs. After determining the S-K transition, the amount of InAs coverage is optimised. Further growth parameters, including growth rate and V/III ratio for the QD growth, are studied and optimised. Following the growth optimisation of a single QD layer structure, multiple QD layer structures are studied. This identifies an issue with surface morphology, which is rectified by optimising the V/III ratio used during the growth of the QD capping layer.

Section 2.6 studies the effect of changing the initial QD capping layer thickness and introduces an annealing step after the initial cap growth in an attempt to remove an unintentional indium diffusion layer, which is observed above every QD layer.

1.3 Chapter 3 Outline

Chapter three discusses the development of strain balancing which is of significant importance for opto-electronic devices such as lasers and optical amplifiers.

Section 3.1, introduces the concept of strain balancing to reduce the overall strain within each period of a QD structure to zero. This should allow a closer separation between QD layers, increasing the QD volumetric density. Section 3.2 provides a background and literature review, with different strain balancing materials and techniques, as used for both QWs and QDs, considered.

Section 3.3 discusses the modelling of the electrical characteristics and lasing threshold current densities of a dual QW with a $\text{GaAs}_z\text{P}_{1-z}$ barrier. Different concentrations of phosphorous are modelled using LaserMod by RSoft to study the effect of different potential barrier heights.

Section 3.4 describes the modelling of X-Ray diffraction (XRD) spectra of different strained material systems, using Leptos software provided by Bruker. Initially single layers, with either compressive or tensile strain, are modelled to understand how the change in strain affects the XRD spectra. Further work models the behaviour of different components of the device structure, such as the repeat thickness, concentration of indium within the QW and the thickness of the QW. Modelling of QW structures, with an average indium concentration similar to that expected for QD layers, is used to predict when the structure will be strain balanced.

Section 3.5 outlines the structure and the method used in the calibration of the MOVPE material flow rate for the strain-balancing layer. The concentration of phosphorus in the grown sample is determined using XRD and the calibrated flow rates will be used in the strain-balancing layer.

Section 3.6 discusses QD structures with different separation thicknesses between each QD layer, which are studied to experimentally determine the effect of $\text{GaAs}_{0.8}\text{P}_{0.2}$ strain-balancing layers. Section 3.7 presents the electrical

Chapter 1: Introduction and Thesis Outline

and optical characteristics of the structures described in section 3.6, revealing the differences between a strain balanced structure and a non-strain balanced structure.

Section 3.8 discusses potential further work required to understand carrier transport mechanisms across the barrier produced by the strain-balancing layer. This would involve the study of different combinations of barrier thickness and height, the latter controlled by the concentration of phosphorus. Section 3.9 summarises the work presented in chapter 3.

1.4 Chapter 4 Outline

Chapter four describes the study of InAs/GaAs edge emitting QD lasers grown by MOVPE and the modelling of a QD-PCSEL.

Following an introduction (section 4.1), section 4.2 reviews relevant literature and provides a background to lasers, especially QD lasers grown by both MOVPE and MBE.

Section 4.3 discusses the differences between positive and negative photoresists and considers dry and wet etching with the advantages and disadvantages for the etch profile described. The fabrication processes used in the thesis are discussed in detail.

Section 4.4 presents the initial results of a study of a structure with five QD layers and a 50 nm separation thickness. A temperature dependent study is conducted to examine the role of carrier capture and escape. Further optimisation of the InAs coverage is described, where a bimodality of the QDs is shown to reduce with an increase in coverage although at the expense of a reduction in the optical efficiency.

Section 4.5 presents the principles behind Fabry-Perot lasers and the differences between stripe and ridge lasers. Two structures with different QD layer separations of 50 and 30 nm and without strain balancing along with three strain-balanced structures with layer separations of 50, 30 and 20 nm, are fabricated into broad area lasers and characterised. The broad area lasers are fabricated with a range of cavity lengths and ridge widths. Threshold current density and emission spectra both above and below threshold are compared over a range of temperatures. In addition, the initial characterisation of recently grown lasers, developed as part of an ongoing optimisation processes, demonstrate room temperature operation.

Section 4.6 discusses the modelling and background to PCSELS, a relatively new type of semiconductor laser. This section outlines the theory behind PCSELS and the benefits of a PCSEL in comparison to more conventional laser

Chapter 1: Introduction and Thesis Outline

structures. Two PCSEL fabrication techniques are discussed and compared. Waveguide modelling of a PCSEL containing InAs/GaAs QDs is performed for different thicknesses of a GaAs ballast layer and an AlAs repulsion layer. Three different structures are considered: void/GaAs, InGaP/GaAs and GaAs/AlAs. The modelling is conducted using Fimmwave software provided by Photon Design.

Section 4.7 presents the initial overgrowth investigation of an eight QD layer sample provided by QD Laser Inc.. The PL and EL emission spectra are compared before and after overgrowth to investigate any change to the QD emission. The effect of using an AlAs layer is investigated by comparing two structures, one containing the AlAs layer above the active region and one with an $\text{Al}_{0.42}\text{Ga}_{0.58}\text{As}$ cladding.

Section 4.8 discusses the further work required to optimise the QD growth and device design to obtain a room temperature strain balanced laser with a small layer separation of 20 nm. In addition, future work required to obtain a QD-PCSEL based on the material provided by QD Laser Inc. is discussed.

Chapter 5 provides a conclusion to the thesis and a summary of possible future work.

1.5 References

- [1] Y. Arakawa and H. Sakaki, "Multidimensional quantum well laser and temperature dependence of its threshold current," *Appl. Phys. Lett.*, vol. 40, no. 11, p. 939, 1982.
- [2] A. W. Bett, F. Dimroth, G. Stollwerck, and O. V. Sulima, "III-V compounds for solar cell applications," *Appl. Phys. A Mater. Sci. Process.*, vol. 69, no. 2, pp. 119–129, Aug. 1999.
- [3] J. Tatebayashi *et al.*, "Low threshold current operation of self-assembled InAs/GaAs quantum dot lasers by metal organic chemical vapour deposition," *Electron. Lett.*, vol. 39, no. 15, p. 1130, 2003.
- [4] I. N. Kaiander *et al.*, "1.24 μm InGaAs/GaAs quantum dot laser grown by metalorganic chemical vapor deposition using tertiarybutylarsine," *Appl. Phys. Lett.*, vol. 84, no. 16, p. 2992, 2004.
- [5] a. Passaseo, G. Maruccio, M. De Vittorio, R. Rinaldi, R. Cingolani, and M. Lomascolo, "Wavelength control from 1.25 to 1.4 μm in $\text{In}_x\text{Ga}_{1-x}\text{As}$ quantum dot structures grown by metal organic chemical vapor deposition," *Appl. Phys. Lett.*, vol. 78, no. 10, p. 1382, 2001.
- [6] N. Nuntawong *et al.*, "Quantum dot lasers based on a stacked and strain-compensated active region grown by metal-organic chemical vapor deposition," *Appl. Phys. Lett.*, vol. 86, no. 19, p. 193115, 2005.
- [7] D. Bhattacharyya *et al.*, "Spectral and dynamic properties of InAs-GaAs self-organized quantum-dot lasers," *IEEE J. Sel. Top. Quantum Electron.*, vol. 5, no. 3, pp. 648–657, May 1999.
- [8] J. Tatebayashi *et al.*, "Lasing at 1.28 μm of InAs–GaAs Quantum Dots With AlGaAs Cladding Layer Grown by Metal-Organic Chemical Vapor Deposition," *IEEE J. Sel. Top. Quantum Electron.*, vol. 11, no. 5, pp. 1027–1034, 2005.
- [9] D. Guimard *et al.*, "Ground state lasing at 1.30 μm from InAs/GaAs quantum dot lasers grown by metal-organic chemical vapor deposition.," *Nanotechnology*, vol. 21, no. 10, p. 105604, Mar. 2010.
- [10] T. Yang, M. Nishioka, and Y. Arakawa, "Optimizing the GaAs capping layer growth of 1.3 μm InAs/GaAs quantum dots by a combined two-temperature and annealing process at low temperatures," *J. Cryst.*

- Growth*, vol. 310, no. 24, pp. 5469–5472, Dec. 2008.
- [11] S. . Park, J. Tatebayashi, and Y. Arakawa, “Structural and optical properties of high-density ($10^{11}/\text{cm}^2$) InAs QDs with varying Al(Ga)As matrix layer thickness,” *Phys. E Low-dimensional Syst. Nanostructures*, vol. 21, no. 2–4, pp. 279–284, Mar. 2004.
- [12] T. Akiyama, N. Hatori, Y. Nakata, H. Ebe, and M. Sugawara, “Pattern-effect-free amplification and cross-gain modulation achieved by using ultrafast gain nonlinearity in quantum-dot semiconductor optical amplifiers,” *Phys. status solidi*, vol. 238, no. 2, pp. 301–304, Jul. 2003.
- [13] C. G. Bailey, D. V. Forbes, R. P. Raffaele, and S. M. Hubbard, “Near 1 V open circuit voltage InAs/GaAs quantum dot solar cells,” *Appl. Phys. Lett.*, vol. 98, no. 16, p. 163105, Apr. 2011.
- [14] A. Martí *et al.*, “Production of Photocurrent due to Intermediate-to-Conduction-Band Transitions: A Demonstration of a Key Operating Principle of the Intermediate-Band Solar Cell,” *Phys. Rev. Lett.*, vol. 97, no. 24, p. 247701, Dec. 2006.
- [15] P. D. L. Greenwood *et al.*, “Quantum Dot Superluminescent Diodes for Optical Coherence Tomography: Device Engineering,” *IEEE J. Sel. Top. Quantum Electron.*, vol. 16, no. 4, pp. 1015–1022, Jul. 2010.
- [16] E. U. Rafailov *et al.*, “Fast Quantum-Dot Saturable Absorber for Passive Mode-Locking of Solid-State Lasers,” *IEEE Photonics Technol. Lett.*, vol. 16, no. 11, pp. 2439–2441, Nov. 2004.
- [17] E. Towe and D. Pan, “Semiconductor quantum-dot nanostructures: Their application in a new class of infrared photodetectors,” *IEEE J. Sel. Top. Quantum Electron.*, vol. 6, no. 3, pp. 408–421, May 2000.
- [18] M. N. Makhonin *et al.*, “Waveguide Coupled Resonance Fluorescence from On-Chip Quantum Emitter,” *Nano Lett.*, vol. 14, no. 12, pp. 6997–7002, Dec. 2014.
- [19] K. Hirose, Y. Liang, Y. Kurosaka, A. Watanabe, T. Sugiyama, and S. Noda, “Watt-class high-power, high-beam-quality photonic-crystal lasers,” *Nat. Photonics*, vol. 8, no. 5, pp. 406–411, May 2014.
- [20] S. Noda, N. Yamamoto, H. Kobayashi, M. Okano, and K. Tomoda, “Optical properties of three-dimensional photonic crystals based on III–V semiconductors at infrared to near-infrared wavelengths,” *Appl. Phys.*

- Lett.*, vol. 75, no. 7, p. 905, Aug. 1999.
- [21] M. Imada, S. Noda, A. Chutinan, T. Tokuda, M. Murata, and G. Sasaki, “Coherent two-dimensional lasing action in surface-emitting laser with triangular-lattice photonic crystal structure,” *Appl. Phys. Lett.*, vol. 75, no. 3, p. 316, Jul. 1999.
- [22] R. J. E. Taylor *et al.*, “Electronic control of coherence in a two-dimensional array of photonic crystal surface emitting lasers,” *Sci. Rep.*, vol. 5, no. 1, p. 13203, Oct. 2015.
- [23] R. J. E. Taylor *et al.*, “Mode Control in Photonic Crystal Surface Emitting Lasers Through External Reflection,” *IEEE J. Sel. Top. Quantum Electron.*, vol. 23, no. 6, pp. 1–8, Nov. 2017.
- [24] R. J. E. Taylor, P. Ivanov, G. Li, D. T. D. Childs, and R. A. Hogg, “Optimisation of photonic crystal coupling through waveguide design,” *Opt. Quantum Electron.*, vol. 49, no. 2, p. 47, Feb. 2017.
- [25] R. J. E. Taylor *et al.*, “All-Semiconductor Photonic Crystal Surface-Emitting Lasers Based on Epitaxial Regrowth,” *IEEE J. Sel. Top. Quantum Electron.*, vol. 19, no. 4, pp. 4900407–4900407, Jul. 2013.
- [26] D. M. Williams *et al.*, “Epitaxially Regrown GaAs-Based Photonic Crystal Surface-Emitting Laser,” *IEEE Photonics Technol. Lett.*, vol. 24, no. 11, pp. 966–968, Jun. 2012.
- [27] E. Miyai, K. Sakai, T. Okano, W. Kunishi, D. Ohnishi, and S. Noda, “Lasers producing tailored beams,” *Nature*, vol. 441, no. 7096, pp. 946–946, Jun. 2006.

Chapter 2:

Epitaxial Growth & Quantum

Dot Optimisation

2.1 Epitaxial Growth techniques

This chapter introduces the two main epitaxial growth techniques used in both industry and research environments for the production of advanced low-dimensional semiconductor structures and devices, the epitaxial growth modes, material characterisation and the growth optimisation of quantum dots (QDs).

The two main epitaxial growth methods are molecular beam epitaxy (MBE) and metal-organic vapour phase epitaxy (MOVPE). MOVPE is also known as metal-organic chemical vapour deposition (MOCVD) but for this thesis, the acronym used is MOVPE. Both epitaxial growth techniques can be used to form a wide range of crystalline materials but here we will focus only on compounds of group III and group V elements, commonly known as III/V semiconductors.

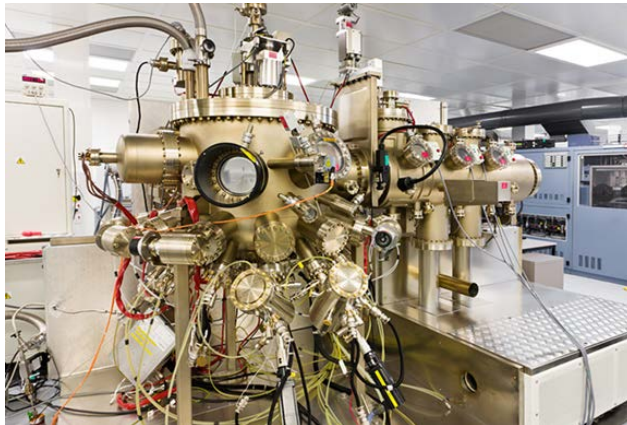


Figure 2.1: Photograph of a V90 MBE growth reactor at the University of Sheffield.

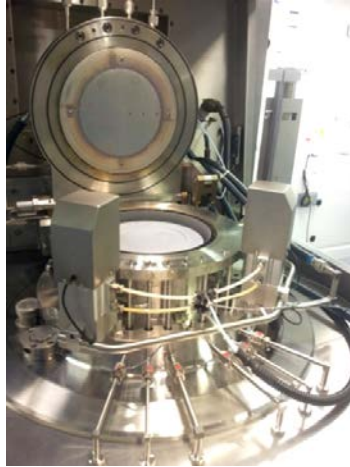


Figure 2.2: Photograph of the inside of a Thomas Swan MOVPE reactor chamber.

A brief introduction into MBE is presented, as MBE growth of QDs is the preferred method of choice for most research groups and industry. A more detailed introduction to MOVPE will be given, as this is the growth method used in this thesis. The state-of-the-art growth of QDs by MBE and MOVPE will be discussed and the main differences between both growth methods explained. Figure 2.1 is a photograph of a VG V90 MBE growth reactor and figure 2.2 is the Thomas Swan closed coupled showerhead MOVPE growth reactor, both are in the clean rooms at the University of Sheffield.

MBE growth is a conceptually simple epitaxial technique, occurring in an ultra-high vacuum (UHV) ($\sim 10^{-9}$ mbar) environment and for a low growth rate

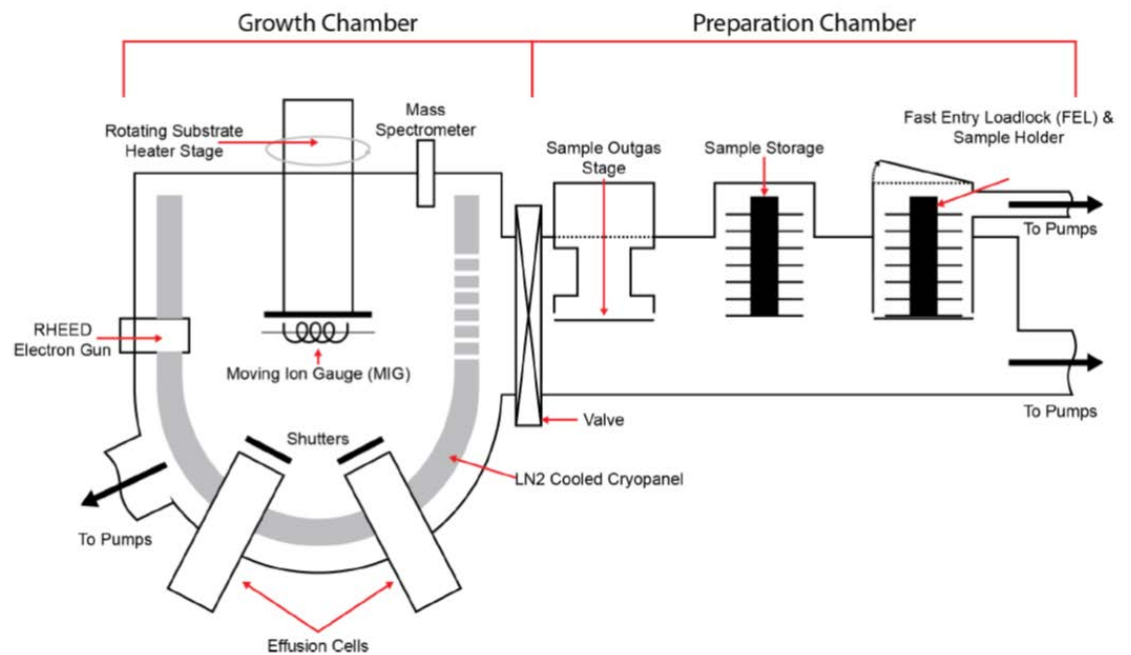


Figure 2.3: Schematic diagram of an MBE reactor.

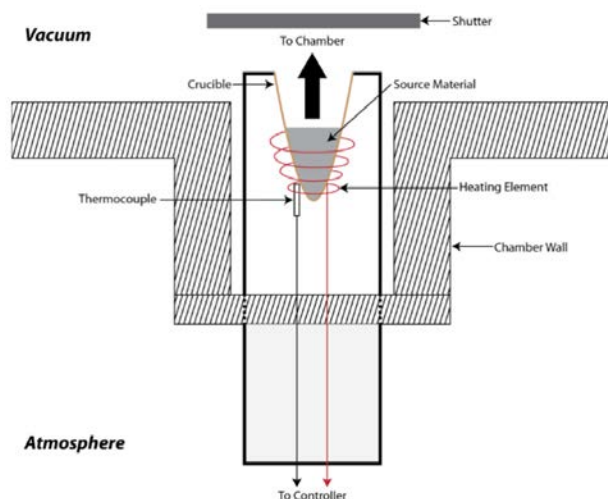


Figure 2.4: Schematic diagram of a group III effusion cell.

(typically $<3 \text{ \AA/s}$). Figure 2.3 shows a diagram of an MBE reactor, there are two parts: the growth chamber and the preparation chamber, separated by a vacuum gate valve. Source materials for MBE are usually elemental compounds such as gallium and arsenic that are in a very pure form in a ceramic crucible, which forms an effusion cell (figure 2.4); heating of the cell causes the elemental source to evaporate/sublimate. The flux of material emitted from each cell is measured using an ion gauge placed in front of the substrate stage prior to growth. In addition, for group V elements, such as arsenic, a cracker cell is added to crack the tetramers (As_4) to dimers (As_2). The temperature of each cell and the substrate can be set independently, which means epitaxial growth can

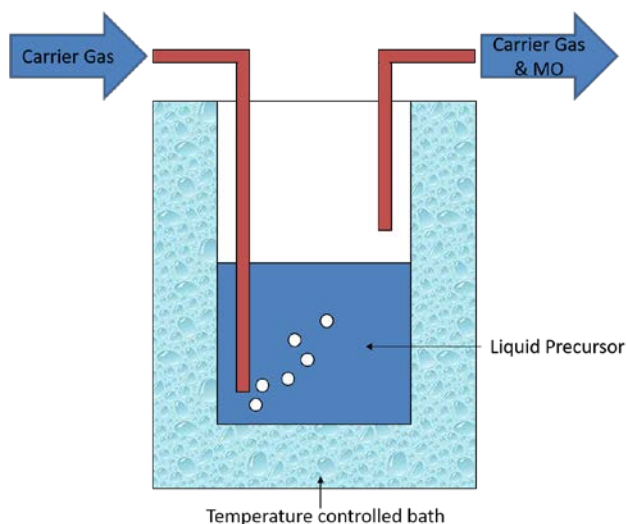


Figure 2.5: Schematic of a metal-organic storage bubbler.

theoretically occur at any temperature. The growth rate of the semiconductor will be mainly determined by the arrival rate of the elements, which in turn is controlled by the temperature(s) of the effusion cells. Mechanical shutters are placed in front of each effusion cell, allowing the switching of the atomic beams and hence the growth of layers of different semiconductors. *In situ* monitoring during the growth is important; temperature control of the cells and substrate is achieved using thermocouple PID loops, with additional temperature monitoring of the substrate by a pyrometer or band-edge thermometry. The epitaxial process can also be monitored directly by reflection high-energy electron diffraction (RHEED). For this technique, high-energy electrons are directed towards the substrate at a glancing angle from which they reflect or diffract to be detected. The form of the diffraction pattern provides real-time information on the surface structure; for example the presence or not of an oxide layer or the change in surface reconstruction that occurs for certain growth conditions (particularly temperature) and the transition between 2D to 3D growth which occurs when QDs are formed.

The MOVPE process uses metal-organics for the group III precursors and hydrides for the group V, although metal-organics can also be used for the latter; these will not be discussed here. The group III metal-organic is transferred to the reactor by a carrier gas, usually hydrogen but nitrogen can also be used. Metal organic precursors are stored in a bubbler, as shown in figure 2.5, the

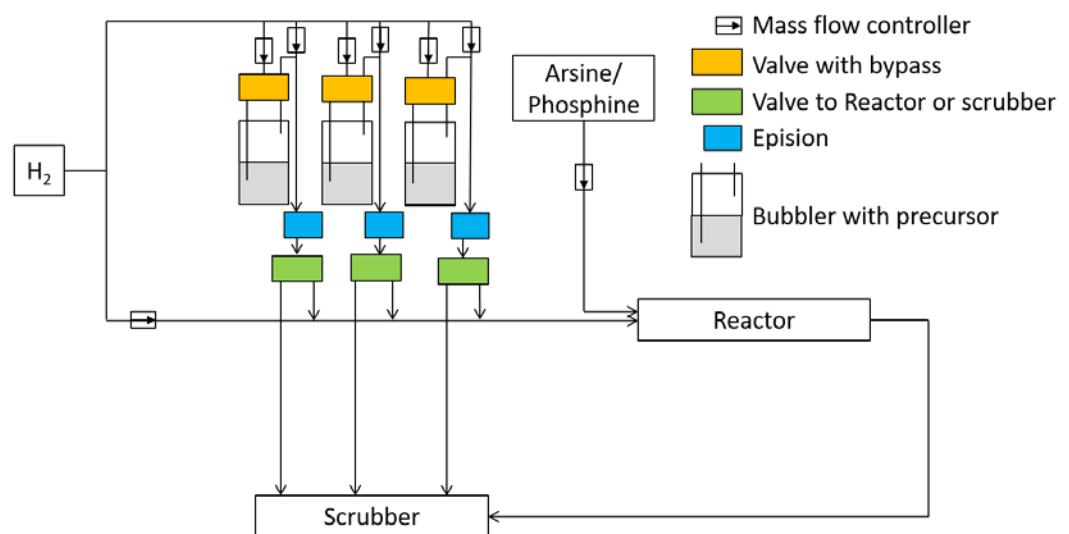


Figure 2.6: Schematic diagram of a typical MOVPE growth reactor.

carrier gas is passed through the precursor and metal organics are picked up and transferred to the reactor. Group V elements are usually stored as metal hydrides in gaseous form and transferred directly to the reactor. Figure 2.6 shows a simplified diagram of an MOVPE reactor. Mass flow controllers control the rate of gas flow that is allowed to pass through the reactor. Above each bubbler is a valve with a bypass so a flow can be established before the selected metal organic is used. The amount of metal-organic can be further diluted by altering the mass flow controller on the dilution line of the source. Epision is a measurement system, which measures the inline gas concentration of the metal organic flow, allowing the flow rate to be adjusted during the growth. The metal-organic is switched via another valve to either flow into the reactor or to bypass it; this allows the flow rate of the group III precursor to be stabilised before the gas enters the reactor. The metal hydride of the group V element is transferred straight to the reactor because it is already in a gaseous form. The scrubber is a heated cylinder on the exhaust side of the reactor containing charcoal; this removes the harmful leftover group III/V elements and compounds.

When the metal-organics and metal hydrides are transferred to the reactor, they need to decompose for the metal to be liberated for epitaxial growth; this is achieved above the heated substrate, through heat and in the absence of oxygen causing a process called pyrolysis. Pyrolysis is the separation of the metal from the organic material or hydrogen. A chemical reaction occurs between the group III and V metals to form a III-V compound, which is deposited as the epitaxial layer. With the group V metal being more volatile the group V compound is usually present in excess. The cracking of the precursors is an important part of the MOVPE epitaxial process. If the temperature is too low, the precursors do not fully crack causing carbon to become incorporated into the epitaxial semiconductor, creating unwanted dopants. If the temperature is too high, the metals will have too much energy to remain on the growth surface and will not be incorporated into the epitaxial material. Therefore, the control of the substrate temperature is critical to ensure good quality crystal growth. To achieve this, *in-situ* monitoring by emissivity-corrected pyrometry is used to control the true temperature of the substrate, this is referred to as epitaxial true

temperature (EpiTT). The minimum growth temperature is usually determined by the group V element because a higher energy is generally needed to break both the chemical bonds between the metal-organic and the metal-hydrogen of the group V elements. In this thesis, we will only be interested in MOVPE mass flow growth mechanism, where the growth rate is independent of substrate temperature. Optimum growth temperatures vary for different materials. For example GaAs is usually grown at 630°C to achieve the highest quality material, for an indium containing tertiary material, such as InGaAs, a much lower growth temperature, in the region of 560°C, is used, this is required to minimise indium desorption which starts to occur above 540°C. For aluminium containing layers, a much higher temperature, in the region of 680°C, is used due to the short diffusion length of the aluminium atoms. The growth rate is controlled by the group III molecule. *In-situ* monitoring during the epitaxial growth, is important to ensure good morphology, correct growth temperature and growth rates. The surface morphology can be monitored using reflectivity measurements and if a problem occurs during the growth, corrective actions such as increasing the growth temperature or altering the growth rates can be applied. Although measuring the true temperature of the epitaxial wafer and reflectivity monitoring are very useful tools, the lack of an ultra-high vacuum prevents the greater range of monitoring techniques that are available in MBE, such as RHEED.

There are two main organic molecules that can be attached to the group III metal to form the metal-organic compound: trimethyl and triethyl. Trimethyl is made up of three methyl groups (CH₃) and triethyl is made up of three ethane groups (C₂H₆). The pyrolysis of the trimethyl group occurs at a higher temperature compared to that of the triethyl group due to the reduced bonding strength of the (C₂H₆) group compared to the (CH₃) group. According to G. Stringfellow the pyrolysis temperatures of trimethylgallium (TMGa) and triethylgallium (TEGa) are 500°C and 400°C respectively, and a similar difference is found for other group III precursors. [1]

Carbon incorporation from the organic is an important factor when considering precursor choice, with carbon acting as a dopant of III-V materials. Trimethyl groups can produce unintentional doping due to the CH₃ group decomposing

into highly reactive CH_2 , which decomposes readily into carbon, and can subsequently be incorporated in the epitaxial layer. This unwanted effect can be mitigated through the use of hydrides to provide hydrogen on the surface, which aids the removal of carbon. This issue of carbon incorporation does not occur as readily with the use of triethyl groups because the pyrolysis process does not produce the CH_3 radical. However, the most commonly used precursor is trimethyl due to the higher stability of the metal-organic and higher vapour pressure. The triethyl metal-organic is reported to produce parasitic reactions and can decompose within the storage bottle. [1]

For the group III elements, the precursors available on the MOVPE system used for this work were TMGa, trimethylaluminium (TMAI) and trimethylindium (TMIn). Metal hydrides, such as arsine (AsH_3) and phosphine (PH_3), are common precursors for the group V element. The main disadvantage of using these hydrides is their high toxicity level; this requires significant safety measures to ensure they do not leak. Safer precursors are available, such as tertiarybutylarsine (TBAs) and trimethylarsine (TMAs). However, the lower pyrolysis temperatures of TBAs and TMAs, compared to AsH_3 and PH_3 , can result in an increase in unintentional carbon doping. [1] Lower carbon doping levels are achieved with the hydrides, due to the elemental hydrogen present on the substrate surface aiding the removal of the methyl radical, whilst providing the group V element. The group V precursors used in this thesis are arsine and phosphine.

For electrical devices, extrinsic doping is required to increase the conductivity from the low levels that result from intrinsic carriers. In addition, both n- and p-type doping are required to form a p-n junction, which is the basis of all electro-optical devices. To achieve the required doping levels impurities are added to the semiconductor to dope either p-type (holes) or n-type (electrons). Figure 2.7 shows a schematic diagram of p-type and n-type doping. p-type doping is the addition of extra holes; to achieve p-type doping in III-V's, group II elements, such as beryllium and magnesium, are used, in addition some transition metals can also be used, e.g. zinc. n-type doping is the addition of extra electrons; to

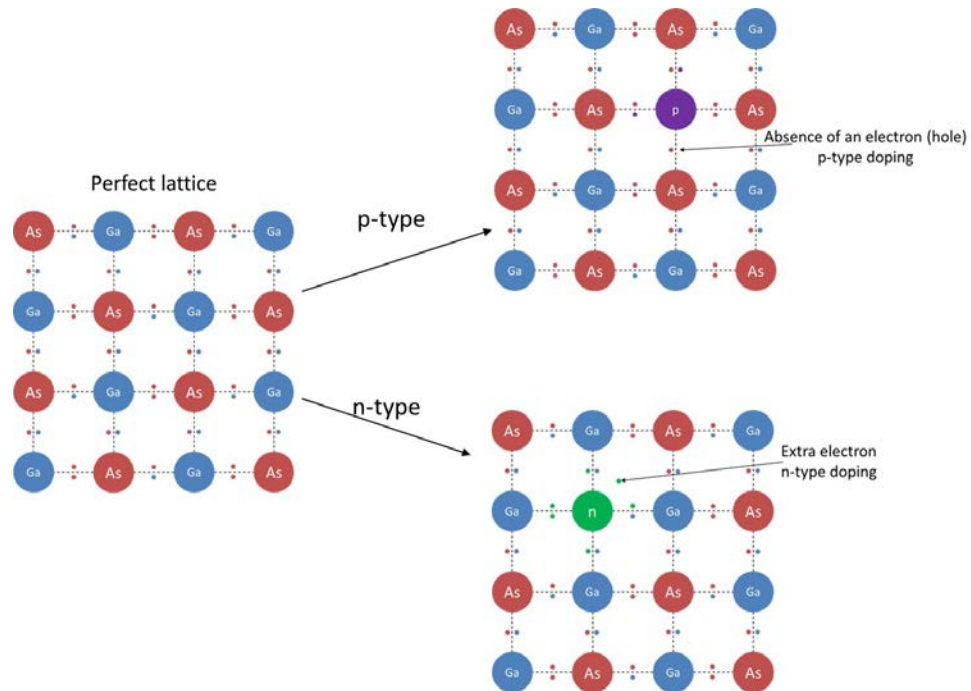


Figure 2.7: Diagram representing p- and n-type doping in the GaAs material system.

achieve n-type doping group VI elements, such as tellurium and selenium, are used. Group IV elements, such as silicon and carbon, can produce both n- and p-type doping, when the group III element is replaced by a group IV element the resulting doping is n-type, this occurs if silicon is used as a dopant. When the group V element is replaced by a group IV element, the resulting doping is p-type; this occurs if carbon is used as a dopant. Precursors for dopants include hydrides (e.g. silane (SiH_4)), or metal-organics (e.g. dimethylzinc (DMZn)) both these dopant precursors are available on the MOVPE growth system used in this thesis. Precise control of the amount of zinc used for p-type doping is found to be difficult due to the high vapour pressure of DMZn , in particular low doping levels are difficult to achieve and control. For the work described in this thesis, silicon was used as the n-type dopant, with SiH_4 as a precursor and carbon was used as the p-type dopant, with carbon tetrachloride (CCl_4) as the precursor.

The main differences between MBE and MOVPE is the difference between the precursors, with MBE a molecular source is used and in MOVPE a metal-organic is used. MBE has the advantage of the separation of the substrate and source temperatures, whilst MOVPE does not. Therefore, the growth temperatures in MBE are usually lower than in MOVPE. MBE has the benefit

of RHEED, which can directly observe the Stranski-Krastanov (S-K) transition, which is used to form self-assembled quantum dots (QDs). Measuring the true wafer temperature is important in both MOVPE and MBE. The temperature is controlled using pyrometry in both epitaxial techniques. However, band edge thermometry is also available for MBE but this measurement of temperature relies upon relevant data for the material being grown. Therefore, new materials can be difficult to monitor with this technique.

A major advantage of MOVPE is the relative ease of scalability to grow on a large number of large substrates simultaneously, giving high throughput. In addition, the lack of an ultra-high vacuum results in shorter downtimes following problems and/or maintenance of the reactor. As a result, MOVPE is the chosen growth technique for most commercial applications. With MOVPE, the growth of phosphorous containing structures is more straight forward than with MBE. The use of phosphine presents few additional complications as all the required safety precautions are already in place for the handling of arsine. An additional benefit of MOVPE is that epitaxial regrowth is significantly more mature, with polycrystalline-free selective area regrowth being highly challenging with MBE. However, as the growth of self-assembled QDs was developed in research laboratories, where MBE is considerably more common, the MOVPE growth of these structures is relatively immature. In particular, the real time observation of the S-K transition by RHEED and the slower growth rates available in MBE are advantageous for QD growth. However, commercial exploitation is likely to require MOVPE growth.

2.2 Epitaxial Growth Modes

This section will introduce the different growth modes that can occur in semiconductor epitaxial growth.

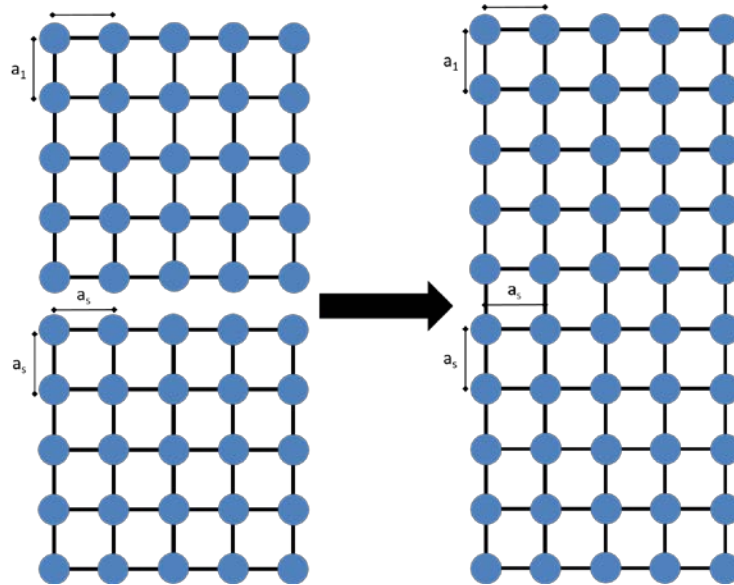


Figure 2.8: Diagram of the crystal formation for homoepitaxy.

Homoepitaxy is growth of an epitaxial layer (epi-layer), which comprises the same material as the substrate. An example of this would be growth of GaAs on a GaAs substrate; figure 2.8 shows the crystal structure with a constant lattice spacing.

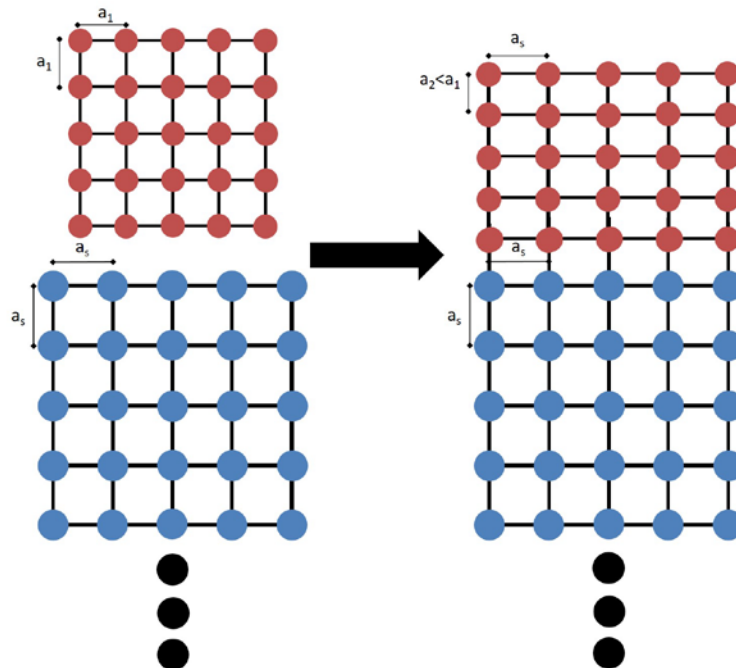


Figure 2.9: Diagram of the crystal formation for tensile strained heteroepitaxy.

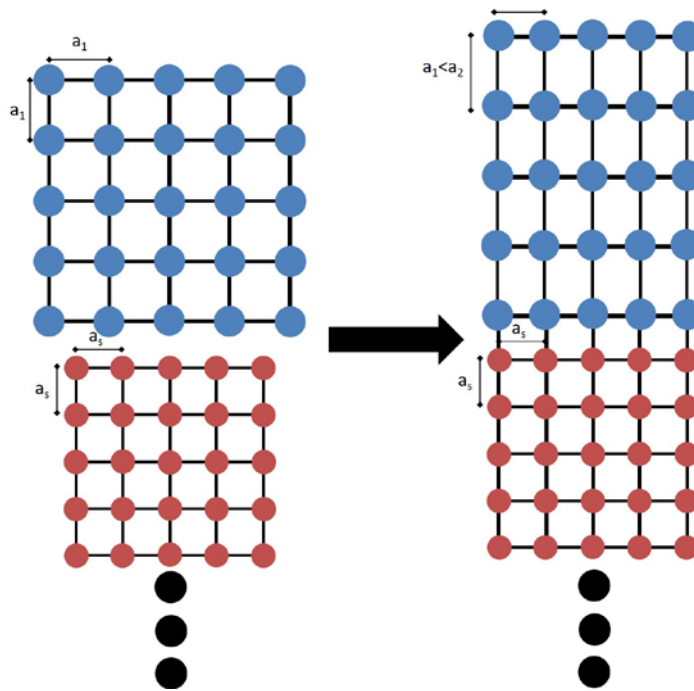


Figure 2.10: Diagram of the crystal formation for compressively strained heteroepitaxy.

Heteroepitaxy is growth of an epi-layer, which comprises a different material from the substrate. An example of this would be InGaAs on a GaAs substrate. Although some semiconductor combinations, e.g. $\text{Ga}_{0.5}\text{In}_{0.5}\text{P}$ and GaAs, have the same lattice constant, the vast majority of combinations involves two or more materials with different lattice constants. For heteroepitaxy with two latticed mis-matched semiconductors, two possible outcomes can occur. If the lattice parameter of the epi-layer is smaller than the lattice parameter of the previous layer, then tensile strain will result in the epilayer. As shown in figure 2.9, the lattice constants for both in-planes directions expand to match the previous layer and the lattice constant in the growth direction is reduced via the Poisson effect. If the lattice parameter of the epi-layer is larger than the lattice constant of the previous layer, then compressive strain will result. As shown in figure 2.10, the lattice constants in both in-plane directions reduces to match the parameter of the previous layer and the lattice constant in the growth direction increases via the Poisson effect. If there is a large lattice mismatch between the epi-layer and the substrate, strain energy quickly builds up and dislocation defects are generated which act to relax the strain energy. In this case, the epi-layer returns to its original lattice constant, this is known as a relaxed lattice. The presence of dislocations will adversely affect the optical and electronic properties of the semiconductor and must be avoided.

There are three growth modes that can be used in epitaxy; these are described in the following. Frank Van Der Merwe (FM) growth is also known as pseudomorphic growth. Pseudomorphic growth is the growth of a regular two dimensional crystal layer on a crystal of a different material, with the amount of deposited material kept below the critical thickness as shown in figure 2.11 (a). The critical thickness is the point at which the elastic strain energy is sufficient for the formation of defects or dislocations. Pseudomorphic growth is used for the formation of quantum wells (QWs) and superlattices, with high quality interfaces formed between the different layers.

Stranski-Krastanov (S-K) growth utilises the lattice mismatch between different materials. S-K growth was first described by Ivan Stranski and Lubomir Krastanov in 1938. [2] The growth consists of a larger lattice parameter material on a smaller lattice parameter material. A typical example of S-K growth is InAs on GaAs where the lattice mismatch is 7%. The initial growth is a two-dimensional wetting layer of highly compressive strained material. If the InAs growth is stopped at this point and further GaAs is grown, a thin InAs QW results, with an expected emission wavelength of 920 nm, as shown in figure 2.12. As more InAs is added a critical thickness is reached beyond which the formation of 3D islands occurs, as shown in figure 2.11 (b), increasing the expected emission wavelength to 1250 nm - figure 2.12. The formation of the 3D island reduces the elastic energy in the material but increases the surface

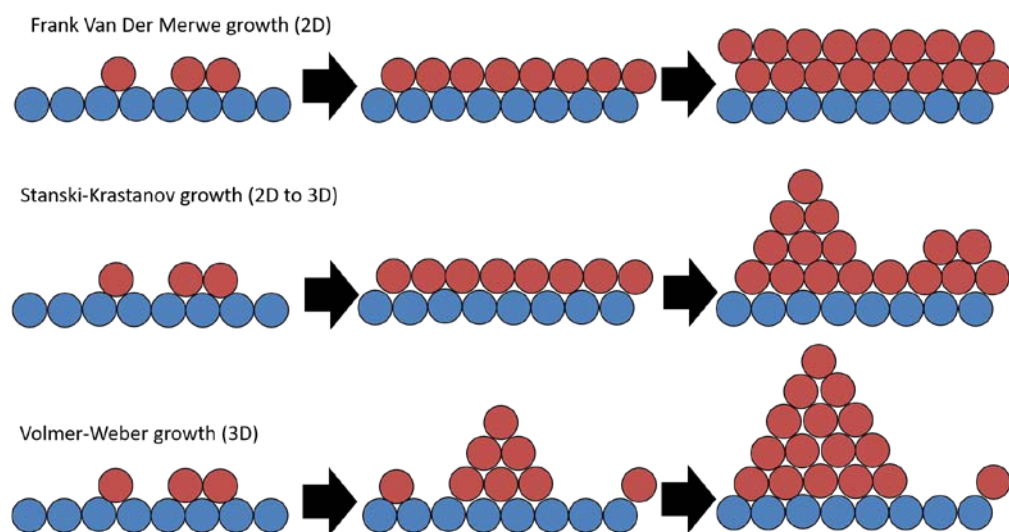


Figure 2.11: Diagram of the three epitaxial growth modes: Frank Van Der Merwe growth (pseudomorphic growth), where the growth forms a 2D layer (top), Stranski-Krastanov growth, where a 2D to 3D transition is observed (middle) and Volmer-Weber growth, where 3D islands are formed without a 2D layer (Bottom).

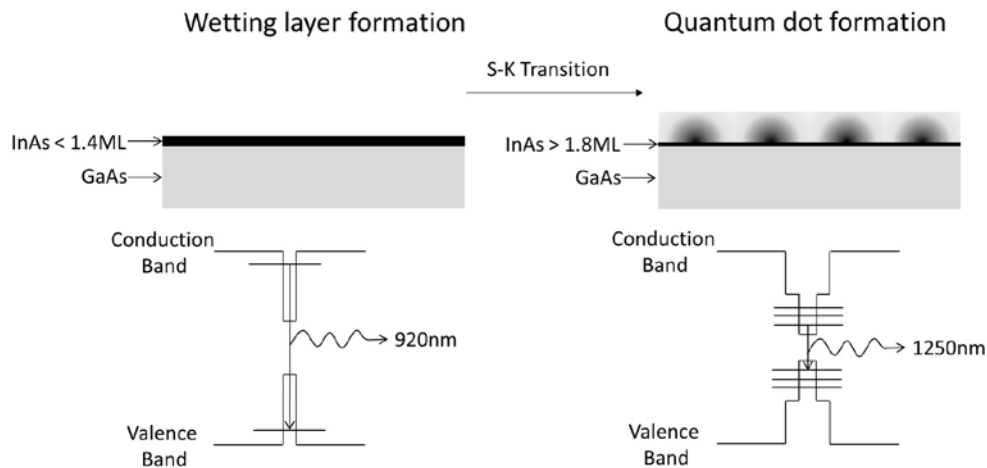


Figure 2.12: Diagram showing the S-K transition and the associated electronic band structure.

energy. The initial 3D islands are very small, typically ~ 15 nm inplane and ~ 10 nm along the growth direction, they hence act as QDs with full quantisation of the electronic states. The QDs are coherent and dislocation free, although further InAs deposition will lead to the formation of dislocations. [3], [4] To enable the S-K growth mode the reduction in elastic energy has to be greater than the increase in the surface energy, this appears to require a minimum lattice mismatch of around 3%.

The third growth mode is Volmer-Weber (V-W) growth, which occurs for materials where the atomic bonding is much greater within the epilayer than between the epilayer atoms and the substrate. Nucleation of 3D islands occurs immediately, as shown in figure 2.11 (c). An example of this type of growth is droplet epitaxy, where for III/V materials the group III material is deposited to form small droplets without the presence of the group V material, this is provided later. All the samples studied in this thesis use a combination of pseudomorphic and S-K growth.

2.3 Material Characterisation

This section will briefly describe the characterisation methods used in the thesis. The first technique applied to characterise newly grown material is differential interference contrast microscopy, also known as Nomarski imaging. Nomarski imaging was developed by Professor Georges Nomarski in 1952 [5] and is a technique that uses polarised light to enhance the contrast of surface defects on a semiconductor wafer. By modifying the polarisation of the light, different surface features, such as defects, become visible. Using this technique, a decision can be made on what growth parameters to change to reduce the number of defects or to eliminate lattice relaxation. Ensuring good quality epitaxial growth is important and with Nomarski imaging a decision can be made very quickly, reducing the amount of potentially wasted time. Figure 2.13 shows two Nomarski images with a magnification of x50, one where the surface of the wafer shows very few defects and one with a very rough surface with a high level of defects, which hence makes it unusable.

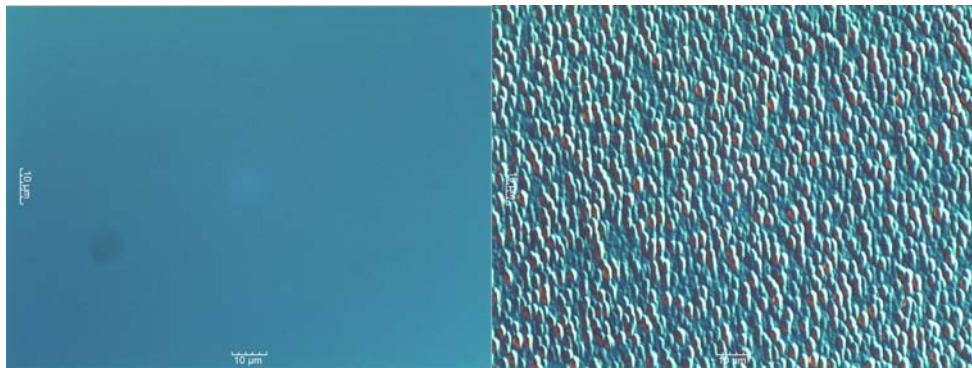


Figure 2.13: Nomarski images of two samples at x50 magnification, one with a smooth surface (left) and one with a very rough surface (right).

X-Ray diffraction (XRD) is a non-destructive technique that uses a $\text{CuK}\alpha$ X-Ray source with a wavelength of 0.15418 nm and can determine changes to the out-of-plane lattice parameters. In order for the lattice parameters to be extracted, the wavelength of the X-Ray needs to be of the same order of magnitude as the lattice spacing. For this thesis, a Bruker D8 was used to extract omega-two theta scans, more details will be presented in chapter 3. Using XRD

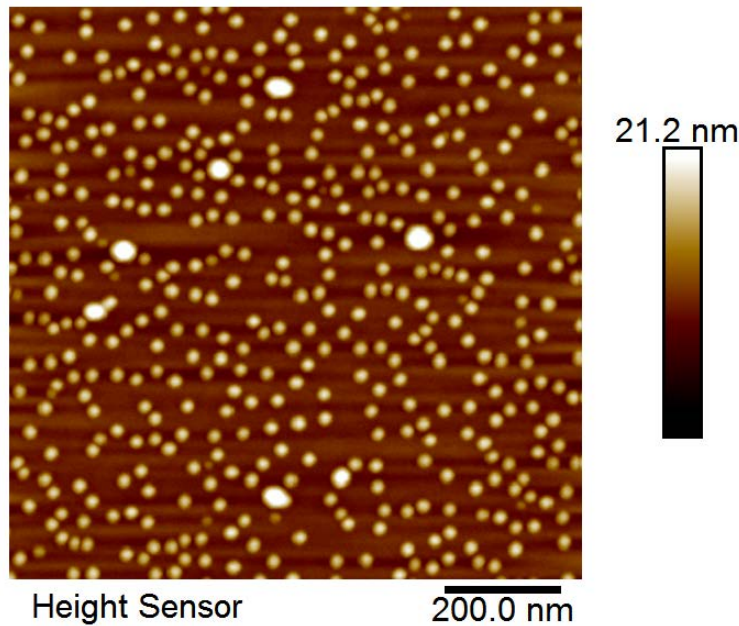


Figure 2.14: AFM image of QDs grown by Dr Edmund Clarke using MBE with the image taken by Miss Charlotte Overden.

the change in the out-of-plane lattice constant between the substrate and epi-layer can be extracted and the strain produced by the epi-layer determined.

Atomic force microscopy (AFM) was invented at IBM in 1982 and is a technique used to characterise surface morphology on the atomic scale. [6] AFM can be used to determine the density of surface QDs and, assuming the same number of QDs are nucleated within a structure, an estimate of the density in full structures can be made. The basic principle of AFM is the use of a laser to measure the deflection of a cantilever as its tip moves across the surface, the movement of the tip can be either continuous (dragged along the surface) or periodic (tapping the surface). AFM analysis was attempted for four of the MOVPE grown QD structures where a layer of surface dots was grown using the same growth parameters as the buried dot layers. However, due to the long cool down time, no surface QDs were observed. Figure 2.14 shows a typical AFM image of surface QDs grown by MBE, where the areal density is calculated to be $4.2 \times 10^{10} \text{ cm}^{-2}$ and the size distribution of the QDs is approximately Gaussian. The Gaussian distribution of the QDs is associated with the inhomogeneous broadening of the emission spectra.

Scanning electron microscopy (SEM) is a technique that utilises a focused beam of high-energy electrons that scans across the sample surface. The electrons

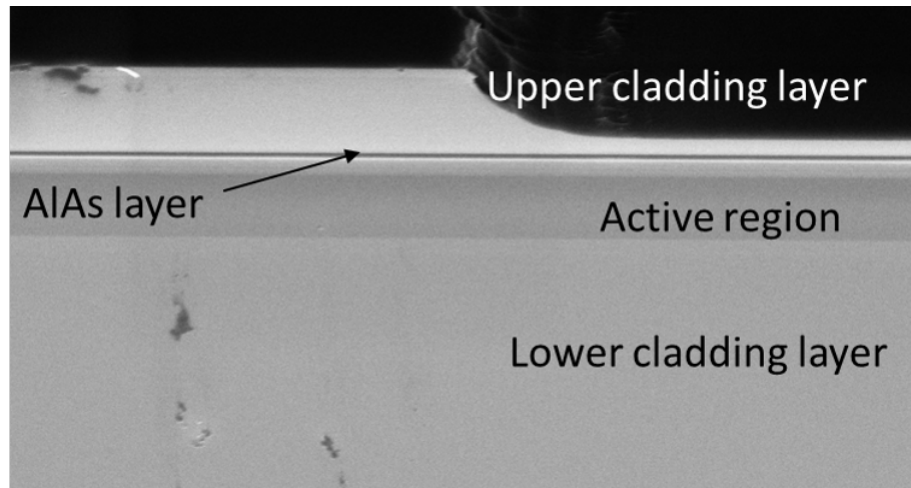


Figure 2.15: SEM image of a mesa etched laser structure.

interact with the surface atoms producing secondary electrons, which are detected and an image is produced. This technique can be used to study large surface QDs but it can also provide feedback on the etching process used in the fabrication of devices. Figure 2.15 shows a typical SEM image of a mesa etched laser diode, where the top contact layer has been isolated.

Transmission electron microscopy (TEM) is a technique that utilises the transmission of electrons through the sample and was first demonstrated in 1931 by Max Knoll and Ernst Ruska. [7] For this technique the sample has to be thinned (~ 100 nm) to allow sufficient electron transmission. The electrons are diffracted by the material to produce an image as the position of a focussed electron beam is scanned across the sample. The resolution of TEM is limited by the de Broglie wavelength of the electrons, which determines the focussed

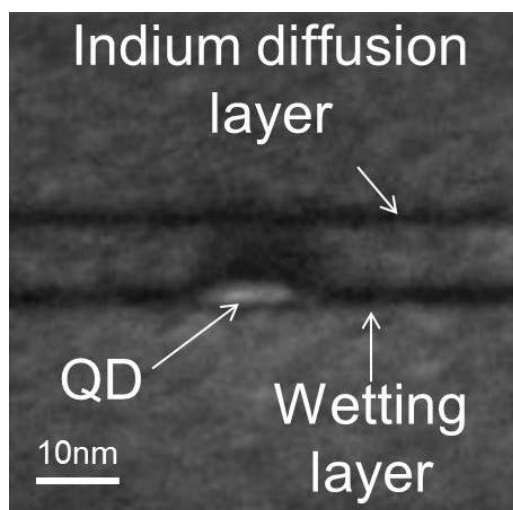


Figure 2.16: TEM image of a QD grown at 485°C with 2 ML InAs coverage, 0.18 ML/s growth rate, and 50 sccm arsine flow rate.

spot size. For a high electron energy (100-300 kV), the typical maximum resolution of a standard TEM system is of the order of 0.2 nm. TEM can provide information about the sample structure, including the thicknesses of layers and, if of sufficient resolution, defects can be observed. For QD structures, the dot size can be measured and an estimation of the QD density can be obtained. [8] Figure 2.16 shows a typical TEM bright field image of a buried QD grown by MOVPE, where the white region is the QD.

Doping is important for reducing the electrical resistance of the device. However, the doping level needs to be controlled as high doping levels can introduce photon absorption by free carriers within the structure. Therefore, techniques are required to aid the calibration of the amount of doping being used. Two methods are available at the University of Sheffield to characterise the doping level, Hall measurement and electrochemical capacitance voltage (eCV). Hall measurements can only measure the doping in a single layer, as this technique will measure the overall current/voltage between the contacts and analysis of multiple layers is very complicated. Therefore, additional growths are required for each doped layer; multiple doped layers in a real structure cannot be measured. The Hall effect was discovered by Edwin Hall in 1879, where the application of a magnetic field to a current flow creates an electric field perpendicular to both the current flow and field. [9] The size of this field is related to the density of free carriers and the direction of the field allows the carrier type, electrons or holes, to be determined. By placing the semiconductor in a magnetic field, the Hall voltage, which results from the Hall field, can be measured. [10] Hall measurement requires four Ohmic contacts to the semiconductor wafer, formed by diffusing a suitable metal into the semiconductor, and formation of a particular sample geometry. Whilst a Hall measurement determines the free charge carrier density and type within a layer, eCV determines the density and charge of dopant ions within a depletion region formed at the surface. It is possible to probe doped layers at different depths with eCV; reducing the number of calibration samples required. The eCV technique was developed by T. Ambridge and M. Faktor in 1975. [11] It uses an electrolyte to etch away the layers of the semiconductor, by measuring the current required to etch the semiconductor an etch depth can be calculated. To

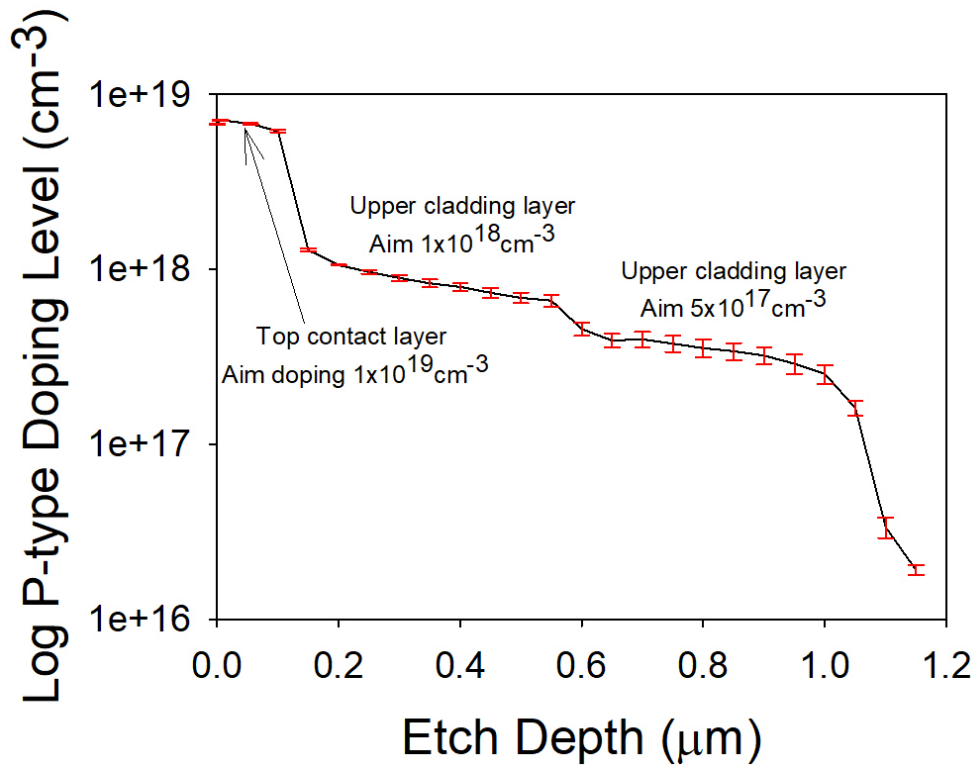


Figure 2.17: eCV profile of the cap layer and upper cladding layer of a laser structure doped with carbon.

measure the doping concentration a capacitance-voltage (C-V) measurement is performed. This takes place with the sample in reverse bias, creating a capacitance between the charge on the surface and the impurity ions within the depletion layer. [12] As with the Hall measurement, this technique is destructive. Figure 2.17 shows a typical eCV doping profile of a test structure containing three different doping levels, the top GaAs contact layer was doped to $1 \times 10^{19} \text{ cm}^{-3}$ and the upper $\text{Al}_{0.42}\text{Ga}_{0.58}\text{As}$ cladding layer was doped to 1×10^{18} and $5 \times 10^{17} \text{ cm}^{-3}$. The doping level is reduced close to the active region to reduce optical losses associated with high doping levels due to free carrier absorption. The measured doping level differs slightly from the intended doping levels especially as the etch depth becomes deeper. This is due to non-uniformity during the etch process, where a layer with a higher doping level, such as the top contact layer, may still be present when a layer with a much lower doping level, such as the $\text{Al}_{0.42}\text{Ga}_{0.58}\text{As}$ cladding layer, is being measured and vice versa.

Studying the optical spectra of a structure is an important part of understanding the material quality and composition. In this thesis, the two related techniques of photoluminescence (PL) and electroluminescence (EL) were used. Both PL

and EL initially create carriers in excited states but by two different methods. PL is the measurement of light emitted from a sample, with the carriers excited by absorption of higher energy photons. EL is the measurement of light emitted from a sample, where electrons and holes are electrically injected – figure 2.18. PL is typically excited with a laser having a photon energy higher than that of the barrier material so that strong absorption occurs. Hence electrons and holes are initially created in the barrier, however they diffuse and are quickly captured by the QDs or quantum well (QW) before recombination in the barrier occurs, due to the significantly longer recombination time (\sim ns) for the electrons and holes in the barrier compared to the relaxation time (\sim ps). A similar process occurs for EL although here the electrons and holes reach the QDs or QW from opposite directions. Although capture by QDs is via an excited state rapid carrier relaxation results in only emission from the QD ground state being observed. Particularly at low temperatures, following random capture by the dots

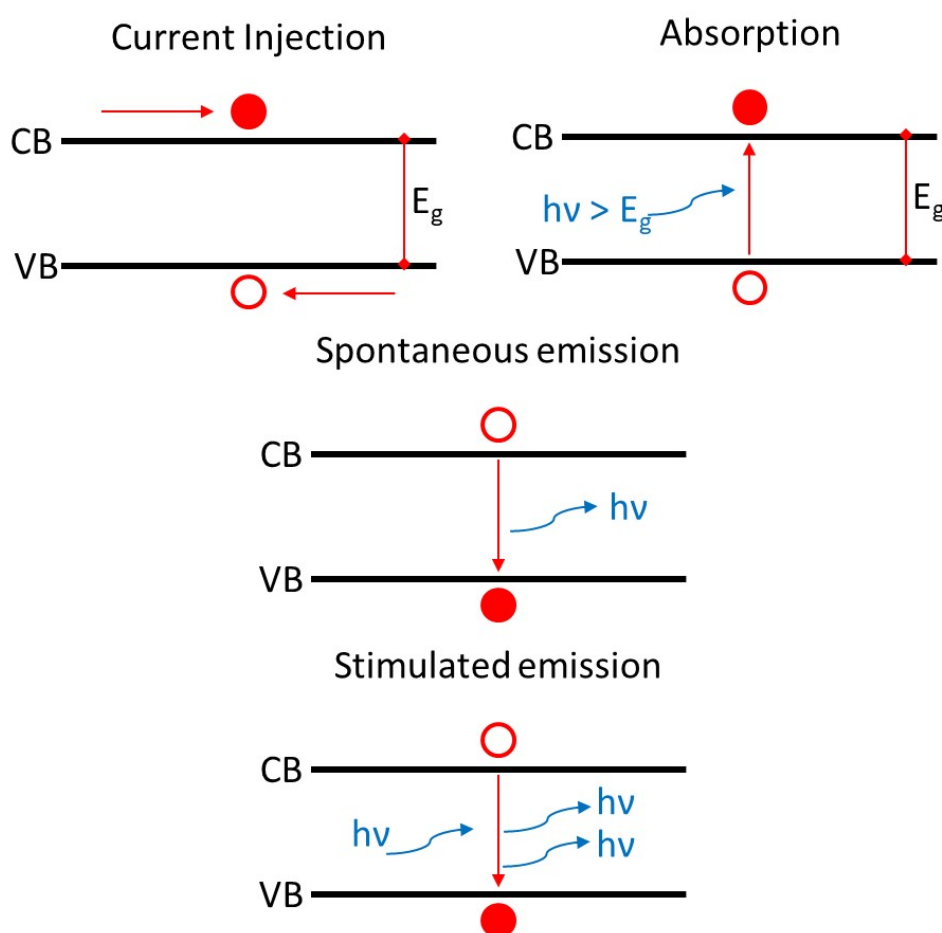


Figure 2.18: Schematic diagram showing the transport of carriers and photon generation for current injection (top left), absorption (top right), spontaneous emission (middle) and stimulated emission (bottom).

recombination occurs and hence the emission spectra reflect the inhomogeneous distribution of dot shapes and sizes. As the temperature is increased carriers may be excited out of the dots and recaptured by a different dot, with recombination now weighted towards the larger dots with a deeper confining potential. If the exciting laser power or injection current is increased, it is possible to saturate the ground state of the QDs and excited state emission is observed. At very high powers / currents it may be possible to saturate all the QD states in which case emission from the wetting layer and possibly the barrier material will occur. In a non-laser structure, electrons and holes recombine to produce photons with a random direction and phase as shown in figure 2.18. For a laser structure, where there is a population inversion of the electrons and holes and a large photon density, recombination can be stimulated by an incident photon as shown in figure 2.18. This stimulated emission gives photons with the same phase, polarisation, wavelength and direction as the incident photon. The detailed principles of a laser will be discussed in chapter 4.

PL is an important non-destructive measurement technique, which is extensively used to characterise a wide range of semiconductor structures. PL does not require any further fabrication following sample growth and produces quick feedback to aid in the optimisation of new and novel materials or structures. The PL set-up shown in figure 2.19 was used to test all the samples discussed in section 2.5 of this thesis. The excitation is provided by a frequency doubled 532 nm neodymium doped yttrium aluminium garnet (Nd:YAG) laser producing 1 W of continuous output power. An optical chopper with a 50% duty cycle was used at 15 Hz to modulate the laser with a reference signal being

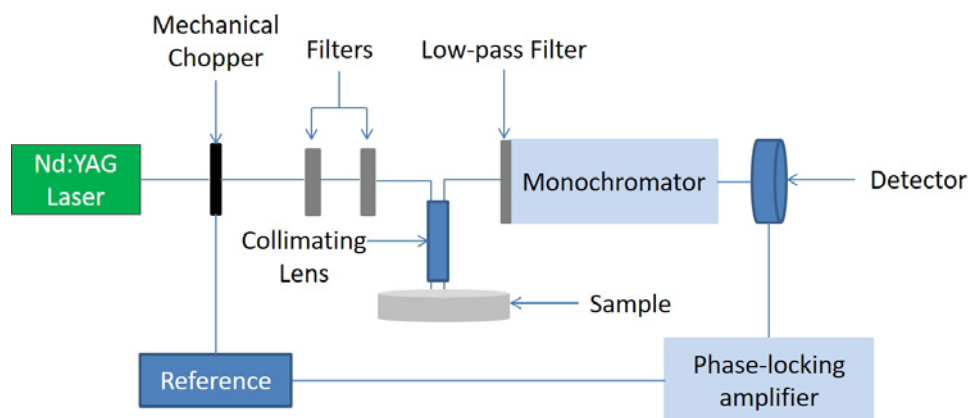


Figure 2.19: Schematic diagram of the set-up used to measure PL spectra.

provided to a lock-in amplifier. The power incident on the sample can be varied from 1000 to 0.03 mW by the use of neutral density (ND) filters. The emission from the sample is collected and collimated by the same lens and the emission is passed through a low pass filter to remove the laser light. However, for all samples studied a feature at 1064 nm is observed, this is due to emission from the Nd:YAG laser. The PL is passed through a monochromator, which selects a narrow band of wavelengths to be detected using an InGaAs photodiode. The photodiode has a wavelength sensitivity range of 800 to 1650 nm and the output voltage is measured using the lock-in amplifier. The sample could be placed within a helium cryostat allowing the temperature to be varied from 5 up to 300 K. Before all the measurements, the monochromator is set to the wavelength of the ground state emission of the sample and the lenses are adjusted to obtain the highest intensity signal.

EL is a technique that requires fabrication of electrical injection devices, as described in chapter 4. It is hence more complex experimentally than PL but has the advantage of better control of the injected carrier density. The EL set-up shown in figure 2.20 was used to test all the mesa diode and broad area laser samples studied in chapter 4. Two types of current source were used to measure optical access mesa diodes, a continuous wave (CW) and a pulsed current source, the latter had a duty cycle of 1% and a pulse width of 1 μ s. Pulsing the current reduces sample heating and allows higher injection currents up to 1 A. The emission from the sample is collected, collimated and focussed into a monochromator, which selects a narrow band of wavelengths to be detected using a liquid nitrogen cooled germanium photodiode. The photodiode has a

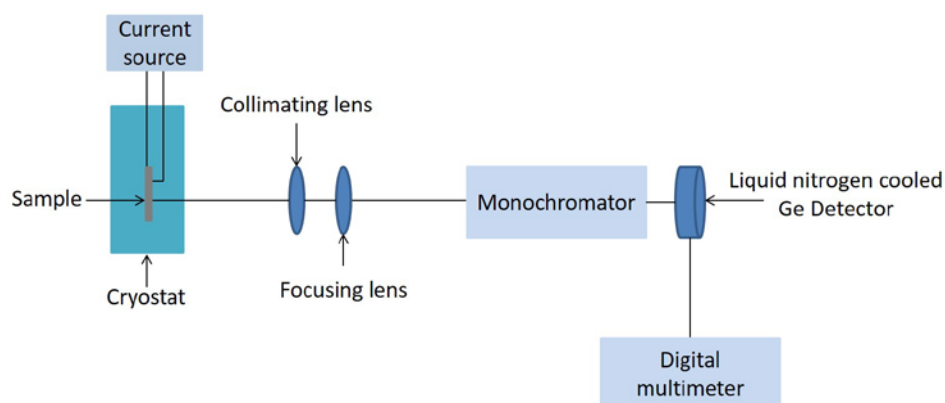


Figure 2.20: Schematic diagram of the set-up used to measure EL emission.

Chapter 2: Epitaxial Growth & Quantum Dot Optimisation

wavelength sensitivity range of 800 to 1800 nm and the output voltage is measured using a digital multimeter. The sample holder could be placed within a liquid nitrogen cooled cryostat where the temperature can be varied from 77 up to 300 K.

2.4 Low-Dimensional structures

The electronic and optical properties of a semiconductor can be significantly changed by altering its dimensionality, achieved by reducing the size in one or more dimensions to of order a few 10's nm or less. This modifies the carrier motion along these directions and results in energy quantisation.

For bulk semiconductors there is no quantum confinement in any direction and therefore carriers are free to move in all three directions, resulting in an electronic density of states which varies as $E^{1/2}$, as shown in figure 2.21. For quantum wells (QWs), there is quantum confinement in the growth direction (1D) and therefore carriers are free to move in only two directions, giving a constant density of states for each confined state, as shown in figure 2.21. For quantum wires (QWRs), there is quantum confinement in the growth direction and one in plane direction (2D). Free movement of carriers is only possible along one in plane direction, resulting in a density of states of the form $E^{-1/2}$ for each sub-band, as shown in figure 2.21. For quantum dots (QDs), there is quantum confinement in all directions (3D). Electrons and holes energies are fully quantized with a discrete density of states; this can be represented by delta functions, as shown in figure 2.21. This energy level structure is similar to that of an atom, with optical transitions expected to produce spectrally narrow emission. QDs are therefore often referred to as 'artificial atoms', figure 2.22.

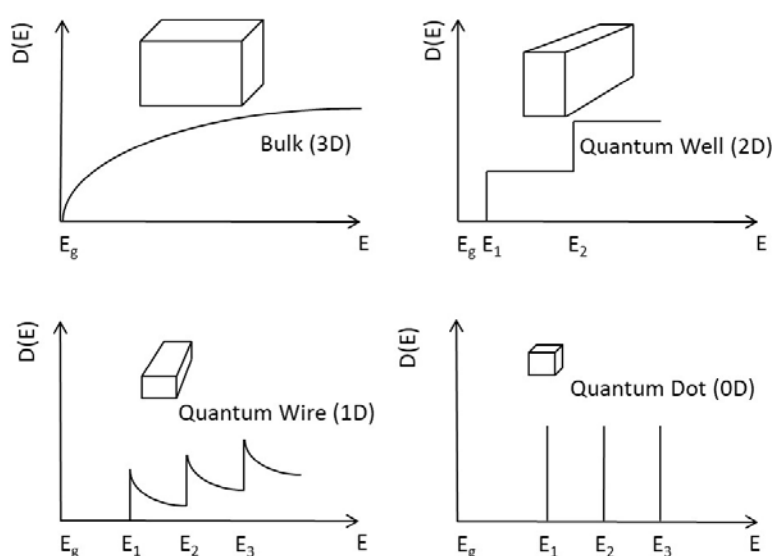


Figure 2.21: Schematic diagram of the density of states versus energy for bulk (3D) (top left), quantum well (2D) (top right), quantum wire (1D) (bottom left) and quantum dot (0D) (bottom right).

A complication of Stranski-Krastanov dots is that they exhibit a spread of size and shape. This causes a variation of the confined energy levels and hence an inhomogeneous broadening of the emission from a QD ensemble. At low temperatures the emission line width of a single QD, the homogeneous linewidth ΔE_{hom} , can be as small as a few μeV , while the inhomogeneous linewidth of an ensemble of QDs, ΔE_{inhom} , will be >10 meV. [13], [14] The formation of QDs will follow a normal distribution (Gaussian distribution) as shown in the AFM image in figure 2.14, with the peak of the distribution centred at the most common QD size, composition and aspect ratio, all of which affect the wavelength of emission. A significant drawback of this inhomogeneous broadening is that the gain in a QD laser is spread over a significant wavelength range, reducing the peak gain available. However, this inhomogeneous gain is useful for broadband amplifiers and tunable lasers, as the gain region is broadened due to the size difference of QDs within an ensemble.

For low carrier injection levels, the average number of electrons or holes in a QD (the carrier occupancy) will be much less than one and hence only emission from the lowest energy transition is observed. With increasing carrier injection rate, the QD spectra will start to exhibit state filling effects. State filling occurs because the occupancy of the ground state is limited to two carriers (one spin up and one spin down), a result of the Pauli Exclusion Principle which states

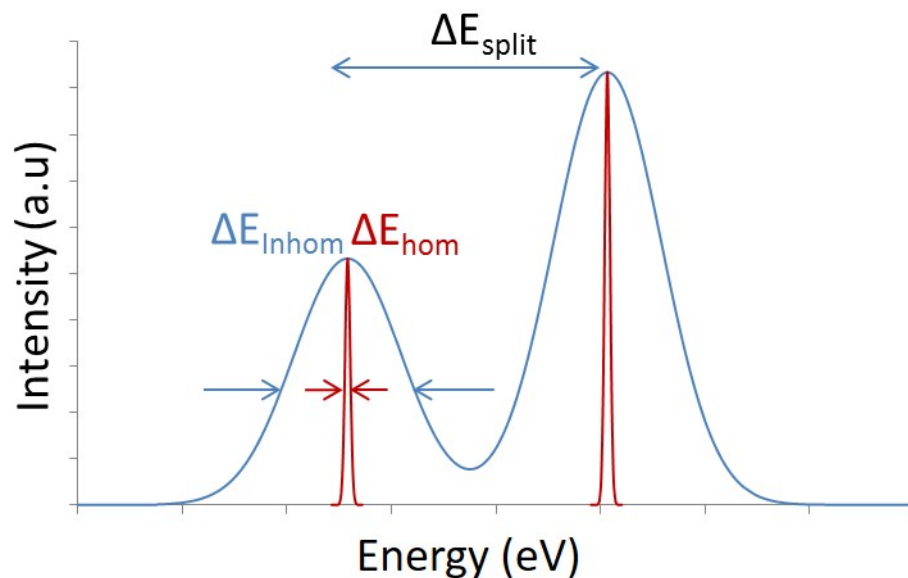


Figure 2.22: Diagram showing the spectral emission of a single QD (in red) and an ensemble of QDs (in blue). At low temperature, ΔE_{hom} can be as low as a few μeV , while ΔE_{inhom} will be >10 meV. [13], [14]

that no two electrons or holes can occupy the same quantum state. [15] In addition, the recombination times of the carriers is significantly longer than the relaxation time. Therefore, with the injection of additional carriers, higher energy states (excited states) will begin to be occupied. The recombination of carriers in these higher energy states will produce photons of higher energies (shorter wavelength). As the degeneracy of the excited states is greater than that of the ground state (a factor of two for the first excited state) [15]–[17] the maximum emission intensity of the first excited state is expected to be twice that of the ground state, as shown in figure 2.22. In a laser device, the maximum available gain will also be greater for the excited state in comparison to the ground state. Hence, if the ground state gain is insufficient to give lasing then lasing may occur via an excited state, although this will be at shorter wavelength and for a higher threshold current density. When studying QD structures it is important to determine the amount of inhomogeneous broadening and growth optimisation may be required to reduce this. As discussed previously, at high temperatures, carriers may transfer between QDs and not all QDs will contribute to the emission. Hence, measuring the EL or PL for low injection (average carrier occupancy $\ll 1$) and at low temperatures so that only ground state emission is observed, is necessary. [16]

2.5 Literature review

Research into quantum dots (QDs) has been ongoing over the past 35 years due to their potential for new physics and the promise of reduced laser threshold current density and temperature insensitive threshold current density, as predicted by Arakawa and Sakaki in 1982. [18] Formation of QDs initially focused on the growth of QW structures (quantised in 1D) and then patterning of the wafer after growth using lithographic techniques. At the time, this was the only method available to fabricate QDs. Optical lithography techniques based on ultra-violet (UV) light provided limitations on the resolution (down to 0.2 μm), this was overcome by using electron beam (e-Beam) lithography, with resolution down to 10 nm. [19] The patterned wafer was etched, either wet or dry, to form the free standing QDs. However, the etching, gave issues with the sidewall uniformity and damage to the surface layer, whilst residual strain in the structure was also an issue. Hence, these QDs were found not to produce bright luminescence and would be difficult to integrate within a laser structure. [19]

With growth on patterned structures it is possible to overcome many of the issues associated with free standing QDs. Patterning of the substrate, using optical or e-Beam lithography, is used to define the position and potential size of the QD, as the growth is controlled by the holes. However, regardless of the starting template, including etched hole, V-grooves or inverted pyramids; there are issues with growth non-uniformity. [19] Several reports of QD growth on pattern substrates have appeared but issues with uniformity, reproducibility, density, optical quality and homogenous line width occur. [19]–[28] The best linewidth for a single QD is 7 μeV with typical linewidths on the order of 10's μeV due to spectral jitter caused by Coulomb interactions from trapped charges at surfaces or defects. [29], [30] However, due to applications such as single photon sources, QDs fabricated on pattern wafers are still being developed due to their improved scalability. However, it is difficult to see how this technique could be used to fabricate the large number/density of QDs required for a laser. Self-assembled QDs, which uses the S-K growth mode, is the dominant method for fabricating InAs/GaAs QDs. QD formation is driven by the strain which

results when InAs is grown on GaAs. The QDs form *in situ* in the growth reactor so that their growth is fully compatible with both MBE and MOVPE. The material quality is very high, with excellent radiative efficiencies as long as no defects are allowed to form. A high density of dots is possible and the growth is reproducible. In addition, the incorporation of self-assembled QDs in optoelectronic devices, such as the laser diode, is easier than other QD growth techniques, leading to commercially viable new and novel devices. [16], [17], [19]

Understanding when the S-K growth transition occurs for the InAs/GaAs system is very important for the formation of the QDs. S-K growth of InAs/GaAs QDs occurs due to the 7% lattice mismatch between the lattice constants of GaAs (5.65325 Å) and InAs (6.0583 Å). When InAs is deposited on GaAs, elastic strain energy builds up in the initial 2D InAs QW, with the transition to 3D island growth allowing relaxation of this energy at the expense of increased surface energy. [17], [31] The 2D-3D transition was reported to occur above 1.5 ML by D. Bimberg, but no QDs were observed for InAs deposition of 1.6 ML, as reported by A. A. El-Emawy *et al.* [17], [32] J. X. Chen *et al.* reported that RHEED patterns showed the 2D to 3D transition to occur at approximately 1.8 ML. [33] Therefore, the S-K transition for self-assembled InAs/GaAs appears to be between 1.6 and 1.8 ML of InAs deposition. However, the amount of material required to give this transition will increase with increasing gallium concentration within the QDs, due to the smaller lattice constant difference, and hence lower strain. [17] Increasing the InAs coverage (up to 4 ML) beyond the 3D transition causes the QDs to ripen and increase in size, leading to a longer emission wavelength, which is beneficial when aiming for emission at 1.3 μm and beyond. [32], [34]–[41] However, as more InAs is deposited the QDs can become too large, resulting in defect formation and/or coalesced QDs, creating non-radiative recombination sites and significantly degraded the radiative efficiency. To avoid these issues, the InAs deposition should ideally be between 2 and 3 MLs. [32], [34], [37], [42]–[44] A related method of forming QDs is through the droplet epitaxy technique. As discussed in section 2.2, only the group III (indium) is used to

initially form island using the VW growth mode, after which the group V (arsenic) is used to create a crystalline QD. [45]–[48]

MBE growth of InAs/GaAs QDs has been established for many years with the first reported growth in 1985 by L. Goldstein *et al.*. [49] Growth conditions for MBE InAs/GaAs QDs can vary significantly for all of the growth parameters, e.g. temperature from 450 to 520 °C, growth rate from 0.001 to 0.015 ML/s with the InAs coverage needing to be above the S-K transition at 1.7ML. The highest QD density reported using MBE is $7.76 \times 10^{11} \text{ cm}^{-2}$ by Chia *et al.*. [50] However, a QD density of $\sim 6 \times 10^{10} \text{ cm}^{-2}$ is more commonly achieved and ground state lasing $\geq 1.3 \text{ }\mu\text{m}$, with threshold current densities down to 13 A/cm^2 have been reported. [51]–[57]

MOVPE growth of InAs/GaAs QDs has the advantage of ease of commercialisation due to the volume scalability and high uptime of the growth reactor. MOVPE growth of InAs/GaAs QDs has been studied by a number of research groups and some of the relevant work will be reviewed here. The first reported MOVPE growth of self-assembled InAs/GaAs QDs was in 1994 by J. Oshinowo *et al.*. [28] Understanding the effects of the basic growth parameters is of paramount importance in developing the ability to successfully grow self-assembled InAs/GaAs QDs and apply them to electro-optical devices.

Growth temperature is possibly the most important parameters; it has been reported to affect the diffusion length of the indium atoms, and to alter the QD density, size, and emission wavelength. [32], [34], [35], [37], [44], [58]–[64] A growth temperature below 500°C is reported to produce small QDs (giving a short emission wavelength), with high densities achievable. However, with increasing temperature up to 500°C, the emission shifts towards $1.3 \text{ }\mu\text{m}$, which has been reported as being due to a change in QD shape from small pyramids to larger domes. [32], [34], [35], [37] Increasing the growth temperature above 500°C can result in a reduction in the emission wavelength, with out-diffusion of indium into the capping layer and gallium diffusion in from the surrounding GaAs reducing the indium concentration in the QDs. [32], [34], [59]–[61], [65] In addition to this reduction in indium content, a reduction in the QD density can occur due to desorption of indium from the surface. Most reported optimal growth temperatures are between 485 and 520°C, although this can be increased

to 550°C to improve surface morphology, but with a decrease in QD density. QD formation has been reported up to 600°C, although this is for the formation of In_{0.5}Ga_{0.5}As QDs, with a low density and large coalesced islands formed. [37], [61]

The QD growth rate can also affect the QD formation in a number of ways, such as altering their size and shape, density, emission wavelength and the number of coalesced QDs. [32], [34], [35], [37], [44], [59], [60], [63], [64] Using a high growth rate will increase the number of nucleation sites. Increasing the amount of InAs deposited over a shorter period of time will cause an increase in the localised elastic strain and will form dots to relieve the strain, causing an increase in the number of nucleation sites. An increase in the density of nucleation sites will create smaller QD with a higher density (towards $6 \times 10^{10} \text{ cm}^{-2}$), with a consistent amount of InAs is deposited there will be less material available for larger QDs to form. [32], [34], [35] Using a higher growth rate can result in a bimodal distribution of QDs, within which there are two distinct populations of dots that can be modelled by two Gaussian functions. Additional InAs deposition can aid the ripening of QDs, resulting in more dots in the population of larger QDs but can also create more coalesced dots. [66] Reducing the growth rate has the opposite effect, resulting in larger QDs with a lower density and longer emission wavelength (towards 1.3 μm). The growth rates reported vary substantially from 0.01 up to 2 ML/s. [32], [34], [35], [44], [59], [60], [63], [64]

The V/III ratio during QD growth will affect the migration length of the indium atoms, influencing the size, density and emission wavelength. [32], [34], [35], [37], [44], [63], [64], [67] With a low V/III ratio, large QDs are formed having a longer emission wavelength but with a lower density. With a high V/III ratio, small QDs are formed having a shorter emission wavelength and a high density. However, if the V/III ratio is too high the defect density will increase, creating non-radiative recombination centres. Increasing the availability of the group V atoms at the growth surface reduces the indium migration length, allowing more nucleation sites for QDs to form and hence increasing the density. V/III ratios of 0.3 to 180 have been reported, giving a large parameter space to study. [32], [37], [59]–[61], [63], [64], [67], [68]

Extending the emission wavelength of InAs/GaAs self-assembled QDs, in order to reach 1.3 μm and beyond, is important for telecommunication applications. Initial studies of InAs/GaAs QDs with the dots grown in a GaAs matrix, showed that it was very difficult to reach 1.3 μm whilst maintaining a high optical efficiency. [63], [64], [68] A number of different methods can be used to extend the emission wavelength. QD seeding, by depositing an InGaAs layer before the deposition of the QDs, has been shown to extend the QD wavelength towards 1.3 μm . Incorporating a strained InGaAs QW before the growth of the QDs reduces their elastic strain, allowing the formation of larger dots. The higher indium concentration below the QDs also reduces the out diffusion of indium as well as reducing the strain around the QD, extending their emission wavelength and improving their homogeneity and hence the emission linewidth. [69] Deposition of an InGaAs strain-reducing layer (SRL) above the QDs also reduces the strain around the dot, extending the wavelength towards 1.3 μm and beyond. [34], [35], [70]–[74] Here the QD formation occurs on GaAs but the dots are capped with a few nanometres of InGaAs. The strain around the QD is reduced due to the InGaAs layer, which has a much smaller lattice constant difference to InAs compared to GaAs. A lower QD strain directly decreases the band gap, red shifting the emission wavelength. [75] A related method is to grow the QDs within an InGaAs QW, referred to as a dot-in-a-well (DWELL) structure. Both the out diffusion of indium from the QD and the QD strain are reduced. This technique has been shown to extend the wavelength to 1.3 μm and beyond whilst giving devices with extremely low threshold current densities. [35], [55], [76], [77]

Introduction of a growth interruption allows surface indium to desorb, which lowers the strain by removing excess indium, allowing for a more uniform epitaxial growth of the GaAs spacing layer. If this pause follows the growth of a thin GaAs cap layer the tips of larger QDs will be exposed above this layer with desorption from these dots creating a more uniform dot ensemble. The effects of capping with increasing concentration of aluminium in an AlGaAs layer has been shown to increase the QD emission efficiency, state separation and to give an initial red shift of the emission although a small blue shift is observed for high percentage aluminium. [78]

Surfactant growth using antimony is reported to enhance both the emission wavelength, increase the QD density and reduce the density of coalesced QDs. Antimony on the growth surface will lower the interfacial strain between the GaAs and InAs. This will allow the QDs to grow much larger and produce a higher QD indium concentration. In addition, a reduction in the number of relaxed QDs is observed. Overall the use of antimony as a surfactant is found to enhance the PL intensity and redshift the emission towards 1.5 μm . [79]–[85]

Other techniques used to increase the QD density include growth on AlGaAs, which roughens the surface. QDs will nucleate at sites on this surface, increasing their density. However, a blueshift of the emission is observed and, due to the high strains involved with the nucleation, a high density of relaxed QDs is likely to form. [86]

The growth conditions used for the upper cladding layer is important as the optimum MOVPE growth temperature for AlGaAs is significantly higher than the indium desorption and diffusion temperatures. The nominal growth temperature for aluminium containing layers is 680°C. Many annealing studies have reported the effect of high temperature on the QD properties with a blueshift in the QD emission observed due to the out diffusion of indium. Growth above 580°C is not advisable, so the growth of the AlGaAs upper cladding layer has to be performed significantly lower than the optimal temperature. [44], [68], [73], [87]–[95] However, growth of AlGaAs at low temperatures can cause the formation of dislocations and defects, with resultant surface morphology issues. [36], [67], [74], [96]–[101]

2.6 Quantum dot growth optimisation

As described previously in section 2.2, InAs/GaAs QD growth is achieved by the deposition of InAs on GaAs, where the S-K growth mode and the 7% lattice mismatch between the InAs epilayer and the GaAs drives the QD formation. This project aimed to establish QD growth by MOVPE on the Thomas Swan reactor at the University of Sheffield, and to develop strain balancing using a layer of GaAsP. The following QD properties are required: a QD ground state wavelength between 1.2 and 1.3 μm , a narrow linewidth < 50 meV, a high optical efficiency and a QD density per layer higher than $1 \times 10^{10} \text{ cm}^{-2}$. The growth parameters studied to attain the desired QD properties are: InAs coverage, growth rate and V/III ratio during both QD growth and capping. Each growth parameter was investigated to understand how the QDs are affected. Initial growth was for a single QD layer at a substrate temperature of 485°C , InAs growth rate of 0.04 ML/s and V/III ratios of 208 and 95 during QD growth and capping layer growth respectively. The growth temperature used is not a measured pyrometry true temperature of the substrate surface, the EpiTT, but the temperature taken from a reference step at 525°C and with the thermocouple temperature lowered by 40°C . This is because the lowest EpiTT was 520°C . Due to these difficulties in reliable temperature determination, the growth temperature was kept constant at 485°C . This temperature was used based on reports from the literature, as discussed in section 2.5. [32], [84] However, growth at a low temperature can cause issues with the reduction in cracking efficiencies and an increase in carbon incorporation, as discussed in section 2.1. [1] The indium growth rate was calibrated from the previous growth of an $\text{In}_{0.48}\text{Ga}_{0.52}\text{P}$ layer, where the thickness was measured using TEM and the

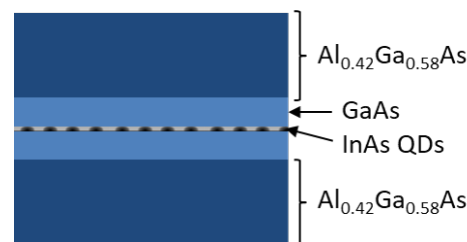


Figure 2.23: Diagram of the test structure used for the growth optimisation of the QDs.

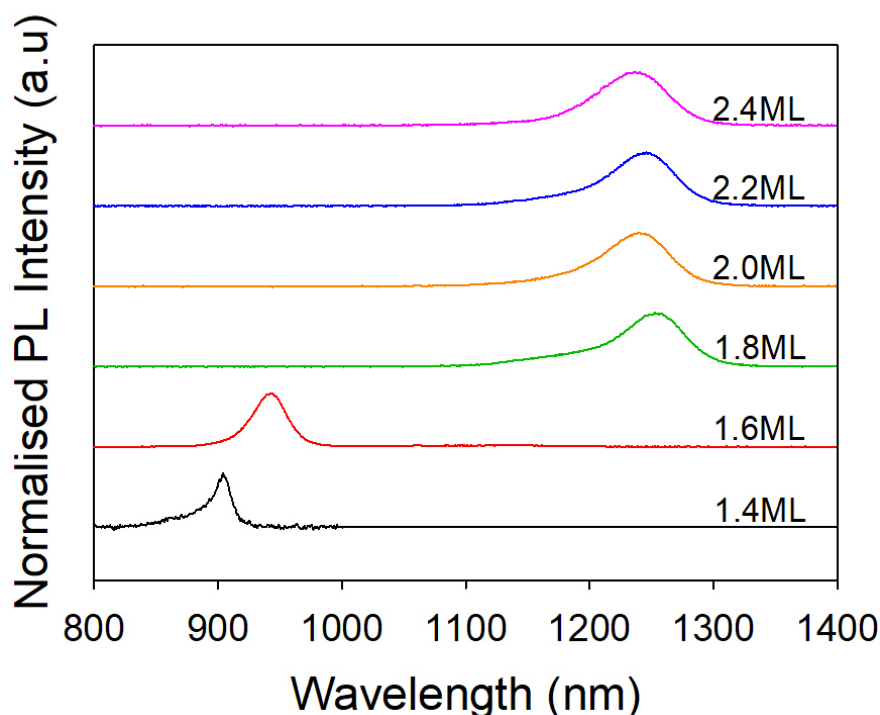


Figure 2.24: Room temperature normalised PL emission of single QD layers for different InAs coverage.

composition was determined using XRD. The arsine flow rate for the QDs was taken from the nominal growth conditions for an InGaAs QW. GaAs capping arsine flow rate is taken from the nominal optimum growth conditions stated for the MOVPE reactor. All devices were grown on 2" Si doped (001) GaAs substrates, cut 3° off towards (110). A two stage capping process was used, with the initial 8 nm of GaAs grown at the same temperature as the QDs, and the subsequent 22 nm and Al_{0.42}Ga_{0.58}As cladding layer grown at the higher temperature of 525°C. The sample structure is shown in figure 2.23.

PL spectra of the test structures were obtained using the set-up described in section 2.3. The samples were excited with a 1 W 532 nm Nd:YAG laser, with the optical power varied using neutral density (ND) filters, and the PL detected by an InGaAs detector. Identifying the S-K transition by altering the deposition of InAs from 1.4 to 2.4 ML was the first aim of the optimisation. PL spectra were obtained from all samples. As shown in figures 2.24 & 2.25 a significant shift in the peak wavelength is observed from 940 nm at 1.6 ML to 1250 nm at 1.8 ML, with a sharp discontinuity between 1.6 and 1.8 ML, corresponding to the S-K transition.

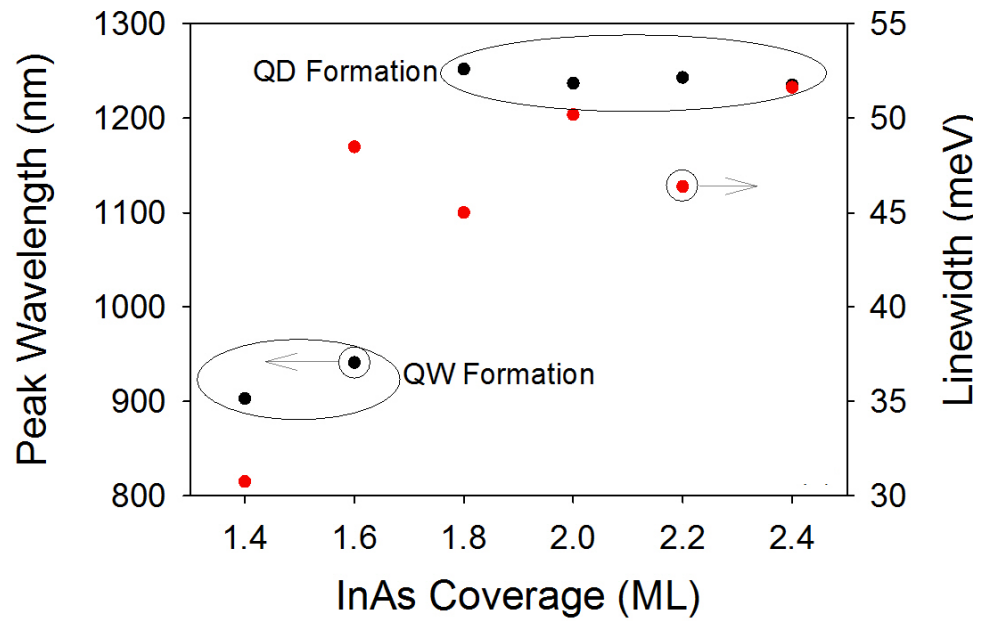


Figure 2.25: Peak room temperature PL wavelength and ground state linewidth of a single QD layer as a function of InAs coverage.

Below 1.6 ML, all of the emission is from the wetting layer with no observable emission at longer wavelength, as shown in figure 2.26. The shift in wavelength between 1.4 ML and 1.6 ML is due to the increase in thickness of the wetting layer reducing the confinement energies. Above 1.8 ML all the emission is in the 1250 nm region, which is where QD emission at room temperature is expected. From the literature, the expected critical thickness for the S-K transition is 1.7 ML, which agrees with the present observation. Once QDs have formed very little or no emission is observed from the wetting layer due to efficient carrier capture by the QDs. However, at high excitation powers the wetting layer can be observed at 940 nm with no shift being observed with increasing InAs coverage. This suggests that the additional InAs causes ripening of the QDs and does not add to the wetting layer. [102]–[105]

The shape of the QD emission is assumed to be Gaussian and can be fitted using equation (2.2),

$$I(\lambda) = I_0 e^{-\frac{(\lambda-\lambda_0)^2}{\left(\frac{\Delta\lambda}{2\sqrt{2\ln 2}}\right)^2}} \quad (\text{Eqn 2.2})$$

where I_0 is the maximum intensity, λ_0 is the centre wavelength and $\Delta\lambda$ is the full width at half maximum. $\Delta\lambda$ gives an indication of the QD uniformity. The Gaussian is fitted to the low energy side of the lowest excitation power spectra (0.4 mW), to remove complications from higher energy states. The linewidths extracted from this fitting procedure are plotted in figure 2.25. The linewidth of the wetting layer is expected to be narrower than the linewidth of the QDs, for the 1.4 ML sample the linewidth is ~ 30 meV whereas it is of order 45~50 meV for all other samples. Even though the S-K transition appears not to have occurred for the 1.6 ML sample, based on its emission wavelength, the linewidth of this sample is significantly larger than that of the 1.4 ML and comparable with the linewidths of samples where QDs are known to be present. It is possible that there are already significant thickness variations in the QW of the 1.6 ML sample. Once QDs have formed, there is no systematic change in the emission linewidth.

Power dependent PL was recorded for all samples. Samples with InAs coverage above 1.8 ML showed state filling effects. However, for samples with an InAs coverage less than 1.8 ML, high power (500 mW) spectra yield two peaks, the most intense peak is associated with the wetting layer and a secondary less

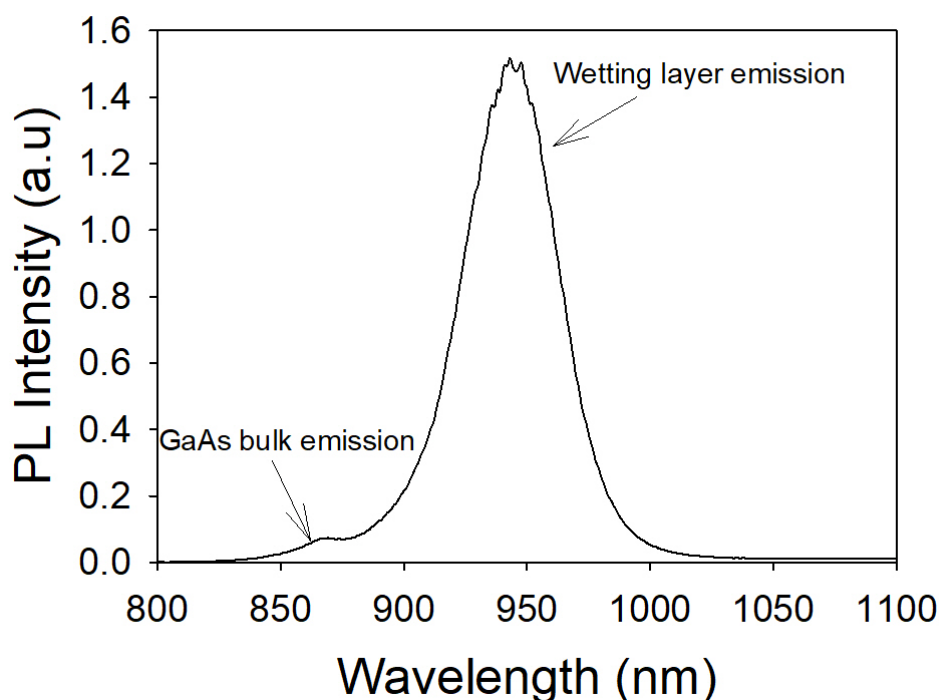


Figure 2.26: Room temperature high excitation PL of a sample with an InAs coverage of 1.6 ML.

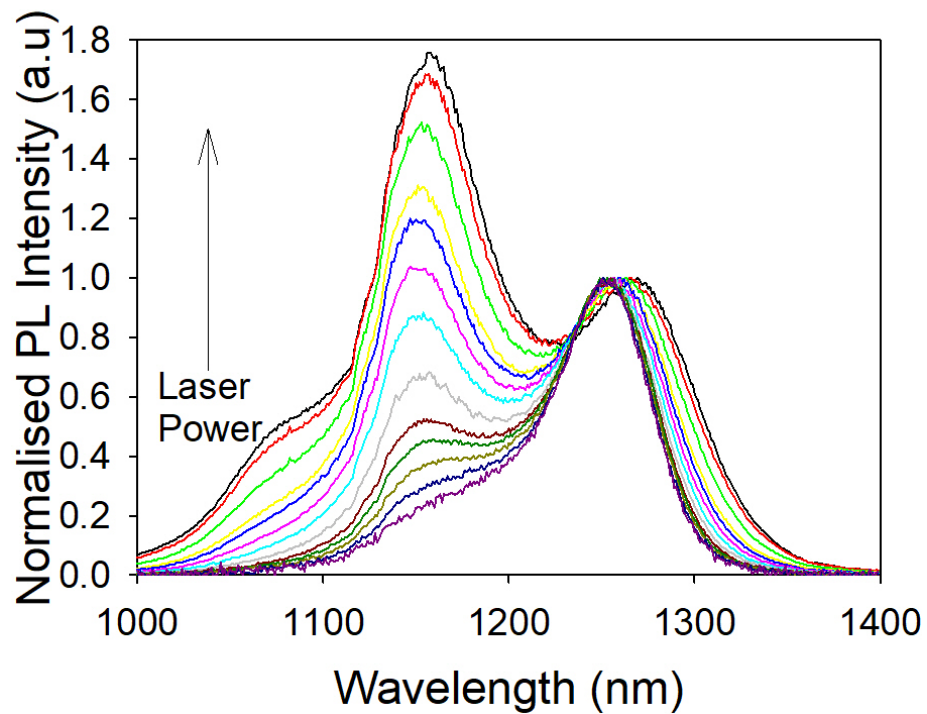


Figure 2.27: Room temperature power dependant PL of a single QD layer with an InAs coverage of 1.8 ML.

intense peak at higher energy (shorter wavelength) is associated with bulk GaAs, as shown in figure 2.26. Figure 2.27 shows the power dependent PL for an InAs coverage of 1.8 ML, where the spectra are normalised to the ground state emission. At low laser excitation power only the ground state of the QDs is visible due to the low average number of excited excitons per QD ($\ll 1$). In addition, the carrier lifetime for carrier capture into the QDs via the wetting layer is in the region of picoseconds, which is faster than the recombination time of the GaAs and the wetting layer, in the region of nanoseconds. In some samples an additional higher energy (shorter wavelength) feature maybe visible at low excitation power due to population of a subset of smaller QDs. In addition, the carrier recombination time for the QD is in the region of nanoseconds compared to the capture time of picoseconds, which leads to state blocking and the carriers sit in excited states. With increasing laser power more carriers are available, allowing higher energy states to become occupied, this is indicative of QD behaviour. Inhomogeneous broadening of the emission occurs due to occupancy of different sized QDs, as discussed in section 2.3. A red shift of the emission is observed at high powers, which results from sample heating and the Coulomb effect, as discussed in section 2.3. Figure 2.28 shows that the

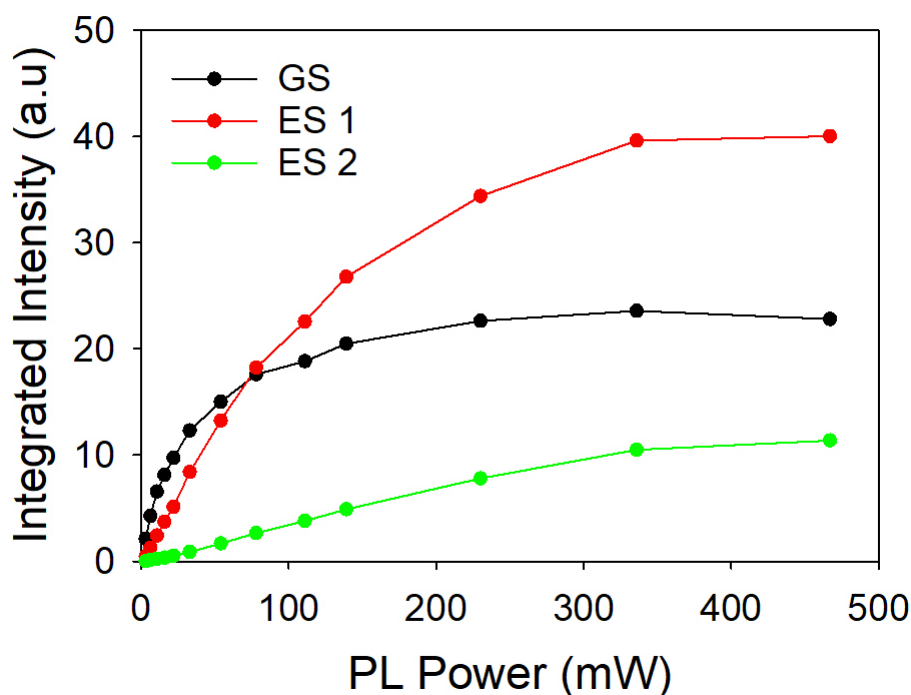


Figure 2.28: Integrated PL intensities for different QD states. The data is for the sample with 1.8 ML and is recorded at room temperature.

integrated intensities of the GS and first excited state saturate, with the latter reaching a maximum value twice that of the former, reflecting its higher degeneracy (four compared to two). The area under a Gaussian peak is calculated by integrating the Gaussian function to give equation 2.3

$$I(\lambda) = \int_{-\infty}^{\infty} I_0 e^{-\frac{(\lambda-\lambda_0)^2}{2\left(\frac{\Delta\lambda}{2\sqrt{2\ln 2}}\right)^2}} d\lambda = I_0 \frac{\Delta\lambda}{2\sqrt{2\ln 2}} \sqrt{2\pi} \quad (\text{Eqn 2.3})$$

At very high laser powers, emission from a second excited state is observed. [106] Figure 2.27 for the 1.8 ML sample shows the ground state at 1252 nm, the first excited state at 1150 nm and the second excited state at 1070 nm. The

Sample	InAs Coverage (ML)	Peak wavelength		Linewidth		State Separation		PL Intensity (a.u)
		nm	eV	nm	meV	nm	meV	
TS1459	1.4	903	1.37	20	30.7	N/A	N/A	N/A
TS1466	1.6	941	1.32	35	48.5	N/A	N/A	N/A
TS1468	1.8	1252	0.990	57	45	108	91.2	1.1
TS1470	2.0	1237	1.002	62	50.2	98	86.8	1.2
TS1472	2.2	1243	0.997	58	46.4	100	84.5	1.2
TS1474	2.4	1235	1.004	63	51.6	102	77.3	0.9

Table 2.1: Summary of the sample properties with changing InAs coverage.

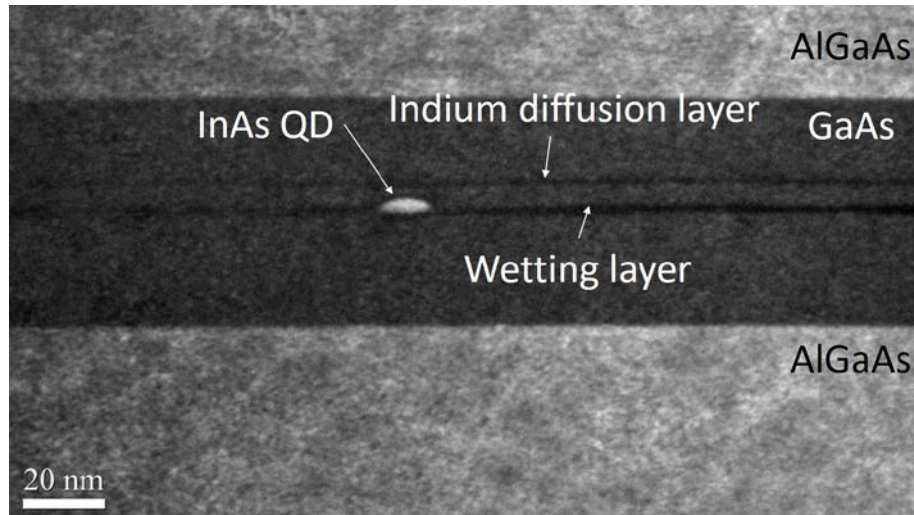


Figure 2.29: TEM image of a QD structure grown at 485°C with 2 ML InAs coverage, 0.04 ML/s growth rate and 50 sccm arsine flow.

inhomogeneous linewidth is 60 meV and the state separation between the ground state and first excited state is 87 meV. A large state separation is desirable as more energy is required for thermalisation of carriers into higher energy non-lasing states reducing the temperature sensitivity of the laser threshold current. Table 2.1 summarises the peak wavelengths, linewidths obtained from low excitation power spectra, and the state separation obtained from high excitation power (500 mW) spectra. The QD emission intensity, as measured using a PL mapper, is also given. The PL mapper excitation laser is a 633 nm HeNe laser with an optical power of 8 mW and the detector is an InGaAs photodiode. The slit width used in all the measurements is 0.1 mm, a grating of 150 g/mm and an 800 nm low pass filter was used. The intensities quoted are all peak intensities. Table 2.1 shows that once QDs have formed there is a decrease in the state separation as more InAs is added. This reduction most probably results from a change in the in plane dot size, suggesting that the QDs are becoming larger. There appears to be a decrease in the emission intensity for InAs coverage above 2.0 ML which may indicate the onset of the formation of dislocations. There is no systematic change in the emission linewidth. The results of Table 2.1 suggest that the optimum InAs coverage is 2.0 ML.

Only one sample was sent for transmission electron microscopy (TEM), the 2.0 ML coverage sample, which from the optical studies appears to be the optimum InAs coverage. From TEM images the average width and height of the QDs is determined using the software ImageJ. ImageJ is an image processing software

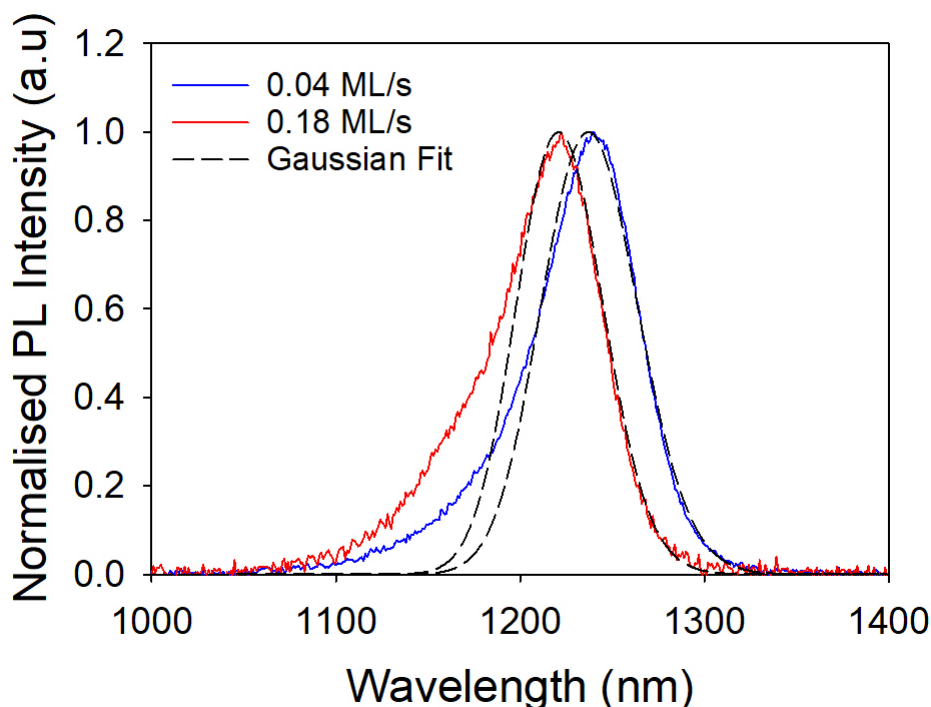


Figure 2.30: Room temperature low power PL spectra of two QD structures for different growth rates.

that can be used to extract the size of QDs or their separation in multiple-layer structures. By using the scale bar, the number of pixels per nanometre can be defined and this is used in conjunction with a line drawn manually on the TEM image to extract a distance in nanometres. Figure 2.29 shows a dark field, cross-sectional TEM image of the 2.0 ML coverage sample. The QD formation occurs on a wetting layer and the sample also shows an indium diffusion layer accumulated at the top of the low temperature grown GaAs cap. The mechanism behind the formation of this layer is unclear and also how this layer affects carrier capture and recombination remains to be studied. Attempts at removing this layer will be discussed in section 2.6. From TEM images of this sample 30 QDs are measured to give an average width of 13 nm is measured, with a standard deviation of 2.5 nm, and average height of 5 nm with a standard deviation of 3 nm.

Optimisation of the QD growth continued with an investigation of the effect of growth rate, keeping the InAs coverage constant at 2.0 ML. Figure 2.30 shows the effect of growth rate on QD emission, comparing room temperature low power PL spectra for two representative samples, and figure 2.31 plots the peak wavelength and line width for all samples studied. As the growth rate increases

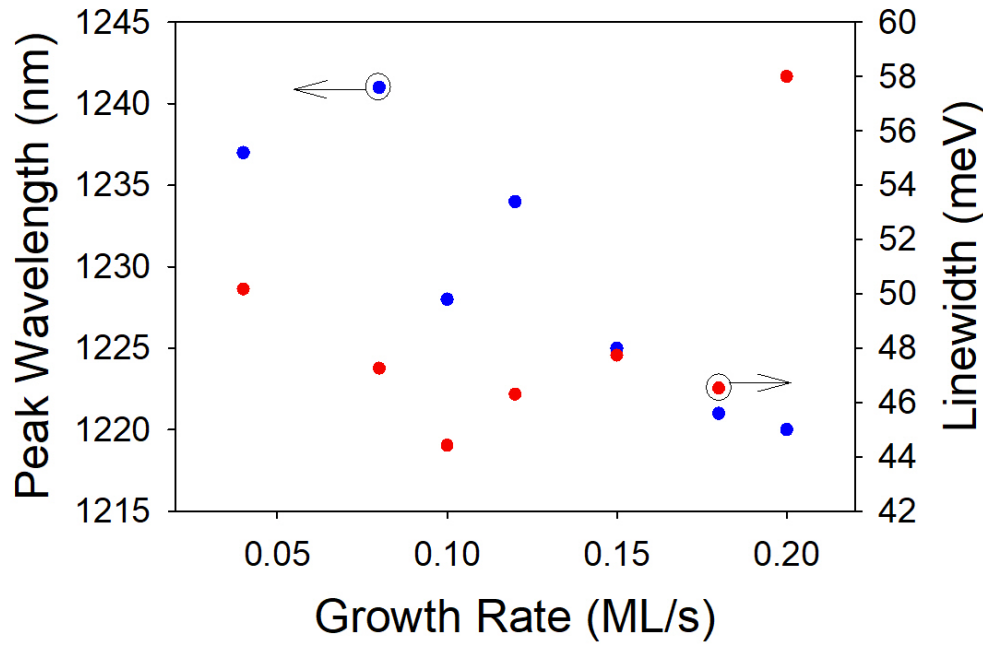


Figure 2.31: Room temperature peak PL wavelength and the ground state linewidth for different growth rates

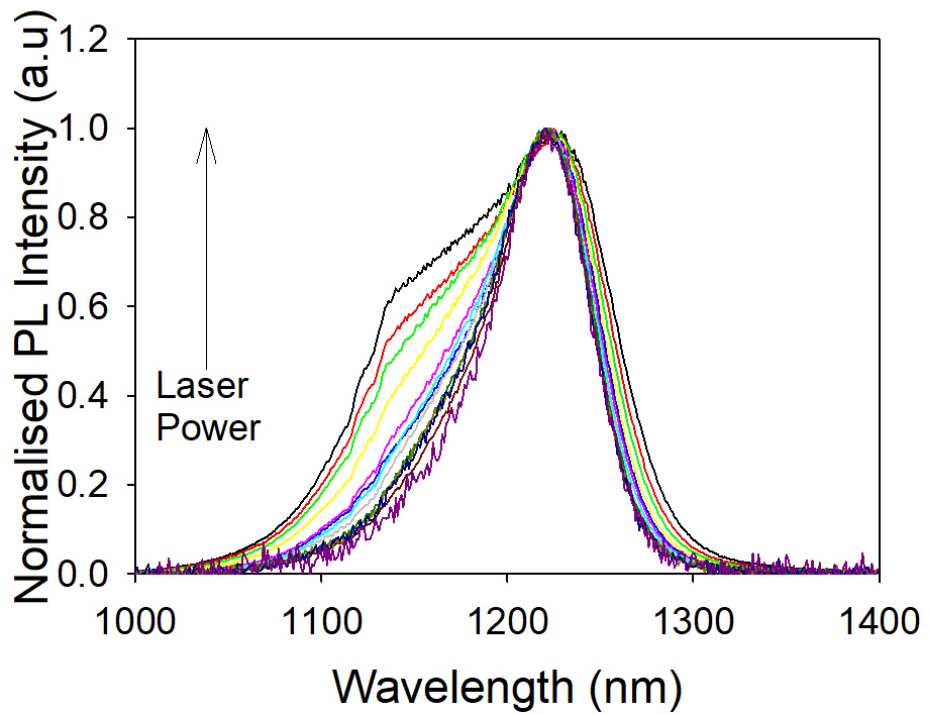


Figure 2.32: Room temperature power dependant PL spectra of a single QD layer with a growth rate of 0.18 ML/s

from 0.04 ML/s to 0.18 ML/s, a reduction in the ground state wavelength from 1237 nm to 1220 nm is observed. As discussed in section 2.4, an increase in growth rate will increase the number of nucleation sites during the growth, increasing the QD density whilst producing smaller QDs. The smaller QDs are expected to blue shift the PL emission, as shown in figure 2.31 and summarized in table 2.2. The two samples with different growth rates (0.04 ML/s and 0.18 ML/s) shown in figure 2.30 were sent for TEM imaging by Dr Richard Beanland. At the higher growth rate, the average dot size is reduced from a width of $13 \text{ nm} \pm 2.5 \text{ nm}$ to $7 \text{ nm} \pm 3.5 \text{ nm}$, and using the technique described in R. Beanland *et al.*, the QD density was estimated to have increased by almost an order of magnitude from $4.5 \times 10^9 \text{ cm}^{-2}$ to $2.5 \times 10^{10} \text{ cm}^{-2}$. [8] From the PL mapper measurement an increase in peak emission intensity was observed (table 2.2) as the growth rate is increased although with a decrease at the highest growth rate. There is an initial reduction in the linewidth up to 0.1 ML/s followed by a small increase at higher growth rates.

Figure 2.32 shows power dependent PL spectra for the sample with a growth rate of 0.18 ML /s, where the spectra are normalised with respect to the ground state. The ground state emission is at 1221 nm and the excited state emission is at 1150 nm, with an inhomogeneous linewidth of 55 meV and state separation of 69 meV. Figure 2.32 shows a weaker excited state emission at high powers in comparison to previously studied samples (figure 2.27), observed as a high energy shoulder to the ground state peak. This reduction is due to the increase in QD density with increased growth rate, with more carriers required to fill the ground states of the QDs. However, the state separation is smaller than the

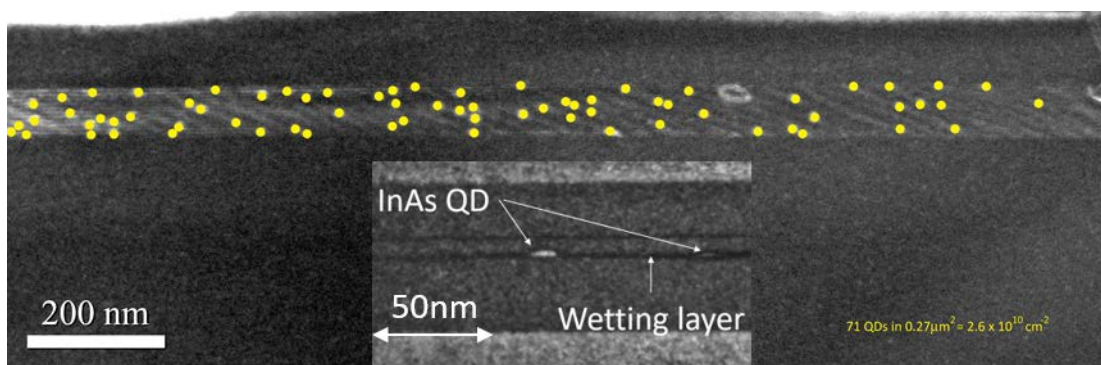


Figure 2.33: TEM image used to estimate the QD density of sample with a growth rate of 0.18 ML/s, where the QDs have been marked with yellow dots for ease of counting. Inset magnified TEM image.

Sample	Growth Rate (ML/s)	Peak wavelength		Linewidth		State Separation		PL Intensity (a.u)	QD Density (cm ⁻²)
		nm	eV	nm	meV	nm	meV		
TS1470	0.04	1237	1.002	62	50.2	98	86.8	1.2	4.5x10 ⁹
TS1477	0.08	1241	0.999	59	47.3	102	87.8	1.3	N/A
TS1481	0.10	1228	1.010	54	44.4	93	81.5	1.3	N/A
TS1483	0.12	1234	1.005	57	46.3	93	80.5	1.3	N/A
TS1486	0.15	1225	1.012	58	47.7	83	72.3	1.4	N/A
TS1499	0.18	1221	1.015	56	46.5	78	68.7	1.6	2.6x10 ¹⁰
TS1522	0.20	1220	1.016	68	58.0	84	74.4	0.8	N/A

Table 2.2: Summary of the sample properties with changing growth rate.

samples with a slower growth rate, suggesting a change in the size of the QDs; this is shown in the TEM images. Figure 2.33 shows a tilted TEM image of the sample with a growth rate of 0.18 ML/s, where the QD density is estimated to be $2.6 \times 10^{10} \text{ cm}^{-2}$. Yellow markers have been added to allow the ease of counting for calculating the QD density. The method is described in R. Beanland *et al.* [8]. The inset of figure 2.33 shows an expanded TEM image. The average size of 107 QDs is determined to be $7 \text{ nm} \pm 3.5 \text{ nm}$ width and height $4 \text{ nm} \pm 3 \text{ nm}$. This shows a significant reduction in the QD size compared to the sample grown at 0.04 ML/s. Therefore, due to the increase in QD density and the increase in emission intensity the optimum growth rate is determined to be 0.18 ML/s. Table 2.2 summarises the measured peak wavelengths, linewidths state separations, QD emission intensities and, where known, QD density.

The next optimisation step is the V/III ratio used during the QD growth. For this investigation the InAs coverage was kept constant at 2.0 ML and the growth rate kept constant at 0.18 ML/s. As discussed at the start of section 2.6, the initial V/III ratio was taken from the growth conditions previously used for the growth of InGaAs QWs. As the V/III ratio is increased, it is expected that there will be a reduction in the emission wavelength and an increase in QD density, as discussed in section 2.4. Figure 2.34 demonstrates this behaviour, showing low power, room temperature PL spectra obtained from two samples, one with a low V/III ratio (100, equivalent to 25 sccm arsine flow) and the second with a high V/III ratio (625, equivalent to 150 sccm arsine flow). As the V/III ratio is increased from 100 to 625 the peak ground state emission wavelength is reduced

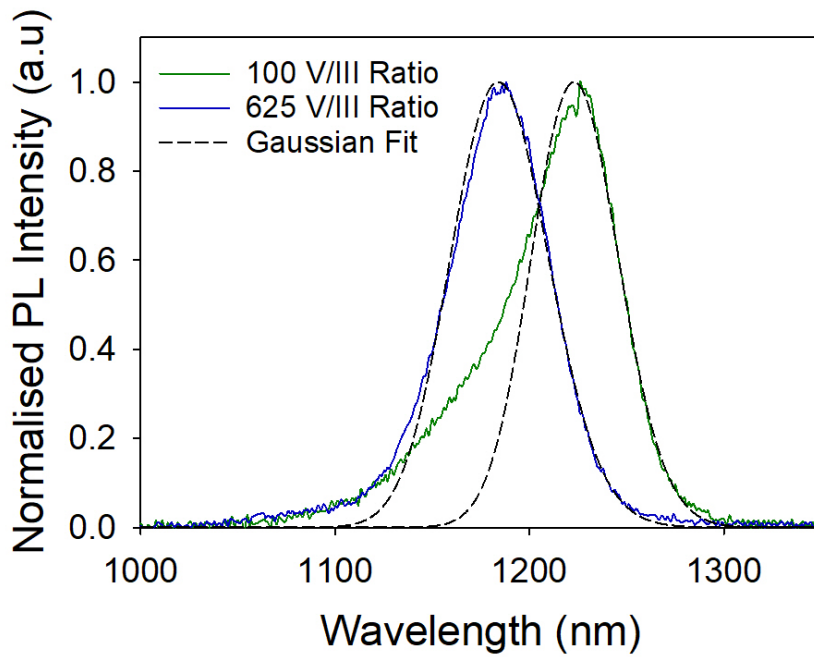


Figure 2.34 Room temperature PL spectra for low excitation power obtained from two samples with different V/III ratios during the QD growth.

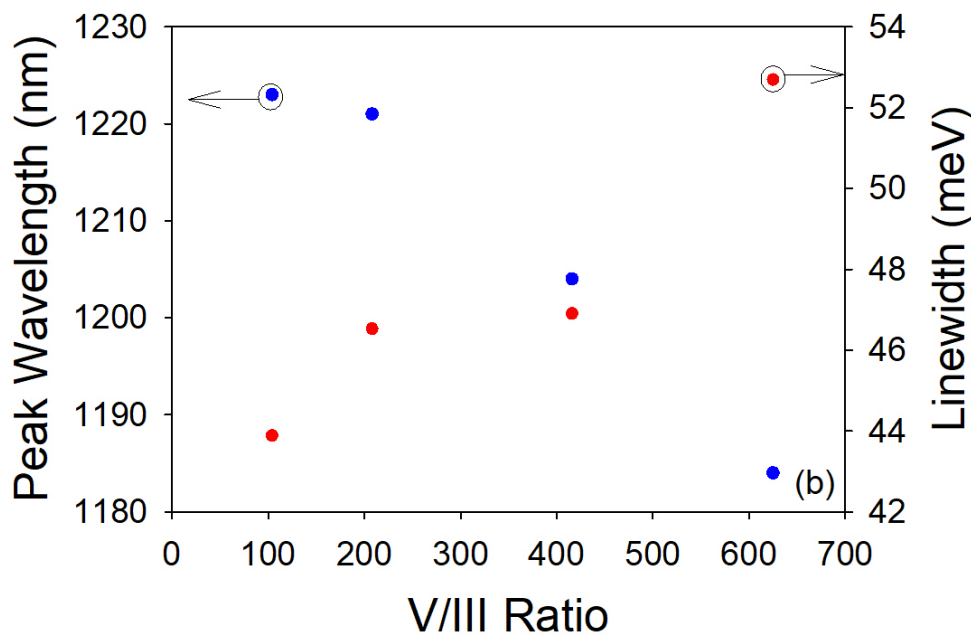


Figure 2.35: Room temperature peak PL wavelength and ground state linewidth for different V/III ratios during the QD growth.

from 1220 to 1190 nm, the expected behaviour. This reduction in emission wavelength is due to a larger amount of group V being available at the growth surface, which reduces the migration length of indium, allowing greater QD nucleation and hence smaller QDs to form. Due to the higher number of nucleation sites a reduction in uniformity is expected, which corresponds to the increased linewidth, as shown in figure 2.35. A decrease in QD size is seen in the blue shift of the emission as the V/III ratio increases. Due to excess group V atoms on the growth surface, an increase in V/III ratio should yield a higher QD density. However, TEM measurements of the QD density show a reduction in density as the V/III ratio is increased from 208 to 625. It is unclear why this decrease occurs, as it is the opposite effect to that reported in the literature. The optimum V/III ratio is a trade-off between QD intensity and wavelength. The highest emission intensity observed was at a V/III ratio of 416. However, due to the blueshift of the emission wavelength towards and below 1200 nm as the V/III ratio is increased, and the reduction in the QD density to $1 \times 10^{10} \text{ cm}^{-2}$ observed for the highest V/III ratio, the V/III ratio was kept at 208. Table 2.3 summarises the measured peak wavelengths, linewidths, state separations, QD emission intensities and, where known, QD density.

Sample	V/III Ratio QD	Peak wavelength		Linewidth		State Separation		PL intensity (a.u)	QD density (cm^{-2})
		nm	eV	nm	meV	nm	meV		
TS1527	100	1223	1.014	52	43.9	77	67.7	1.4	N/A
TS1499	208	1221	1.015	56	46.5	78	68.7	1.6	2.6×10^{10}
TS1530	416	1204	1.030	55	46.9	75	67.9	1.7	N/A
TS1535	625	1184	1.047	59	52.7	90	85.4	1.2	1×10^{10}

Table 2.3: Summary of the sample properties with different V/III ratios during QD growth.

In summary, for the growth optimisation of a single QD layer, the InAs coverage was varied from 1.4 to 2.4 ML, and the S-K transition observed between 1.6 and 1.8 ML. The optimum InAs coverage was found to be 2.0 ML, where the highest QD intensity was observed and with a ground state wavelength of 1237 nm and linewidth of 50.2 meV. Following optimisation of the InAs coverage, the growth rate was varied from 0.04 to 0.2 ML/s. A blue shift of the ground state emission was observed with increasing growth rate. In addition, an increase in QD density was observed from $4.5 \times 10^9 \text{ cm}^{-2}$ at 0.04 ML/s to

$2.6 \times 10^{10} \text{ cm}^{-2}$ at 0.18 ML/s. The optimum growth rate was 0.18 ML/s, where both the highest QD density and highest QD emission intensity occurred. The ground state wavelength reduced to 1221 nm but the linewidth improved slightly to 46.5 meV. The last single layer parameter optimised was the V/III ratio used for the growth of the QDs. The V/III ratio was altered over the range 100 to 625, with this change causing the ground state wavelength to be reduced to 1180 nm. The optimum V/III ratio chosen for future growth was 208, which gave the highest intensity and emission closest to the overall aim of 1300 nm.

Following the optimisation process for a single QD layer, stacking of the optimised QD layers was attempted with further optimisation. Stacking of QD layers is important for the fabrication of lasers, amplifiers and solar cells. Increasing the number of QD layers is required to increase the amount of material gain within the active region. Increasing the material gain can reduce the threshold current density of a laser and increase the optical output power. This is beneficial in both amplifiers and laser devices. In addition, high number of layers are required for solar cells, where an increase in the absorption of incident photons is increased. Therefore, understanding the effects of stacking multiple QD layers and the effect on the QD properties is important. For this thesis, the V/III ratio used during the growth of the capping layer and the separation between QD layers is studied. Studies of the separation are discussed in detail in chapters 3 and 4. For the current study of the V/III ratio used during the growth of the capping layer, a stack of five QD layers was grown with a separation of 50 nm. Growth parameters were those of the optimised single QD layer: 2.0 ML for the InAs coverage, 0.18 ML/s for the growth rate and a V/III

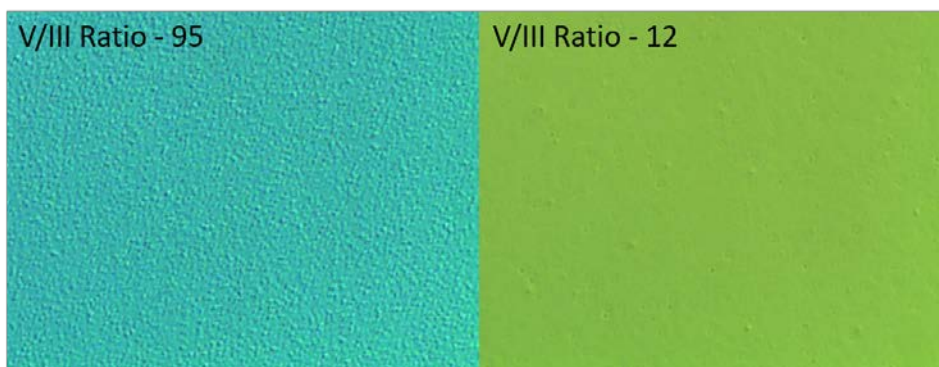


Figure 2.36: Nomarski image of two samples to show improved surface quality with a reduction in the V/III ratio used for the capping layer growth.

ratio during QD growth of 208. The initial V/III ratio for the capping layer was the standard V/III ratio used for previous growth of 95. However, after the first growth of stacked QDs with this V/III ratio, an issue with the surface morphology was observed, as shown in figure 2.36. Therefore, to solve this morphology issue an exploration of V/III ratios used during the capping layer growth was performed. The significant surface roughness visible in figure 2.36 for a sample grown with a capping layer V/III ratio of 95 could be related to the low temperature growth of both the capping layer and upper cladding layer. To overcome this surface roughness there are a number of approaches that can be tried. The first approach is to grow the upper cladding and capping layers at a nominal temperature above 600°C, but this will blue shift the QDs due to out diffusion of indium. [78] An alternative approach is to reduce the V/III ratio to increase the diffusion length of the group III atoms, which should smooth the surface after the growth of the QDs. Unexpectedly, the V/III ratio used during the capping layer growth significantly affects the ground state wavelength and linewidth of the QDs. Therefore, the V/III ratio used during capping growth was explored in some detail.

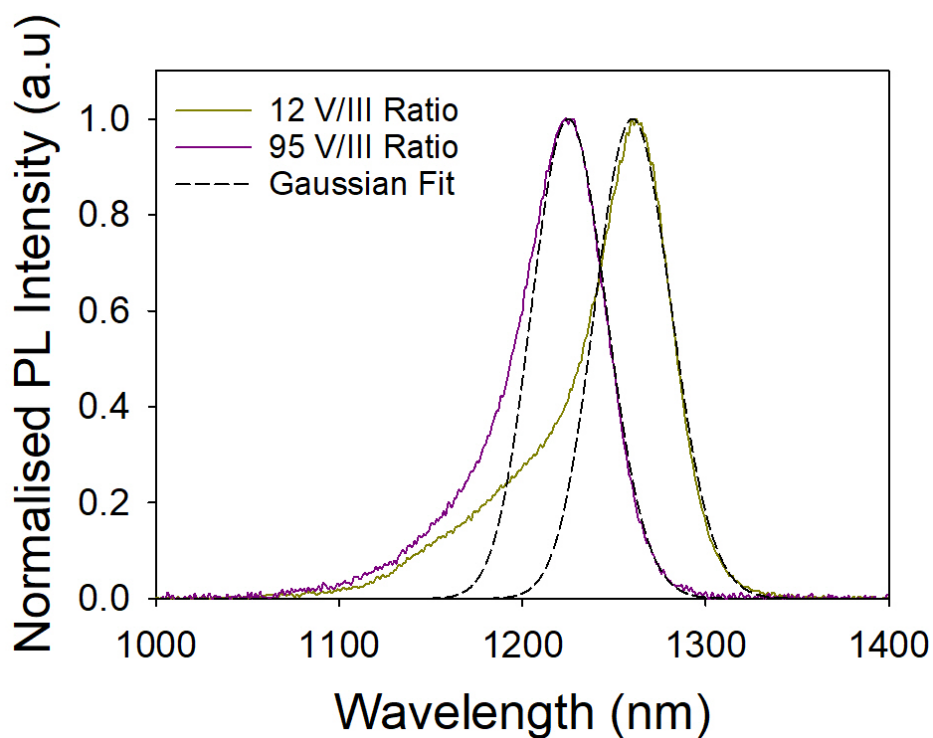


Figure 2.37: Room temperature PL spectra for low excitation power obtained from two samples with different V/III ratios during the capping layer growth.

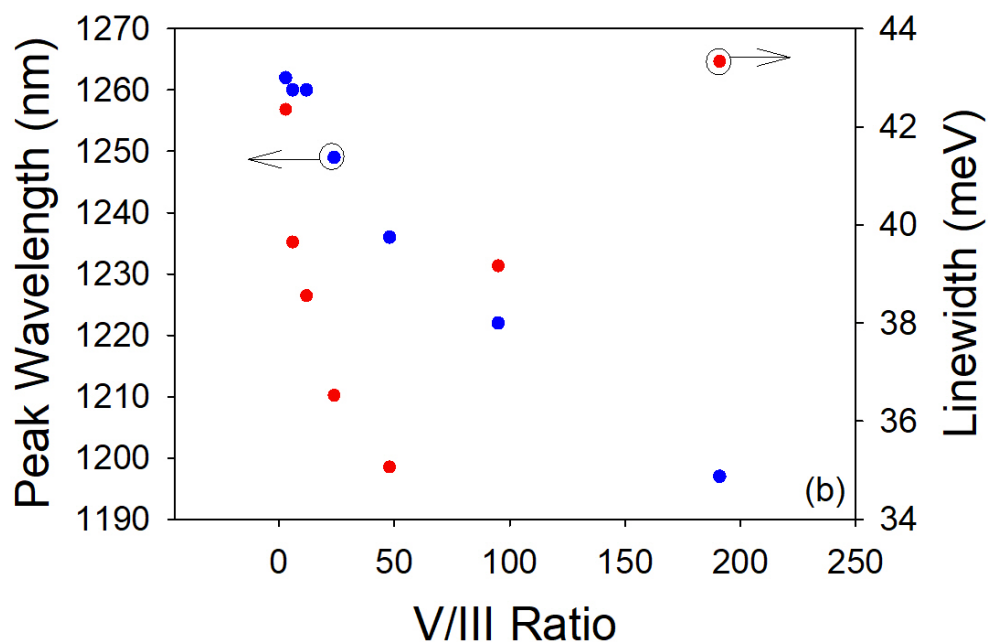


Figure 2.38: Room temperature peak PL emission wavelength and ground state linewidth for different V/III ratios.

The V/III ratio was changed from 3 (5 sccm) to 191 (340 sccm) for both the initial 8nm cap and the subsequent 42 nm GaAs spacing layer. As the arsine flow is decreased from 191 (340 sccm) to 3 (5 sccm), an increase in the ground state emission is observed, from 1197 nm to 1262 nm, as shown in figure 2.37. The mechanism behind this extension in wavelength is currently unknown, but it does seem an effective process in increasing the emission wavelength without using a SRL, previously discussed in section 2.5. Figure 2.38 shows how the ground state emission wavelength and linewidth are affected by altering the V/III ratio during the capping layer growth. This data and related parameters are given in table 2.5. As the V/III ratio is decreased from 191 there is an initial reduction in the QD ground state linewidth, with the narrowest linewidth (35.1 meV) occurring for a V/III ratio of 48. An initial weak increase in ground state emission intensity is also observed; at lower V/III ratios, the intensity increases more rapidly but with a weak decrease below a ratio of 12. The highest emission intensity occurs for a V/III ratio of 12, at this value there is only a small increase in linewidth (38.6 meV) compared to the lowest value, which occurs for a ratio of 48. The QD density was determined using TEM for the sample with a V/III ratio of 12; here the average QD density for the five layers is $2.7 \times 10^{10} \text{ cm}^{-2}$, where the QD density varies layer by layer from 3.1×10^{10} to $2.5 \times 10^{10} \text{ cm}^{-2}$ - figure 2.39. The QD density of the single layer sample grown using the same growth conditions is $2.6 \times 10^{10} \text{ cm}^{-2}$. This is in agreement with the dot density of the five layer sample and suggests that the reduction in V/III ratio during the capping layer growth does not affect the dot density.

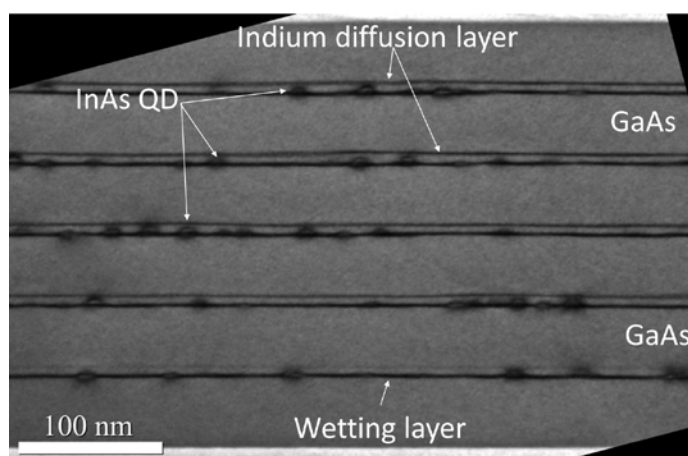


Figure 2.39: TEM image of a five-layer QD structure grown at 485°C with 2 ML InAs coverage, 0.18 ML/s growth rate, 208 and 12 V/III ratios for the QD growth and capping layer growth respectively.

As well as the intrinsic QD properties, the final surface morphology is important. As the capping layer V/III ratio is reduced, the surface morphology improves with fewer defects and a smoother surface, as shown in figure 2.36. The optimum V/III ratio during the capping layer growth was identified to be 12, giving a peak wavelength of 1260 nm, a narrow linewidth of 38.6 meV and the highest intensity of 5.9. Lowering the arsine flow will increase the group III migration length allowing infilling of defects, which reduces the number of defects and non-radiative recombination centres. Table 2.4 summarises the measured peak wavelengths, linewidths, state separations and QD emission intensity, for the samples grown with different V/III ratios for the capping layer. The TEM image of figure 2.39 shows the five QD layers with a 50 nm

Sample	V/III ratio	Peak wavelength		Linewidth		State separation		PL Intensity (a.u)
		nm	eV	nm	meV	nm	meV	
TS1575	191	1197	1.036	54	43.3	105	65.4	0.7
TS1543	95	1222	1.015	51	39.2	102	71.7	1.6
TS1579	48	1236	1.003	49	35.1	100	78.1	2.0
TS1584	24	1249	0.993	46	36.5	97	82.8	3.7
TS1602	12	1260	0.984	43	38.6	90	83.7	5.9
TS1604	6	1260	0.984	47	39.7	81	85.5	5.4
TS1608	3	1262	0.982	50	42.4	71	88.0	3.5

Table 2.5: Summary of the sample properties for variation of the V/III ratio used during the capping layer growth.

separation, which is thick enough for the strain produced by the QDs not to interfere with the nucleation sites of the QDs in the subsequent layer. As with the previous single layer devices, an indium diffusion layer is observed above each of the five QD layers in the stack.

In summary, the effect of different growth parameters on the QD properties has been studied for a single QD layer and a five QD layer structure. The optimum single layer growth parameters are an InAs coverage of 2.0 ML, a QD growth rate of 0.18 ML/s and a V/III ratio of 208. For the stacked QD layers, as the V/III ratio was reduced the surface morphology improved. However, an unexpected red shift of the ground state emission wavelength was observed,

leading to a detailed investigation of the V/III ratio used during the capping layer growth. As the V/III ratio was reduced from 191 to 12 the ground state wavelength increased from 1197 to 1262 nm with a narrowing of the ground state linewidth down to 35.1 meV at a V/III ratio of 48. As the V/III ratio was reduced further, an increase in peak wavelength was observed but below a value of 12 the QD emission intensity decreased suggesting an optimum V/III ratio during the capping layer growth of 12.

2.7 Removal of the Indium Diffusion Layer

From the TEM images discussed in section 2.6 an additional uncontrolled layer is observed above the QDs. It is thought this layer is due to indium desorbing from the QDs and floating on the surface due to the low growth temperatures of the capping layer. In an attempt to remove the unintentional indium diffusion layer observed above in all QD layers samples studied, four new samples were grown under the same growth conditions but with a modification to the capping layer. The parameters used for the capping layer are shown in table 2.5. Two different methods were used in an attempt to remove the unintentional indium diffusion layer. As with the samples discussed in section 2.5 a two stage capping process was used. An initial GaAs layer of 8 nm for samples A and D, and 15 nm for samples B and D, was grown at the same temperature as the QDs. For the remaining GaAs capping layer and $\text{Al}_{0.42}\text{Ga}_{0.58}\text{As}$ cladding, the temperature was increased to 525°C for samples A and B and 580°C for samples C and D. The sample structures are shown in figure 2.40. The first method is to keep the

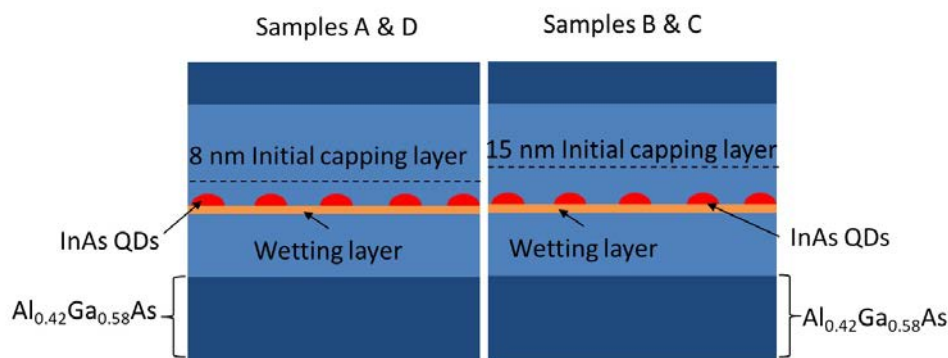


Figure 2.40: Diagram of the test structures for altering the initial cap thickness and the growth temperature of the subsequent cap.

Sample	Initial Cap thickness (nm)	Cap growth Temperature (°C)
A	8 nm	525
B	15 nm	525
C	15 nm	580
D	8 nm	580

Table 2.5: Summary of the capping layer growth temperatures and initial capping layer thicknesses.

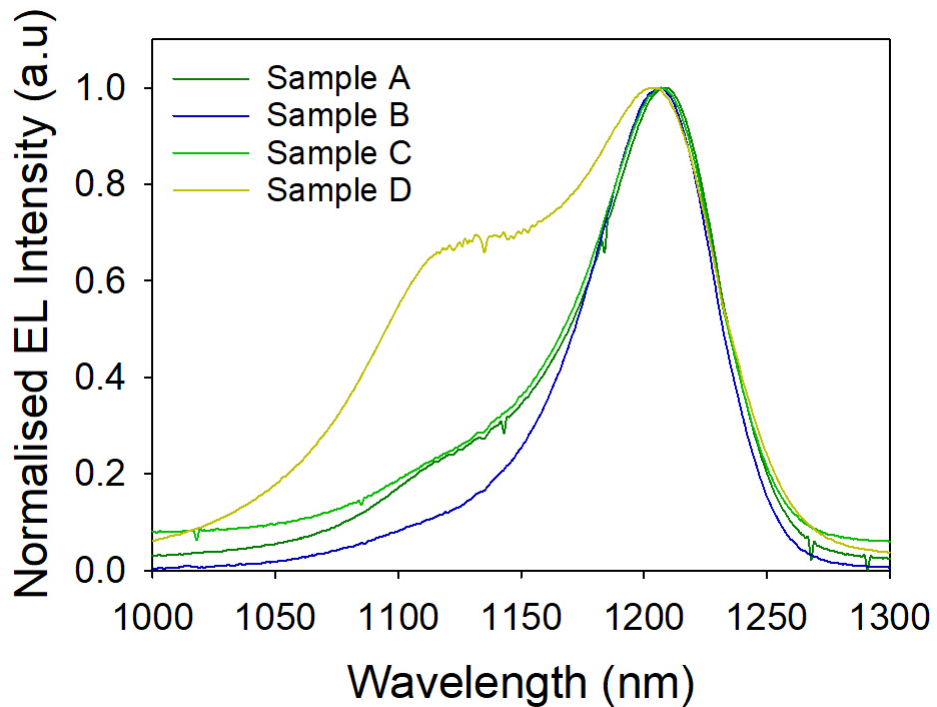


Figure 2.41: Room temperature EL spectra for low injection current of samples A, B, C and D to show the effect of the capping layer thickness and temperature.

capping layer growth temperature constant at 525°C but to attempt to bury all of the deposited indium by increasing the capping layer thickness to 15 nm. The second method is to increase the temperature to 580°C of the secondary cap layer to attempt to remove excess indium from the growth surface by indium desorption. With increasing temperature the upper capping layer and cladding layers are grown closer to their nominal optimum temperatures, improving the surface morphology. All four samples were fabricated into mesa diodes as described in chapter 4. Room temperature EL spectra for low injection current are shown in figure 2.41. All four samples have a similar ground state linewidth and all emit at the same peak wavelength, this is expected, as the QD growth conditions are identical. The identical emission wavelength confirms that the use of a higher temperature for the growth of the capping and cladding layers does not significantly alter the QD structure. Sample D shows a high-energy shoulder, which could result from a low density of QDs and hence saturation of the ground state and population of the excited state. However, due to the QD growth parameters being identical for all four samples a significant change in QD density is unlikely. A more likely reason is a bimodal QD distribution in

sample D. Low temperature (77 K) and low current spectra were recorded for samples A and D, shown in figure 2.42. The high-energy shoulder for sample D is still observed strongly suggesting bimodal behaviour.

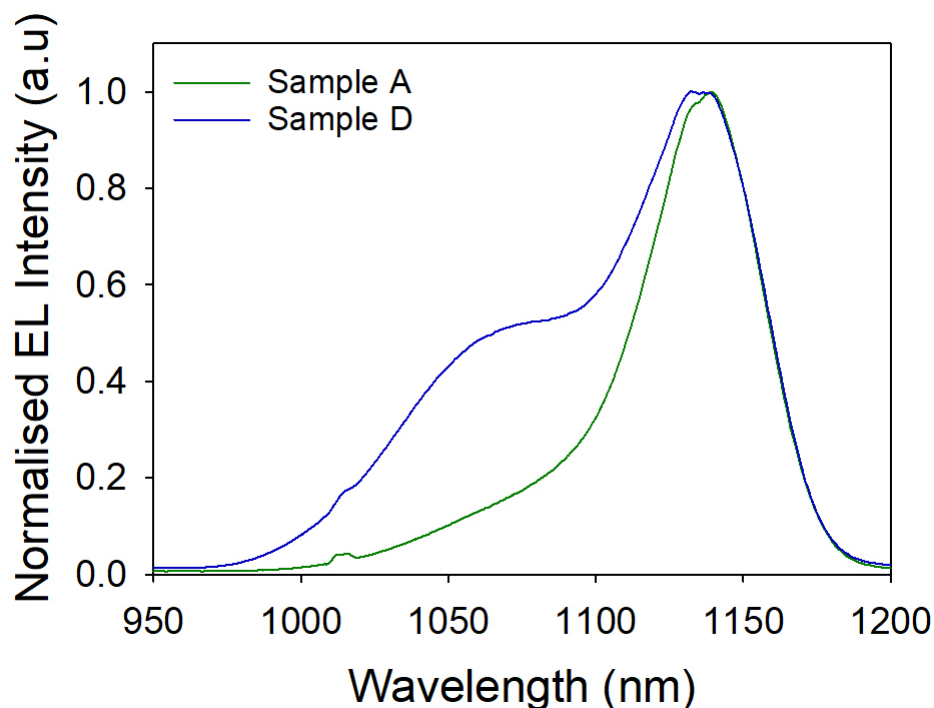


Figure 2.42: Low temperature (77K) EL spectra for low injection current of samples A and D to show the effect of capping layer growth temperature.

All four samples were sent for TEM studies from which the QD density was estimated for sample A, B, C and D to be $1.7 \times 10^{10} \text{ cm}^{-2}$, $1.53 \times 10^{10} \text{ cm}^{-2}$, $2.1 \times 10^{10} \text{ cm}^{-2}$ and $1.7 \times 10^{10} \text{ cm}^{-2}$, respectively. From the TEM images shown in figure 2.43, the indium diffusion layer is still present. As the initial capping

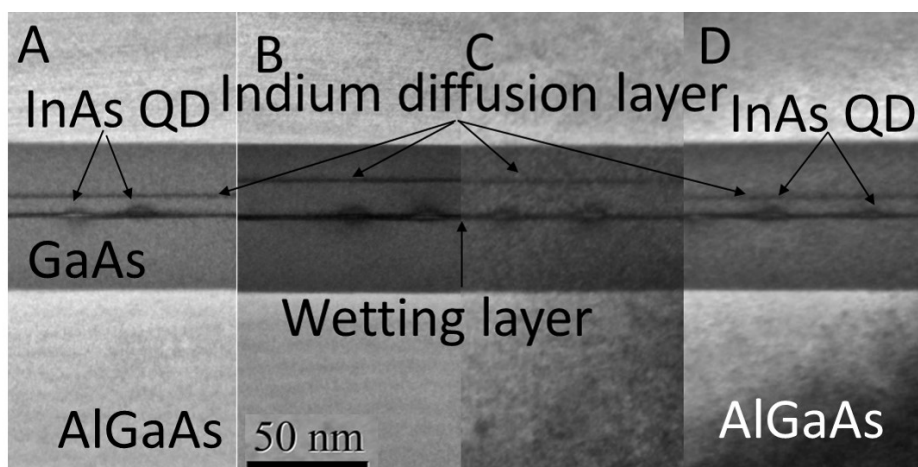


Figure 2.43: TEM images of all four samples showing the presence of the indium diffusion layer

layer is increased from 8 to 15 nm (figure 2.40), the indium diffusion layer is shifted to the top of the initial capping layer, as shown in the TEM images (figure 2.43). This means that indium is present on the surface during the growth of the initial capping layer. Increasing the temperature of the subsequent capping layer to 580°C for samples C and D, was expected to remove the indium via desorption, as discussed in section 2.1 and 2.5. However, this is not the case for this set of QD samples, as the TEM images show the presence of the indium diffusion layer at the top of the initial capping layer of 15 nm for sample C and at 8 nm for sample D.

In summary, increasing the initial capping layer thickness from 8 to 15 nm, whilst keeping the capping temperature constant, was not successful in removing the indium diffusion layer. Increasing the growth temperature of the capping layer to remove the excess indium through desorption again failed to eliminate the indium diffusion layer. However, increasing the growth temperature of the capping layer resulted in the growth of this layer and subsequent layers being closer to the nominal optimum temperatures; this improves the final surface morphology. However, both increasing the temperature and increasing the capping layer thickness has failed to remove the indium diffusion layer.

2.8 Further Quantum Dot Optimisation

In this section, the QD growth was completed by Mr Brett Harrison. Following the optimisation of the growth of InAs/GaAs QDs discussed in this chapter, the QDs were found to be grown with a substantially higher V/III ratio compared to values reported in the literature. A recent study, has looked at QDs grown at a much lower V/III ratio (5 - 40), more similar to literature reported values. However, the growth temperature (500°C) and growth rates (0.95 ML/s) were both increased, which led to the expected blue-shift of the QD ground state wavelength. In this study, an increase in the V/III ratio was found to surprisingly blue-shift the ground state wavelength (figure 2.44) and the intensity also improves, suggesting a larger number of smaller QDs in contrast to the study in this thesis and also as reported in the literature. [32], [37], [61], [64], [67] The expected effect of a decrease in V/III ratio is for the indium adatom migration to be lower, leading to a smaller but higher density of QDs, which is not seen here. Therefore, a different process, such as arsenic saturation at the surface or

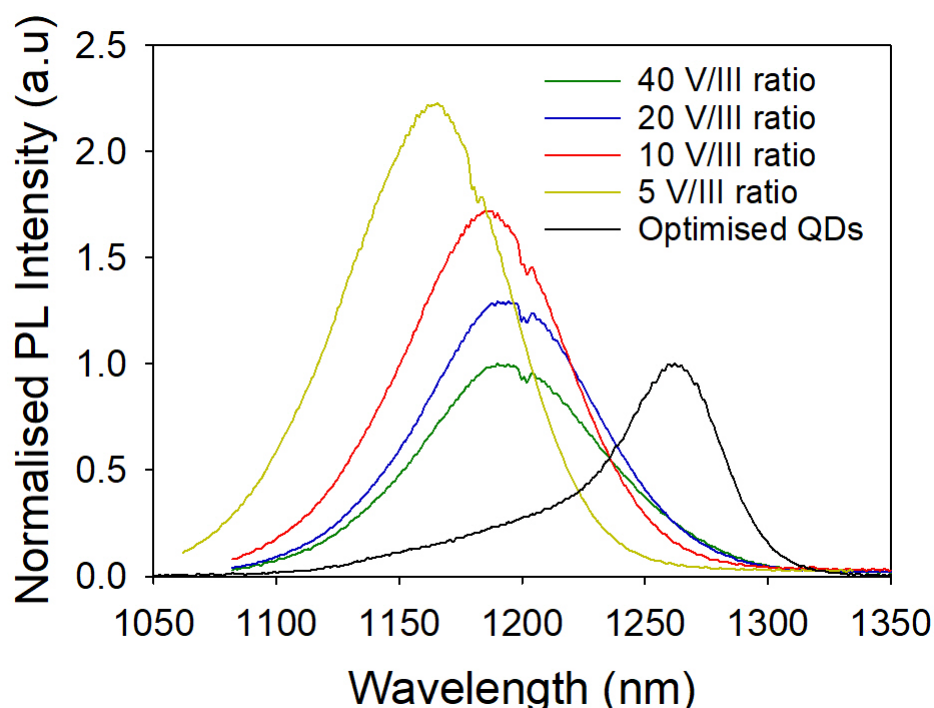


Figure 2.44: Room temperature PL spectra of samples where the V/III ratio has been changed. These samples were grown by Brett Harrison. Comparison is made with a spectrum of an optimised QD sample developed in this thesis. The new samples and the reference sample were measured under different experimental conditions.

changes in the surface morphology where the QDs are nucleated, must be occurring. Work is still ongoing to determine the QD density and to see if the indium diffusion layer has been removed. Figure 2.44 also shows a spectrum of the optimised single QD layer sample developed via the work in this thesis. Comparing with the more recent growth at significantly reduced V/III ratios it is seen that they exhibit a shorter wavelength ground state emission, but that their emission intensity is greater when measured under the same experimental conditions. This is due to the temperature and growth rate changes with the QDs in the new samples appearing to be related to the subset of smaller QDs seen in the bimodal distribution of some of the current QD samples - see chapter 4. Therefore, the revised growth parameters appear to significantly enhance the number of smaller QDs, which explains the observed blue-shift and possibly the higher PL efficiency as smaller dots are less likely to generate defects.

In addition to lowering the V/III ratio, there is a continuation of attempts to remove the indium diffusion layer and also to study the effect of this layer on the QD wavelength, carrier capture and intensity. The only growth parameter not changed in the studies described in this thesis was the growth temperature due to the limitations of the EpiTT in reliably determining the substrate temperature. The growth temperature stated above is controlled by a reference temperature of 525°C, the QDs were grown 40°C below this as indicated by the thermocouple. The more recent QDs grown by Brett Harrison were grown at the higher temperature of 500°C. Therefore, a comprehensive study of the effect of growth temperature on the QD properties is required.

2.9 Conclusions

In this chapter, the MBE and MOVPE growth techniques have been described, discussing their pros and cons along with the different epitaxial growth modes. The PL and EL characterisation set-ups and methods are introduced and discussed. Optimisation of the QD growth has been performed and this is discussed in section 2.6. The S-K transition occurs between 1.6 ML and 1.8 ML of InAs, which is in agreement with literature reports and also MBE growth. An InAs coverage of 2 ML was found to be the optimum value. It was observed that increasing the QD growth rate increases their density but also decreases the ground state emission wavelength. Using a growth rate of 0.18 ML/s was deemed to be optimum due to the reported QD density of $3 \times 10^{10} \text{ cm}^{-2}$. Increasing the V/III ratio for the QD growth resulted in a blue shift of the QD emission but did not produce the expected increase in QD density, therefore the V/III ratio was fixed at 208. In more recent work there is some evidence to suggest a much lower V/III ratio has advantages, in line with literature reported values. However, this study is still on going and the results are only preliminary. Stacking of QD layers is required to increase the material gain. To improve the surface morphology the V/III ratio during the capping layer growth was studied. Decreasing this ratio had the unexpected effect of red shifting the QD emission whilst also improving the final surface morphology. The V/III ratio for the capping layer was found to be optimum at 12. During the optimisation process, TEM images showed an indium diffusion layer above the QDs, Attempts were made to remove this layer by increasing the thickness of the initial cap and increasing the capping layer growth temperature. Neither method was found to be successful in removing the indium diffusion layer but the surface morphology was improved with the increase to 580°C of the capping layer growth temperature.

2.10 References

- [1] G. B. Stringfellow, *Organometallic Vapor-Phase Epitaxy: Theory and Practice*. Academic Press, 1999.
- [2] I. N. Stranski and L. Krastanov, “Abhandlungen der Mathematisch-Naturwissenschaftlichen Klasse IIb,” *Akad. der Wissenschaften Wien*, vol. 146, pp. 797–810, 1938.
- [3] D. J. Eaglesham and M. Cerullo, “Dislocation-free Stranski-Krastanow growth of Ge on Si (100),” *Phys. Rev. Lett.*, vol. 64, no. 16, pp. 1943–1946, Apr. 1990.
- [4] D. Beigie, A. Leonard, and S. Wiggins, “Statistical relaxation under nonturbulent chaotic flows: Non-Gaussian high-stretch tails of finite-time Lyapunov exponent distributions,” *Phys. Rev. Lett.*, vol. 70, no. 3, pp. 275–278, Jan. 1993.
- [5] W. Lang, “Nomarski differential interference-contrast microscopy,” *ZEISS Inf.*, vol. 70, pp. 114–120, 1968.
- [6] G. Binnig, C. F. Quate, and C. Gerber, “Atomic Force Microscope,” *Phys. Rev. Lett.*, vol. 56, no. 9, pp. 930–933, Mar. 1986.
- [7] E. Ruska and translation by T. Mulvey, *The early development of electron lenses and electron microscopy*. Hirzel, 1980.
- [8] R. Beanland, “Dark field transmission electron microscope images of III–V quantum dot structures,” *Ultramicroscopy*, vol. 102, no. 2, pp. 115–125, 2005.
- [9] E. H. Hall, “On a New Action of the Magnet on Electric Currents,” *Am. J. Math.*, vol. 2, no. 3, p. 287, Sep. 1879.
- [10] S. S. Li, *Semiconductor physical electronics*. Springer, 2010.
- [11] T. Ambridge and M. M. Faktor, “An automatic carrier concentration profile plotter using an electrochemical technique,” *J. Appl. Electrochem.*, vol. 5, no. 4, pp. 319–328, Nov. 1975.
- [12] P. Blood, “Capacitance-voltage profiling and the characterisation of III-V semiconductors using electrolyte barriers,” *Semicond. Sci. Technol.*, vol. 1, no. 1, pp. 7–27, Jul. 1986.
- [13] M. Bayer and A. Forchel, “Temperature dependence of the exciton homogeneous linewidth in $\text{In}_{0.60}\text{Ga}_{0.40}\text{As}$ / GaAs self-assembled quantum dots,” *Phys. Rev. B*, vol. 65, no. 4, p. 41308, Jan. 2002.

- [14] Z. Mi and P. Bhattacharya, "Molecular-beam epitaxial growth and characteristics of highly uniform InAs/GaAs quantum dot layers," *J. Appl. Phys.*, vol. 98, no. 2, p. 23510, Jul. 2005.
- [15] P. Harrison, *Quantum Wells, Wires and Dots: Theoretical and Computational Physics of Semiconductor Nanostructures*. John Wiley & Sons, 2011.
- [16] M. (Anthony) Fox, *Optical properties of solids*. Oxford University Press, 2001.
- [17] D. Bimberg, *Semiconductor nanostructures*. Springer, 2008.
- [18] Y. Arakawa and H. Sakaki, "Multidimensional quantum well laser and temperature dependence of its threshold current," *Appl. Phys. Lett.*, vol. 40, no. 11, p. 939, 1982.
- [19] D. Bimberg, M. Grundmann, and N. N. Ledentsov, *Quantum dot heterostructures*. John Wiley, 1999.
- [20] E. Kapon, M. C. Tamargo, and D. M. Hwang, "Molecular beam epitaxy of GaAs/AlGaAs superlattice heterostructures on nonplanar substrates," *Appl. Phys. Lett.*, vol. 50, no. 6, pp. 347–349, Feb. 1987.
- [21] J. a. Lebens, C. S. Tsai, K. J. Vahala, and T. F. Kuech, "Application of selective epitaxy to fabrication of nanometer scale wire and dot structures," *Appl. Phys. Lett.*, vol. 56, no. 26, p. 2642, 1990.
- [22] T. Fukui, S. Ando, T. Honda, and T. Toriyama, "GaAs tetrahedral quantum dot structures fabricated using selective area MOCVD," *Surf. Sci.*, vol. 267, no. 1–3, pp. 236–240, Jan. 1992.
- [23] S. Ando and T. Fukui, "Facet growth of AlGaAs on GaAs with SiO₂ gratings by MOCVD and applications to quantum well wires," *J. Cryst. Growth*, vol. 98, pp. 646–652, 1989.
- [24] K. Kumakura, J. Motohisa, and T. Fukui, "Formation and characterization of coupled quantum dots (CQDs) by selective area metalorganic vapor phase epitaxy," *J. Cryst. Growth*, vol. 170, no. 1–4, pp. 700–704, Jan. 1997.
- [25] K. C. Rajkumar, K. Kaviani, J. Chen, P. Chen, and A. Madhukar, "Nanofeatures on GaAs (111)B via photolithography," *Appl. Phys. Lett.*, vol. 60, no. 7, pp. 850–852, Feb. 1992.
- [26] A. Madhukar, "Growth of semiconductor heterostructures on patterned substrates: defect reduction and nanostructures," *Thin Solid Films*, vol. 231, no. 1–2, pp. 8–42, Aug. 1993.

- [27] R. Bhat, "Non-planar and masked-area epitaxy by organometallic chemical vapour deposition," *Semicond. Sci. Technol.*, vol. 8, no. 6, pp. 984–993, Jun. 1993.
- [28] J. Oshinowo, M. Nishioka, S. Ishida, and Y. Arakawa, "Highly uniform InGaAs quantum dots (~ 15nm) grown by MOVPE on GaAs," *J. Cryst. Growth*, vol. 145, pp. 986–987, 1994.
- [29] K. D. Jöns et al., "Triggered Indistinguishable Single Photons with Narrow Line Widths from Site-Controlled Quantum Dots," *Nano Lett.*, vol. 13, no. 1, pp. 126–130, Jan. 2013.
- [30] M. K. Yakes et al., "Leveraging Crystal Anisotropy for Deterministic Growth of InAs Quantum Dots with Narrow Optical Linewidths," *Nano Lett.*, vol. 13, no. 10, pp. 4870–4875, Oct. 2013.
- [31] V. A. Shchukin, N. N. Ledentsov, P. S. Kop'ev, and D. Bimberg, "Spontaneous Ordering of Arrays of Coherent Strained Islands," *Phys. Rev. Lett.*, vol. 75, no. 16, pp. 2968–2971, Oct. 1995.
- [32] A. A. El-Emawy et al., "Formation trends in quantum dot growth using metalorganic chemical vapor deposition," *J. Appl. Phys.*, vol. 93, no. 6, p. 3529, 2003.
- [33] J. X. Chen et al., "Tuning InAs/GaAs quantum dot properties under Stranski-Krastanov growth mode for 1.3 μm applications," *J. Appl. Phys.*, vol. 91, no. 10, p. 6710, May 2002.
- [34] J. Tatebayashi et al., "1.28 μm lasing from stacked InAs/GaAs quantum dots with low-temperature-grown AlGaAs cladding layer by metalorganic chemical vapor deposition," *Appl. Phys. Lett.*, vol. 86, no. 5, p. 53107, Jan. 2005.
- [35] J. Tatebayashi, M. Nishioka, and Y. Arakawa, "Over 1.5 μm light emission from InAs quantum dots embedded in InGaAs strain-reducing layer grown by metalorganic chemical vapor deposition," *Appl. Phys. Lett.*, vol. 78, no. 22, p. 3469, May 2001.
- [36] F. Heinrichsdorff, A. Krost, D. Bimberg, A. O. Kosogov, and P. Werner, "Self organized defect free InAs/GaAs and InAs/InGaAs/GaAs quantum dots with high lateral density grown by MOCVD," *Appl. Surf. Sci.*, vol. 123–124, pp. 725–728, Jan. 1998.
- [37] A. Passaseo et al., "Structural study of InGaAs/GaAs quantum dots grown by metalorganic chemical vapor deposition for optoelectronic applications at 1.3 μm ," *J. Appl. Phys.*, vol. 89, no. 8, p. 4341, 2001.
- [38] G. Saint-Girons et al., "Metal-organic vapor-phase epitaxy of defect-free InGaAs/GaAs quantum dots emitting around 1.3 μm ," *J. Cryst. Growth*, vol. 235, no. 1–4, pp. 89–94, Feb. 2002.

- [39] S. Liang, H. L. Zhu, and W. Wang, "Size distributions of quantum islands on stepped substrates," *J. Chem. Phys.*, vol. 131, no. 15, p. 154704, Oct. 2009.
- [40] H. Wang, D. Ning, and S. Feng, "Temperature dependence of the optical properties of InAs/GaAs self-organized quantum dots with bimodal size distribution," *J. Cryst. Growth*, vol. 209, no. 4, pp. 630–636, 2000.
- [41] F. Franchello, L. D. de Souza, E. Laureto, A. A. Quivy, I. F. L. Dias, and J. L. Duarte, "Influence of bimodal distribution and excited state emission on photoluminescence spectra of InAs self-assembled quantum dots," *J. Lumin.*, vol. 137, pp. 22–27, 2013.
- [42] M. De Giorgi et al., "Open issues for lasing at 1.3 μm in MOCVD-grown quantum dots," *Phys. status solidi*, vol. 238, no. 2, pp. 349–352, Jul. 2003.
- [43] G. Saint-Girons, I. Sagnes, and G. Patriarche, "De-relaxation of plastically relaxed InAs/GaAs quantum dots during the growth of a GaAs encapsulation layer," *J. Cryst. Growth*, vol. 310, no. 3, pp. 536–540, Feb. 2008.
- [44] L. Chu, M. Arzberger, G. Böhm, and G. Abstreiter, "Influence of growth conditions on the photoluminescence of self-assembled InAs/GaAs quantum dots," *J. Appl. Phys.*, vol. 85, no. 4, p. 2355, Feb. 1999.
- [45] Z. B. Chen et al., "Elemental diffusion during the droplet epitaxy growth of In(Ga)As/GaAs(001) quantum dots by metal-organic chemical vapor deposition," *Appl. Phys. Lett.*, vol. 104, no. 2, p. 22108, Jan. 2014.
- [46] Z.-B. Chen et al., "Can misfit dislocations be located above the interface of InAs/GaAs (001) epitaxial quantum dots?," *Nanoscale Res. Lett.*, vol. 7, no. 1, p. 486, Jan. 2012.
- [47] S. Bietti, L. Esposito, A. Fedorov, A. Ballabio, A. Martinelli, and S. Sanguinetti, "Characterization and Effect of Thermal Annealing on InAs Quantum Dots Grown by Droplet Epitaxy on GaAs(111)A Substrates.," *Nanoscale Res. Lett.*, vol. 10, no. 1, p. 930, Dec. 2015.
- [48] Z. B. Chen et al., "Preferential nucleation and growth of InAs/GaAs(001) quantum dots on defected sites by droplet epitaxy," *Scr. Mater.*, vol. 69, no. 8, pp. 638–641, Oct. 2013.
- [49] L. Goldstein, F. Glas, J. Y. Marzin, M. N. Charasse, and G. Le Roux, "Growth by molecular beam epitaxy and characterization of InAs/GaAs strained-layer superlattices," *Appl. Phys. Lett.*, vol. 47, no. 10, p. 1099, 1985.
- [50] C. K. Chia et al., "Saturated dot density of InAs/GaAs self-assembled quantum dots grown at high growth rate," *Appl. Phys. Lett.*, vol. 90, no. 16, p. 161906, Apr. 2007.

- [51] P. G. Eliseev et al., “Transition dipole moment of InAs/InGaAs quantum dots from experiments on ultralow-threshold laser diodes,” *Appl. Phys. Lett.*, vol. 77, no. 2, p. 262, Jun. 2000.
- [52] Xiaodong Huang, A. Stintz, C. P. Hains, G. T. Liu, J. Cheng, and K. J. Malloy, “Very low threshold current density room temperature continuous-wave lasing from a single-layer InAs quantum-dot laser,” *IEEE Photonics Technol. Lett.*, vol. 12, no. 3, pp. 227–229, Mar. 2000.
- [53] P. G. Eliseev, H. Li, T. Liu, T. C. Newell, L. F. Lester, and K. J. Malloy, “Ground-state emission and gain in ultralow-threshold InAs-InGaAs quantum-dot lasers,” *IEEE J. Sel. Top. Quantum Electron.*, vol. 7, no. 2, pp. 135–142, 2001.
- [54] I. R. Sellers et al., “1.3 μm InAs/GaAs multilayer quantum-dot laser with extremely low room-temperature threshold current density,” *Electron. Lett.*, vol. 40, no. 22, p. 1412, 2004.
- [55] G. T. Liu, A. Stintz, H. Li, K. J. Malloy, and L. F. Lester, “Extremely low room-temperature threshold current density diode lasers using InAs dots in In_{0.15}Ga_{0.85}As quantum well,” *Electron. Lett.*, vol. 35, no. 14, p. 1163, 1999.
- [56] D. L. Huffaker, G. Park, Z. Zou, O. B. Shchekin, and D. G. Deppe, “Continuous-wave low-threshold performance of 1.3 μm InGaAs-GaAs quantum-dot lasers,” *IEEE J. Sel. Top. Quantum Electron.*, vol. 6, no. 3, pp. 452–461, May 2000.
- [57] M. A. Majid et al., “Toward 1550-nm GaAs-Based Lasers Using InAs/GaAs Quantum Dot Bilayers,” *IEEE J. Sel. Top. Quantum Electron.*, vol. 17, no. 5, pp. 1334–1342, Sep. 2011.
- [58] D. Guimard et al., “Ground state lasing at 1.30 microm from InAs/GaAs quantum dot lasers grown by metal-organic chemical vapor deposition,” *Nanotechnology*, vol. 21, no. 10, p. 105604, Mar. 2010.
- [59] F. Heinrichsdorff et al., “Self organization phenomena of quantum dots grown by metalorganic chemical vapour deposition,” *J. Cryst. Growth*, vol. 170, no. 1–4, pp. 568–573, Jan. 1997.
- [60] F. Heinrichsdorff et al., “InAs/GaAs Quantum Dots Grown by Metalorganic Chemical Vapor Deposition,” *Jpn. J. Appl. Phys.*, vol. 36, no. Part 1, No. 6B, pp. 4129–4133, Jun. 1997.
- [61] V. Tasco, B. Potì, M. De Vittorio, M. De Giorgi, R. Cingolani, and A. Passaseo, “Improved performances of 1.3 μm InGaAs QD structures grown at high temperature by metal organic chemical vapour deposition,” *Microelectronics J.*, vol. 36, no. 3–6, pp. 180–182, Mar. 2005.
- [62] L. Lin, L. Guo-Jun, W. Xiao-Hua, L. Mei, L. Zhan-Guo, and W. Chun-Ming, “Low Density Self-Assembled InAs/GaAs Quantum Dots Grown by

Metal Organic Chemical Vapour Deposition,” *Chinese Phys. Lett.*, vol. 25, no. 2, pp. 667–670, Feb. 2008.

[63] K. Sears, J. Wong-leung, M. Buda, H. H. Tan, and C. Jagadish, “Growth and characterisation of InAs/GaAs quantum dots grown by MOCVD,” *IEEE*, pp. 6–9, 2005.

[64] K. Sears, H. Tan, M. Buda, J. Wong-Leung, and C. Jagadish, “Growth and Characterization of InAs/GaAs Quantum Dots and Diode Lasers,” 2006 Int. Conf. Nanosci. Nanotechnol., pp. 505–508, 2006.

[65] P. B. Joyce, T. J. Krzyzewski, G. R. Bell, B. A. Joyce, and T. S. Jones, “Composition of InAs quantum dots on GaAs(001): Direct evidence for (In,Ga)As alloying,” *Phys. Rev. B*, vol. 58, no. 24, pp. R15981–R15984, Dec. 1998.

[66] G. Y. Zhou, Y. H. Chen, X. L. Zhou, B. Xu, X. L. Ye, and Z. G. Wang, “Different growth mechanisms of bimodal InAs/GaAs QDs,” *Phys. E Low-dimensional Syst. Nanostructures*, vol. 43, no. 1, pp. 308–311, Nov. 2010.

[67] K. Sears, H. H. Tan, J. Wong-Leung, and C. Jagadish, “The role of arsine in the self-assembled growth of InAs/GaAs quantum dots by metal organic chemical vapor deposition,” *J. Appl. Phys.*, vol. 99, no. 4, p. 44908, Feb. 2006.

[68] A. O. Kosogov et al., “Structural and optical properties of InAs–GaAs quantum dots subjected to high temperature annealing,” *Appl. Phys. Lett.* 69, 3072 (1996);.

[69] S. Kiravittaya, A. Rastelli, and O. G. Schmidt, “Photoluminescence from seeded three-dimensional InAs/GaAs quantum-dot crystals,” *Appl. Phys. Lett.*, vol. 88, no. 4, p. 43112, 2006.

[70] J. Tatebayashi, M. Nishioka, and Y. Arakawa, “Luminescence in excess of 1.5 μm at room-temperature of InAs quantum dots capped by a thin InGaAs strain-reducing layer,” *J. Cryst. Growth*, vol. 237–239, pp. 1296–1300, Apr. 2002.

[71] K. Nishi, H. Saito, S. Sugou, and J.-S. Lee, “A narrow photoluminescence linewidth of 21 meV at 1.35 μm from strain-reduced InAs quantum dots covered by In_{0.2}a_{0.8}As grown on GaAs substrates,” *Appl. Phys. Lett.*, vol. 74, no. 8, p. 1111, Feb. 1999.

[72] T. Yang, M. Nishioka, and Y. Arakawa, “Optimizing the GaAs capping layer growth of 1.3 μm InAs/GaAs quantum dots by a combined two-temperature and annealing process at low temperatures,” *J. Cryst. Growth*, vol. 310, no. 24, pp. 5469–5472, Dec. 2008.

- [73] O. Nasr, M. H. Hadj Alouane, B. Ilahi, B. Salem, L. Sfaxi, and H. Maaref, "Postgrowth intermixing of strain engineered InAs/GaAs quantum dots," *J. Alloys Compd.*, vol. 615, pp. 683–686, Dec. 2014.
- [74] T. D. Germann, A. Strittmatter, T. Kettler, K. Posilovic, U. W. Pohl, and D. Bimberg, "MOCVD of InGaAs/GaAs quantum dots for lasers emitting close to 1.3 μm ," *J. Cryst. Growth*, vol. 298, pp. 591–594, Jan. 2007.
- [75] H. Shin, J.-B. Kim, Y.-H. Yoo, W. Lee, E. Yoon, and Y.-M. Yu, "Enhanced strain of InAs quantum dots by an InGaAs ternary layer in a GaAs matrix," *J. Appl. Phys.*, vol. 99, no. 2, p. 23521, Jan. 2006.
- [76] R. Krebs, S. Deubert, J. P. Reithmaier, and A. Forchel, "Improved performance of MBE grown quantum-dot lasers with asymmetric dots in a well design emitting near 1.3 μm ," *J. Cryst. Growth*, vol. 251, no. 1–4, pp. 742–747, Apr. 2003.
- [77] Y. Fu, S. M. Wang, F. Ferdos, M. Sadeghi, and A. Larssonb, "InAs Quantum Dots Capped by GaAs, In_{0.4}Ga_{0.6}As Dots, and In_{0.2}Ga_{0.8}As Well," *J. Nanosci. Nanotechnol.*, vol. 2, no. 3, pp. 421–426, Jul. 2002.
- [78] H. Z. Song, Y. Tanaka, T. Yamamoto, N. Yokoyama, M. Sugawara, and Y. Arakawa, "AlGaAs capping effect on InAs quantum dots self-assembled on GaAs," *Phys. Lett. A*, vol. 375, no. 40, pp. 3517–3520, Sep. 2011.
- [79] D. Guimard et al., "Interface properties of InAs quantum dots produced by antimony surfactant-mediated growth: Etching of segregated antimony and its impact on the photoluminescence and lasing characteristics," *Appl. Phys. Lett.*, vol. 94, no. 10, p. 103116, Mar. 2009.
- [80] D. Guimard et al., "Ground state lasing at 1.34 μm from InAs/GaAs quantum dots grown by antimony-mediated metal organic chemical vapor deposition," *Appl. Phys. Lett.*, vol. 90, no. 24, p. 241110, Jun. 2007.
- [81] D. Guimard, M. Nishioka, S. Tsukamoto, and Y. Arakawa, "Effect of antimony on the density of InAs/Sb:GaAs(100) quantum dots grown by metalorganic chemical-vapor deposition," *J. Cryst. Growth*, vol. 298, pp. 548–552, Jan. 2007.
- [82] K. Pötschke et al., "Ripening of self-organized InAs quantum dots," *Phys. E Low-dimensional Syst. Nanostructures*, vol. 21, no. 2–4, pp. 606–610, Mar. 2004.
- [83] D. Guimard et al., "CW Lasing at 1.35 μm From Ten InAs–Sb : GaAs Quantum-Dot Layers Grown by Metal–Organic Chemical Vapor Deposition," *IEEE Photonics Technol. Lett.*, vol. 20, no. 10, pp. 827–829, May 2008.
- [84] D. Guimard et al., "Ground state lasing at 1.30 microm from InAs/GaAs quantum dot lasers grown by metal-organic chemical vapor deposition.," *Nanotechnology*, vol. 21, no. 10, p. 105604, Mar. 2010.

- [85] D. Bimberg, “Onion like growth and inverted many-particle energies in quantum dots,” *Appl. Surf. Sci.*, vol. 255, no. 3, pp. 799–801, Nov. 2008.
- [86] S. Park, J. Tatebayashi, and Y. Arakawa, “Structural and optical properties of high-density ($>10^{11}/\text{cm}^2$) InAs QDs with varying Al(Ga)As matrix layer thickness,” *Phys. E Low-dimensional Syst. Nanostructures*, vol. 21, no. 2–4, pp. 279–284, Mar. 2004.
- [87] S. Malik, C. Roberts, R. Murray, and M. Pate, “Tuning self-assembled InAs quantum dots by rapid thermal annealing,” *Appl. Phys. Lett.* 71, 1987 (1997)
- [88] L. Finger et al., “Modification of energy relaxation of InGaAs quantum dots by postgrowth thermal annealing,” in *Conference Proceedings. 1998 International Conference on Indium Phosphide and Related Materials (Cat. No.98CH36129)*, 1998, pp. 151–154.
- [89] T. Yang, J. Tatebayashi, M. Nishioka, and Y. Arakawa, “Improved surface morphology of stacked 1.3 μm InAs/GaAs quantum dot active regions by introducing annealing processes,” *Appl. Phys. Lett.*, vol. 89, no. 8, p. 81902, 2006.
- [90] T. V. Torchynska, R. C. Tamayo, G. Polupan, A. Stints, and L. Shcherbyna, “InAs quantum dot emission and annealing impact in quantum wells with strain reduced InAlGaAs layers,” *J. Lumin.*, vol. 163, pp. 40–46, Jul. 2015.
- [91] J. Tatebayashi et al., “InAs/GaAs self-assembled quantum-dot lasers grown by metalorganic chemical vapor deposition—Effects of postgrowth annealing on stacked InAs quantum dots,” *Appl. Phys. Lett.*, vol. 85, no. 6, p. 1024, Aug. 2004.
- [92] H. Wang and H. P. Ho, “Effect of annealing ambient flux on InAs islands grown on GaAs(001) substrates by metal–organic vapor phase epitaxy,” *Mater. Chem. Phys.*, vol. 96, no. 2–3, pp. 223–227, Apr. 2006.
- [93] G. X. Shi et al., “Thermal annealing effect on InAs/InGaAs quantum dots grown by atomic layer molecular beam epitaxy,” *J. Cryst. Growth*, vol. 269, no. 2–4, pp. 181–186, Sep. 2004.
- [94] S. J. Xu et al., “Effects of rapid thermal annealing on structure and luminescence of self-assembled InAs/GaAs quantum dots,” *Appl. Phys. Lett.* 72, 3335 (1998);
- [95] D. Biswas, S. Kumar, and T. Das, “Interdiffusion induced changes in the photoluminescence of $\text{In}_x\text{Ga}_{1-x}\text{As}/\text{GaAs}$ quantum dots interpreted,” *J. Appl. Phys.*, vol. 101, no. 2, p. 26108, Jan. 2007.
- [96] C. Yang, J. Kim, U. Sim, J. Lee, W. J. Choi, and E. Yoon, “Competitive growth mechanisms of InAs quantum dots on $\text{In}_x\text{Ga}_{1-x}\text{As}$ layer during post

growth interruption,” *Thin Solid Films*, vol. 518, no. 22, pp. 6361–6364, Sep. 2010.

[97] L. G. Wang, P. Kratzer, M. Scheffler, and Q. K. K. Liu, “Island dissolution during capping layer growth interruption,” *Appl. Phys. A Mater. Sci. Process.*, vol. 73, no. 2, pp. 161–165, Aug. 2001.

[98] J. Kim et al., “Growth mechanism of highly uniform InAs/GaAs quantum dot with periodic arsine interruption by metalorganic chemical vapor deposition,” *J. Appl. Phys.*, vol. 110, no. 4, p. 44302, Aug. 2011.

[99] J.-S. Lee, H.-W. Ren, S. Sugou, and Y. Masumoto, “In_{0.5}Ga_{0.5}As quantum dot intermixing and evaporation in GaAs capping layer growth,” *J. Appl. Phys.*, vol. 84, no. 12, p. 6686, Dec. 1998.

[100] E. Steimetz et al., “Optimizing the growth procedure for InAs quantum dot stacks by optical in situ techniques,” *J. Cryst. Growth*, vol. 221, no. 1–4, pp. 592–598, Dec. 2000.

[101] T. Kaizu, M. Takahashi, K. Yamaguchi, and J. Mizuki, “Modification of InAs quantum dot structure during annealing,” *J. Cryst. Growth*, vol. 301–302, pp. 248–251, Apr. 2007.

[102] M. Galluppi et al., “Atomic equilibrium concentrations in (InGa)As quantum dots,” *Appl. Phys. Lett.*, vol. 78, no. 20, pp. 3121–3123, May 2001.

[103] R. Leon and S. Fafard, “Structural and radiative evolution in quantum dots near the In_xGa_{1-x}As/GaAs Stranski-Krastanow transformation,” *Phys. Rev. B*, vol. 58, no. 4, pp. 1726–1729, 1998.

[104] F. Heinrichsdorff, A. Krost, M. Grundmann, D. Bimberg, A. Kosogov, and P. Werner, “Self-organization processes of InGaAs/GaAs quantum dots grown by metalorganic chemical vapor deposition,” *Appl. Phys. Lett.*, vol. 68, no. 23, p. 3284, Jun. 1996.

[105] F. Adler et al., “Self-assembled InAs/GaAs quantum dots under resonant excitation,” *J. Appl. Phys.*, vol. 83, no. 3, p. 1631, Jun. 1998.

[106] R. J. Warburton, C. S. Dürr, K. Karrai, J. P. Kotthaus, G. Medeiros-Ribeiro, and P. M. Petroff, “Charged Excitons in Self-Assembled Semiconductor Quantum Dots,” *Phys. Rev. Lett.*, vol. 79, no. 26, pp. 5282–5285, Dec. 1997.

Chapter 3:

Strain Balancing of Quantum Dot Layers

3.1 Introduction

The aim of this chapter is to introduce strain balancing, which has the potential to reduce the spacing thickness between the quantum dot (QD) layers without degrading device performance. Strain balancing removes the strain produced by a material layer with a material of the opposite strain, for instance, balancing a compressively strained layer (InGaAs on GaAs) with a tensile strained layer (GaP). [1] Therefore, the average strain in the complete structure can be reduced to zero. In this thesis, strain-balancing is introduced to try and reduce the total strain of each QD period to zero. Without this, successive layers of QDs, particularly if placed too close together, would cause a build-up of the total strain, quickly reaching the point where strain relaxation and dislocation formation occurs. Achieving strain balance should therefore allow closer vertical stacking; increasing the number of QD layers that can be placed close to the maximum of the cavity mode, hence achieving a higher total gain. Reports have suggested a maximum number of QD layers achievable without strain balancing is 10, whilst introducing strain balancing can increase the number of QD layers to 300. [2] Figure 3.1 shows the difference between a sample with a 50 nm spacing thickness without the incorporation of a GaAs_{0.8}P_{0.2} strain-balancing layer and a 20 nm spacing layer with the incorporation of a GaAs_{0.8}P_{0.2} strain-balancing layer. The strain-balancing layer achieves a net strain of zero for each QD layer repeat, allowing the separation between the QD layers to be reduced. For a layer QD areal density of $3.0 \times 10^{10} \text{ cm}^{-2}$, reducing the separation from 50 to 20 nm will increase the volumetric density by 2.5 times from 6.0×10^{15} to $1.5 \times 10^{16} \text{ cm}^{-3}$. This increase in the volumetric QD density can, if placed close to the maximum of the cavity optical mode, increase the available gain, leading to a

lower threshold current density for a QD laser. InAs QDs grown on a GaAs substrate have a compressive strain (as high as 7% for InAs QDs). Hence, to achieve strain balancing a material with a tensile strain when grown on GaAs is needed. Although a phosphide containing material is an obvious choice, such materials are challenging to grow by molecular beam epitaxy (MBE) due to the difficulty in phosphorous management. In contrast, phosphide materials can be much more easily grown by metal-organic vapour phase epitaxy (MOVPE). Furthermore, MOVPE lends itself to large-scale manufacturing, due to a higher growth uptime and volume scalability. In addition, epitaxial regrowth is significantly more mature in MOVPE, with polycrystalline-free selective area regrowth being highly challenging for MBE. Therefore, growth of new and novel devices that require epitaxial regrowth and also a high volumetric density of QDs is much more feasible using MOVPE. This is the motivation behind the work described in this chapter. The strain balancing described in this thesis may

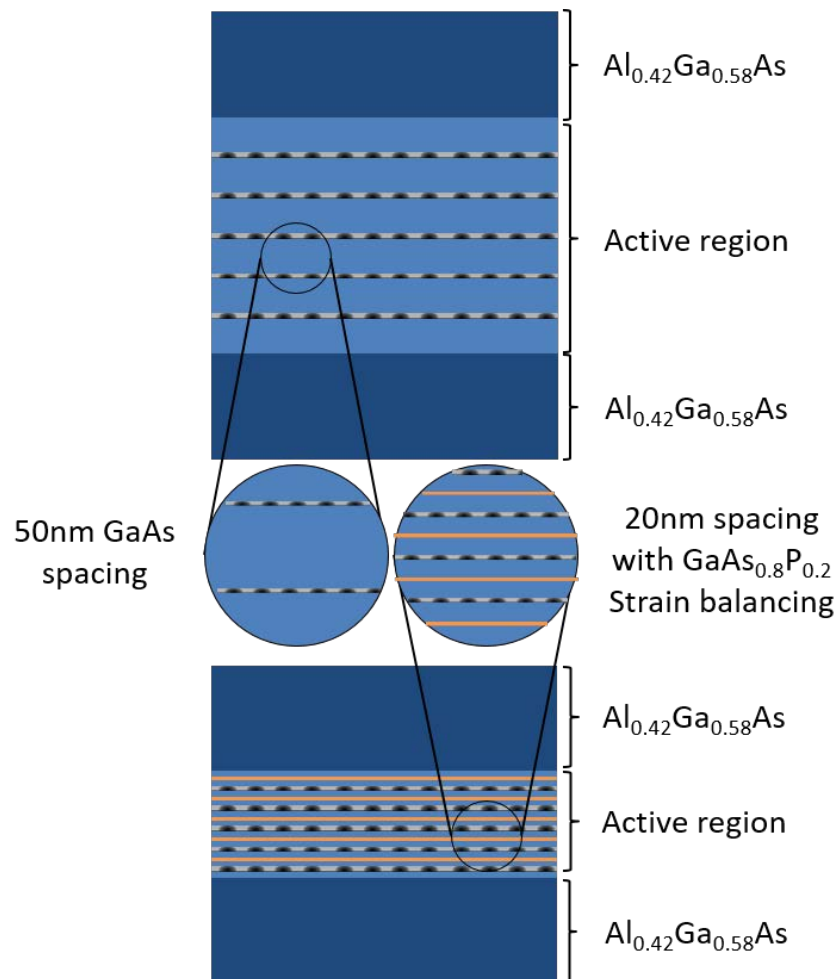


Figure 3.1: Schematic of the strain-balancing scheme discussed in this chapter.

Chapter 3: Strain Balancing of Quantum Dot Layers

also find application in solar cells, which also require a large number of QD layers for efficient power conversion.

3.2 Background and Literature review

This literature review aims to outline the current progress and state-of-the-art in strain-balancing material systems containing quantum wells (QWs) and/or QDs in optoelectronic devices. Strain occurs when two materials of different lattice constant are placed within a structure. There are two types of strain that occurs in epitaxy, compressive strain where a larger lattice constant material is grown on a smaller lattice constant material, and tensile strain where a smaller lattice constant material is grown on a larger lattice constant material. [1] For the GaAs based system, materials containing indium will produce compressive strain and materials containing phosphorous will produce tensile strain. This is unavoidable in most semiconductor material systems but is usually avoided by using materials of a similar lattice constant to reduce the amount of strain. When materials with a larger lattice mismatch have to be used then strain mitigation has to be achieved. The most common method is not to grow materials above the critical thickness for defect formation and to have a large spacing between successive highly strained layers. However, when the inter-layer spacing needs to be reduced, or the number of layers is increased, a more novel approach is needed.

Devices containing highly strained material can exhibit imperfections within the crystal structure. A number of potential possibilities can occur including defects, threading dislocations, vacancies and polycrystalline formation. [1], [3] The build-up of elastic energy due to the strained layers is reduced by the formation of these imperfections. Their formation hence results from a trade-off between elastic energy and the energy required to form the imperfection. Defects or dislocations in particular can act as non-radiative recombination centres, which reduce the optical efficiency. LEDs with a significant number of defects or dislocations would exhibit a reduced quantum efficiency and the threshold current density of a laser would increase significantly or the device may not lase at all. In addition, rapid aging and premature failure of laser devices may occur. [4], [5] None of these is a desirable outcome. The lattice relaxation that results from the formation of defects and/or dislocations causes the lattice constant of the strained material to be returned towards its original,

unstrained lattice constant. Lattice relaxation can result in a lattice constant between that of the substrate, where the relaxation will be zero, to that of the lattice constant of the original material, where the relaxation will be 100%. [6], [7]

Strain balancing techniques are of great interest for epitaxial solar cells as it is desirable to have many QD layers and studies of potential materials suitable to compensate compressive strain. Many papers have been published on strain balancing solar cells containing large numbers of $\text{In}_{1-x}\text{Ga}_x\text{As}$ QWs using different thicknesses and concentrations of phosphorous in a $\text{GaAs}_z\text{P}_{1-z}$ barrier. [8] Successful strain balancing has been shown to improve the crystallinity of the material, which in turn has improved the emission and absorption properties. [9] A consequence of producing a solar cell with too much strain is a reduction in the external quantum efficiency (EQE). A study looking at the impact of strain accumulation in multiple InGaAs QWs grown with different indium concentrations on GaAs has been reported by Sodabanlu *et al.* In this study, the effects of under compensating, over compensating and balancing the strain with a thin $\text{GaAs}_{0.81}\text{P}_{0.19}$ layer were investigated. [4] The under and over compensated devices showed a deterioration in both the open-circuit voltage and EQE when compared to a GaAs p-i-n reference device. This deterioration was linked to an increase in the number of dislocations, point defects and potential for lattice relaxation. However, the strain-balanced device was shown to have the highest EQE and improved open-circuit voltage, whilst also increasing the absorption wavelength range, suggesting improved crystallinity and a reduction in the number of defects. Improving the crystalline quality is important to maximise the EQE. However, a large number of QWs are required to absorb a large fraction of the incident sunlight; some papers suggest more than 100 QWs are required. [9] If the QWs are strained, then very efficient strain balancing is required. The only practical choice of material is a phosphorus containing one, such as GaAsP. [10] The concentration of phosphorous will affect the material thickness required to achieve strain balancing but may also affect other device parameters, such as the electrical characteristics. For example, a large phosphorous composition will introduce potential barriers, potentially impeding efficient carrier transport. This issue is modelled and

tested in sections 3.3 and 3.6 of this thesis respectively. A number of different phosphorous concentrations have been reported in the literature of solar cells. [11]–[13] Lower concentrations of phosphorous have been reported to significantly improve solar cell performance with the short-circuit current density and open circuit voltage both showing improvements. For high phosphorous concentrations, the large barriers appear to be overcome by thermal assisted tunnelling. [14] In addition, higher phosphorous compositions extend the wavelength range over which strong absorption and efficient energy extraction occur, improving the internal quantum efficiency (IQE) and the short-circuit current density. [14] However, for an InGaAs MQW laser diode, large phosphorous concentration barriers have been found to increase the threshold current density. [15], [16] The optimum barrier concentration appears to be $\text{GaAs}_{0.655}\text{P}_{0.145}$, as reported by H. Dong *et al.* [16] A consideration of effects occurring at the interfaces between the phosphorous and arsenic containing layers also needs to be considered and controlled. At the interface an exchange between phosphorous and arsenic atoms can occur, due to the phosphorous desorbing and being replaced by arsenic. If this occurs, the phosphorous concentration of the strain-balancing layer can be reduced, reducing its effectiveness. [17]

Research into the strain balancing of structures and devices containing InAs QDs has focussed on the use of GaP, with both MBE and MOVPE grown structures studied. J. Tatebayashi *et al.* reported that a 4 ML thick GaP layer was sufficient to compensate for the strain caused by InAs/GaAs QDs. In addition to using GaP they reported the use of $\text{In}_x\text{Ga}_{1-x}\text{P}$ at two concentrations of indium $x = 0.3$ and 0.36 , with a reduction in compressive strain of 25 to 35%. Improvements to the PL emission with the use of the strain compensating layers compared to the non-strain compensated device were found, with a 1.8, 6.2 and 12.5 factor increase in PL emission for: 8 ML $\text{In}_{0.36}\text{Ga}_{0.64}\text{P}$, 8 ML $\text{In}_{0.30}\text{Ga}_{0.70}\text{P}$ and 4 ML GaP, respectively. [18] The optimal thickness for the GaP was determined theoretically by elasticity theory to be 3.8 ML for full strain balance. However, an X-ray diffraction (XRD) and optical study, where the GaP thickness was varied from 3.1 to 5 ML in thickness found a slightly higher thickness. From XRD the strain peak was determined to be coincident with the

substrate peak for a thickness of 4.2 ML, this was confirmed by studies of the measured integrated PL intensity. [19], [20]

Reducing the QD spacing thickness can be achieved with the introduction of a strain-compensating layer, which can allow the total number of QD layers to be significantly increased. However, some care is needed if the spacing thickness is reduced to a very small value as coupling between QDs in successive layers may occur, this can result in increased inhomogeneity of the QD electronic states. [20] An increase in the number of QD layers up to 300 has been reported, with the use of a strain-compensating layer. However, this was achieved for growth of InAs QDs on an InP substrate using an InGaAlAs spacing layer, which has a slightly smaller lattice constant than InP. Without a strain-compensating layer, the growth of this large number of QD layers was not possible where a limit of 10 layers is reported. [2], [22], [23] Room temperature ground state lasing has been reported for strain-compensated QD layers grown by both epitaxial methods, with MOVPE grown GaP strain compensated devices achieving a threshold current density of 108 Acm^{-2} at a wavelength of $1.33 \mu\text{m}$, which is similar to MOVPE grown QDs without strain compensation (see chapter 4). [18], [24]–[27] Lasing has been reported up to 100°C . However, introduction of these strain compensation layers maybe detrimental to the electrical characteristics due to the incorporation of large potential barriers, as revealed by device modelling (section 3.3). It is hence desirable to study the use of GaAsP strain-compensation layers where a lower barrier height is introduced but at the expense of less strain compensation for a given layer thickness. An alternative strain-balancing approach, previously reported, is the incorporation of InAs QDs directly into a $\text{GaAs}_{1-z}\text{P}_z$ matrix. However, this causes an unwanted blue shift of the emission wavelength. [28], [29] This blue shift of the ground state wavelength has also been reported by P. Lever *et al.* where they grew InAs QDs directly on a GaP strain compensating layer. Both a reduction in the emission intensity and a blue shift of the wavelength was observed. [30]

Chapter 3: Strain Balancing of Quantum Dot Layers

In addition to laser devices, strain-compensating layers, such as the GaP, have proven vital in the balancing of strained layers in solar cells and semiconductor optical amplifiers. [4], [9], [11]–[14], [23], [31]–[33]

3.3 LaserMOD Modelling

Strain balancing of InAs/GaAs QDs can be achieved using a $\text{GaAs}_z\text{P}_{1-z}$ layer. Therefore, it is important to understand the effects of placing a larger bandgap material between the QD layers on the electrical characteristics and also on the lasing threshold current density. Due to the additional complexity in modelling QDs, the modelling in this section will use the QW produced by the wetting layer as the active region. Modelling of the structures was achieved using LaserMOD provided by RSoft. Finite element analysis simulations are used to model the optical, electronic, gain characteristics and thermal properties of semiconductor photonic devices, such as lasers, super-luminescent diodes and light emitting diodes. LaserMOD is a self-consistent simulation software, where the gain is obtained from an 8×8 **k.p** calculation of the electronic band structure, allowing for an accurate determination of the density of states and the profile of the band states within the QW. [34]

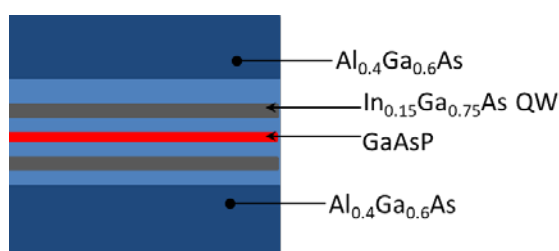


Figure 3.2: Diagram of the modelled QW device with the inclusion of a variable composition GaAsP barrier.

All simulation work was completed by another Ph. D. student, Mr Ian Tooley, using the device structure and emission wavelength provided by myself, the data was analysed and plotted by myself. The structure modelled was a dual 8 nm

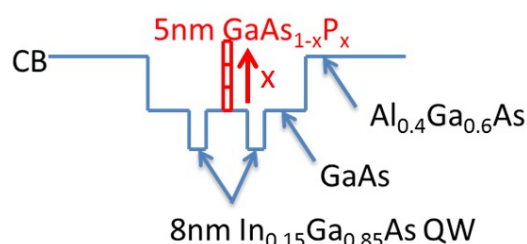


Figure 3.3: Conduction band profile of the modelled device

$\text{In}_{0.19}\text{Ga}_{0.81}\text{As}$ QWs emitting at 980 nm, with a 5 nm $\text{GaAs}_z\text{P}_{1-z}$ strain-balancing layer placed between the two QWs to study the effects of varying the phosphorous concentration. The device structure is shown in figure 3.2. $\text{In}_{0.19}\text{Ga}_{0.81}\text{As}$ QWs emitting at 980 nm were chosen, as these will produce a similar strain to that produced by a layer of QDs, as calculated by the strain peak position with respect to the substrate peak position as discussed for the X-ray data in section 3.4. An emission wavelength of 980 nm gives a bandgap similar to that of the wetting layer in the QDs structure. The wetting layer is important for carrier transport in QD structures. Figure 3.3 shows the conduction band profile used in the model where it is clear that a barrier exists for electron transport across the active region. A similar effect is expected in the valence band; however, there is expected to be a smaller barrier compared to the conduction band. For a given barrier thickness there are competing effects of greater strain balance but higher barrier height as the phosphorus concentration is increased.

The energy bandgaps of bulk unstrained $\text{GaAs}_z\text{P}_{1-z}$ increase with phosphorous concentration, following equations 3.1 and 3.2, from these bandgap values the

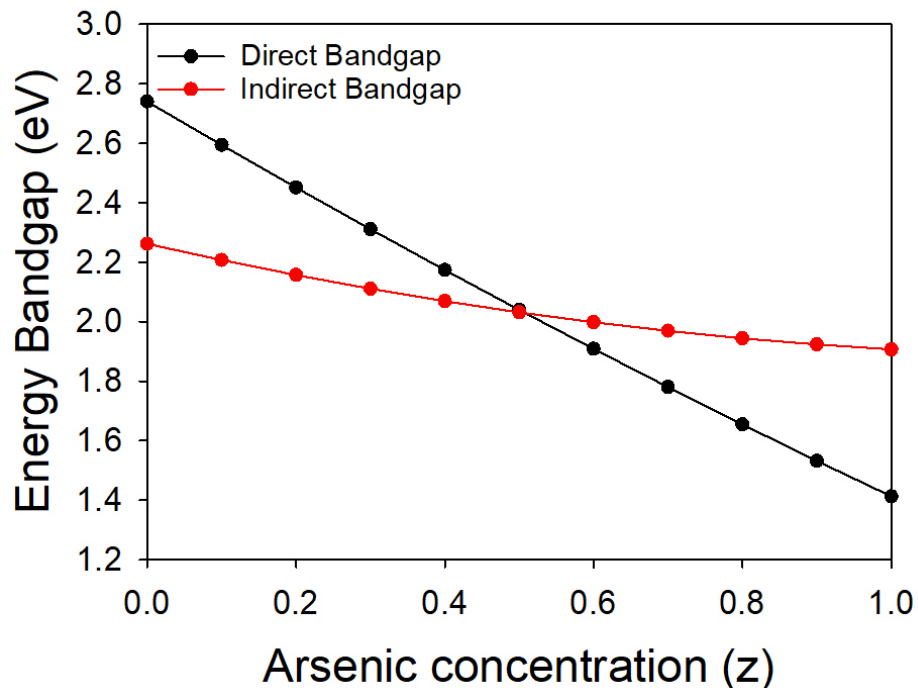


Figure 3.4: Direct and indirect bandgap energies of an unstrained GaAsP layer as a function of arsenic concentrations.

barrier heights can be found from a knowledge of the band offsets, which is 0.14 eV for GaAs_{0.8}P_{0.2}. The direct bandgap of GaAs_zP_{1-z} is given by equation 3.1, [35]

$$E_{gF} = 2.74 - 1.473z + 0.146z^2 \text{ Eqn (3.1)}$$

where E_{gF} is the direct bandgap energy and z is the arsenide concentration. The bandgap energy of the indirect transition associated with the X-valley is given by equation 3.2 [35]

$$E_{gX} = 1.907 + 0.144(1 - z) + 0.211(1 - z)^2 \text{ Eqn (3.2)}$$

where E_{gX} is the indirect bandgap energy. The two equations are plotted in figure 3.4, where a clear transition from a direct bandgap below GaAs_{0.5}P_{0.5} to an indirect bandgap at higher phosphorous concentrations is seen. To understand how the band structure of the GaAs_zP_{1-z} affects device performance the electrical characteristics are modelled for different compositions.

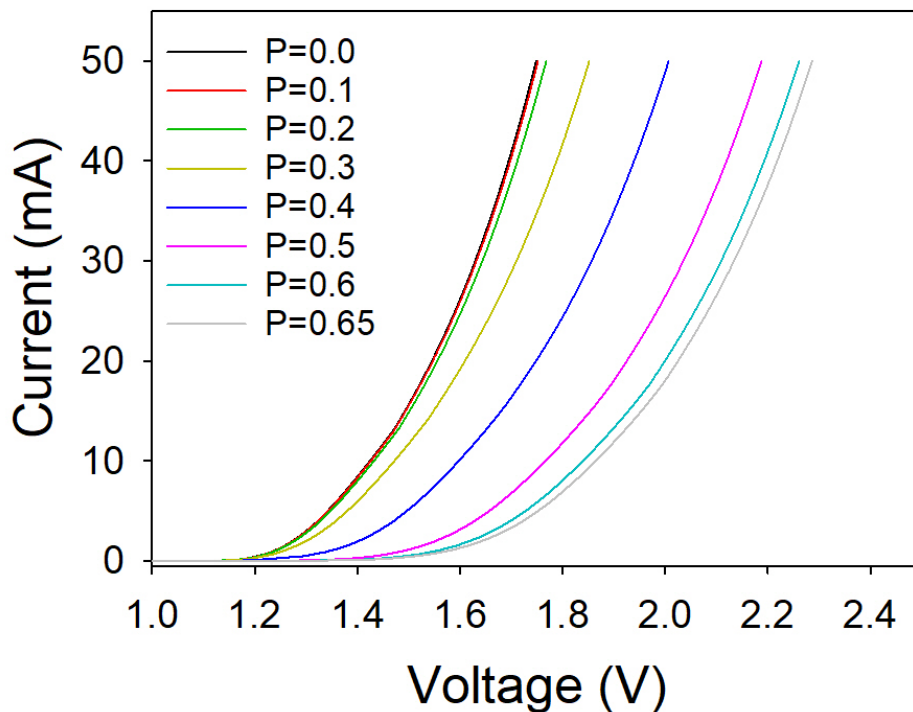


Figure 3.5: Modelled IV characteristics for different phosphorus concentrations in a structure containing a 5nm strain-compensating layer

Figure 3.5 shows the modelled current-voltage (IV) behaviour, using the thermal activation over the barrier only, for a structure containing a 5 nm GaAsP strain-compensating layer for different phosphorous concentrations. As expected, the turn-on voltage for high phosphorous concentrations is increased. However, for phosphorous concentrations below GaAs_{0.8}P_{0.2}, there is no noticeable effect on the turn-on voltage or IV behaviour. This is due to the height of the barrier (0.14 eV for a concentration of 20%) being sufficiently low not to impede electron transport across the device. Above $I-z = 0.2$, the turn-on voltage increases as the higher barrier starts to impede the carrier transport. This increase is linear for concentrations up to $I-z = 0.5$, above $I-z = 0.5$ the turn-on voltage increase is weaker most probably reflecting the reduction in the increase of the bandgap change, relating to the transition from a direct to an indirect band gap of GaAsP due to the increase in P concentration, as shown in figure 3.4.

Further modelling was performed to understand the effects of the barrier height due to the GaAs_zP_{1-z} layer on the light-current characteristics of a laser. Again, for a GaAs_zP_{1-z} layer below $I-z = 0.2$ no increase in the predicted threshold current is observed, Figure 3.6. Above $I-z = 0.2$ the threshold current increases, changing from 13.2 mA at $I-z = 0$ to 17.9 mA at $I-z = 0.5$, a 26% increase, Figure 3.6 (inset). As was the case for the turn-on voltage there is a less rapid increase above $I-z = 0.5$ due to the transition to an indirect bandgap. From these modelling results it can be concluded that the use of a GaAs_{0.8}P_{0.2} strain-balancing layer should not significantly affect either the IV turn-on behaviour or the lasing threshold current.

3.4 LEPTOS Modelling

In this section X-Ray Diffraction (XRD) modelling is used to investigate how the different elements of the device structure, such as the repeat thickness and number of layers within the active region, will affect the XRD spectra, which are used to identify the achievement of successful strain balancing in section 3.6.

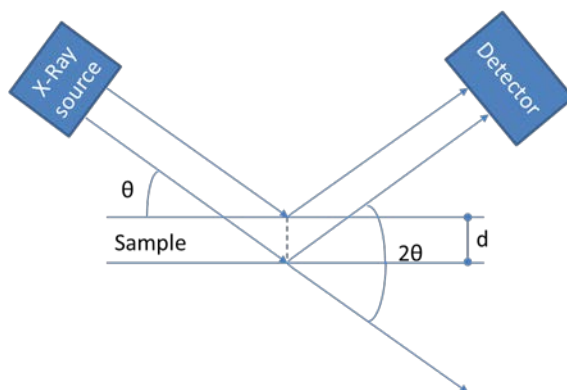


Figure 3.8: XRD set-up. The two waves, which reflect of successive atomic planes, have a path difference of $2d\sin\theta$. For constructive interference (X-Ray diffraction), this path difference must equal an integral number of wavelengths.

The LEPTOS simulation package can model and extract real structure parameters from high-resolution X-Ray diffraction scans. This will be the focus of this thesis but other types of measurements, such as X-Ray reflectivity (XRR), grazing incidence diffraction (GID), stress measurements and reciprocal space mapping, can also be used. LEPTOS uses a recursion matrix extension to dynamical X-ray diffraction theory as developed by S. A. Stepanov *et al.* [36] Using this approach the algorithm calculates the scattering of X-rays over the entire range of incidence and exit angles for both strained and relaxed layers. This thesis will only consider the presence of strained layers (but including layers with zero strain) and assumes that all layers exhibit zero relaxation. Figure 3.8 shows the position of the X-ray source and detectors for an omega-two theta scan. X-rays are incident on the crystal at an angle θ . A small fraction of the beam is reflected from each layer of atoms in the crystal, scattering is observed if the reflections from all the layers interferes constructively. In any crystal, there will be many sets of atomic planes that can potentially scatter the X-rays. The angular difference between the scattered and incident beams is 2θ .

Before any simulations are performed or samples measured experimentally, the Bragg angle of the GaAs substrate needs to be calculated. To calculate this diffraction angle the wavelength of the X-Rays used and the nature of the diffraction needs to be known. The X-Ray source used is $\text{CuK}\alpha_1$, which has a wavelength of 1.540549 Å. A number of different reflections can be used but the [004] reflection was used for the work described in this thesis. The spacing between the [004] planes can be calculated using equation 3.3 [37]–[39]

$$d = \frac{a}{\sqrt{h^2 + k^2 + l^2}} \text{ Eqn (3.3)}$$

where d is the spacing of the diffracting planes, a is the lattice constant of GaAs (5.65325Å), and h , k and l are the Miller indices. d for [004] diffraction in GaAs is calculated to be 1.4133Å. This value can now be substituted into the Bragg equation 3.4 to calculate the diffraction angle for bulk GaAs [37]–[39]

$$n\lambda = 2d \sin \theta \text{ Eqn (3.4)}$$

where n is a positive integer, λ is the X-Ray wavelength and θ is the Bragg angle. For bulk GaAs and [004] diffraction, θ is calculated to be 33.0259°. This is the incident angle of the X-Ray beam needed to observe the GaAs substrate peak. The detector angle will be twice (2θ) the Bragg angle as the work in this thesis will focus on symmetric scans (incident and scattered beams having the same angle), which can be used to determine the out of plane lattice parameter. The Bragg angle and the detector angle calculated here are used as the initial values to align the XRD experiment in section 3.6. If a bulk GaAs sample is measured, only one diffraction peak will be observed at 33.0259°. If a layer of $\text{In}_{0.19}\text{Ga}_{0.81}\text{As}$ is grown on the GaAs substrate, and is compressively strained to fit the inplane GaAs lattice constant, then a second diffraction peak will be observed. This is because, via the Poisson effect, the out of plane lattice constant of the $\text{In}_{0.19}\text{Ga}_{0.81}\text{As}$ will expand slightly from that of the GaAs lattice constant. Because in the Bragg equation $d\sin\theta$ is a constant, a larger value of d will give a smaller value for θ . The scattering angle of the $\text{In}_{0.19}\text{Ga}_{0.81}\text{As}$ can be determined using equations 3.3 and 3.4 if the Poisson ratio is also known.

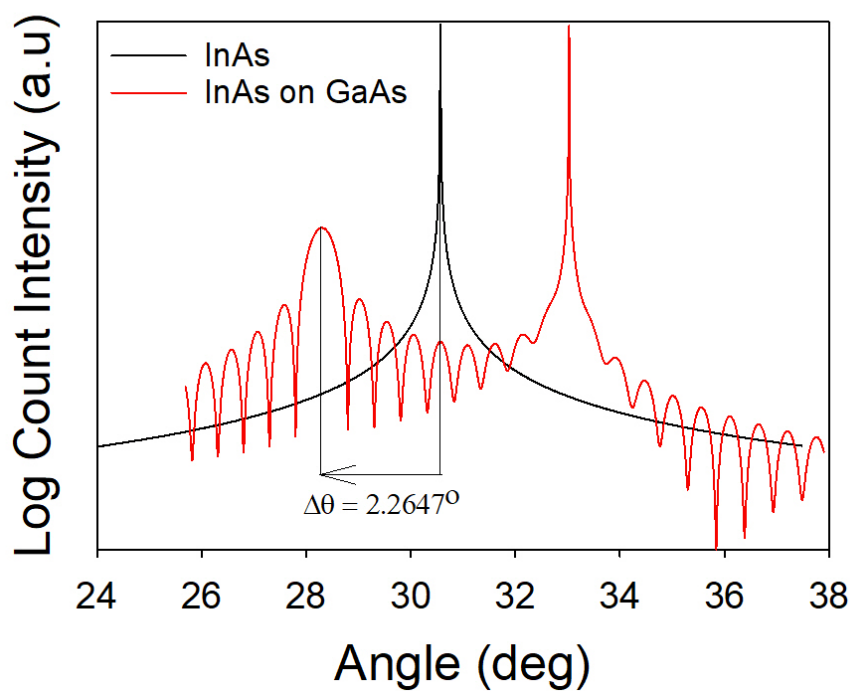


Figure 3.9: [004] reflection modelling XRD spectra of a bulk InAs layer and thin InAs layer grown on a GaAs substrate.

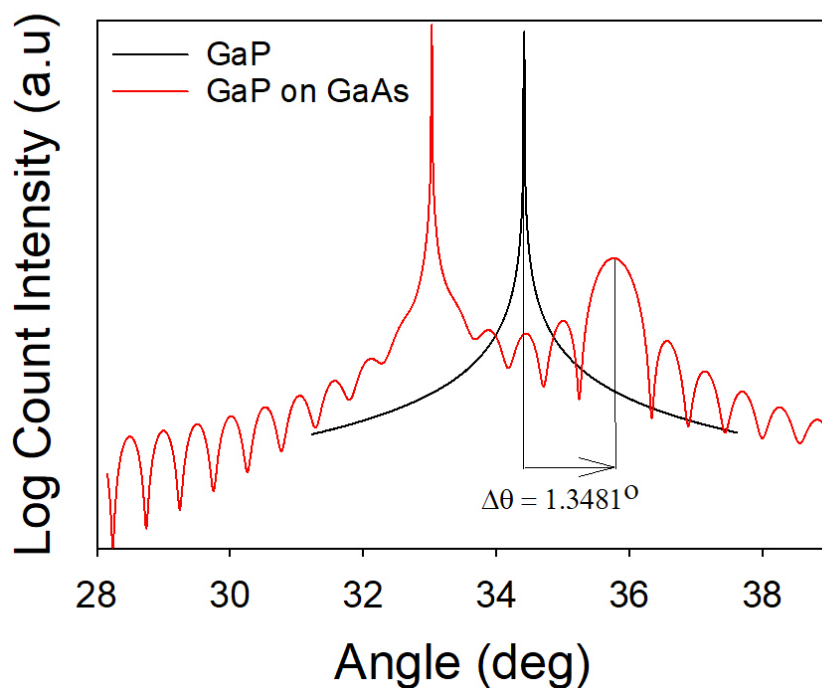


Figure 3.10: [004] reflection modelling XRD spectra of a bulk GaP layer and thin GaP layer grown on a GaAs substrate.

The lattice constant for unstrained $\text{In}_{0.19}\text{Ga}_{0.81}\text{As}$ can be calculated using equation 3.5 [40]

$$a_{\text{InGaAs}} = (a_{\text{InAs}} - 0.405y) \text{ Eqn (3.5)}$$

where a_{InAs} is the lattice constant in Angstroms for InAs (6.0583 Å) and y is the gallium concentration. Using equation 3.3 the [004] separation is calculated to be 1.4326 Å, corresponding to a Bragg angle of 32.5265°. This is the Bragg angle of an unstrained $\text{In}_{0.19}\text{Ga}_{0.81}\text{As}$ layer, but is not the measured value because of the strain in the $\text{In}_{0.19}\text{Ga}_{0.81}\text{As}$ layer. As discussed previously, with the layer being compressively strained in plane, the out of plane lattice parameter will increase, increasing the value of d used in the Bragg equation. Therefore, the Bragg angle for a compressively strained layer will be smaller than the Bragg angle of an unstrained layer. For an inplane tensile strained material, the out of plane lattice parameter decreases. Therefore, the Bragg angle for a tensile strained layer will be larger than the Bragg angle of the corresponding unstrained layer. Modelling of bulk InAs, as shown in figure 3.9, gives a Bragg angle of 30.5668°. When a thin InAs layer is grown on GaAs the Bragg angle is reduced by 2.2647°, to 28.3021°. Using this new Bragg angle

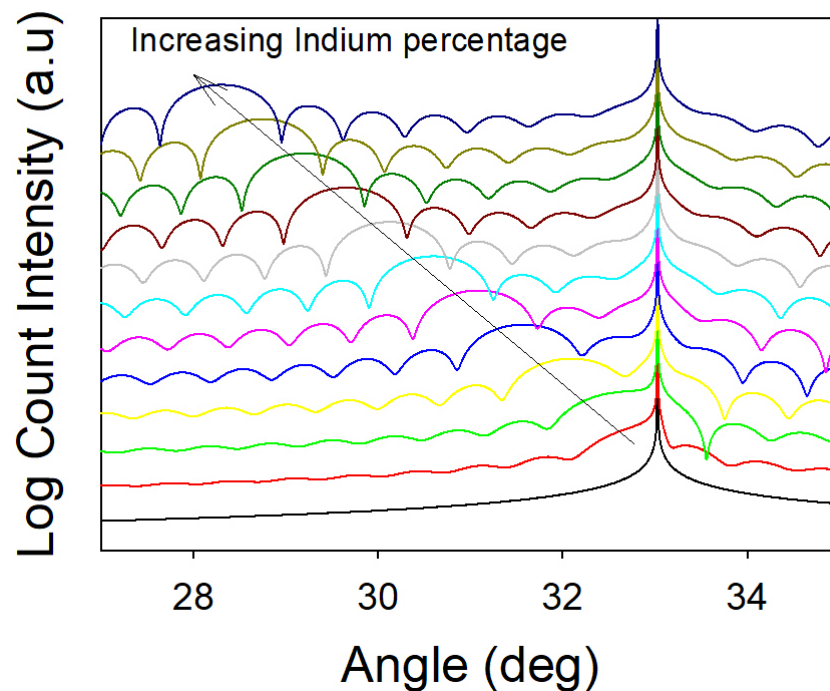


Figure 3.11: [004] reflection modelling XRD spectra for a thin InGaAs layer grown on GaAs as a function of In composition.

and equations 3.3 and 3.4, a new out of plane lattice constant of 6.4986 Å is calculated, giving an increase of 6.7% with respect to original InAs lattice constant.

A similar analysis can be applied for GaP grown on GaAs, as shown in figure 3.10. An increase from 34.4188° for a bulk GaP layer with a lattice constant of 5.451 Å, to 35.7669° for GaP grown on GaAs, an increase of 1.3481°, is observed. Using this new Bragg angle and equations 3.3 and 3.4, a new out of plane lattice constant of 5.2714 Å is calculated, giving a decrease of 3.3% with respect to the original GaP lattice constant.

A study of how varying the indium composition of a thin $\text{In}_{1-x}\text{Ga}_x\text{As}$ layer grown on GaAs affects the X-ray spectra was performed. Figure 3.11 shows simulated spectra for a 7.6 nm $\text{In}_x\text{Ga}_{1-x}\text{As}$ layer on a bulk GaAs substrate, for a range of indium compositions. Increasing the indium percentage increases the in plane compressive strain, increasing the out of plane lattice constant and decreasing the Bragg angle. The Bragg angle decreases linearly with indium composition, as shown in figure 3.12; this analysis is used to estimate the indium percentage in QD structures studied later in this thesis. Similarly, a 50 nm $\text{GaAs}_z\text{P}_{1-z}$ layer grown on a GaAs substrate was modelled for different phosphorous compositions. The lattice constant for $\text{GaAs}_z\text{P}_{1-z}$ can be calculated using equation 3.6 [41]

$$a_{\text{GaAsP}} = a_{\text{GaP}} + 0.2021z \quad \text{Eqn}(3.6)$$

where a_{GaP} is the lattice constant in Angstroms for GaP (5.4505 Å) and z is the arsenic concentration. Figure 3.13 shows that the diffraction peak increasing with increasing phosphorus content as the in plane tensile strain increases. The shift of the diffraction peak with composition is also plotted in figure 3.12. The diffraction peak of $\text{GaAs}_z\text{P}_{1-z}$ is seen to be less sensitive to composition in comparison to the diffraction peak of $\text{In}_x\text{Ga}_{1-x}\text{As}$ this is due to the larger mismatch of InAs (6.7%) with GaAs compared to GaP (3.6%) with GaAs.

Modelling of X-ray spectra for a single layer of $\text{In}_{0.19}\text{Ga}_{0.81}\text{As}$ grown on a GaAs substrate, as a function of layer thickness from 0 to 100 nm, was performed.

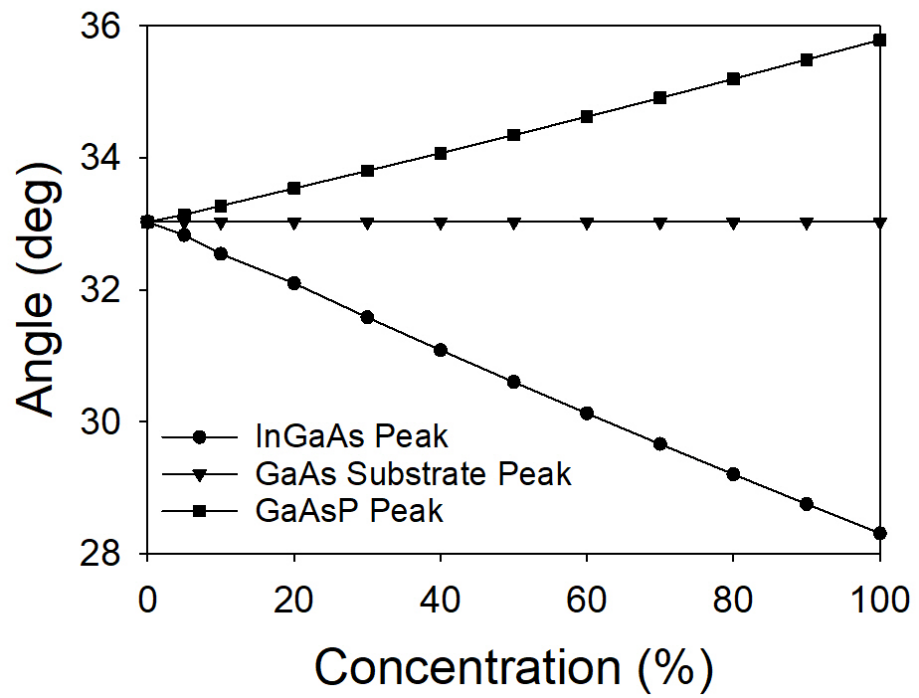


Figure 3.12: Strain peak and substrate diffraction angles of both thin InGaAs and GaAsP layers grown on GaAs as a function of In or P concentration.

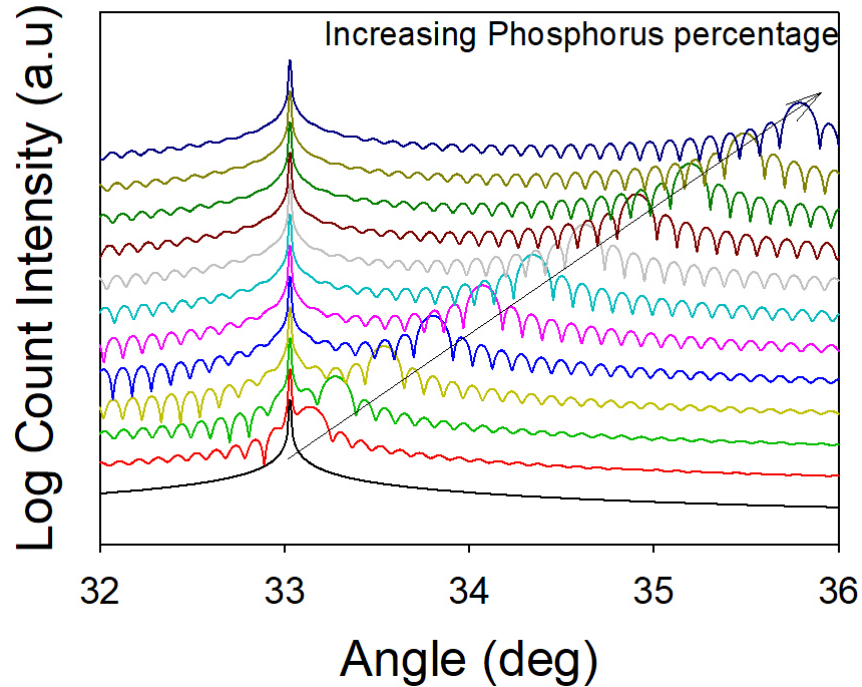


Figure 3.13: [004] reflection modelling XRD spectra for variation of the phosphorous concentration of a $\text{GaAs}_z\text{P}_{1-z}$ layer.

Figure 3.14 shows the simulated spectra, which demonstrate a narrowing of the diffraction peak and reduction in the spacing between the Pendellosung (satellite) peaks for increasing $\text{In}_{0.19}\text{Ga}_{0.81}\text{As}$ thickness. Satellite peaks are produced by the constructive and destructive interference of the diffracted X-rays from the layers within the structure and the period of these peaks is determined by the thicknesses of the layers. A narrower diffraction peak for increasing thickness results from more atomic layers contributing to the diffraction; in the limit of a perfect bulk layer the diffraction peak would have zero width. Figure 3.15 plots the separation between the satellite peaks as a function of layer thickness; the separation reduces as the layer thickness increases. The relationship between the thickness of an epitaxial layer, t , and the period of the Pendellosung peaks is given by equation 3.6, [37]

$$t = \frac{\lambda}{2\Delta\theta \sin \theta_B} \text{ Eqn (3.6)}$$

where λ , is the X-Ray wavelength, θ_B is the Bragg angle and $\Delta\theta$ is period of the satellite peaks. These results allow the thickness of a single epitaxial layer to be determined from the experimentally measured satellite peak separation.

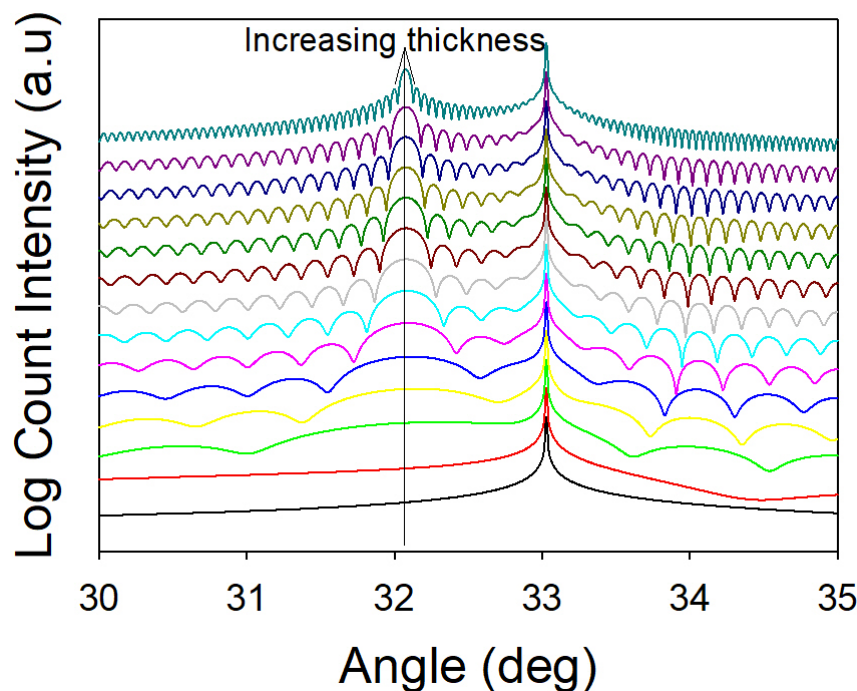


Figure 3.14: [004] reflection modelling XRD spectra for an $\text{In}_{0.19}\text{Ga}_{0.81}\text{As}$ layer grown on GaAs for thickness varying between 0 and 100 nm.

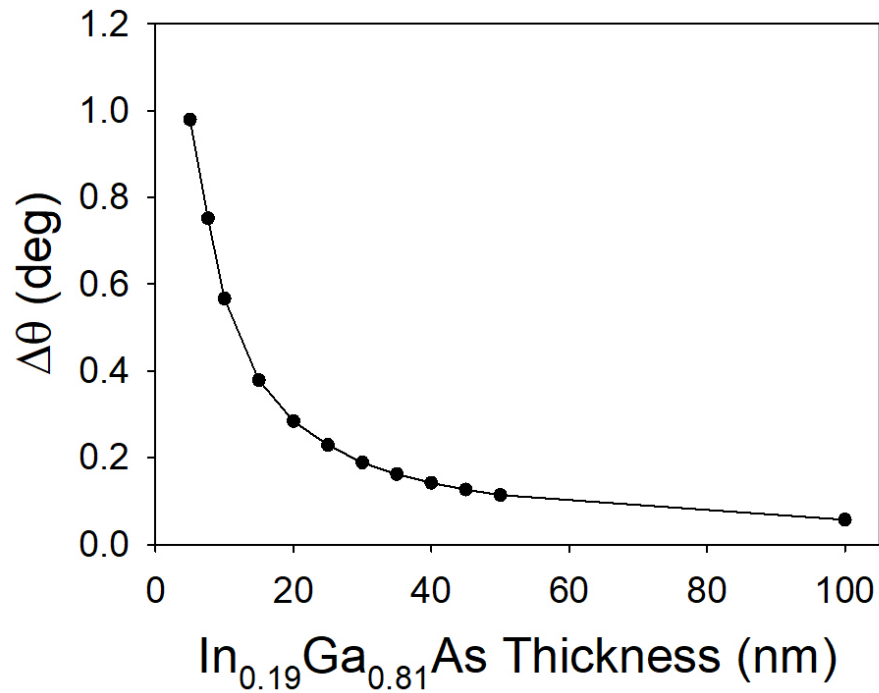


Figure 3.15: Satellite peak separation as a function of In_{0.19}Ga_{0.81}As layer thickness.

The effect of increasing the number of repeats within a structure on the X-ray spectra was studied. Figure 3.16 shows a schematic diagram of the modelled structure, d_1 and d_2 (the thicknesses of the GaAs barriers and In_{0.19}Ga_{0.81}As QWs respectively) are kept constant, whilst the number of repeats is increased. Both the GaAs and In_{0.19}Ga_{0.81}As Bragg peaks remain at the same position for all spectra and the separation between the satellite peaks is constant, as the thicknesses of the layers are constant. However, the number of local minima between each satellite peak is related to the number of repeats in the structure. Figure 3.17 is a magnified plot of the region between two satellite peaks. This shows an increase in the number of local maxima and minima with increasing number of layer repeats as the number of repeats is increased from one to ten.

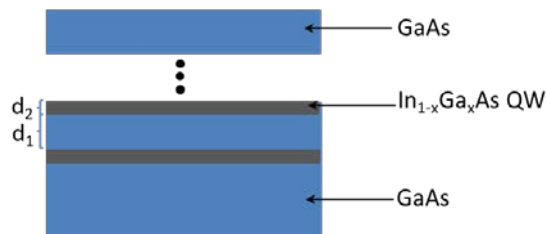


Figure 3.16: Schematic diagram of the XRD modelled QW device with variation in the number of repeats, spacing thickness and repeat thickness.

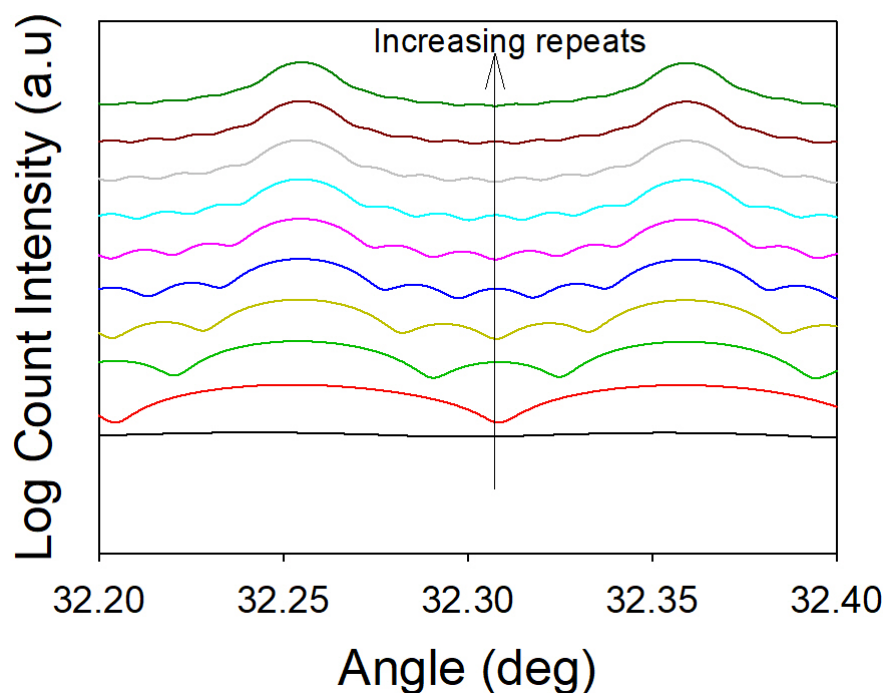


Figure 3.17: [004] reflection modelling XRD spectra for variation of the number of QW repeats.

The number of minima plus one equals the number of repeats in the structure, a similar relationship is found for diffraction of light by a periodic array of slits. [37]–[39], [42] However, due to the resolution of the simulations the minima in the XRD spectra for the larger number of layer repeats becomes less defined. For the devices used in this thesis, only single layer and five layer samples were grown and studied. The XRD spectra for the five layer sample is expected to show four local minima.

Increasing the separation between QWs has a similar effect to increasing the thickness of a single layer, where the spacing between the satellite peaks is reduced with an increasing thickness, as shown in the simulated spectra of figure 3.18. Figure 3.19 plots the separation between satellite peaks as a function of QW separation; the total repeat thickness ($d_1 + d_2$) can be found using equation 3.6 but not the individual thicknesses of the separation layer or the QW. However, as the separation layer thickness increases (this is the thickness of GaAs between the QWs) and the QW thickness is kept constant, the average concentration of indium within the active region is reduced. As a result, a shift in the zeroth order peak (z_0) (the strain peak) is observed. The strain peak is the

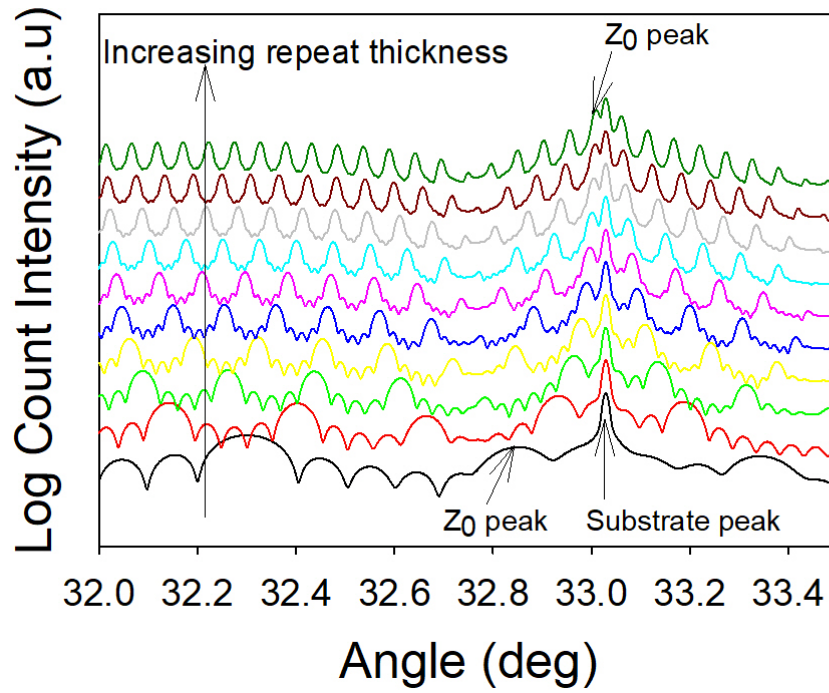


Figure 3.18: [004] reflection modelling XRD omega-two theta spectra for variation of the repeat thickness of a MQW sample.

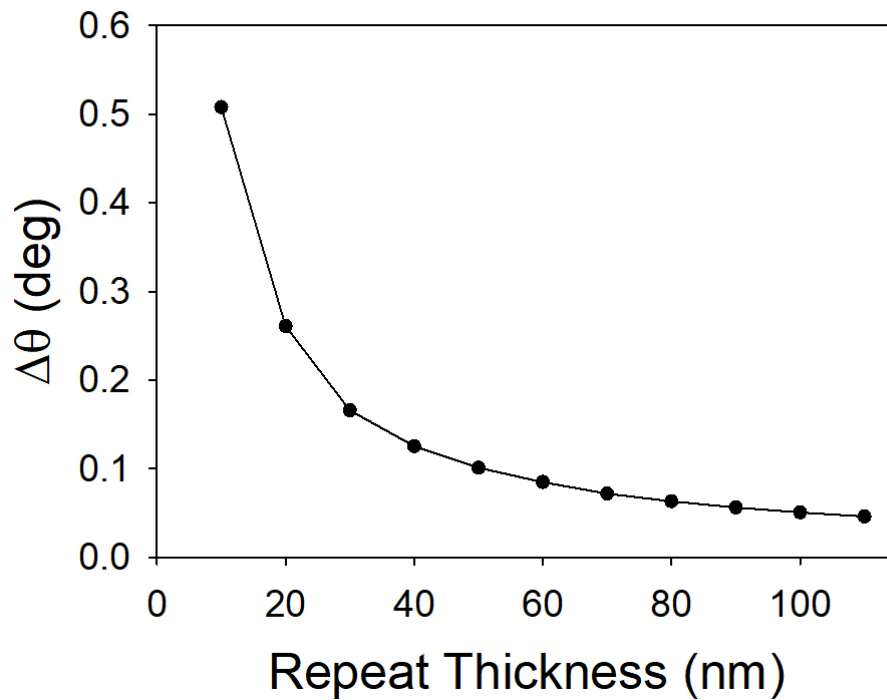


Figure 3.19: Separation of the satellite peaks as a function of the repeat thickness.

addition of the two Bragg reflections from the component parts of the repeat structure, GaAs and the $\text{In}_{0.19}\text{Ga}_{0.81}\text{As}$ QW in this case. Satellite peaks are created centred around the strain peak; these can be used to calculate the thickness of the repeat structure as described previously. As shown in figure 3.18, the strain peak is shifted closer to the substrate peak as the average composition of a repeat becomes closer to GaAs as the separation thickness increases. This was not the case for the single layer structure as shown in figure 3.14 as the average concentration was kept constant and only the thickness of the InGaAs layer was changed.

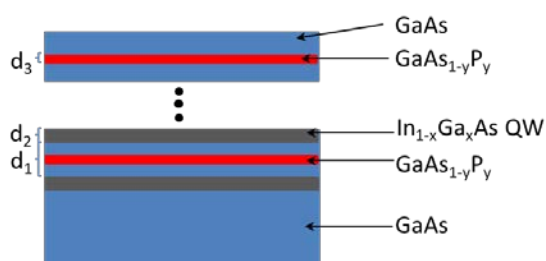


Figure 3.20: Schematic diagram of the XRD modelled QW device with variation in the concentration of phosphorous and $\text{GaAs}_{0.8}\text{P}_{0.2}$ thickness.

As with increase of the layer periodicity (figure 3.18), the addition of a strain-compensating layer, $\text{GaAs}_{0.8}\text{P}_{0.2}$ in this case, can affect the position of the strain peak. To study this effect, modelling of a five layer 7.6 nm $\text{In}_{0.19}\text{Ga}_{0.81}\text{As}$ QW in a GaAs matrix structure with a strain-compensating $\text{GaAs}_{0.8}\text{P}_{0.2}$ layer of varying thickness, figure 3.20, was used to calculate the thickness needed to achieve strain balance. Figure 3.21 shows simulated spectra for different thicknesses of $\text{GaAs}_z\text{P}_{1-z}$ for $1-z = 0.2$. This composition was chosen as a result of the modelling discussed in section 3.3. Figure 3.22 shows how the strain peak varies with the thickness of the $\text{GaAs}_{0.8}\text{P}_{0.2}$ layer. The net strain is found to be minimised for a thickness of 4 nm, where difference between the strain peak and the substrate peak is zero. A related analysis can be performed if the thickness of the strain-compensating layer is fixed and the phosphorus concentration needs to be determined. As with increasing the thickness of a $\text{GaAs}_{0.8}\text{P}_{0.2}$ layer, the strain peak shifts from compressive to tensile strain as the phosphorus concentration is increased.

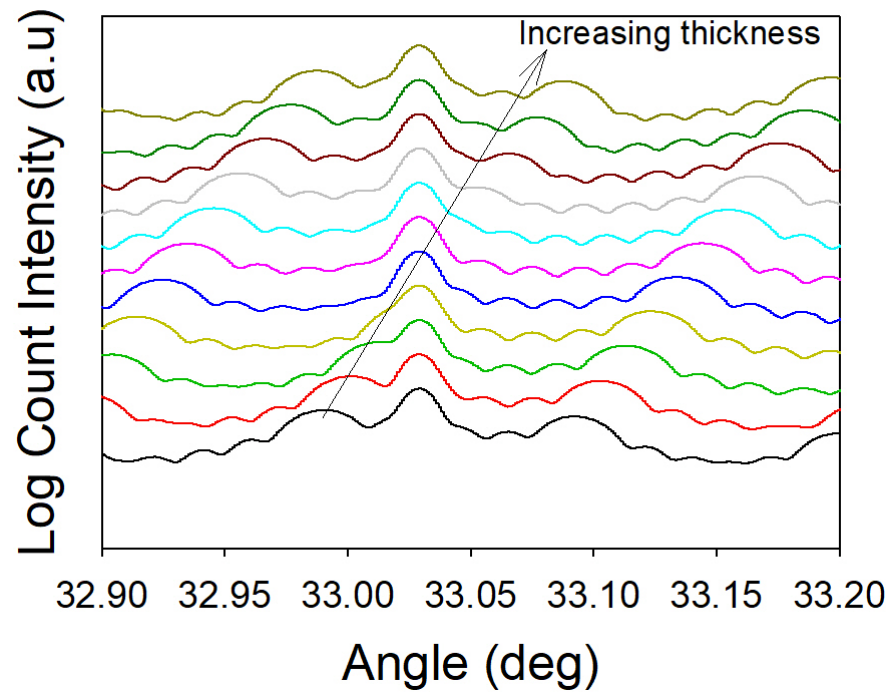


Figure 3.21: [004] reflection modelling XRD spectra for variation of the thickness of the GaAs_{0.8}P_{0.2} layer in the QW structure.

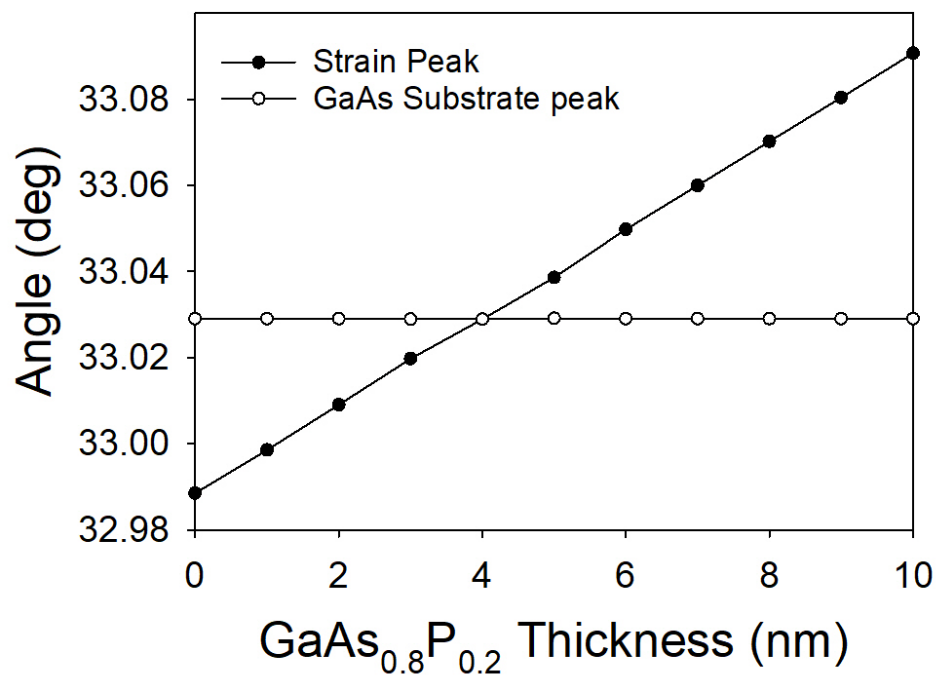


Figure 3.22: Variation of the diffraction angle of the strain peak and substrate as a function of the thickness of the GaAs_{0.8}P_{0.2} layer.

The required GaAs_{0.8}P_{0.2} layer thickness required to strain balance the structure can also be found from the XRD spectra; using the Bragg angle of the substrate peak and angle of the strain peak the average lattice mismatch produced can be determined. The average mismatch, which is calculated from the non-strained balanced XRD. The lattice mismatch between GaAs and GaAs_{0.8}P_{0.2} will produce an average strain depending on the relative thickness of the strain-balancing layer and the spacing layer, which is dependent on the lattice mismatch between the two materials. The required strain balancing thickness can be calculated from equation 3.7

$$t_{sb} = t_{sl} \frac{\left(\frac{\sin \theta_{Sub}}{\sin \theta_{Strain}} - 1 \right) a_{Sub}}{(a_{GaAsP} - a_{Sub})/a_{Sub}} \text{ Eqn 3.7}$$

where t_{sb} is the thickness of the GaAs_{0.8}P_{0.2}, θ_{Sub} is the Bragg angle for the substrate peak, θ_{Strain} is the strain peak angle, t_{sl} is the layer thickness separation, a_{Sub} is the GaAs (substrate) lattice parameter and a_{GaAsP} is the lattice parameter of the GaAs_{0.8}P_{0.2} strain compensating layer. Using equation 3.7 the GaAs_{0.8}P_{0.2} thickness required to strain balance a 7.6 nm In_{0.19}Ga_{0.81}As QW is calculated to be 4 ± 0.5 nm, which is in line with the value of 4 nm calculated from the modelling.

In this section, modelling of the behaviour of both compressive (InGaAs) and tensile (GaAsP) strained materials has been performed. The compositional dependence of the Bragg angle has been found, allowing angles measured from real structures to be used to determine compositions. Modelling of spectra for a variation in thickness of a single In_{0.19}Ga_{0.81}As layer grown on GaAs shows a small change in the position of the strain peak. However, this change is significantly smaller to the change observed in composition. In addition, the spacing between satellite peaks is reduced with an increase of thickness and the thickness of the layer can be calculated from the spacing of these peaks. Keeping the thickness of the In_{0.19}Ga_{0.81}As layer constant and changing the separation thickness has a similar effect, with the spacing between the satellite peaks decreasing with increasing separation allowing a determination of the total thickness of the repeat. In addition, a change in the average composition

of the repeat layers causes a shift in the strain peak. As the separation thickness is increased the strain peak shifts towards the GaAs substrate peak as the average indium content of one period decreases. Adding a strain-compensating layer (a layer with opposite strain to that of the $\text{In}_{0.19}\text{Ga}_{0.81}\text{As}$ QW) can be used to balance the strain in the structure, which should allow the separation between highly strained QD layers to be reduced. For an $\text{In}_{0.19}\text{Ga}_{0.81}\text{As}$ QW, which has a strain estimated to be similar to that of an InAs QD layer, a 4 nm $\text{GaAs}_{0.8}\text{P}_{0.2}$ layer placed between the QWs was shown to fully compensate the strain caused by the QWs.

3.5 Growth Calibration

In this section, the growth calibration required to obtain $\text{GaAs}_{0.8}\text{P}_{0.2}$ is discussed. To calibrate the $\text{GaAs}_z\text{P}_{1-z}$ composition the structure shown in figure 3.25 was used. A 2 nm $\text{GaAs}_{0.8}\text{P}_{0.2}$ layer with a 50 nm GaAs separation with 30 repeats was used to calibrate the phosphorous composition. The calibration of the growth rate is obtained from the growth of GaAs layers because the growth rate is controlled by the group-III flow. From previous calibrations, growth parameters were selected to obtain a phosphorous concentration of 20%. However, the achieved concentration depends on the ratio of the flow rates of the arsine and the phosphine as well as the growth temperature and can vary with time. The concentration of phosphorus in a grown sample can be determined using X-ray diffraction; a diffraction peak will be visible at a larger Bragg angle compared to the GaAs Bragg peak. This occurs because the GaAsP layer will be tensile strained as discussed in section 3.4. Figure 3.26 shows an X-ray spectrum of the calibration sample. The repeat thickness can be determined from the difference between the substrate peak and the GaAsP peak. Using equation 3.6 and the measured separation the thickness is found to be 52.3 nm, giving an error of 0.3 nm in comparison to the intended value. The phosphorous concentration can be calculated using equation 3.8, [37], [38]

$$x = \frac{c_{GaAs} \left(1 + \left(\frac{1 - \nu}{1 + \nu} \left(\frac{\sin \theta_s}{\sin \theta_l} - 1 \right) \right) \right) - c_{GaAs}}{c_{GaP} - c_{GaAs}} \quad \text{Eqn (3.8)}$$

where c_{GaAs} is the lattice constant of GaAs, c_{GaP} is the out of plane lattice constant of GaP, ν is the Poisson ratio and $\theta_{s,l}$ are the Bragg peak angles of the

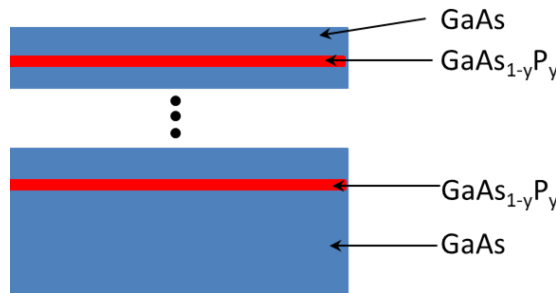


Figure 3.25: Schematic structure of the GaAsP calibration sample.

substrate and epitaxial material respectively. The concentration of phosphorous is calculated to be 19%. Based on this value, the flow of phosphine was increased in subsequent growths to give the desired phosphorous concentration of 20%.

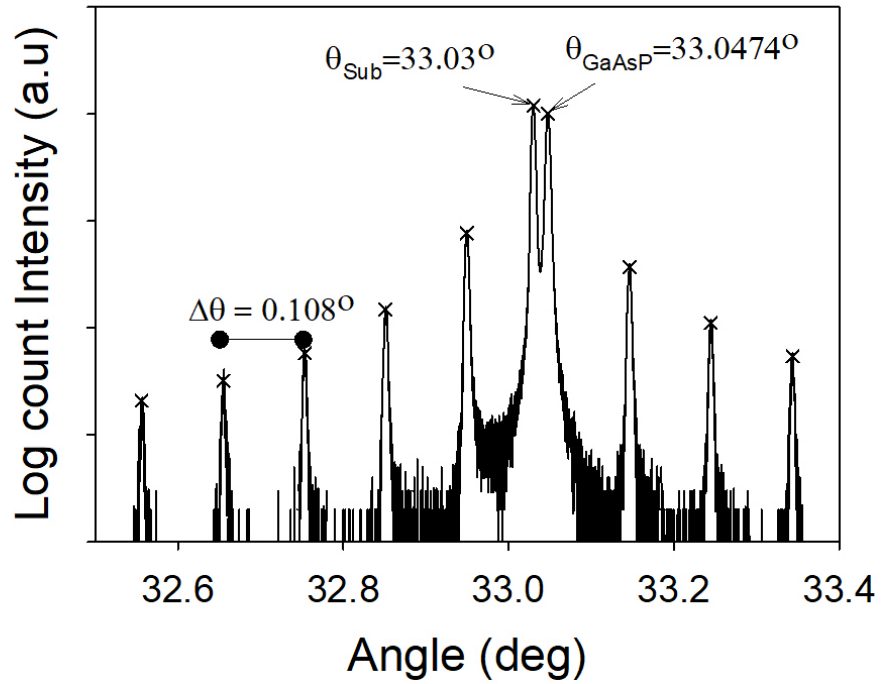


Figure 3.26: [004] reflection XRD spectra of the GaAsP calibration sample.

3.6 X-ray Diffraction Studies of Device Structures

In this section, six structures are studied consisting of three pairs of samples with QD layer separations of 50, 30 and 20 nm. For each pair one sample is a strained strain-balanced structure, the other has no compensating $\text{GaAs}_{0.8}\text{P}_{0.2}$ layer. All six samples contain five QD layers with 1.5 μm thick $\text{Al}_{0.42}\text{Ga}_{0.58}\text{As}$ top and bottom cladding with doping levels of $1 \times 10^{18} \text{ cm}^{-3}$ carbon and $5 \times 10^{17} \text{ cm}^{-3}$ silicon for the top and bottom layers respectively. A final 50 nm GaAs top contact layer is p-type doped with carbon to $1 \times 10^{19} \text{ cm}^{-3}$. XRD spectra are used to determine the strain and to confirm the number of repeats and the repeat thickness. TEM images are also used to confirm the sample parameters in conjunction with ImageJ software, which is used to extract distances from TEM images.

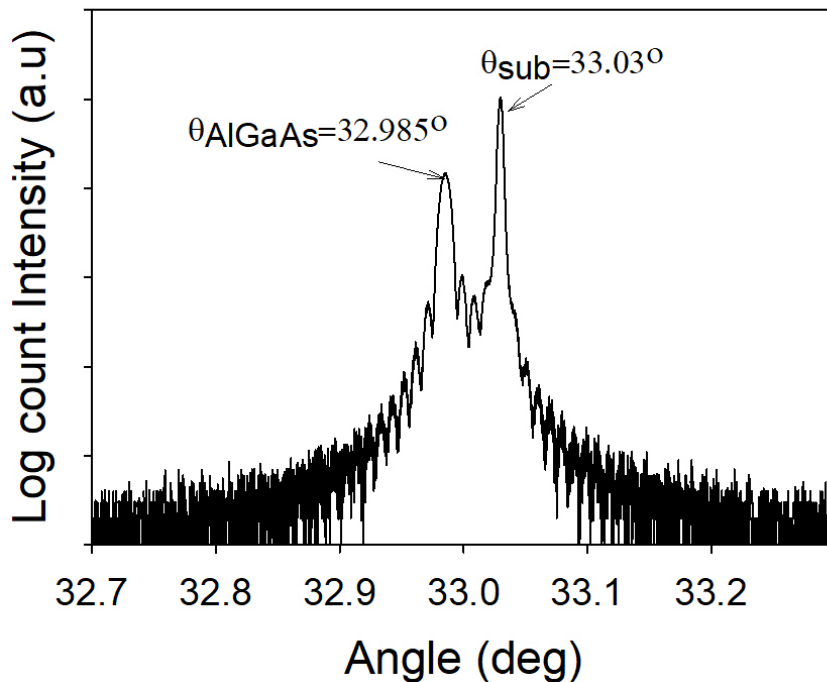


Figure 3.27: [004] reflection XRD spectra of the AlGaAs calibration sample.

All structures were studied in XRD using [004] symmetric reflections. Identifying the features in the XRD spectra is important to ensure correct labelling of the associated peaks and reliable extraction of structural parameters. To aid the identification of the XRD features, a sample with a thick

$\text{Al}_{0.42}\text{Ga}_{0.58}\text{As}$ layer was grown on a GaAs substrate to identify the associated Bragg peak and to calculate the aluminium concentration.

Figure 3.27 shows the XRD spectrum of the $\text{Al}_{0.42}\text{Ga}_{0.58}\text{As}$ calibration sample. The nominal $\text{Al}_{0.42}\text{Ga}_{0.58}\text{As}$ thickness is 1.5 μm . The spectrum shows two strong diffraction peaks. The peak at angle 33.03° is due to the GaAs substrate; this is the dominant peak due to the large amount of GaAs present in comparison to the epi-layer. The feature to the left of the substrate peak is the $\text{Al}_x\text{Ga}_{1-x}\text{As}$ peak; the two peaks do not coincide due to the difference between the lattice constants of the two materials. The $\text{Al}_x\text{Ga}_{1-x}\text{As}$ layer is compressively strained due to it having a larger unstrained lattice constant. Using equation 3.8 the concentration of aluminium is calculated to be $x = 0.41$, an error of 0.01 compared to the intended concentration. Again future growth parameters were altered slightly to obtain the desired aluminium concentration of $x = 0.42$.

Sample A is a five layer 50 nm separation structure without $\text{GaAs}_{0.8}\text{P}_{0.2}$. Sample A' has the same parameters except that a 5 nm $\text{GaAs}_{0.8}\text{P}_{0.2}$ layer, which is experimentally calculated from the XRD, is placed at the centre of the GaAs spacer layer between the QD layers and a final $\text{GaAs}_{0.8}\text{P}_{0.2}$ layer is added between the final QD layer and the top cladding (5 $\text{GaAs}_{0.8}\text{P}_{0.2}$ layer in total). In the sample with the $\text{GaAs}_{0.8}\text{P}_{0.2}$ layer, the total thickness of the GaAs spacer layer is reduced by 5 nm to keep the spacing between the QD layers constant. Samples B and B' follow A and A' except that the QD layer separation is reduced to 30 nm and for samples C and C' the QD layer separation is reduced to 20 nm. For all the samples, the QD layers are grown at a temperature of 485°C , with 2 ML InAs coverage, a rate of 0.18 ML/s and an arsine flow of 50 sccm.

XRD spectra of samples A and A' are shown in figure 3.28. Focussing on sample A, the amount of strain balancing needed to overcome the total strain, is calculated by analysis of the position of the strain peak with respect to the substrate peak. The strain peak is the addition of the two Bragg reflections from the component parts of the repeat structure, as discussed in section 3.6. The dominant peak is associated with the GaAs substrate at 33.03° because the thickness of the substrate is far greater than any epitaxial layer within the

structure. The $\text{Al}_{0.42}\text{Ga}_{0.58}\text{As}$ cladding layer is at 32.9832° and is identified with reference to figure 3.27, where the $\text{Al}_{0.41}\text{Ga}_{0.59}\text{As}$ peak was observed to be at 32.985° . The cladding layer peak is usually the second most dominant peak due to the thicknesses of the cladding layers. However, the current sample is complicated because the strain peak is close to the $\text{Al}_{0.42}\text{Ga}_{0.58}\text{As}$ peak; the former is superimposed on the side of the latter peak. From analysis of the sample with just GaAs and $\text{Al}_{0.42}\text{Ga}_{0.58}\text{As}$, the strain peak is attributed to the stronger peak at a slightly smaller angle than the $\text{Al}_{0.42}\text{Ga}_{0.58}\text{As}$ peak. This is confirmed by calculating the position of the strain peak from the observed fringes, the strain peak will be $\Delta\theta$ (0.105°) away from the nearest satellite peak at θ_{s1} (32.8719°). Therefore, the position of the strain peak for sample A is 32.9769° , producing a compressive strain ($\Delta a/a_s$) of 0.001428. Using equation 3.7 (section 3.4), the thickness of $\text{GaAs}_{0.8}\text{P}_{0.2}$ required is calculated from the positions of the substrate Bragg angle (33.03°), the position of the strain peak (32.9769°) and the thickness of the separation between the QD layers (50 nm). The thickness calculated is 5.6 nm. However, 5 nm is used for the strain-compensating layer as over-compensating for the strain could cause the formation of additional defects. Previously, in section 3.4 a 4 nm $\text{GaAs}_{0.8}\text{P}_{0.2}$ strain balancing layer was modelled to successfully strain balance a 7.6 nm

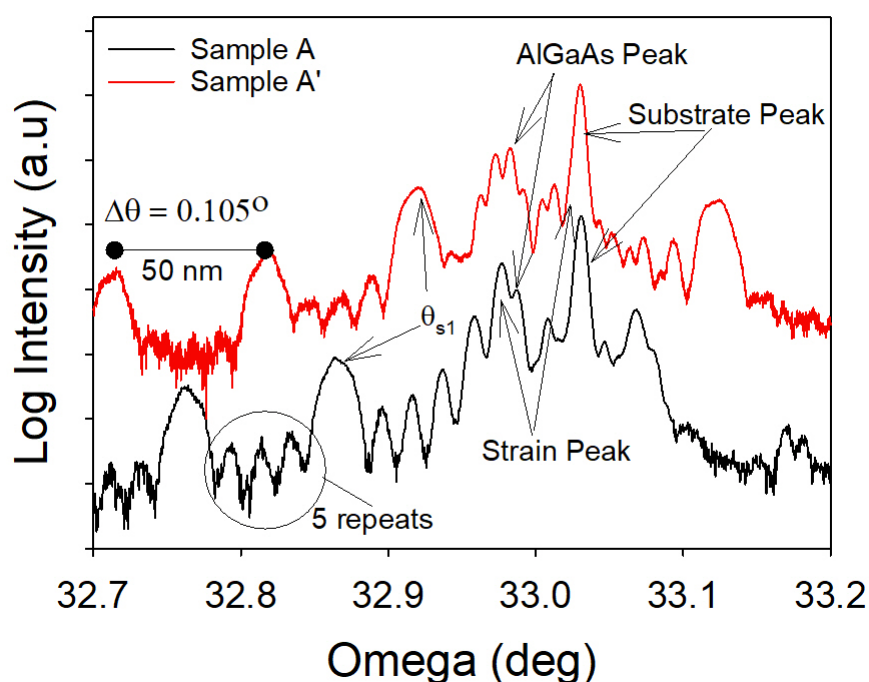


Figure 3.28: 004 reflection XRD spectra of samples A and A'.

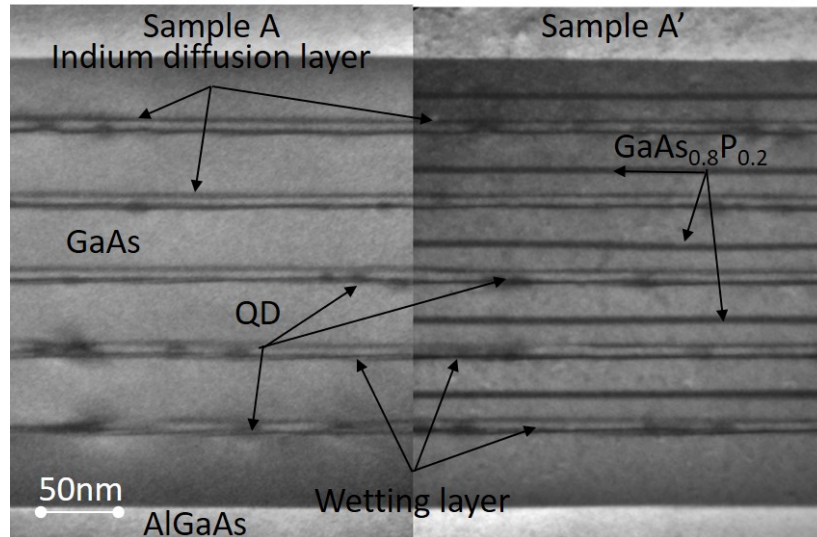


Figure 3.29: TEM images of samples A and A' with a layer separation of 50 nm.

$\text{In}_{0.19}\text{Ga}_{0.81}\text{As}$ QW. The difference in the required thickness is due to the difference in the average indium composition in the repeat. The model used the InGaAs QW from the LaserMod modelling, which could also be used as an estimate of the strain produced by the InAs QDs. However, it is not expected to require the same thickness of $\text{GaAs}_{0.8}\text{P}_{0.2}$. The separation between the satellite fringes ($\Delta\theta$) can be used to determine the thickness of the repeat using equation 3.6; a value of 50 ± 3 nm is obtained. ImageJ was used to measure the separation between the QD layers shown in the TEM images in figure 3.29, the spacing thickness between the QD layers was determined to be 50 ± 2 nm, which is in agreement with the XRD measurement. From the TEM it is observed the QDs are nucleated on a wetting layer, in addition an indium diffusion layer is observed above the QD, which is discussed in chapter 2. The number of repeats within the structure is confirmed by both XRD and TEM, where the number of minima between the satellite peaks equals the number of repeats plus one, as discussed in section 3.4.

Sample A' has the same $\text{Al}_{0.42}\text{Ga}_{0.58}\text{As}$ cladding layer as sample A, which gives a very similar angle of 32.9829° , the number of repeats and repeat thickness are also the same. This similarity is confirmed by the number of minima between the fringes (4 minima) and the fringe separation (0.105°), respectively; this is also shown in the TEM image (figure 3.29). In addition, the TEM image shows the 5 nm $\text{GaAs}_{0.8}\text{P}_{0.2}$ layer between the QD layers; the thickness of this layer is

confirmed using ImageJ to be 5 ± 1 nm. To confirm that the addition of the GaAs_{0.8}P_{0.2} layer has balanced the strain the position of the strain peak is determined. The strain peak angle can be calculated from the position of θ_{s1} (32.915°) plus the fringe separation of 0.105° to give a strain peak position of 33.02° . Therefore, the strain peak is almost in line with the substrate peak meaning the structure is almost strain balanced. The angular difference between the strain peak and the substrate peak is 0.0102° . From the position of the

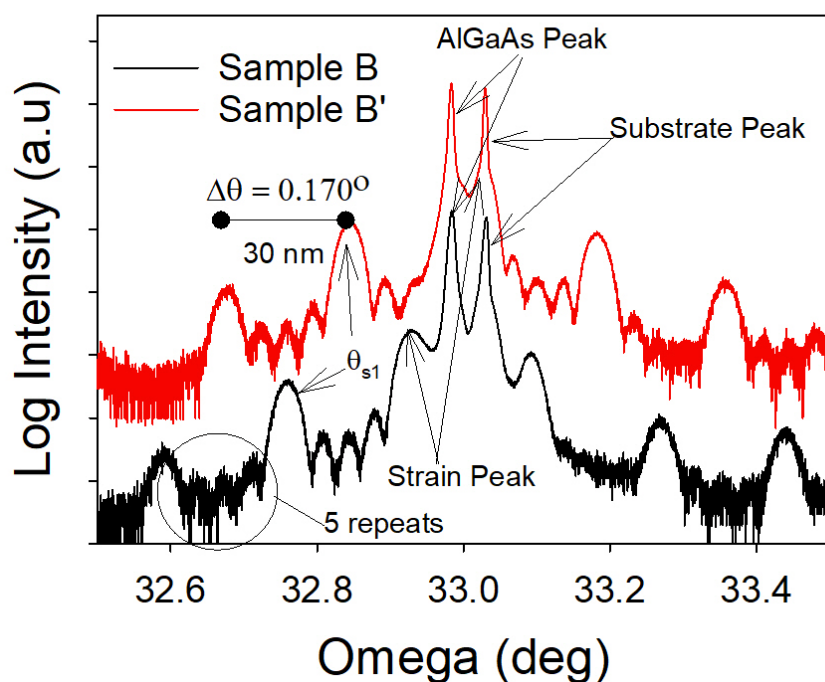


Figure 3.30: 004 reflection XRD spectra of samples B and B'.

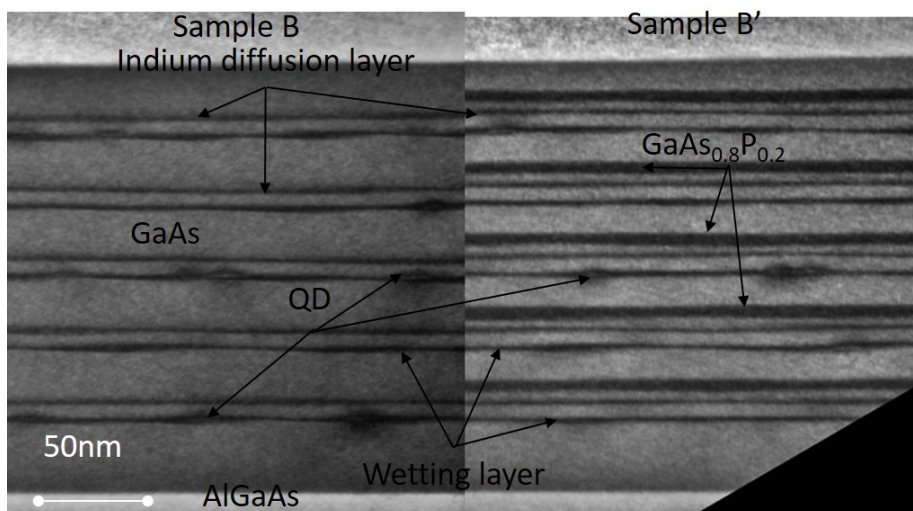


Figure 3.31: TEM images of samples B and B' with a separation of 30 nm.

substrate and strain peak, the remaining strain ($\Delta a/a_s$) within the structure is calculated to be 0.0002739 and to be compressive.

XRD spectra of samples B and B' are shown in figure 3.30. As with samples A and A' the dominant peak is attributed to the substrate at 33.03° . However, the second most dominant peak for both samples B and B' is associated with the $\text{Al}_{0.42}\text{Ga}_{0.58}\text{As}$ cladding layers (32.9824°), due to a shift in the strain peak in sample B. This shift is associated with the average strain within the active region, which, because of the reduction in the spacing thickness, increases. Each QD layer produces the same amount of strain but when averaged over a smaller periodicity this leads to a higher average strain, a compressive strain of 0.002747 is calculated. However, the structure will require the same amount of $\text{GaAs}_{0.8}\text{P}_{0.2}$ to achieve strain balance, a thickness of 5 nm. This can also be calculated from equation 3.7. As with samples A and A' the QD layer separation can be calculated using the spacing between the satellite peaks. This spacing is increased to 0.170° in comparison to samples A and A' and using equation 3.6 this equates to a thickness of 30 ± 3 nm. In addition to the XRD measurement, ImageJ was used to measure the separation between the QD layers in the TEM images of figure 3.31. The spacing thickness between the QD layers was determined to be 30 ± 3 nm, in agreement with the XRD determined value. The number of repeats within the structure is the same as samples A and A' as confirmed by the XRD spectra from the number of minima between the fringes (4 minima), and in the TEM image (figure 3.31).

Sample B' has the same $\text{Al}_{0.42}\text{Ga}_{0.58}\text{As}$ cladding layer as sample B, exhibiting the same angle of 32.9824° . Both XRD and TEM (figures 3.30 & 3.31) confirm the number of repeats and repeat thickness. Again the TEM image shows the additional 5 nm $\text{GaAs}_{0.8}\text{P}_{0.2}$ layer visible between the QD layers and the thickness is confirmed using ImageJ to be 5 ± 1 nm. To confirm that the $\text{GaAs}_{0.8}\text{P}_{0.2}$ layer has balanced the strain within the structure the position of the strain peak is measured to occur at 33.0234° . The angular difference between the strain peak and the substrate peak is 0.0066° . From the position of the substrate and strain peak, the remaining strain ($\Delta a/a_s$) within the structure is calculated to be 0.0001772 and to be compressive.

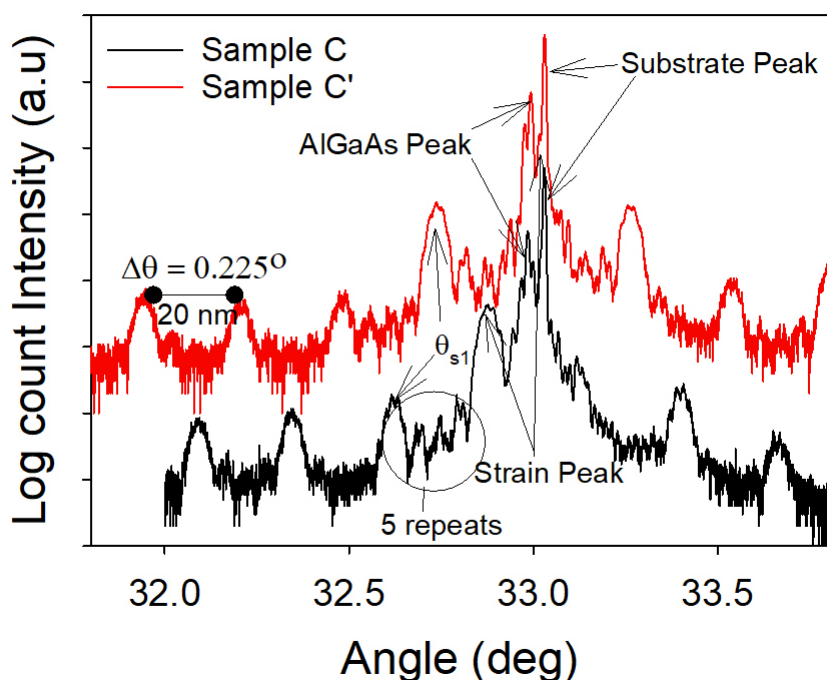


Figure 3.32: 004 reflection XRD spectra of samples C and C'.

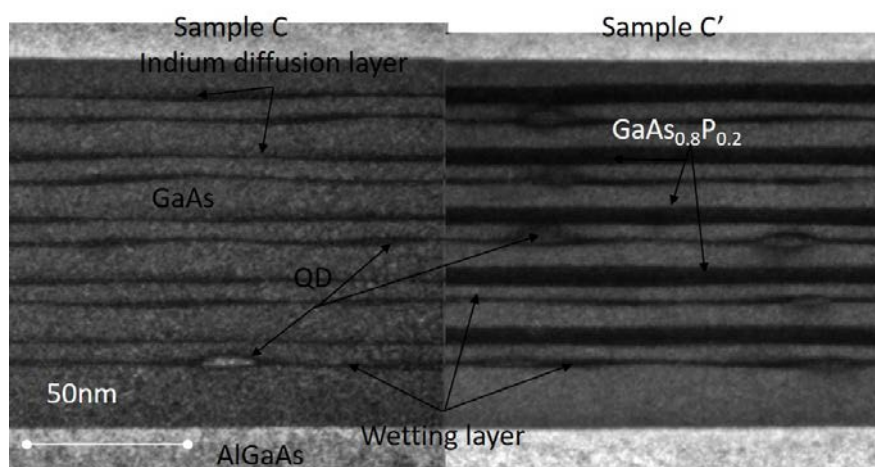


Figure 3.33: TEM images of samples C and C' with a separation of 20nm.

XRD spectra of samples C and C' are shown in figure 3.32. Again, the dominant peak is attributed to the substrate at 33.03°. As with samples B and B' the second most dominant peak for both samples is associated with the Al_{0.42}Ga_{0.58}As cladding layers (32.9827°). Again, a shift in the strain peak for sample C is observed, resulting from the average strain within the active region increasing due to the reduction in the spacing thickness, a compressive strain of 0.004426 is calculated. However, the structure will require the same amount of GaAs_{0.8}P_{0.2} to achieve full strain balance, a thickness of 5 nm. From the spacing

between the satellite peaks and using equation 3.6 the QD layer separation is determined as 20 ± 2 nm. The TEM images in figure 3.33, also gives a value of 20 ± 2 nm. The angular difference between the strain peak and the substrate peak is 0.0033° . From the position of the substrate and strain peak, the remaining strain ($\Delta a/a_s$) within the structure is calculated to be 0.0000886 and to be compressive.

Table 3.1 summarises the measured parameters of the six QD structures grown using the optimised conditions and the introduction of a $\text{GaAs}_{0.8}\text{P}_{0.2}$ strain-balancing layer. Strain balancing of three structures with three different separation thicknesses has been confirmed using XRD. All six structures show the expected fringe separation for QD layer separations of 50, 30 and 20 nm and all show the same number of repeats (five); this has also been confirmed from the TEM images.

Sample	Intended Separation	Calculated Separation	Strain within the structure	Type of strain
A	50 nm	50 ± 3 nm	0.001428	Compressive
A'	50 nm	50 ± 3 nm	0.0002739	Compressive
B	30 nm	30 ± 3 nm	0.002747	Compressive
B'	30 nm	30 ± 3 nm	0.0001772	Compressive
C	20 nm	20 ± 2 nm	0.004426	Compressive
C'	20 nm	20 ± 2 nm	0.000086	Compressive

Table 3.1: Summary of the XRD positions of the substrate, strain peak and the fringe separation of all samples

3.7 Preliminary Electrical and optical characterisation

Device fabrication and full characterisation will be discussed in detail in Chapter 4. Here preliminary electrical and optical measurements of 400 μm mesa diode structures fabricated from all 6 samples A, A', B, B', C and C' are presented and discussed. All devices show essentially the same room temperature IV characteristics and all showing a comparable differential resistance of 1.5-2 Ω , figure 3.34. In particular, there appears to be no detrimental effects on the turn-on behaviour due to the addition of the GaAs_{0.8}P_{0.2} layer. This is in agreement with the modelling presented in section 3.3 which predicted no significant changes if the phosphorous composition was kept to 20% or lower. This observation strongly suggests that a 5 nm GaAs_{0.8}P_{0.2} layer can be used as an effective strain balancing layer without any significant perturbation of the electrical characteristics.

Electroluminescence (EL) from 400 μm diameter mesa diodes was studied at room temperature using a continuous-wave (CW) current source with applied

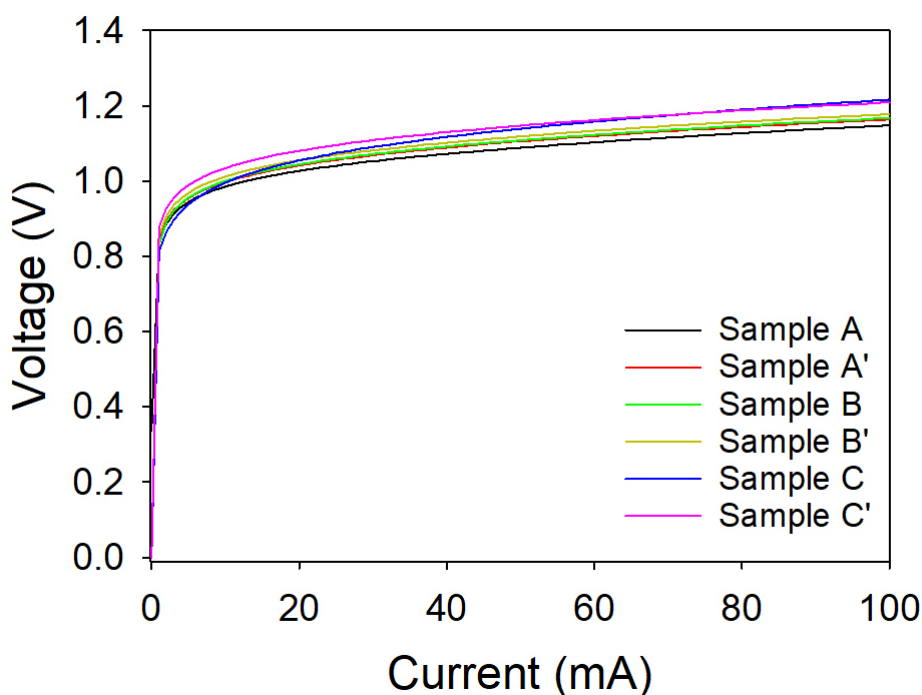


Figure 3.34: Room temperature IV characteristics for QD mesa diodes fabricated for all six samples.

currents between 1 mA and 100 mA. Emitted light was detected by a liquid nitrogen cooled germanium detector. Figure 3.35 shows normalised EL spectra of all six samples at both low (1 mA) and high (100 mA) excitation current, figure 3.36 shows the non-normalised high current EL spectra. Samples A and A' show similar emission spectra with almost identical linewidths (47.2 meV and 47.3 meV) and ground state emission wavelengths (1237 nm and 1239 nm), indicating that there is no detrimental effect on the physical structure and electronic properties of the QDs arising from the incorporation of the GaAs_{0.8}P_{0.2} layer. However, a slight reduction is observed in the absolute emission intensity (7.19 V and 6.35 V), as shown in figure 3.36, although this difference is within the experimental accuracy of the experimental setup. The TEM images of samples A and A', figure 3.29, show similar numbers of QDs spread across the different layers. Samples B and B' show similar low excitation current spectra, indicating that the GaAs_{0.8}P_{0.2} layer has not affected the ground state emission; this is the transition which will be responsible for the lasing. However, an increase in the linewidth is observed compared to samples A and A', with samples B and B' giving linewidths of 54.1 meV and 55.4 meV, respectively but with no change in the ground state emission wavelength (1238 nm and 1241 nm). At high current the excited state emission from sample B' is relatively weak in comparison to the ground state emission than is the case for sample B. However, the overall absolute intensity is improved with the inclusion of the strain-balancing layer 4.57 V compared to 2.12 V for the ground state, figure 3.36. The reason for this difference is unclear although it is consistent with a slightly higher QD density in sample B' so that more injected carriers are required to saturate the ground state. For a given current, this would result in a lower occupancy of the excited state. However, there is no evidence from the TEM images to support a significant difference in the QD densities between samples B and B'. The TEM images of samples B and B', figure 3.31, suggest a reduced number of QD spread across the different layers, in comparison to samples A and A'. The increase in overall intensity in sample B' compared to sample B, figure 3.36, suggests a benefit from the introduction of the strain balancing layer for relatively small separation thicknesses. Samples C and C' show differences in the low current excitation spectra with sample C' exhibiting a broadening of the ground state emission to 76.2 meV compared to

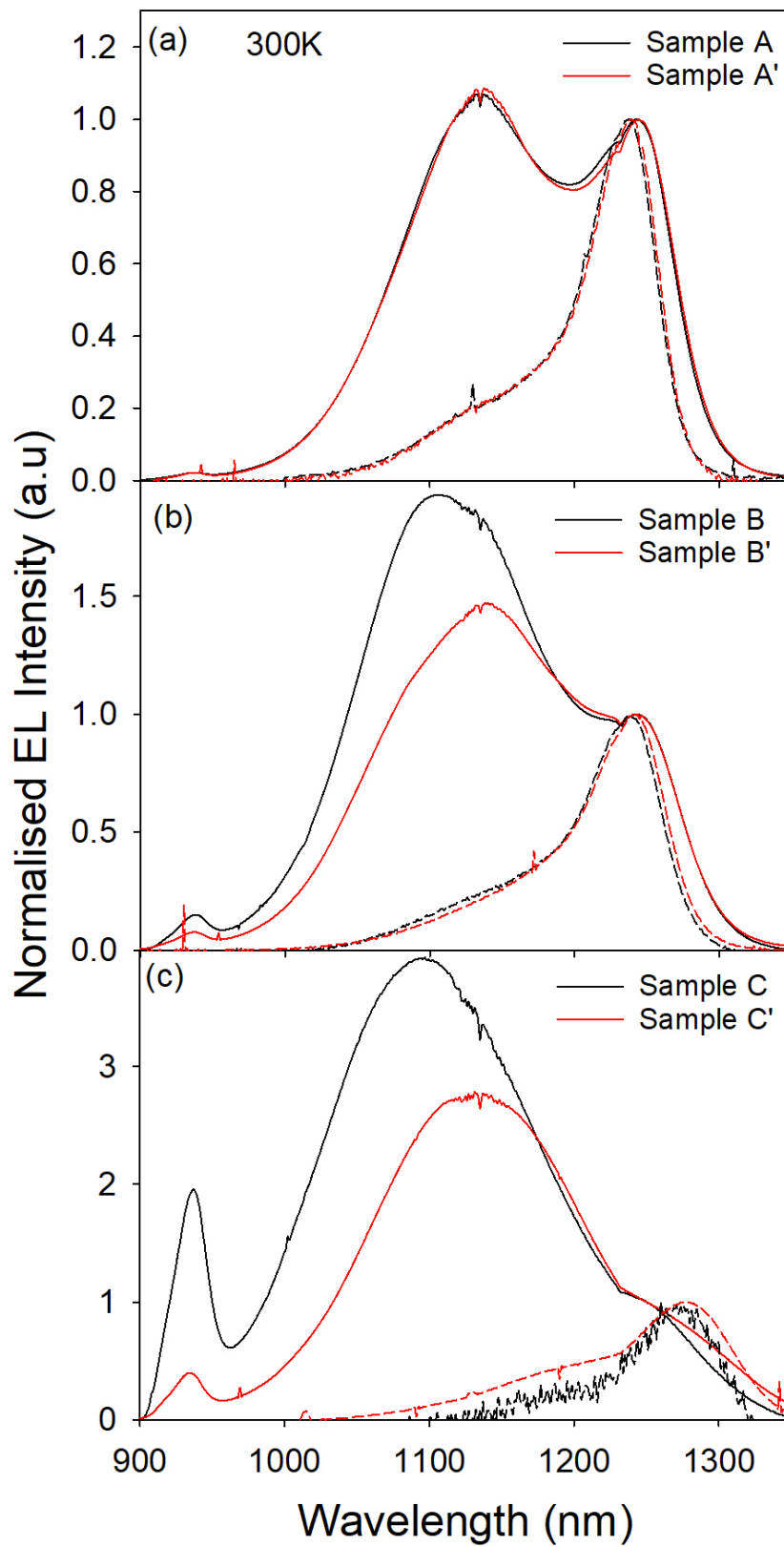


Figure 3.35: Room temperature low and high current CW EL of: (a) samples A & A' (b) samples B & B' and (c) samples C & C' All spectra have been normalised to the ground state emission intensity.

sample C'. As well as the increase in linewidth for sample C', both samples (C and C') have a higher emission wavelength (1260 nm and 1276 nm) compared to the previous four samples. At high current the excited state emission from sample C' is relatively weak with respect to the ground state emission than is the case for sample C, as shown in figure 3.36. However, similar to sample B' the absolute intensity of this sample is higher than that of sample C, the intensity of the ground state is increased from 0.2 V to 1.08 V as shown in figure 3.36. Again, there is some evidence to suggest that the addition of the strain-balancing layer has an advantageous effect on the overall optical efficiency. The high current spectra of all six samples show a relatively sharp, high-energy feature at ~930 nm. This is attributed to emission from the wetting layer. This emission is particularly strong for sample C and less so for sample C', this suggests a lower QD density in these samples so that a lower injection current is required to saturate the QD states and start populating the higher energy wetting layer states.

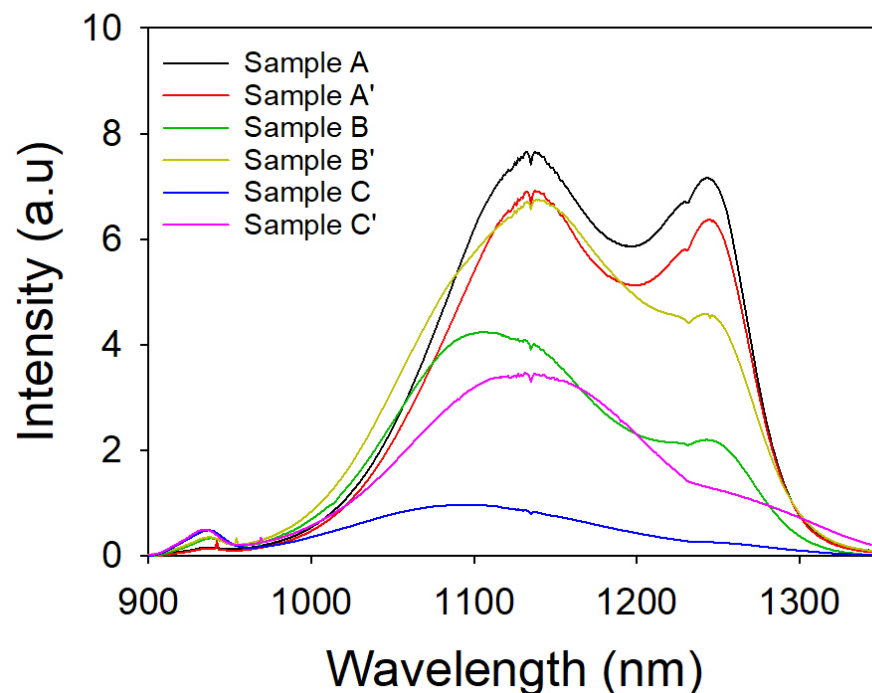


Figure 3.36: Room temperature high current CW EL of samples A, A', B, B', C and C'.

The TEM image of sample C', figure 3.33, shows that there is a vertical alignment of the QDs in different layers, with the QDs increasing in size in successive layers; this may explain why the QD emission is broader than for the other samples. Vertical alignment of QDs when the separation between layers

is small has previously been reported. [43]–[47] This behaviour has been attributed to the strain field produced by QDs in the first layer acting as nucleation sites for QDs in the second layer etc. Because the QDs in the second and subsequent layers are affected by this strain field, their physical size and shape can be altered. The TEM image of sample C shows only a single QD in the first layer and no QDs in the subsequent layers, this may explain why there is a difference in the excited state emission at higher currents and why strong wetting layer emission is observed for this sample.

Table 3.2 summarises the ground state wavelength, linewidth and intensities of both the ground and excited state for all six samples. Clearly, the behaviour of these six samples is complex and it is difficult to draw any strong conclusions. Addition of the strain-balancing layer appears to cause no significant effect on the electrical characteristics for all three QD separations. In addition, for a 50 nm separation the incorporation of the 5 nm GaAs_{0.8}P_{0.2} layer produces no significant effect on the optical properties. For a separation of 30 nm (sample B'), a slight increase in the emission intensity results from the addition of the GaAs_{0.8}P_{0.2} layer and a more significant improvement occurs for the 20 nm separation sample (sample C'). However, the spectra of samples B, B', C and C' show broadening of the emission and for C and C' a significant blue shift. The reason for this behaviour is unclear but there is evidence for a decreasing QD density and vertical alignment of QDs for a layer separation of 20 nm.

Sample	Ground state wavelength		Linewidth		Ground state Intensity (a.u)	Excited state Intensity (a.u)
	nm	eV	nm	meV		
A	1237	1.002	58	47.2	7.19	7.64
A'	1239	1.001	58	47.3	6.35	6.85
B	1238	1.001	67	54.1	2.12	4.23
B'	1241	0.999	68	55.4	4.57	6.69
C	1260	0.984	68	53.5	0.2	0.97
C'	1276	0.972	101	76.2	1.08	3.41

Table 3.2: summary of the EL spectral data obtained for the six samples

3.8 Further Work

Further work is required to understand the mechanism(s) of carrier transport across the $\text{GaAs}_z\text{P}_{1-z}$ barrier layer. The modelling described in section 3.3 only considered a barrier thickness of 5 nm. This barrier thickness will change depending on the concentration of the phosphorous layer. Modelling of the different barrier thickness required for different concentrations of phosphorous would be of interest. Figure 3.37 shows the required thickness for different phosphorus concentrations, where the thicknesses have been calculated using equation 3.7. As the concentration of the phosphorus is increased, the thickness required to strain balanced is reduced. This is due to the larger difference between the lattices constant of the GaAs spacer layer and the $\text{GaAs}_z\text{P}_{1-z}$ strain-compensation layer. The lattice mismatch between GaAs and $\text{GaAs}_z\text{P}_{1-z}$ will produce an average strain depending on the relative thickness of the strain-balancing layer and the spacing layer, which is dependent on the lattice mismatch between the two materials. Therefore, a higher concentration of phosphorous in the strain balancing layer will require a thinner $\text{GaAs}_z\text{P}_{1-z}$ layer to compensate the strain produced by the QDs.

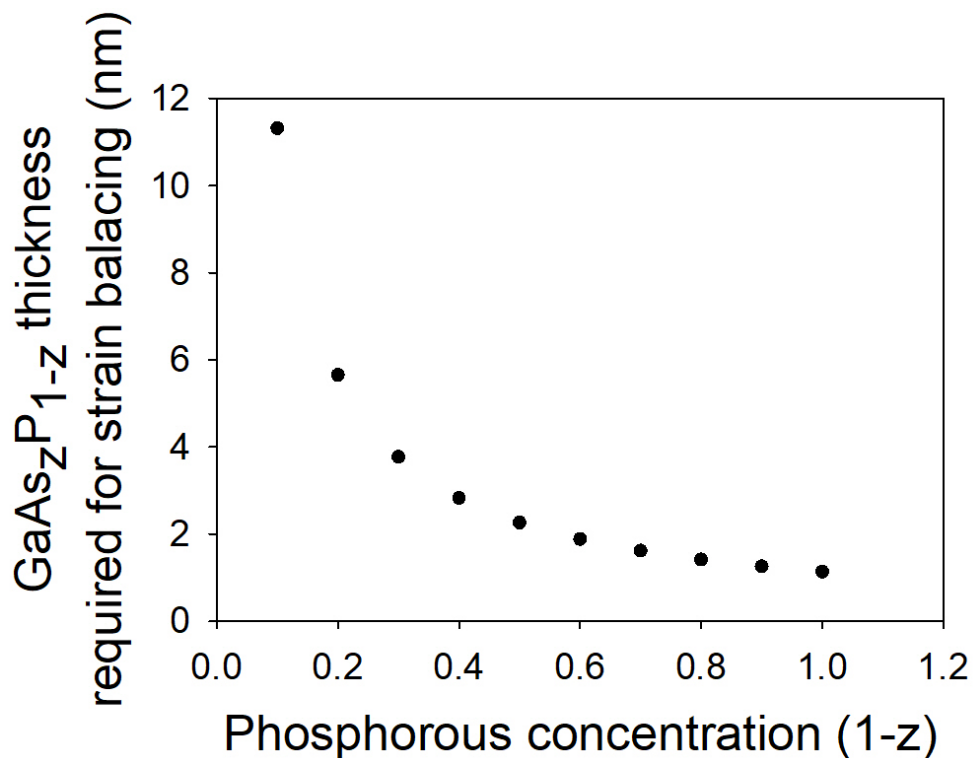


Figure 3.37: Calculated required GaAsP thickness for a strain balancing layer of varying phosphorous concentration

Chapter 3: Strain Balancing of Quantum Dot Layers

There are two mechanisms by which carriers can be transported through the $\text{GaAs}_x\text{P}_{1-x}$ barrier; thermal excitation over the barrier or quantum mechanical tunnelling through the barrier. The effectiveness of these two transport processes is expected to depend on both the height and width of the barrier for tunnelling and the height for thermal excitation. Hence, a study of different combinations of width and composition may allow these two processes to be studied and the composition that allows the most efficient carrier transport to be identified. For example, there may be advantages in using a concentration greater than 20% phosphorous. Growth of different strain-balanced samples will provide experimental confirmation of the modelling. In addition, studies of the positioning on the GaAsP layer could be performed. For example, this layer could be placed before the QD layers or split into two separate layers placed before and after each QD layer. Finally, a QD layer separation intermediate between 30 and 20 nm should be grown to determine the lower limit for non-coupled QD layers.

3.9 Conclusions

This chapter has introduced the concept of strain balancing with the aim of reducing the spacing thickness between QD layers in a laser structure. This reduction in the spacing thickness will lead to a higher volumetric density of QDs, which will aid in reducing the threshold current density and permit new and novel devices. In the literature review, the material systems and methods of strain balancing applied to solar cells and other opto-electronic devices have been discussed. Modelling of devices using LaserMod has shown the potential effects of the phosphorous concentration in a GaAsP strain-compensation layer on the electrical and optoelectronic characteristics of a simple dual QW device.

Modelling of XRD spectra using Leptos software allows the interpretation of experimental spectra. The effects of varying the indium composition of an InGaAs layer and phosphorous composition of a GaAsP layer have been simulated. The former system gives compressive strain and the latter tensile strain. The effect of varying structural parameters, including layer thickness and repeat thicknesses, on the XRD spectra have been modelled. XRD modelling of a QW structure designed to replicate the strain in a QD system has shown that a 4nm GaAs_zP_{1-z} layer with $z = 0.2$ should fully strain balance the QD structure. A growth calibration to ensure the correct phosphorous concentration has been performed, with the resulting structural parameters determined from the XRD spectrum.

Six QD laser structures have been grown and mesa devices fabricated to study the effectiveness of strain balancing. Initially a 50 nm device (sample A) was grown to calculate the thickness of GaAs_{0.8}P_{0.2} required to balance the strain in the structure. The required thickness was calculated to be 5.6 nm; however, a value of 5 nm was used to ensure the structure is not over compensated. Samples with three different spacing thicknesses of 50 nm (A and A'), 30 nm (B and B') and 20 nm (C and C') were grown with and without the GaAs_{0.8}P_{0.2} strain-balancing layer. All devices showed similar electrical characteristics and samples A and A' also showed very similar optical characteristics. There is some evidence that the addition of the GaAs_{0.8}P_{0.2} strain-balancing layer improves the QD emission efficiency of the 30 and 20 nm spacing samples but

Chapter 3: Strain Balancing of Quantum Dot Layers

the results for these samples are complicated by changes to the intrinsic QD properties.

3.10 References

- [1] J. E. Ayers, T. Kujofsa, P. Rango, and J. E. Raphael, *Heteroepitaxy of semiconductors : theory, growth, and characterization*. 2007.
- [2] K. Akahane, N. Yamamoto, and T. Kawanishi, “Fabrication of ultra-high-density InAs quantum dots using the strain-compensation technique,” *Phys. status solidi*, vol. 208, no. 2, pp. 425–428, Feb. 2011.
- [3] G. B. Stringfellow, *Organometallic Vapor-Phase Epitaxy: Theory and Practice*. Academic Press, 1999.
- [4] H. Sodabanlu, S. Ma, K. Watanabe, M. Sugiyama, and Y. Nakano, “Impact of Strain Accumulation on InGaAs/GaAsP Multiple-Quantum-Well Solar Cells: Direct Correlation between *In situ* Strain Measurement and Cell Performances,” *Jpn. J. Appl. Phys.*, vol. 51, no. 10S, p. 10ND16, Oct. 2012.
- [5] T. Smyth *et al.*, “Hot Carrier Cooling in $\text{In}_{0.17}\text{Ga}_{0.83}\text{As}/\text{GaAs}_{0.80}\text{P}_{0.20}$ Multiple Quantum Wells: The Effect of Barrier Thickness,” *IEEE J. Photovoltaics*, vol. 6, no. 1, pp. 166–171, Jan. 2016.
- [6] J. H. Davies, D. M. Bruls, J. W. A. M. Vugs, and P. M. Koenraad, “Relaxation of a strained quantum well at a cleaved surface,” *J. Appl. Phys.*, vol. 91, no. 7, p. 4171, Mar. 2002.
- [7] H. Dong *et al.*, “Interfacial relaxation analysis of InGaAs/GaAsP strain-compensated multiple quantum wells and its optical property,” *Superlattices Microstruct.*, vol. 114, pp. 331–339, Feb. 2018.
- [8] N. J. Ekins-Daukes *et al.*, “Strain-balanced GaAsP/InGaAs quantum well solar cells,” *Appl. Phys. Lett.* 75, 4195 (2000).
- [9] A. Fukuyama *et al.*, “Effect of internal electric field on non-radiative carrier recombination in the strain-balanced InGaAs/GaAsP multiple quantum well solar cells,” *Phys. status solidi*, vol. 211, no. 2, pp. 444–

- 448, Feb. 2014.
- [10] C. I. Cabrera, J. C. Rimada, J. P. Connolly, and L. Hernandez, “Modelling of GaAsP/InGaAs/GaAs strain-balanced multiple-quantum well solar cells,” *Journal of Applied Physics* 113, 024512 (2013).
- [11] Y. Wen, Y. Wang, K. Watanabe, M. Sugiyama, and Y. Nakano, “Effect of GaAs Step Layer on InGaAs/GaAsP Quantum Well Solar Cells,” *Appl. Phys. Express*, vol. 4, no. 12, p. 122301, Nov. 2011.
- [12] D. Alonso-Álvarez *et al.*, “InGaAs/GaAsP strain balanced multi-quantum wires grown on misoriented GaAs substrates for high efficiency solar cells,” *Appl. Phys. Lett.*, vol. 105, no. 8, p. 83124, Aug. 2014.
- [13] N.J. Ekins-Daukes *et al.*, “Strain-balanced GaAsP/InGaAs quantum well solar cells,” *Appl. Phys. Lett.*, vol. 75, no. 26, p. 4195, Dec. 1999.
- [14] G. K. Bradshaw, C. Z. Carlin, J. P. Samberg, N. A. El-Masry, P. C. Colter, and S. M. Bedair, “Carrier Transport and Improved Collection in Thin-Barrier InGaAs/GaAsP Strained Quantum Well Solar Cells,” *IEEE J. Photovoltaics*, vol. 3, no. 1, pp. 278–283, Jan. 2013.
- [15] V. P. Duraev *et al.*, “Effect of GaAsP barrier layers on the parameters of InGaAs/AlGaAs laser diodes emitting in the 1050–1100-nm spectral range,” *Quantum Electron.*, vol. 35, no. 10, pp. 909–911, Oct. 2005.
- [16] H. Dong *et al.*, “Effect of potential barrier height on the carrier transport in InGaAs/GaAsP multi-quantum wells and photoelectric properties of laser diode,” *Phys. Chem. Chem. Phys.*, vol. 18, no. 9, pp. 6901–6912, Feb. 2016.
- [17] “Effect of hetero-interfaces on in situ wafer curvature behavior in InGaAs/GaAsP strain-balanced MQWs,” *J. Cryst. Growth*, vol. 352, no. 1, pp. 245–248, Aug. 2012.
- [18] J. Tatebayashi, N. Nuntawong, P. S. Wong, Y.-C. Xin, L. F. Lester, and

- D. L. Huffaker, “Strain compensation technique in self-assembled InAs/GaAs quantum dots for applications to photonic devices,” *J. Phys. D. Appl. Phys.*, vol. 42, no. 7, p. 73002, Apr. 2009.
- [19] C. G. Bailey, S. M. Hubbard, D. V. Forbes, and R. P. Raffaele, “Evaluation of strain balancing layer thickness for InAs/GaAs quantum dot arrays using high resolution x-ray diffraction and photoluminescence,” *Appl. Phys. Lett.*, vol. 95, no. 20, p. 203110, 2009.
- [20] S. J. Polly, C. G. Bailey, A. J. Grede, D. V. Forbes, and S. M. Hubbard, “Calculation of strain compensation thickness for III–V semiconductor quantum dot superlattices,” *J. Cryst. Growth*, vol. 454, pp. 64–70, Nov. 2016.
- [21] N. Nuntawong, J. Tatebayashi, P. S. Wong, and D. L. Huffaker, “Localized strain reduction in strain-compensated InAs/GaAs stacked quantum dot structures,” *Appl. Phys. Lett.*, vol. 90, no. 16, p. 163121, 2007.
- [22] T. Kageyama *et al.*, “InAs/GaAs quantum dot lasers with GaP strain-compensation layers grown by molecular beam epitaxy,” *Phys. status solidi*, vol. 213, no. 4, pp. 958–964, Apr. 2016.
- [23] K. Akahane, N. Yamamoto, T. Umezawa, A. Kanno, and T. Kawanishi, “A semiconductor optical amplifier comprising highly stacked InAs quantum dots fabricated using the strain-compensation technique,” *Jpn. J. Appl. Phys.*, vol. 53, no. 45, p. 04, Jan. 2014.
- [24] T. D. Germann, A. Strittmatter, T. Kettler, K. Posilovic, U. W. Pohl, and D. Bimberg, “MOCVD of InGaAs/GaAs quantum dots for lasers emitting close to 1.3 μm ,” *J. Cryst. Growth*, vol. 298, pp. 591–594, Jan. 2007.
- [25] N. Nuntawong *et al.*, “Quantum dot lasers based on a stacked and strain-compensated active region grown by metal-organic chemical vapor deposition,” *Appl. Phys. Lett.*, vol. 86, no. 19, p. 193115, 2005.

- [26] N. Nuntawong, S. Huang, Y. B. Jiang, C. P. Hains, and D. L. Huffaker, "Defect dissolution in strain-compensated stacked InAs/GaAs quantum dots grown by metalorganic chemical vapor deposition," *Appl. Phys. Lett.*, vol. 87, no. 11, p. 113105, Sep. 2005.
- [27] J. Tatebayashi *et al.*, "Ground-state lasing of stacked InAs/GaAs quantum dots with GaP strain-compensation layers grown by metal organic chemical vapor deposition," *Appl. Phys. Lett.*, vol. 88, no. 22, p. 221107, May 2006.
- [28] N. H. Kim *et al.*, "Characteristics of InGaAs quantum dots grown on tensile-strained GaAs_{1-x}P_x," *J. Appl. Phys.*, vol. 97, no. 9, p. 93518, May 2005.
- [29] N.-H. Kim, J.-H. Park, L. J. Mawst, T. F. Kuech, and M. Kanskar, "Temperature sensitivity of InGaAs quantum-dot lasers grown by MOCVD," *IEEE Photonics Technol. Lett.*, vol. 18, no. 8, pp. 989–991, Apr. 2006.
- [30] P. Lever, "InGaAs quantum dots grown with GaP strain compensation layers," *J. Appl. Phys.*, vol. 95, no. 10, p. 5710, May 2004.
- [31] P. J. Simmonds *et al.*, "Improved quantum dot stacking for intermediate band solar cells using strain compensation," *Nanotechnology*, vol. 25, no. 44, p. 445402, Nov. 2014.
- [32] N. J. Ekins, Daukes J. M. Barnes, K. W. J. Barnham, J. P. Connolly, M. Mazzer, J. C. Clark, R. Grey, G. Hill, M. A. Pate, J. S. Roberts "Strained and strain-balanced quantum well devices for high-efficiency tandem solar cells," *Sol. Energy Mater. Sol. Cells*, vol. 68, no. 1, pp. 71–87, Apr. 2001.
- [33] T. Aihara *et al.*, "Detection of miniband formation in strain-balanced InGaAs/GaAsP quantum well solar cells by using a piezoelectric photothermal spectroscopy," *J. Appl. Phys.*, vol. 116, no. 4, p. 44509, Jul. 2014.

- [34] “LaserMOD™ - Photonic Device Design Software Tool.” [Online]. Available: <https://www.synopsys.com/optical-solutions/rsoft/active-device-lasermod.html>.
- [35] “Basic Parameters Gallium Indium Arsenide Phosphide (GaInAsP) - NSM Archive.” [Online]. Available: <http://www.ioffe.ru/SVA/NSM/Semicond/GaInAsP/basic.html>.
- [36] S. A. Stepanov, E. A. Kondrashkina, R. Köhler, D. V. Novikov, G. Materlik, and S. M. Durbin, “Dynamical x-ray diffraction of multilayers and superlattices: Recursion matrix extension to grazing angles,” *Phys. Rev. B*, vol. 57, no. 8, pp. 4829–4841, Feb. 1998.
- [37] D. K. (David K. Bowen and B. K. (Brian K. Tanner, *High resolution X-ray diffractometry and topography*. Taylor & Francis, 1998.
- [38] U. Pietsch, V. Holý, and T. Baumbach, *High-resolution X-ray scattering : from thin films to lateral nanostructures*. Springer, 2004.
- [39] P. F. Fewster, *X-Ray Scattering from Semiconductors and Other Materials*. WORLD SCIENTIFIC, 2015.
- [40] “NSM Archive - Basic Parameters of Gallium Indium Arsenide (GaInAs)”
<http://www.ioffe.ru/SVA/NSM/Semicond/GaInAs/basic.html>.
- [41] “NSM Archive - Gallium Indium Arsenide Phosphide (GaInAsP) - Thermal properties.”
[http://www.ioffe.ru/SVA/NSM/Semicond/GaInAsP/thermal.html#Lattice properties](http://www.ioffe.ru/SVA/NSM/Semicond/GaInAsP/thermal.html#Lattice%20properties).
- [42] E. Hecht, *Optics*, Fifth Edit. Pearson, 2017.
- [43] B. Ilahi *et al.*, “Optimizing the spacer layer thickness of vertically stacked InAs/GaAs quantum dots,” *Mater. Sci. Eng. C*, vol. 26, no. 2–3, pp. 374–377, Mar. 2006.
- [44] B. Ilahi *et al.*, “Spacer layer thickness effects on the photoluminescence

- properties of InAs/GaAs quantum dot superlattices,” *Phys. status solidi*, vol. 199, no. 3, pp. 457–463, Oct. 2003.
- [45] J. S. Wang *et al.*, “Optical and structural properties of vertically stacked and electronically coupled quantum dots in InAs/GaAs multilayer structures,” *Nanotechnology*, vol. 18, no. 1, p. 15401, Jan. 2007.
- [46] G. Rainò *et al.*, “Structural and optical properties of vertically stacked triple InAs dot-in-well structure,” *J. Appl. Phys.*, vol. 103, no. 9, p. 96107, May 2008.
- [47] A. Endoh, Y. Nakata, Y. Sugiyama, M. Takatsu, and N. Yokoyama, “Effect of Size Fluctuations on the Photoluminescence Spectral Linewidth of Closely Stacked InAs Self-Assembled Quantum Dot Structures,” *Jpn. J. Appl. Phys.*, vol. 38, no. Part 1, No. 2B, pp. 1085–1089, Feb. 1999.

Chapter 4: Optoelectronic Device Fabrication, Measurement and Modelling

4.1 Introduction

This chapter discusses the principles of device fabrication of devices. The differences between different types of photoresist (positive and negative) and etching techniques (dry and wet) are considered although only positive photoresist and wet etching are used in this thesis. Fabrication of broad area lasers and mesa diodes are discussed in detail in section 4.3, this section describes in detail the processing steps undertaken to produce the devices used in this thesis. After the devices are fabricated, they are tested and studied using a range of techniques. Temperature dependant studies of mesa diodes and laser devices are presented; the difficulties of obtaining a room temperature laser are discussed. Later continuation of the growth development resulted in a room temperature laser; results for this device are presented. The final section of this chapter discusses the potential for introducing quantum dots (QDs) into a photonic crystal surface emitting laser (PCSEL). The initial aim of this work was to use 1.3 μm emitting QD material supplied by the commercial company QD laser Inc. but with overgrowth of the material performed by MOVPE in Sheffield. The proposed QD-PCSEL structure is modelled using Photon Design's FimmWave software. It is found necessary to develop a new waveguide design due to the lack of net modal gain achieved using a previous Sheffield design for photonic crystals using QW active regions. The new design poses many aspects of complication due to the use of AIAs. However, by fabricating the photonic crystals in a GaAs layer and using AIAs as the

overgrowth material, the AlAs would never be exposed therefore an AlAs/GaAs photonic crystal is possible. Initial structures with a planar waveguide have been grown and tested to ascertain any potential issues with the large barriers introduced by the AlAs.

4.2 Background and literature review

The literature review for this chapter, will discuss the principles behind the processing of semiconductor devices, the experimental technique of electroluminescence (EL) of QDs, QD Fabry-Perot laser devices and waveguide modelling with emphasis on structures containing photonic crystals.

To ensure high yield and long device lifetime, it is clear that successful device fabrication requires high cleanliness. If there are particles on the sample this can result in defects occurring in the pattern transfer. For the photolithography step, a photosensitive material, the photoresist, is used to transfer a pattern from a mask to the semiconductor. The photoresist is exposed with ultra-violet (UV) light via the pattern, which alters the structure of the photoresist. Photoresist is available in two forms, positive and negative. For positive photoresist the exposed areas become more soluble in the developer, and therefore removed. With negative photoresist, the exposed areas become less soluble and it is the unexposed areas that are removed by the developer. [1] After removal of some of the photoresist to define exposed and unexposed areas on the sample, either metal deposition or chemical etching can be used to transfer the pattern to the semiconductor wafer. When depositing metals to produce contacts it is important to use metals with an appropriate work function. For an n-type contact, the work function of the metal is required to be smaller than the work function in the semiconductor. Conversely, to produce a p-type contact the work function of the metal is required to be larger than the work function of the semiconductor. [2] For chemical etching, two techniques are possible wet and dry. Wet chemical etching is used more extensively as a blanket etch where no pattern is transferred to the sample but instead a layer of material is to be removed. There are many aspects to wet chemical etching that can affect the process, for example both the concentration and the temperature can affect the etch rates. The profile produced by wet chemical etching is generally isotropic, where the vertical and lateral etch rates are the same and therefore undercutting of the pattern can affect the resolution of the resultant features. However, anisotropic etches can occur depending on the selectivity of the different crystal surfaces. Dry chemical etching produces more uniform sidewalls due to the

lateral etch rate being close to or equal to zero. Other issues, such as etching of the protecting photoresist can pose a problem, but a hard mask produced using an oxide layer can remove this issue, but at the expense of introducing extra processing steps. [1] However, the protecting hard mask can also be etched during the processing; this can be mitigated by deposition of a thicker layer.

EL produced by the spontaneous emission of a QD ensemble provides valuable information about the structural and electronic properties of the QDs. Initial studies in this thesis focus on optical access mesa diode, where the temperature dependence of the EL was measured. The emission energy of all semiconductors is expected to change with temperature due to Varshni's law, a result of the bandgap decreasing with increasing temperature. The increase of the lattice spacing due to the thermal expansion coefficient provides one contribution but the increased phonon population and interaction with the electronic states is the dominant cause. [3] Inhibited thermalization of carriers at low temperature yields the opportunity to study the random population of the full QD ensemble for conditions where the average number of carriers per QD is less than one. In this case, ground state emission produced by the full ensemble can be studied, without higher energy state interference, and QD size and shape bimodality issues can be observed. Reducing QD bimodality is important for maximising modal gain in a laser. Increasing the InAs coverage has been reported to reduce the bimodality of the QDs but at the possible expense of creating defects, which may act as non-radiative centres and also increase the internal loss via photon scattering. A comparison of the EL intensities between different samples allows relative radiative efficiencies to be determined. EL measured as a function of temperature, where the integrated intensity is determined, can be used to deduce an activation energy for the loss of carriers from the optically active states. [4] The activation energy is defined as the additional energy required for carriers to be thermally excited to a higher energy state. Therefore, the higher this energy the less carriers are lost at a given temperature. For QDs an activation energy value in the region of 100 meV has been reported although the nature of the state to which carriers are lost from the ground state of the QDs is not always clear. [5]–[9] Quenching of the QD emission at higher temperatures, as reported by Brusaferrri *et al.*, is attributed to

carrier escape through non-radiative recombination centres in the GaAs. At intermediate temperatures (50–150 K), there is a transfer of carriers out of the high-energy QDs to the low-energy QDs whilst maintaining the same overall integrated intensity. [7] A similar effect has been studied by Dai *et al.* who reported differences in the activation energies of the larger (low-energy) QDs compared to the smaller (high-energy) QDs, with the larger QDs yielding a higher activation energy of 112 meV and the smaller QDs yielding an activation energy of 66 meV. [9] Room temperature spectral measurement of InAs/GaAs QDs reveal emission between 1.1 and 1.5 μm depending on the properties of the QD, such as the indium concentration, strain around the QD and the size of the QD. [10]–[21]

The laser was proposed by Schawlow and Townes at Bell laboratories in 1958, and first demonstrated in 1960 by T. Maiman using optically pumped ruby. [22], [23] The first gas discharge laser was demonstrated in 1961 by A. Javan *et al.* [24] The first semiconductor laser was reported in 1962 by R. Hall *et al.*, although it was not until the development of the heterostructure laser in 1970, by Z. Alferov and I Kroemer, and slightly later or simultaneously by I. Hayashi and M. Panish, that practical semiconductor lasers became a reality. [25] The lasers used in the first part of this thesis all use a Fabry-Perot cavity, where two plane and parallel mirrors create feedback within the active gain region. The Fabry-Perot cavity was first introduced in 1899, where Charles Fabry and Alfred Perot developed the idea. [26] For a laser to work a population inversion is required, for a semiconductor laser this requires an excess of electrons in the conduction band and holes in the valence band. This is typically achieved in a forward biased p-i-n structure. Spontaneous recombination occurs where an electron and hole recombine randomly to produce a photon. If the recombination is stimulated by an existing photon the electron and hole recombines and a photon of light is produced with the same properties as that of the incident photon, the two photons are coherent. As light passes through a cavity with a population inversion, the light will be amplified with the end facet mirrors providing feedback. Once the amount of gain equals the total losses of the cavity (composed of mirror losses and internal loss) the laser will start to lase.

QD lasers have been reported to reduce the threshold current density, compared to QW and bulk lasers, and improve the temperature stability of the threshold current density, as reported by K. Otsubo *et al.* [27]–[29] The lowest reported threshold current density for a QW laser is 50 A cm^{-2} by G. W. Turner *et al.* [30] A number of groups have reported the successful fabrication of InAs/GaAs self-assembled QD lasers by molecular beam epitaxy (MBE) operating in the spectral region close to $1.3 \mu\text{m}$, with varying threshold current densities. The lowest reported threshold current density is by Eliseev *et al.* with a value of 13 A cm^{-2} ; other groups have reported similar low threshold current densities with values below 100 A cm^{-2} , all grown by MBE. [31]–[37] However, such low threshold current densities have proven to be difficult to achieve for metal-organic vapour phase epitaxy (MOVPE) grown InAs/GaAs self-assembled QD lasers. Passaseo *et al.* studied similar QD laser structures grown by MBE and MOVPE. The MOVPE grown laser gave lasing from an excited state and with a much higher threshold current density of 203 A cm^{-2} compared to ground state laser and a threshold current density of 147 A cm^{-2} for the MBE grown device. [38] This difference was attributed to the MOVPE grown QDs having well defined facets which results in strong piezo-electric fields and a strong reduction in the oscillator strength of the ground state emission. For the fabricated devices, the maximum ground state gain was insufficient to allow lasing. For MOVPE grown QD lasers the lowest reported threshold current density is 108 A cm^{-2} for a ground state laser at $1.18 \mu\text{m}$. Higher current densities for ground state QD lasing have been reported, with values typically between 108 and 250 A cm^{-2} for lasing wavelengths between 1.14 and $1.33 \mu\text{m}$. [21], [39]–[46]

The temperature sensitivity of the threshold current density is still an issue for QD lasers, and departs from the ideal predicted constant value due to non-ideal dots. Ideal QDs have uniform size and shape but in reality, there is an inhomogeneous distribution. In addition, the QDs and surrounding matrix contain states with energies above the QD ground state, allowing thermal carrier loss, therefore reducing the number of available carriers in the lasing states. [47], [48] A reduction in the threshold current density has been observed with increasing operating temperatures from 50 to 150 K (so-called negative- T_0 behaviour). This is attributed to a process where, at low temperature, all QDs

are equally populated with carriers, whilst at higher temperatures carriers transfer preferentially into the lowest energy QDs (larger QDs) giving a higher peak gain for a given injection level. [47], [48] By modulation doping the QDs p-type it appears possible to shift this negative- T_0 behaviour and minimum of the threshold current density close to room temperature, possibly via an increase in the confinement potential for electrons via their attraction to the positively charged QDs. This increases the temperature at which thermalisation within the QD ensemble occurs and gives increased stability around room temperature although the absolute threshold current density value is increased, possibly due to increased free carrier absorption. [49], [50]

Fabry-Perot lasers have closely spaced modes and hence typically exhibit multi-mode lasing. Selectivity of the lasing wavelength can be achieved via a photonic structure in which there is a periodic variation in the refractive index. [51] Inhibiting light emission is achieved through multiple reflections with destructive interference to create a photonic band gap. With suitable design, a device can be engineered to produce a single mode laser by inhibiting the spontaneous emission from other modes. [52], [53] For an in-plane Fabry-Perot cavity laser a periodic reflector, known as a Bragg grating, gives distributed feedback (DFB), and can be used instead of a highly reflective mirror to create a single mode device. [53]–[55] The first vertical cavity surface emitting laser (VCSEL) was developed by K. Iga in 1977 and reported in 1979. [56]–[58] A VSCSEL uses two Bragg mirrors placed above and below the active region to give a vertical cavity. Both the DFB and DBR are examples of one-dimensional photonic-structures. [59]

Limitations to the optical output power emitted by VCSELs has led to the development of the photonic crystal surface emitting lasers (PCSELs), which uses a two dimensional photonic crystal. The first report of a PCSEL was by M. Berggren *et al.*, where an organic gain medium is deposited within a photonic crystal formed by fabricating a periodic array of holes in a SiO₂ layer. The device was optically pumped with a nitrogen laser and lasing emission was observed at 830 nm. [60] The first report of an electrically pumped PCSEL was by M. Imada *et al.* in 1999 emitting at 1.28 μm . Two wafers were fused together, one with the active region and the second wafer with a triangular shaped

photonic crystal consisting of InP and air. [61] Five years later the first continuous wave PCSEL was reported by D. Ohnishi *et al.* in 2004, emitting at 960 nm. Again, the fabrication required two wafers, with the active and photonic crystal regions fabricated on one wafer and the upper cladding layer on a second wafer. The photonic crystal was fabricated as a square lattice consisting of GaAs and air. [62] PCSELS have been reported to show single mode operation, the ability to scale output power with area, to produce coherent output and exhibit low divergence of the lasing light. [63]–[65] A PCSEL has been reported to exhibit single mode operation with powers up to one Watt from a single PCSEL by K. Hirose *et al.*. [66] Photonic crystal fabrication using wafer fusion has successfully shown the potential of the PCSEL design but the inclusion of voids within the structure can affect the manufacturability and reliability and result in current spreading and heating issues. [61]–[67] Removing the voids from the photonic crystal and fabricating an all-semiconductor photonic crystal should alleviate these issues. The first report of an all-semiconductor PCSEL was by D. Williams *et al.* in 2012, who demonstrated the successful fabrication of an InGaP/GaAs photonic crystal with single mode lasing at 960 nm. [68]–[70] With further development, continuous wave operation and coherence coupling have been reported. [71]–[74] Waveguide modelling of the optical mode has been applied to optimise the coupling to both the photonic crystal and the active region. [68], [75] Extension of lasing to longer wavelengths is desirable and may require the use of different active regions, for example QDs.

4.3 Device Fabrication

In this section, the device fabrication process used to fabricate devices used in this thesis will be described. Figure 4.1 shows the two different types of photoresist, positive and negative, that can be used in device fabrication. Positive photoresist is shown at the top and negative photoresist is shown below. With positive photoresist, the exposed photoresist is removed by the developer. For negative photoresist, it is the unexposed photoresist that is removed by the developer.

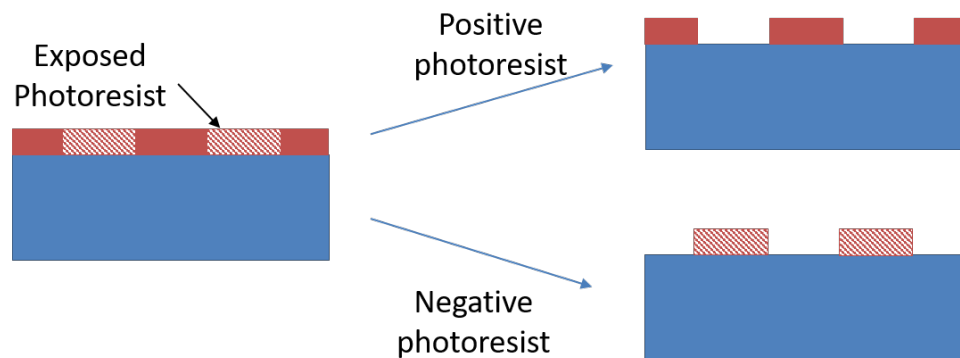


Figure 4.1: Schematic of the different photoresists available for semiconductor processing.

Figure 4.2 shows the two different types of etching, dry and wet, that are used in device fabrication. Dry etching yields an anisotropic etch, where vertical sidewalls can be achieved and is useful for achieving narrow ridge lasers. Wet etching yields, an anisotropic etch, for example producing an undercut of the device features; this can be an issue for narrow ridge laser devices. However, wet etching does have some advantages over dry etching, with wet etching being cost effective and faster.

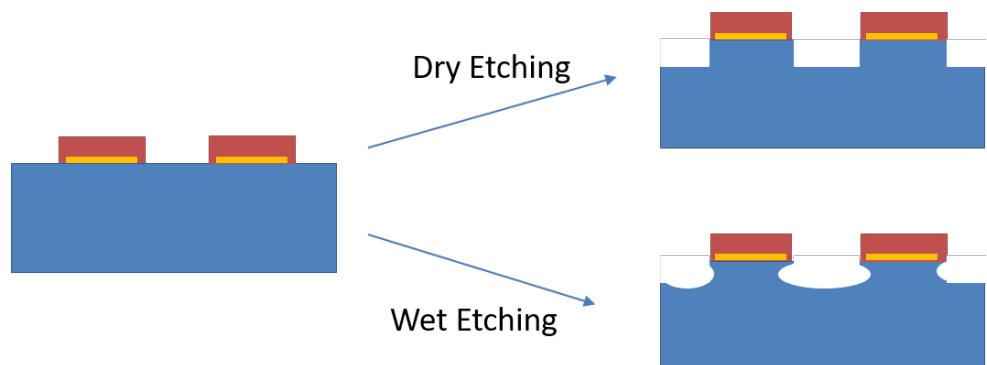


Figure 4.2: Schematic of the different etching techniques available for semiconductor processing.

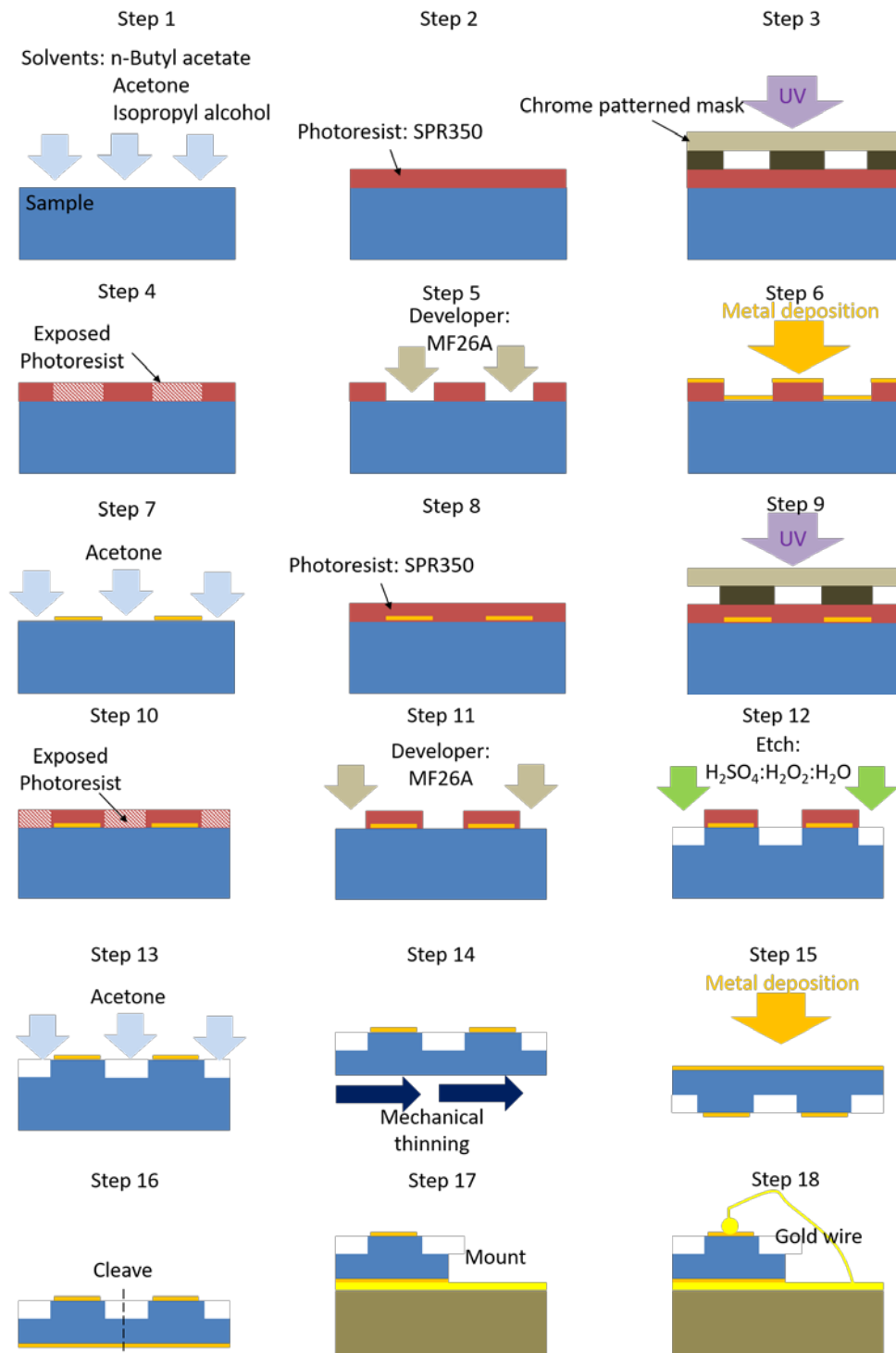


Figure 4.3: The multiple fabrication steps required to process semiconductor wafers into mesa diodes and Fabry-Perot laser devices.

Figure 4.3 shows the steps used to fabricate the devices studied in this thesis. Before depositing photoresist onto the sample, the sample is cleaned with a 3-stage process using heated n-Butyl acetate, acetone and isopropyl alcohol. The use of these three different solvents ensures the removal of any organics present on the surface, leaving the surface in a suitable state for the subsequent steps. The sample is then blown dry using filtered dry nitrogen and checked to see if the surface is clean using an optical microscope. After the surface is confirmed to be clean, the sample is heated to 100°C on a hot plate before placing it on a photoresist spinner and spinning and blowing with filtered dry nitrogen, which removes any water still present, and removing any particulates that might be present on the surface. The first step is to define the top metallic contacts with the sample now ready for the deposition of the photoresist. To aid with the adhesion of the photoresist, hexamethyldisilazane (HMDS) is spun onto the sample at 4000 RPM for thirty seconds, followed by polymethylglutarimide (PMGI), which aids with the lift-off process, followed by a seven-minute hard bake at 180°C. Following this bake, the sample is returned to the spinner and SPR 350 photoresist is added, followed by a spin at 4000 RPM for thirty seconds, yielding a photoresist thickness of 1-2 μm . The sample is then soft baked for one-minute at 100°C. After the sample is coated with the photoresist, the edge bead is removed by overexposure of the edges whilst the rest of the sample is covered. The sample is placed in the developer where the exposed photoresist is removed. The edge bead is where the photoresist is thicker at the edges of the sample, if this edge bead is not removed the sample will have an uneven coating of photoresist possibly causing the sample to stick to the mask and/or increasing the distance between the mask and the sample. After the edge bead has been removed, the sample is ready for patterning using the mask aligner. A mask with the desired pattern is held in place by a vacuum and the sample is placed directly underneath. Using X, Y, Z positioning and rotation the mask pattern is aligned with the sample. After alignment, the sample is exposed for 12 seconds to ultra-violet (UV) light of wavelength of 300 nm and developed for one-minute using MF26A developer. The developed sample is checked under a microscope to ensure that all the exposed photoresist has been removed and that small features are not under or overexposed. If any problems are

identified then the sample can be cleaned and the process repeated. The next step is to deposit contacts on to the sample but this first requires the removal of the native oxides by immersion for 30 seconds in a 1:19 ammonia:deionised water solution. After the oxide removal, the sample is loaded into a bell jar evaporator to deposit the top contact layer. To measure the thickness of the deposited metals a quartz crystal monitor is used to determine the deposition rates and thicknesses. The top contact layer comprises 5 nm of gold, followed by 10 nm of zinc and finally a second 200 nm of gold. This combination produces an Ohmic contact for p-type GaAs. The deposited metals cover the entire sample but some areas have photoresist and others do not. The sample is placed in acetone to remove the photoresist, therefore removing the deposited metal on top of the photoresist, leaving behind the metal in direct contact with the semiconductor. Acetone removes the SPR 350 photoresist but not the PMGI, which is removed by dipping the sample for one-minute in 100°C EKC830 resist stripper. After all of the photoresist and PMGI has been removed, only the metal contact pattern remains on the surface of the sample.

The next step in the fabrication is to define and isolate the devices; this is achieved by etching away the semiconductor material between the devices. Before etching, the sample is again coated with photoresist using the same process as before, except that the PMGI is not needed. Determining the thickness of the photoresist is important to ensure the correct etch depth; this is achieved by using a Dektak surface profiler. The samples are wet etched with sulphuric acid, hydrogen peroxide and deionized water in a ratio of 1:8:80. All samples are etched completely through the active region. After achieving the required etch depth, the sample is cleaned using the 3-stage process. If a broad area laser is being fabricated the sample is thinned by mechanical thinning to reduce the thickness of the substrate to 150 μm ; this aids the formation of high quality cleaved mirror facets and also thermal management of the devices as the thinner the substrate the easier it is to remove the heat produced. If a mesa diode is being fabricated, there is no need to thin the sample. After the thinning process, the sample is carefully cleaned and the native oxide is removed prior to back contact deposition using a 1:19 solution of ammonia:deionized water. The back contact layer comprises of 10 nm of indium-germanium and 200 nm

gold, this gives an Ohmic contact for n-type GaAs. The thickness of the deposited metals is again determined using a quartz crystal monitor. After the back contact is deposited, the samples are annealed at 360°C for thirty seconds to produce an Ohmic contact. Annealing causes intermixing at the metal-semiconductor interface, reducing the height of the metal-semiconductor potential barrier. The samples are now ready to scribe to produce isolated devices. For the broad area lasers a number of different cavity length devices can be produced but for this thesis, only 8 mm and 4 mm devices were studied. The devices are mounted onto a gold-coated ceramic tile with indium epoxy and connected using gold wire and a ball wire bonder. Figure 4.4 shows a typical IV characteristic of a mounted device and the inset of figure 4.4 shows a mounted broad area laser on a ceramic tile.

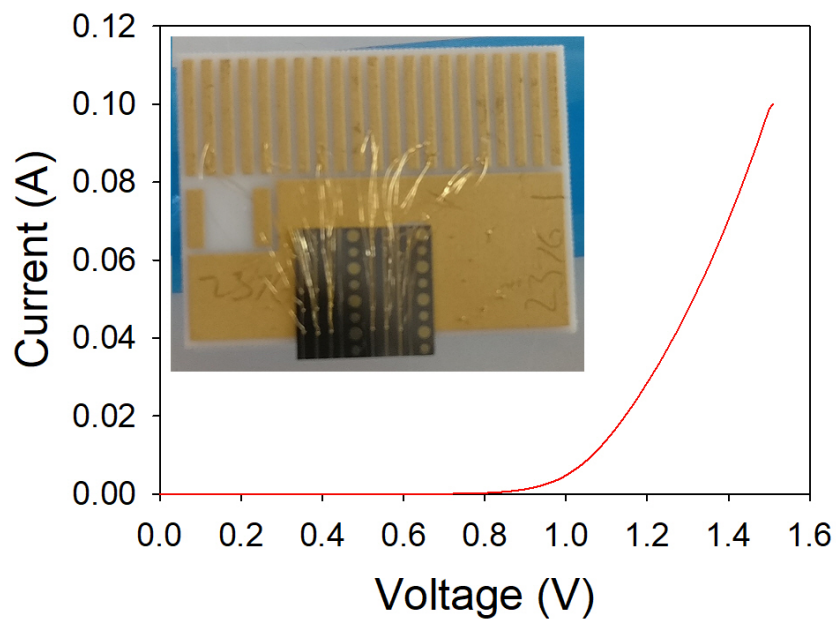


Figure 4.4: Typical IV measurement of a mounted device, the inset shows an image of a mounted broad area laser on a ceramic tile.

4.4 Electroluminescent Mesa Diodes

To study further possible reasons for the difficulties experienced in attaining a room temperature laser and further the work presented in section 3.5, where the use of strain balancing is discussed, mesa devices fabricated from the 50 nm spacer layer sample without strain balancing (sample A) was measured. Table 4.1 summarises the devices studied in chapter 3.

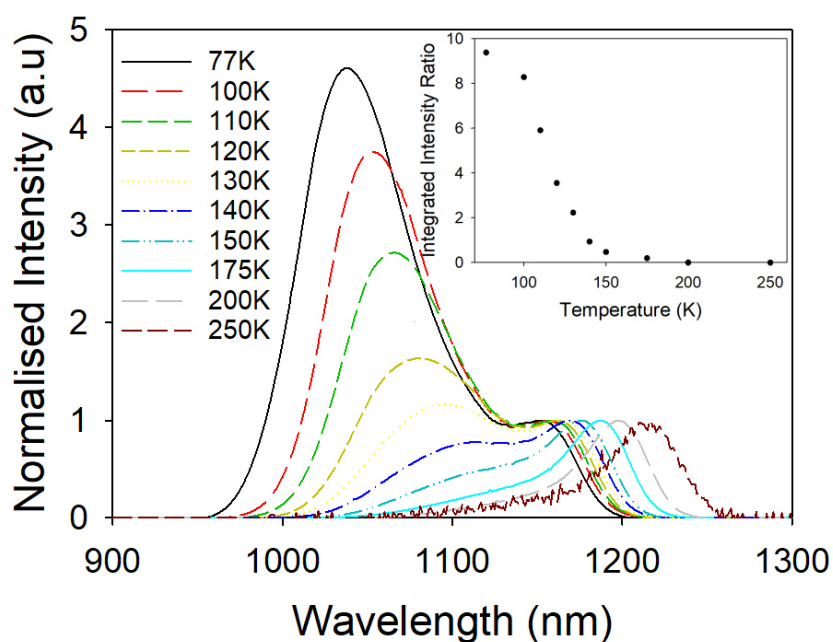


Figure 4.5: Temperature dependence of the EL spectra of sample A using low excitation current. Inset: integrated intensity ratio of the two emission peaks.

Low excitation current 0.1 mA (0.08 A cm^{-2}) EL spectra obtained from sample A are shown in figure 4.5 for a range of temperatures. At these low currents, and particularly at low temperatures, all the QDs will be randomly populated by carriers rather than preferentially occupying the large QDs with deeper confining potentials. The low current ensures that the average dot carrier occupancy is $\ll 1$. The spectra reveal that the QDs have a bimodal size

Sample	Separation	Strain-balancing
A	50 nm	No
A'	50 nm	Yes
B	30 nm	No
B'	30 nm	Yes
C	20 nm	No
C'	20 nm	Yes

Table 4.1: Summary of the strain balancing and reference test devices.

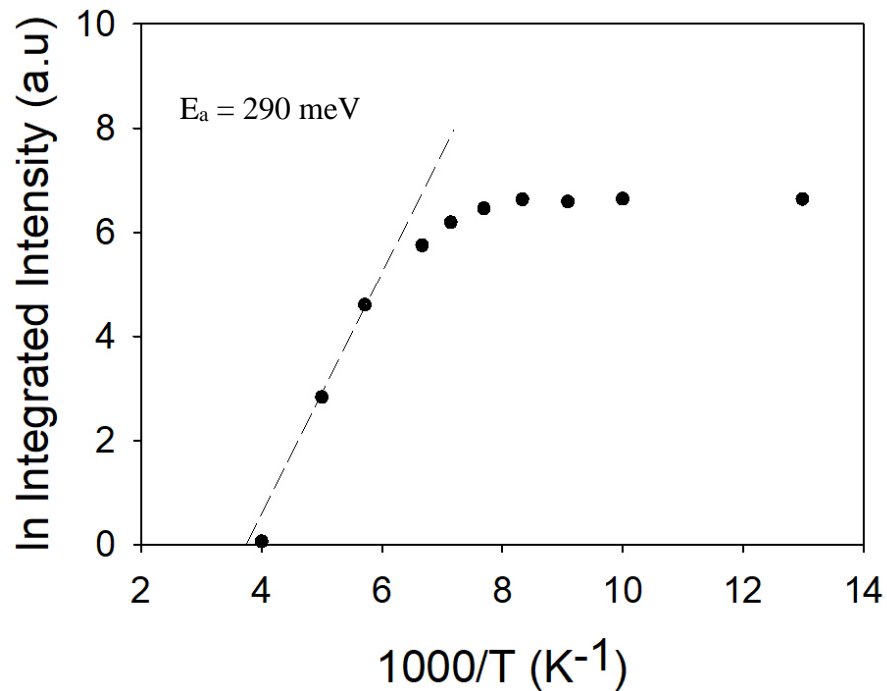


Figure 4.6: Arrhenius plot of the emission from a mesa device fabricated from sample A

distribution. [76], [77] At low temperature (77 K), the emission exhibits two distinct peaks at 1.04 and 1.15 μm reflecting the presence of two subsets of slightly different sized QDs. The long wavelength emitting, larger quantum dots are those required for lasing at 1.3 μm but these appear to have a significantly lower density than the smaller, shorter wavelength emitting QDs. Taking the relative integrated intensities, the shorter wavelength QDs have 9.5 times the intensity of the long wavelength QDs, this factor should give an approximate value for their relative densities. As the temperature is raised, the relative intensity associated with the short wavelength peak is reduced with the longer wavelength peak becoming dominant above 140 K. [78], [79] The inset to figure 4.5 shows the ratio between the short wavelength QDs and the long wavelength QDs over the measured temperature range. Although at high temperatures carriers will transfer preferentially into the long wavelength emitting QDs, these results indicate that the latter subset represent only a relatively small fraction of the total QD density and hence that the available gain close to 1.3 μm will be limited. The bimodal distribution of QDs may occur due to the preferential nucleation on the upper side of step edges as Zhou et al. have observed and Liang et al. have modelled [80], [81]. A similar effect is found in samples A',

B, B', C and C' where two peaks are observed at low temperature, with the high-energy peak reducing in intensity with increasing temperature. The natural log of the integrated emission is plotted against the inverse of the temperature in figure 4.6. The thermal activation energy can be calculated from this graph by fitting the high temperature data to equation 4.1

$$\ln I(T) = \ln(I_0) + \frac{\Delta E_a}{k_b T} \text{ eqn (4.1)}$$

where $\ln I(T)$ is the natural log of the intensity, $I(0)$ is the maximum intensity, ΔE_a is the activation energy, k_b is the Boltzmann's constant and T is the temperature in Kelvin. Using this equation the activation energy is determined to be 230 meV (± 15 meV). This error arises from the fitting procedure but as only a few data points are available, additional data from higher temperatures may give a slightly different value. Taking the average wavelength of the QD emission to be 1100 nm, corresponding to an energy of 1.13 eV, the addition of 230 meV gives a total energy of 1.36 eV. This is less than the bandgap of GaAs at low temperature and so most likely represents a state associated with the wetting layer and/or InGaAs quantum well.

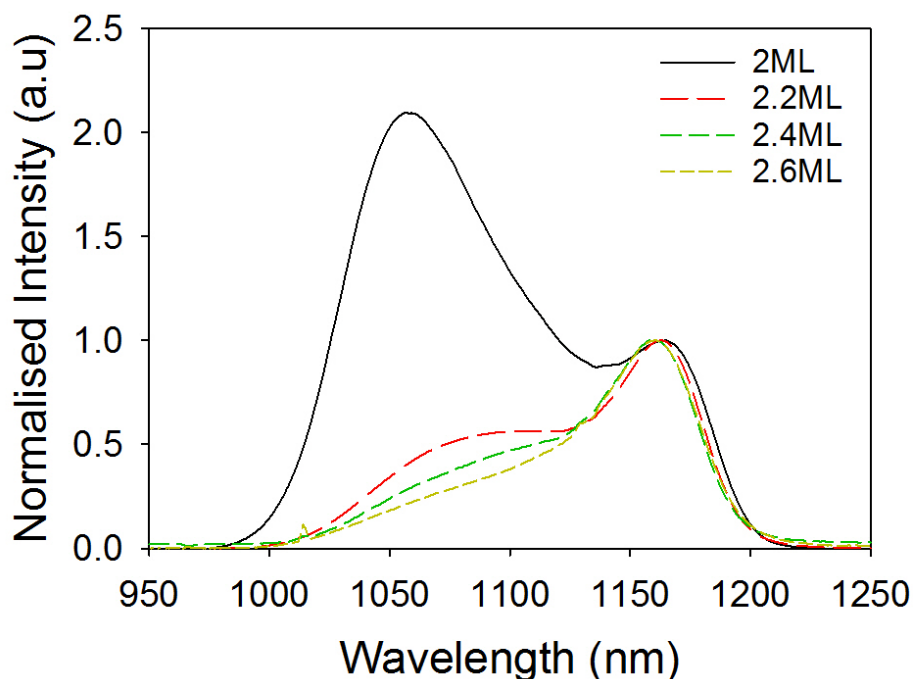


Figure 4.7: Low temperature normalised EL as a function of wavelength for different InAs coverages to give a reduction in QD bimodality.

To achieve room temperature ground state lasing close to 1.3 μm the bimodality of the QDs needs to be reduced. This can be achieved by depositing additional InAs to help ripen the QDs. Low temperature and low current EL spectra of samples grown with different amounts of deposited InAs are shown in figure 4.7. Increasing the amount of InAs from 2 to 2.6 MLs results in a significant reduction of the bimodality, with the emission now dominated by the longer wavelength emitting subset of larger QDs. Table 4.2 summarises the reduction in the low temperature percentage emission from the short wavelength QDs from 79% to 32% whilst the long wavelength QDs, which are dominant above 140 K, shows an increase from 21% to 68% of the integrated emission intensity. However, this reduction is achieved with a commensurate reduction in overall optical efficiency, probably due to the formation of dislocations due to the large amount of deposited strained material. Compared to the 2 ML sample the integrated EL is reduced by 13 and 91% for the 2.2 and 2.4 ML samples respectively. However, increasing the amount of InAs to 2.2 ML significantly improves the bimodality, with only a slight fall in EL intensity. Further device improvement will require a detailed optimisation of the long wavelength emission, balancing a reduction in the bimodality with the decreasing overall optical efficiency. With additional optimisation of the growth parameters, it should be possible to achieve sufficient gain from the long wavelength emitting QDs to give room temperature ground state lasing at 1.3 μm .

Sample	Short wavelength QDs (%)	Long wavelength QDs (%)	Relative Integrated PL (%)
2.0 ML	79	21	100
2.2 ML	39	61	87
2.4 ML	37	63	9
2.6 ML	32	68	7

Table 4.2: Summary of low temperature EL emission of the percentage of short wavelength dots, long wavelength dots and the relative integrated intensity compared to the 2.0 ML sample.

4.5 Broad Area Fabry-Perot Lasers

This section of the thesis will discuss the principles behind Fabry-Perot lasers, the experimental set-up used to test the fabricated QD lasers and present results obtained from these lasers. A Fabry-Perot laser is based on a cavity with two planar and parallel mirrors (figure 4.8) Light reflects between the two mirrors (reflectivities R_1 and R_2) whilst traveling in a gain medium (gain per unit length g_m). For lasing to occur a population inversion is required, with a large density of electrons in the conduction band and holes in the valence band. A population inversion can be produced by electrically injecting carriers using a forward biased p-n junction. As the current is increased, the amplification also increases and lasing occurs when the gain equals the total cavity losses. At and beyond the threshold for lasing the dominant carrier-photon process is stimulated emission. There are a number of different geometries for Fabry-Perot semiconductor lasers; this work uses the ridge geometry. This structure is very useful for developing new laser active region material, due to the ease and speed of fabrication, as discussed in section 4.3. An additional advantage of ridge lasers is the reduction in current spreading, in comparison to stripe lasers, as etching isolates the device, forcing all the injected current to pass through the active region. This makes calculation of the threshold current density (J_{th}) easier. In studying lasers, it is often helpful to measure devices with different cavity lengths. This can allow a determination of the optical losses within the cavity and the use of long cavity lengths may be needed if the maximum gain of the active material is low. Whilst the photons are confined along the cavity by the end mirrors and transverse to the cavity by the etched surfaces of the

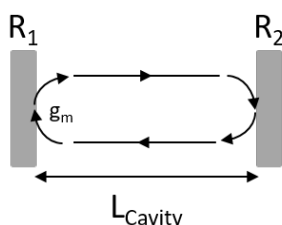


Figure 4.8: Schematic of a Fabry-Perot cavity.

ridge, confinement along the growth direction is also required. In the current devices, the photons are confined in the active region using a simple planar

waveguide structure consisting of $1.5 \mu\text{m}$ $\text{Al}_{0.42}\text{Ga}_{0.58}\text{As}$ cladding layer placed both above and below the active region. The mode produced by this waveguide is designed to overlap as strongly as possible with the gain region of the device, in the present case the QD layers.

Broad area ridge lasers were fabricated from all five samples, as summarised in table 4.1. Sample A was fabricated into a $8 \text{ mm} \times 50 \mu\text{m}$ ridge, sample A' was fabricated into a $4 \text{ mm} \times 50 \mu\text{m}$ ridge, sample B was fabricated into $8 \text{ mm} \times 100 \mu\text{m}$ and $4 \text{ mm} \times 80 \mu\text{m}$ ridges, sample B' was fabricated into $8 \text{ mm} \times 80 \mu\text{m}$ and $4 \text{ mm} \times 50 \mu\text{m}$ ridges. Due to surface roughness caused by defects and dislocations, as discussed in chapter 2, not all of the fabricated devices worked, which has led to the use of two different cavity lengths and three different cavity ridge widths. Devices were tested in an optical cryostat over a range of temperatures, using a pulsed current source with a pulse width of $10 \mu\text{s}$ and a duty cycle of 1% to reduce heating effects. Figure 4.9 shows typical L vs J characteristics measured at 130 K for the 8 mm cavity length devices. Threshold current densities of 50, 125 and 100 A cm^{-2} are obtained for samples A, B and B' respectively. The lowest J_{th} value is obtained for sample A. Reducing the QD layer separation to 30 nm (B and B') increases J_{th} but this increase is less for the sample with the $\text{GaAs}_{0.8}\text{P}_{0.2}$ strain balancing layer

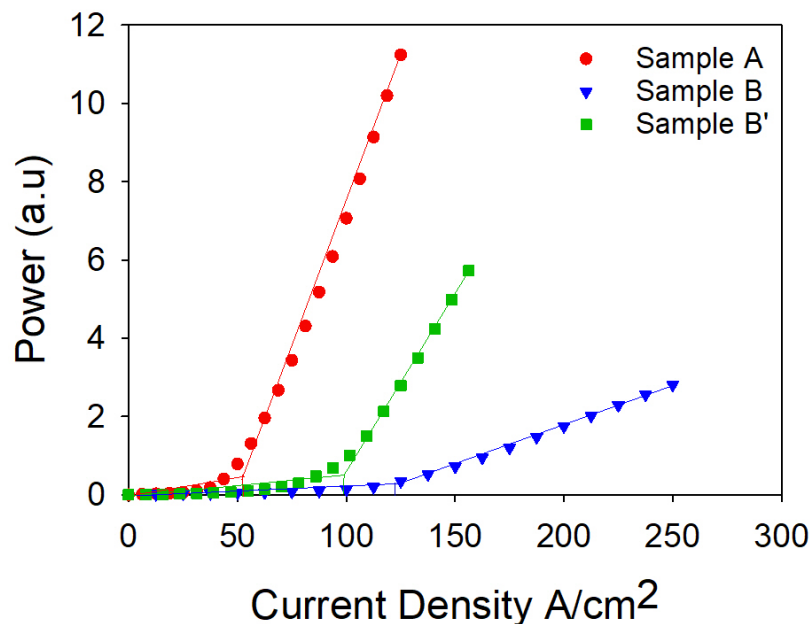


Figure 4.9: Light power output as a function of current density for 8 mm cavity length devices of samples A, B and B' at 130 K.

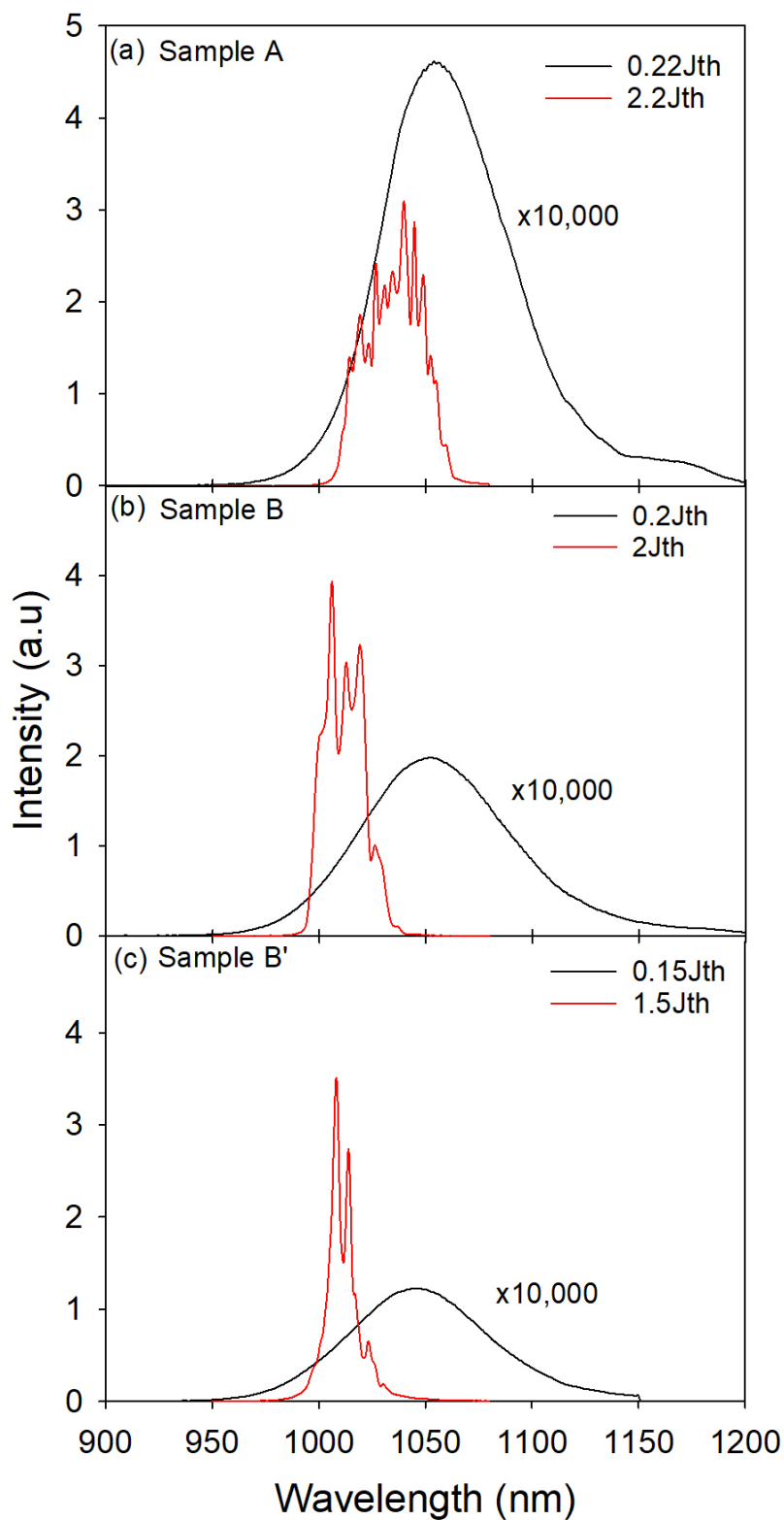


Figure 4.10: Above and below threshold emission spectra at 130 K for the 8 mm cavity length devices of samples A, B and B'.

(sample B') suggesting that its incorporation is beneficial for the device performance and is certainly not detrimental. Figure 4.10 (a), (b) & (c) show emission spectra, recorded below and above threshold at 130 K, for all three 8 mm cavity length devices. All spectra show lasing on the high-energy shoulder of the below threshold emission, indicating that lasing is via an excited state and that there is hence insufficient ground state gain. Comparison to the low current EL spectra of the mesa devices, presented above, indicates that lasing is occurring above the ground state emission of the subset of smaller dots. It is possible that lasing is occurring where different excited states of the two subsets of QDs overlap. Multiple lasing modes are observed due to the non-selective nature of the broad area laser. Figure 4.11 shows typical L vs J characteristics measured at 200 K for the 4 mm cavity length devices. Values of 210 and 290 $A\ cm^{-2}$ are obtained for samples A' and B' respectively. However, this is high when compared to the state-of-the-art for QDs grown by MOVPE of $108\ A\ cm^{-2}$. [39] Reducing the QD layer separation to 30 nm (sample B') increases J_{th} but the device continues to operate at this higher temperature, unlike sample B, which has a highest operating temperature of 190K, where the threshold current density is $260\ A\ cm^{-2}$ (inset of figure 4.12 (c)).

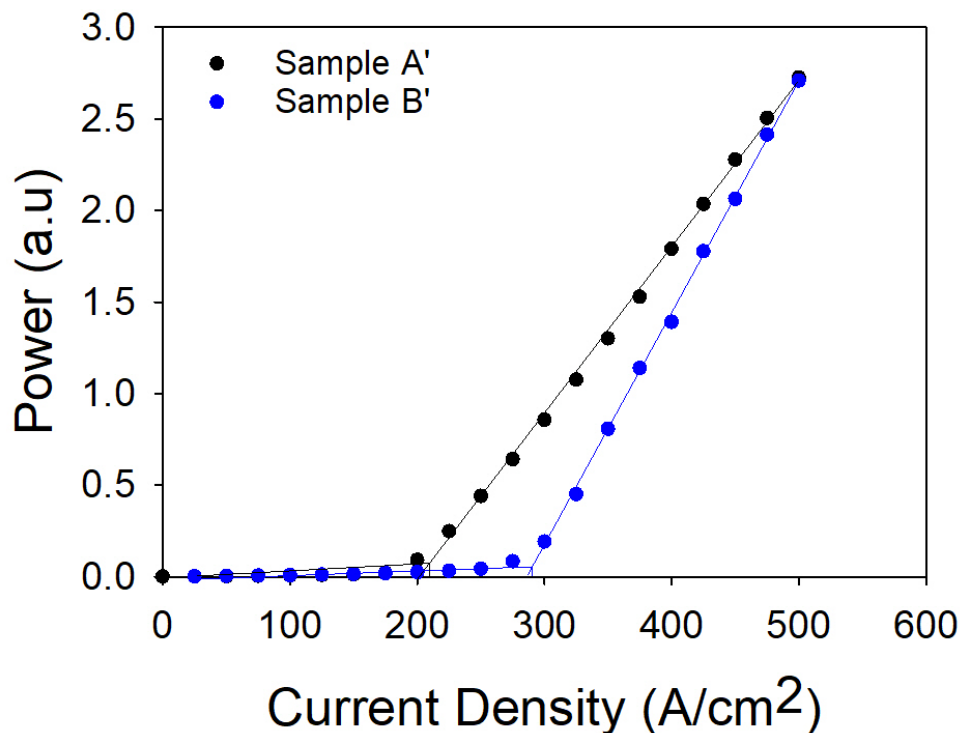


Figure 4.11: Light power output as a function of current density for 4 mm cavity length devices, samples A' and B' at 200 K.

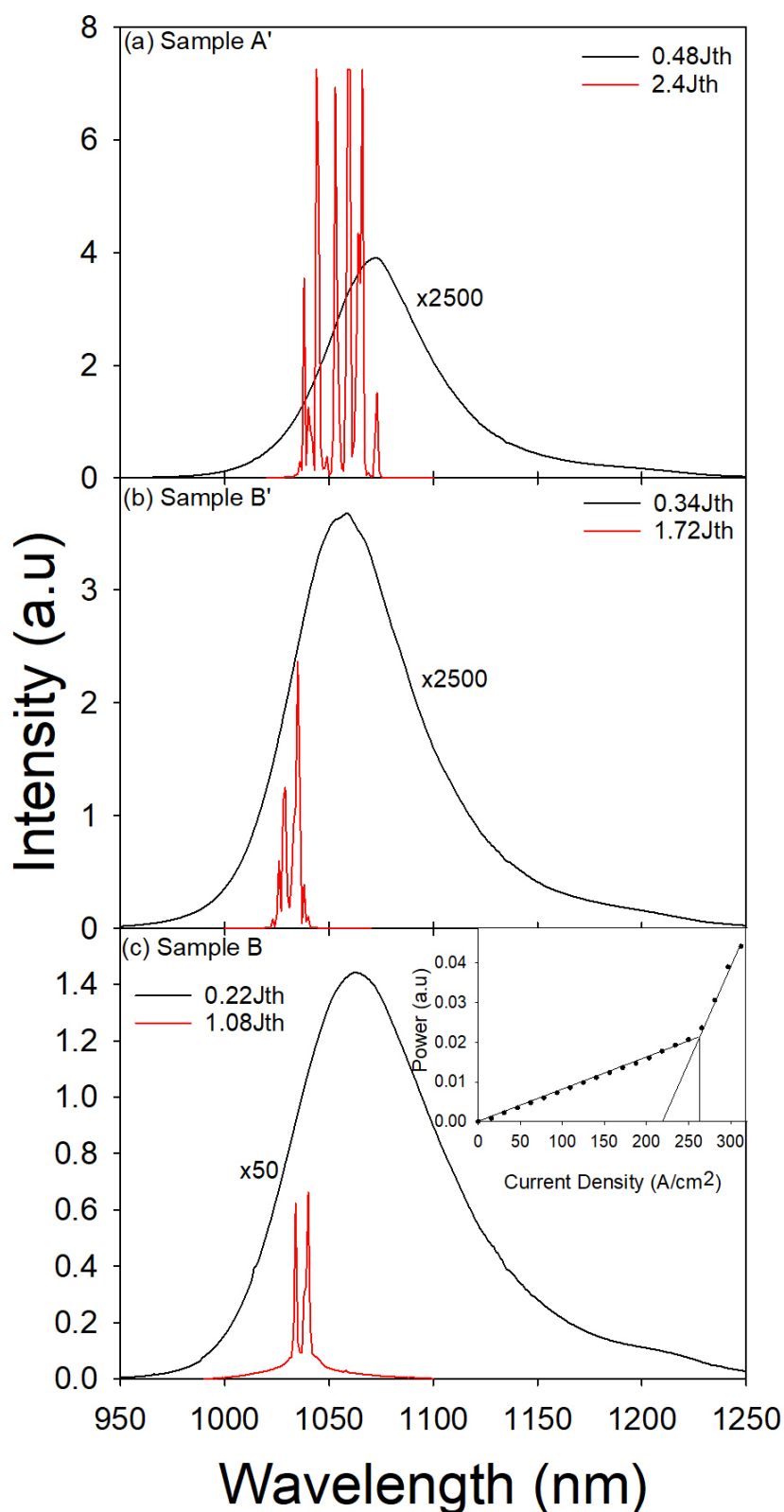


Figure 4.12: Above and below threshold emission spectra at 200 K for 4 mm cavity length devices, samples (a) A' and (b) B'. (c) Above and below threshold emission spectra at 190 K for a 4 mm cavity length for sample B with (inset) light power as a function of current for 4 mm cavity length devices of sample B at 190 K.

This suggests that the GaAs_{0.8}P_{0.2} layer is beneficial for a QD layer spacing of 30 nm but that further work is needed to achieve the device quality obtained for 50 nm spacing. Emission spectra recorded below and above threshold at 200 K for samples A' and B' and 190 K for sample B are shown in Figure 4.12 (a), (b) & (c) respectively. Again all spectra show lasing on the high-energy shoulder of the below threshold emission, consistent with lasing via an excited QD state. Figure 4.13 shows the temperature variation of J_{th} for all the devices studied. All 8 mm cavity length samples exhibit a minimum J_{th} around 125 K due to inter-QD carrier transfer as the temperature increases, as discussed in section 4.2. For the 8 mm cavity length samples the highest temperatures that lasing is achieved is 220 K for sample A and 200 K for samples B and B'; limited by the maximum output of the current source. Over the studied temperature range; J_{th} is always lower for sample B' than for sample B, providing further confirmation that the addition of the strain compensating GaAs_{0.8}P_{0.2} layer is beneficial for device performance as the QD layer separation is reduced below 50 nm. [82] To achieve higher current densities from the same current source the cavity length of the laser has to be reduced. For the 4 mm cavity length samples the highest temperatures that lasing is achieved is 240 K for sample A', 200 K for

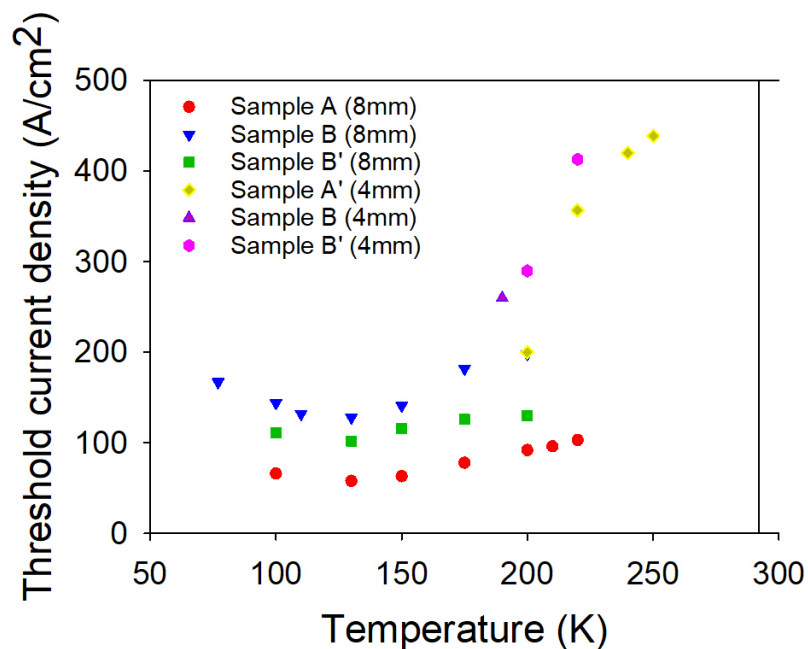


Figure 4.13: Threshold current density as a function of temperature for samples A, A', B and B' for 8 mm and 4 mm cavity length devices.

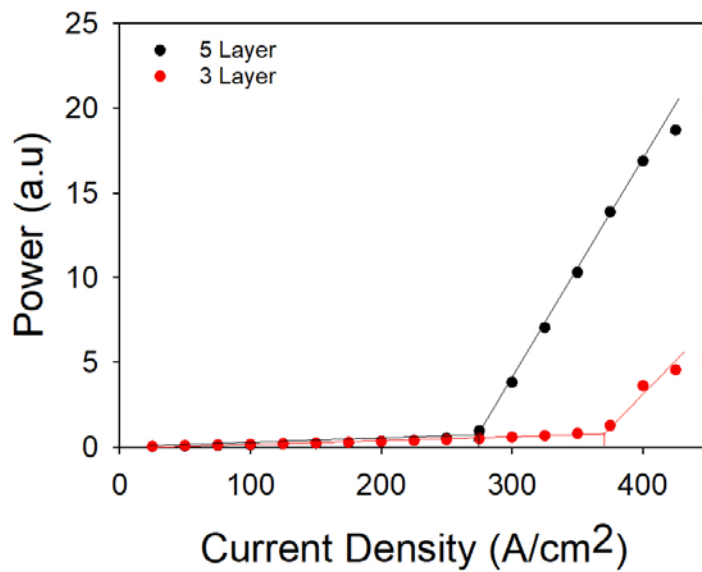


Figure 4.14: Light power as a function of current for 4 mm cavity length devices at room temperature.

sample B and 220 K for sample B'. Again, the incorporation of the strain compensating $\text{GaAs}_{0.8}\text{P}_{0.2}$ layer is seen to improve the performance of the 30 nm QD spacer layer device. Adding high reflectivity coatings to the laser facets will reduce J_{th} and could allow room temperature operation of the present devices. Sample C' (20 nm QD layer separation with a strain compensating $\text{GaAs}_{0.8}\text{P}_{0.2}$ layer) was also fabricated into laser devices. However, it was not possible to achieve lasing at any temperature and for any of the cavity lengths (4 and 8 mm) studied.

4.6 Further Quantum Dot Laser Development

Based on the growth developments described so far, further modifications to the growth were attempted, where the V/III ratio was reduced from 208 to 5. Lowering the V/III ratio will reduce the defect density, reducing the number of non-radiative recombination centres. However, reducing the V/III ratio too far will result in a low QD density, allowing larger QDs to form due to the increase in migration length of the indium. [10], [21], [83], [84] The reactor pressure was reduced from 100 to 50 Torr, lowering the reactor pressure has been linked to uniformity improvement, reducing circulating currents and reducing parasitic reactions. [85] The growth of these new structures was performed by Mr Brett Harrison. All previous growth parameter are the same as previously discussed, where the InAs coverage is 2 ML and the growth rate is 0.18 ML/s. Using these modified growth parameters, two new structures were grown in an attempt to obtain a room temperature laser: a five QD layer and three QD layer device with a 50 nm GaAs spacing layer. The photons are confined in the active region using a simple planar waveguide structure consisting of 1.5 μm $\text{Al}_{0.42}\text{Ga}_{0.58}\text{As}$ cladding layer placed both above and below the active region as used in previous structures discussed above. However, no strain balancing with $\text{GaAs}_{0.8}\text{P}_{0.2}$ was attempted. Broad area lasers were fabricated with 4 mm x 50 μm ridges. Figure 4.14 shows typical $L_{\text{vs}}J$ characteristics measured at room temperature (300 K) for the three and five QD layer devices. J_{th} values of 378 and 281 A cm^{-2} are obtained for the three QD layer and five QD layer devices respectively. The lowest J_{th} value is obtained for the five QD layer device. Emission spectra recorded below and above threshold at room temperature are shown in Figure 4.15 (a) and (b). All spectra show lasing on the high-energy shoulder of the below threshold emission, indicating that lasing is via an excited state and that there is insufficient ground state gain. Multiple lasing modes are observed between 1110 to 1136 nm for the five QD layer device and 1082 to 1094 nm for the three QD layer device, due to the non-selective nature of the broad area laser. Successful room temperature lasing has been achieved but more development is needed to obtain ground state room temperature lasing, for example increasing the number of QDs with a ground state that emits at 1.3 μm at room

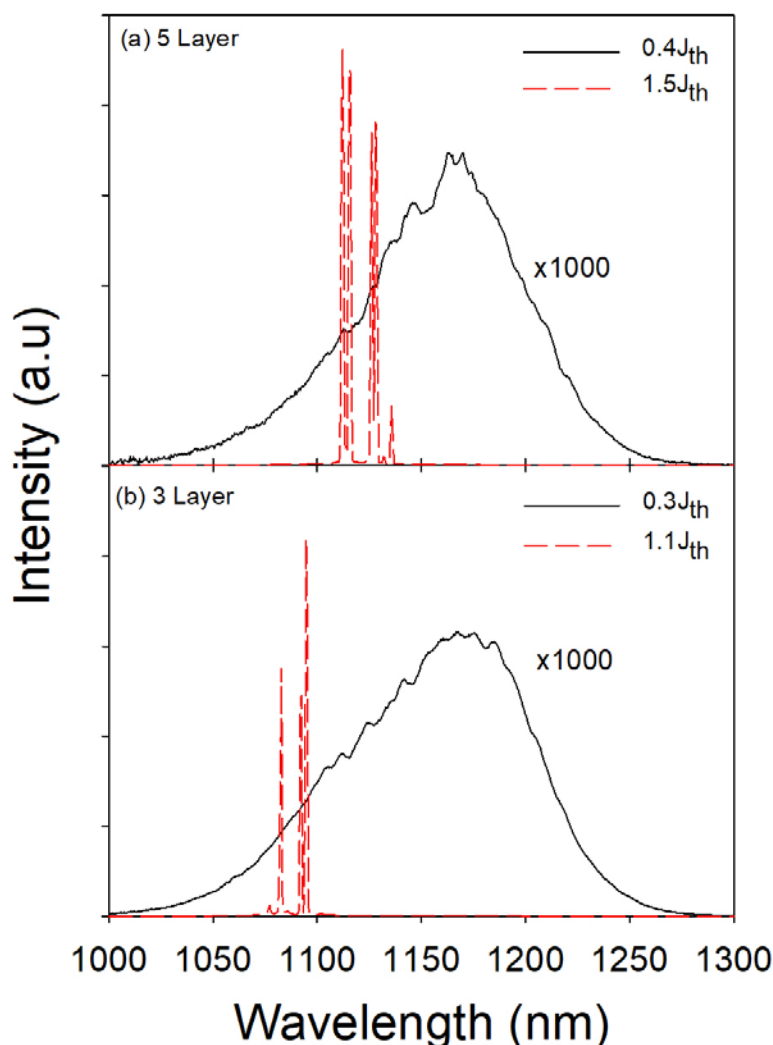


Figure 4.15: Above and below threshold emission spectra at room temperature for 4 mm cavity length devices.

temperature. However, as a room temperature laser has been achieved the next step would be to add the $\text{GaAs}_{0.8}\text{P}_{0.2}$ strain-balancing layer and to reduce the QD layer separation.

It is useful at this point to compare the threshold current density, lasing wavelength and operating temperature obtained for the samples discussed above with MOVPE grown InAs/GaAs QD lasers reported in the literature. The lowest reported threshold current density is 108 A/cm^2 for a ground state laser emitting at 1180 nm for a device contained three QD layers with an InGaAs strain-reducing layer; the laser continued operating up to 80°C . [46] However, higher current densities are more typical for MOVPE grown QD lasers operating at longer wavelengths. For a lasing wavelength of 1240 nm, the reported threshold

current density is increased to 200 A cm^{-2} at room temperature; this device also contains a strain-reducing layer. [42] Increasing the wavelength even further (1302 nm), the threshold current density was reported to be 333 A cm^{-2} . However, this was reduced with the introduction of an antimony surfactant to 111 A cm^{-2} and a slight increase in wavelength to 1308 nm, both samples again contained a strain-reducing layer. [44]

The highest operating temperature for the QD laser devices reported in this thesis is room temperature (300 K), with a threshold current density of 281 A cm^{-2} and emission at 1100 nm for five QD layers without strain reducing layers. The highest operating temperature for a device with a strain-balancing layer was 240 K, with a threshold current density of 420 A cm^{-2} and emission at 1068 nm. The lowest threshold current density achieved was 50 A cm^{-2} at 130 K for a lasing wavelength of 1050 nm (sample A). None of the devices fabricated and studied in this thesis contained an InGaAs strain reducing layer or QW, which should give a significant red shift of the lasing wavelength. In addition, studies of MBE grown QDs have shown that growing InAs QDs on InGaAs can increase their density; applied to the present devices this could allow ground state lasing which would also red shift the emission. Hence, further studies should investigate the addition of an InGaAs layer to red shift the lasing close to 1300 nm. However, this would increase the amount of compressively strained material, requiring a greater degree of strain balancing by the $\text{GaAs}_{0.8}\text{P}_{0.2}$ layer.

4.7 Photonic crystal laser modelling

The laser devices discussed so far are all standard edge emitting Fabry-Perot structures, which are quick and simple devices used for initial investigation of the material quality. For a Fabry-Perot laser the light propagates in the plane of the epitaxial layers and is reflected by parallel-cleaved facets. Photon confinement along the growth axis is achieved using the refractive index contrast provided by the epitaxial layers. Such structures are relatively easy to grow and fabricate but have a number of drawbacks. These include: relatively high and asymmetrical beam divergence, inplane emission, making the fabrication of two dimensional arrays difficult, and multi wavelength mode lasing. In addition, the facet reflectivity is fixed unless post growth coatings are applied. Therefore, it is useful to investigate different, novel designs to improve the QD laser structures.

This section discusses the modelling and background to photonic crystal surface emitting laser (PCSEL), a relatively new type of semiconductor laser. Such lasers offer the possibility of vertical emission, very low beam divergences, as low as 1 degree, beam steering, high power single mode operation and wavelength selectivity. A PCSEL uses a photonic structure, which consists of a periodic variation of the refractive index, to control the photonic properties. Such structures are one of a class of relatively new devices where both the properties of electrons and holes and photons are controlled, offering the possibility of improved or new and novel devices. The following provides a

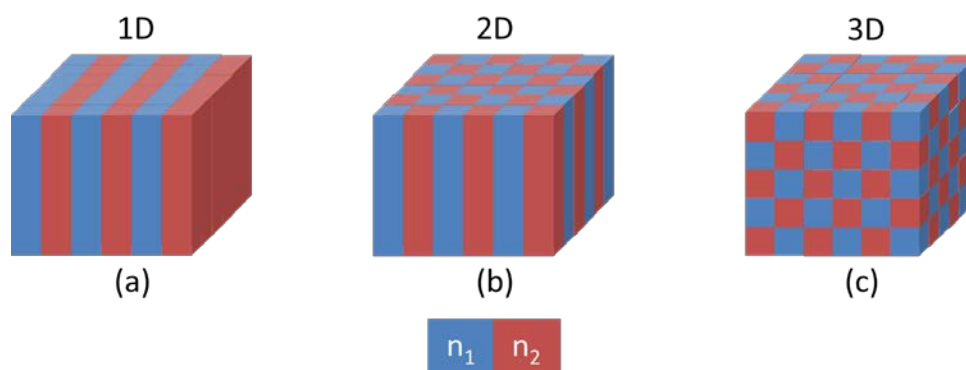


Figure 4.16: Schematic of a one, two and three-dimensional photonic crystal.

brief introduction to photonic crystals before the properties, fabrication and study of PCSELS are discussed in more detail.

The properties of charge carriers in a solid are modified by the periodic nature of the crystal structure. Probably the most obvious and important consequence of this modification is the presence of band gaps in a semiconductor, within which electron energies are forbidden. The analogous structure for photons is a periodic variation of the refractive index, which can be achieved by using two different semiconductors or a semiconductor and air. It is possible, in principle, to construct 1D, 2D or 3D photonic crystals (see Fig 4.16) although a true 3D crystal for visible or near-IR light is still challenging.

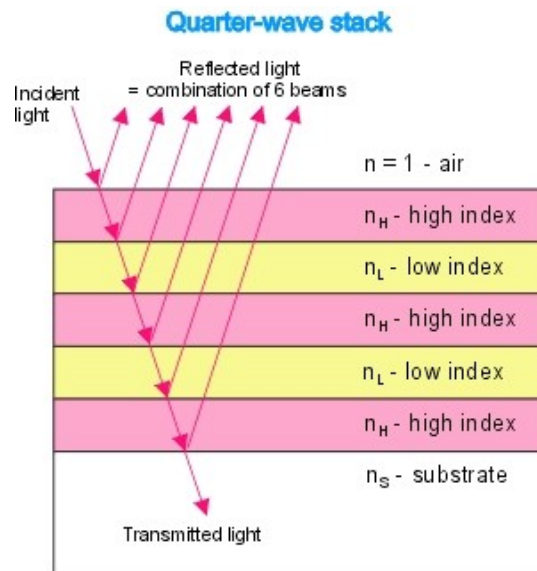


Figure 4.17: Schematic of a 1 D Bragg stack with alternating high and low refractive indexes, showing the incident wave with small-reflected waves at each index change. [86]

The simplest photonic crystal is a 1D Bragg stack, which consists of an alternating sequence of two planar semiconductor layers. Such structures can be readily grown by standard epitaxial techniques. Figure 4.17 shows a typical 1 D Bragg structure. [86] Each layer has a thickness equal to one quarter of the wavelength within the semiconductor. Hence each successive ray travels an additional distance of $\lambda/2$ which, when added to the π phase shift at alternate interfaces, gives a 2π total phase shift between successive reflected rays. Although the reflectivity at each interface is small, due to the relatively small refractive index difference between the two semiconductors, all the reflected rays combine constructively and for a large number of pairs of layers very high reflectivities are achieved. This high reflectivity occurs only across a narrow

range of wavelengths but can be considered to be analogous to the band gap in a semiconductor, giving a small range of wavelengths where photon propagation is not possible. Two Bragg stacks are often used to form an optical cavity where they are separated by a distance equal to an integer number of half wavelengths (this is equivalent to a single Bragg stack with an added defect). Photons matching the cavity mode are strongly confined within the cavity and very high Q-factors are possible. Related to this 1D cavity is the vertical cavity surface emitting laser (VCSEL) where an emitting medium, typically quantum wells, is placed within the cavity close to an anti-node. Photons are emitted into a very low loss cavity although one of the Bragg mirrors must have a slightly lower reflectivity to allow laser light to escape.

A Bragg stack only produces a band gap for photons propagating along the growth direction. Further photonic control is achieved using a 2D photonic crystal. Here an epitaxial semiconductor layer is patterned, typically using e-beam lithography, and then etched to form a periodic array or air holes. The refractive index contrast between air and the semiconductor (in some structures the holes are subsequently filled with a different material or semiconductor) produces the photonic crystal. With careful design of the hole size and pattern it is possible to achieve a photonic bandgap for any inplane propagation direction. A 2D cavity can be formed by removing one or more of the holes, effectively surrounding an unpatterned region with high reflectivity mirrors in all directions – see figure 4.18. Such cavities have a number of applications.

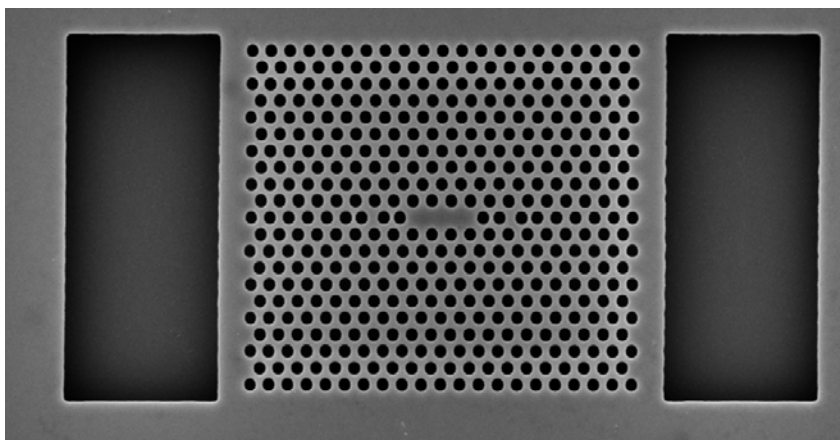


Figure 4.18: SEM image of a periodic photonic crystal with a cavity to localise the electric field. Image courtesy of Dr. B. Royall University of Sheffield Department of Physics and Astronomy.

These include enhancing the spontaneous emission rate of an emitter (e.g. a QD) placed in the cavity by modifying the density of states into which photons are emitted, known as the Purcell effect.

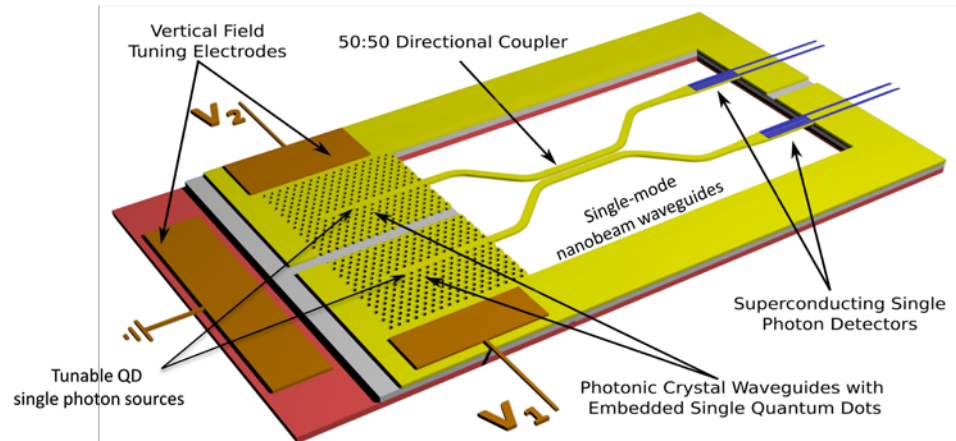


Figure 4.19: Schematic of two single photon source using a photonic crystal to couple photons into the waveguide to study photon interaction. Image courtesy of Prof. M. Fox, University of Sheffield, Department of Physics and Astronomy.

In addition, removal of a line of holes can produce a waveguide along which photons can propagate. Figure 4.19 shows a proposed structure to study the interference of single photons emitted from two QDs.

The QDs are placed within cavities formed in the photon crystal so that the emitted photons are ‘captured’ and directed along the photonic crystal waveguides into a 50:50 directional coupler.

A band gap for photons propagating in any direction requires a true 3D structure but such structures are very challenging to fabricate for visible or near-IR photons due to the small feature size required. As a result, hybrid 2D-3D structures are used where there is no periodicity along the third direction but a waveguide is formed either by placing the semiconductor between layers of a

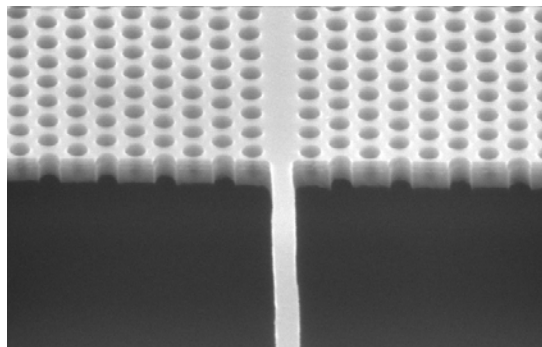


Figure 4.20: SEM image of a suspended photonic crystal with a waveguide. Image courtesy of Dr. B. Royall, University of Sheffield, Department of Physics and Astronomy.

second semiconductor with a lower refractive index or by removing the semiconductor above and below the photonic crystal to give an air-semiconductor-air membrane. The waveguide restricts most photons to propagate in the plane of the semiconductor where the 2D photonic crystal is able to generate a band gap (high reflectivity) for any propagation direction. – See figure 4.20.

Photonic crystals have obvious applications in semiconductor lasers, for example allowing significantly greater control of the mirror geometries and reflectivities than is possible via cleaved facets. The example of 1D Bragg stacks in a VCSEL has already been discussed. Figure 4.21 shows predicted properties of three very different laser designs: a VCSEL, utilising two 1D Bragg stacks, a traditional Fabry-Perot edge emitting laser utilising cleaved

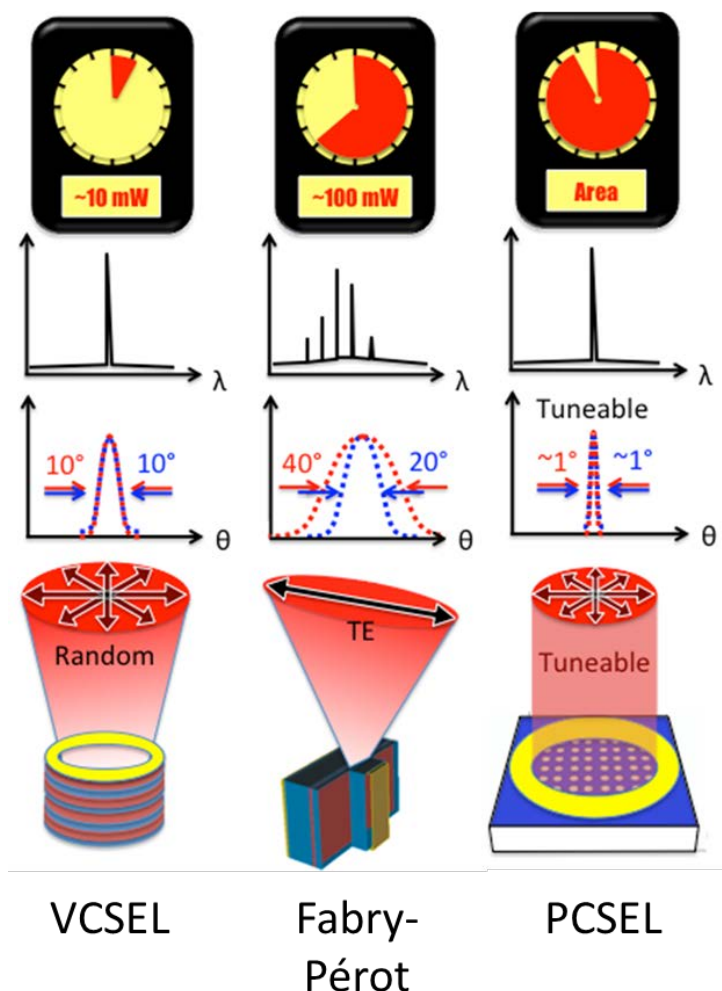


Figure 4.21: Schematic showing the maximum potential power, single/multi-mode operation, the beam divergence and type of polarisation that can be obtained. Image courtesy of Dr. D. Williams, University of Sheffield Department of Electronic and Electrical Engineering.

facets and a PCSEL which uses a 2D photonic crystal. Potential advantages of the latter design include area-power scaling, single mode lasing, very low beam divergence and controllable polarisation. [59], [87]–[89]

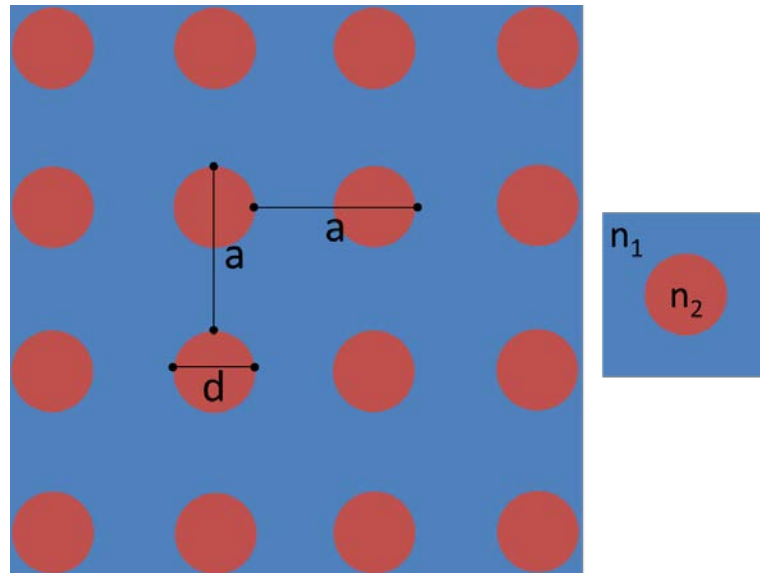


Figure 4.22: Schematic of a two-dimensional square lattice photonic crystal.

In a PCSEL a 2D photonic crystal creates a photonic band gap for all inplane propagation directions. One of the challenges with these devices is to ensure laser light can be sufficiently coupled vertically out of the structure. This occurs via diffraction but careful control of the lasing mode is required. For example, of the four inplane modes at the Γ -point of the photonic crystal, the two that give an electric field symmetrical about the holes couple strongly to modes external to the cavity but this high loss results in very high threshold current densities and in practice these modes never lase. The other two modes, which have an electric field anti-symmetrical about the holes, couple much more weakly, this results in useable threshold current densities but careful design of the lattice is required to ensure sufficient coupling occurs. The following studies use a square lattice, which has been previously determined as the optimum for high power lasers. This lattice is defined in figure 4.22.

The unit cell of this crystal is shown in the inset where the “atom” shape is defined, for this thesis only circular holes are considered. The fill factor is the ratio of the amount of each material and is defined by equation 4.2

$$ff = \pi \left(\frac{d}{2} \right)^2 / a^2 \quad \text{eqn (4.2)}$$

where d is the diameter of the holes and a is the lattice spacing. For all of the photonic crystals modelling in this thesis a 50% fill factor is used. The vertical thickness of the photonic crystal for optimal Bragg scattering to give out of plane light emission can be calculated using equation 4.3

$$T = \frac{(2m - 1)\lambda_0}{2n} \quad \text{eqn (4.3)}$$

where λ_0 is the wavelength of the light in a vacuum, n is the refractive index and m is a positive integer. In the following, the design of the photonic crystal is taken from previous work and no further optimisation is performed.

To avoid degrading the active material in a PCSEL this material, QDs in this work, is physically separated from the photonic crystal. Gain is provided to the band-edge modes of the photonic crystal via evanescent wave coupling. Two methods can be used to fabricate PCSEL devices, the first method, wafer fusion, is shown in figure 4.23. Wafer fusion is the fusion of two separate wafers to form one wafer. For PCSEL devices, the first wafer consists of the bottom cladding, the active region and the photonic crystal layer, although the latter layer can be on the second wafer. The photonic crystal layer initially consists of a single semiconductor of thickness given by equation 4.3, into which the photonic crystal is subsequently fabricated. The second wafer consists of the

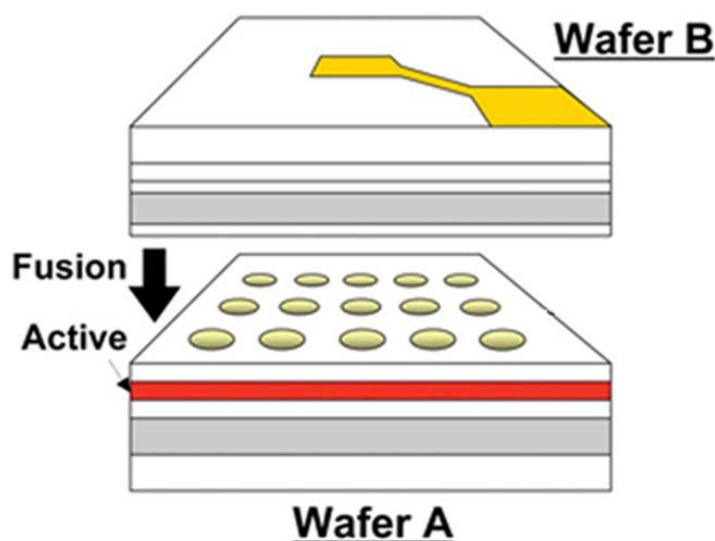


Figure 4.23: Schematic of the wafer fusion process. Image courtesy of Dr. D. Williams, University of Sheffield, Department of Electronic and Electrical Engineering.

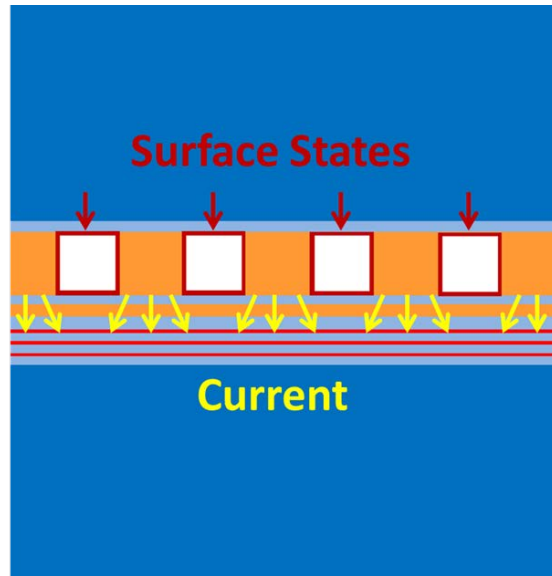


Figure 4.24: Schematic of the issues associated with void photonic crystals. Image courtesy of Dr. R. Taylor, University of Sheffield, Department of Electronic and Electrical Engineering.

top cladding layer and the photonic crystal region if it is not on the first wafer. The two wafers are fused together in an inert atmosphere following the fabrication of the photonic crystal, with this method only void PCSELS can be fabricated. An issue with wafer fusion is their manufacturability and reliability. In addition, with the inclusion of voids there is a non-uniform carrier distribution in the active region, shown in figure 4.24, and spatial variation in the heat extraction. To avoid these issues, an all-semiconductor PCSEL structure was developed at the University of Sheffield based on epitaxial regrowth. [69] In this technique, the wafer is returned to a growth reactor following the fabrication of the photonic crystal, to grow the remaining layers. This allows the voids created by the photonic crystal to be infilled and avoids the difficult wafer-bonding step. In addition, different epitaxial techniques can

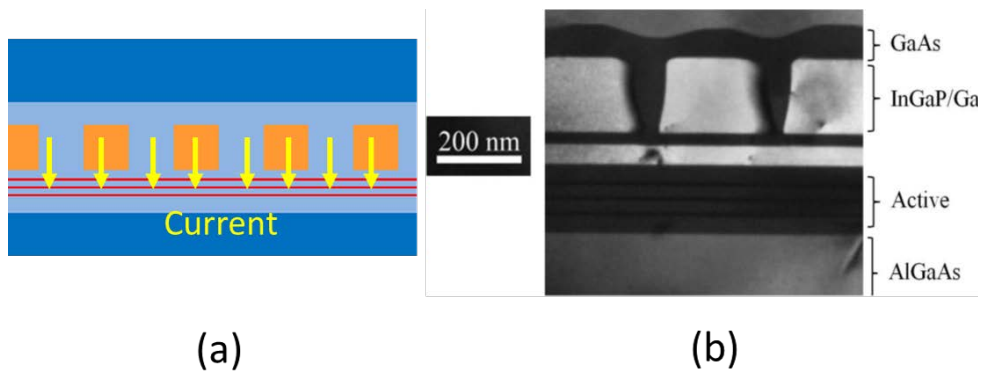


Figure 4.25: Schematic of the all-semiconductor photonic crystal and a TEM image of the fabricated PCSEL. Image courtesy of Prof. R. Hogg, University of Sheffield, Department of Electronic and Electrical Engineering.

be used for the two growth steps. In the first growth step the bottom cladding, active region and photonic crystal layer are deposited. The wafer is then removed from the growth reactor and the photonic crystal patterned and fabricated. Finally the wafer is loaded back into a growth reactor, the photonic crystal region is infilled with a secondary material (InGaP in the current structures), and the top cladding layer is grown. Figure 4.25 (a) shows the more uniform carrier distribution expected in the active region as the InGaP-infilled photonic crystal should allow current to flow unhindered. Figure 4.25 (b) shows a transmission electron microscope (TEM) image of an all-semiconductor photonic crystal with the successful infilling of the GaAs during the overgrowth. When infilling the holes in the photonic crystal it is important to use a semiconductor having a sufficiently large refractive index contrast to the host material. [69]

An important parameter in the design of a PCSEL is the overlap of the vertical cavity mode with the photonic crystal. This can be obtained from modelling of the structure, achieved using the software package FimmWave supplied by Photon Design. For this thesis, only the fundamental mode with transverse electric (TE) polarisation is modelled. The software uses an effective index mode approach, which uses the eigenmode expansion (EME) method to rigorously solve Maxwell's equations to find the form of the optical mode.

Previous work at Sheffield has focussed on the development of 980 nm emitting PCSELS using QWs as the active region and comparing the results for infilled crystals to those of other research groups who have fabricated 980 nm QW PCSELS with void photonic crystals. Williams *et al.* were able to develop an all semiconductor PCSEL emitting at 980 nm. [90] Using an all semiconductor PCSEL can increase the mode overlap with the photonic crystal, improving the coupling coefficient and achieving greater feedback. Figure 4.26 (a) shows the mode profile and refractive index variation for a semiconductor/void photonic crystal; with an active region containing three 8 nm $\text{In}_{0.17}\text{Ga}_{0.83}\text{As}$ QWs with a 20 nm GaAs spacing layer, emitting at 980 nm. This gives a relatively small mode overlap with the photonic crystal of only 5%. Comparing to figure 4.26 (b) an all semiconductor photonic crystal has a mode overlap of 24%. This increase in overlap is due to the reduced refractive index contrast in the in-filled

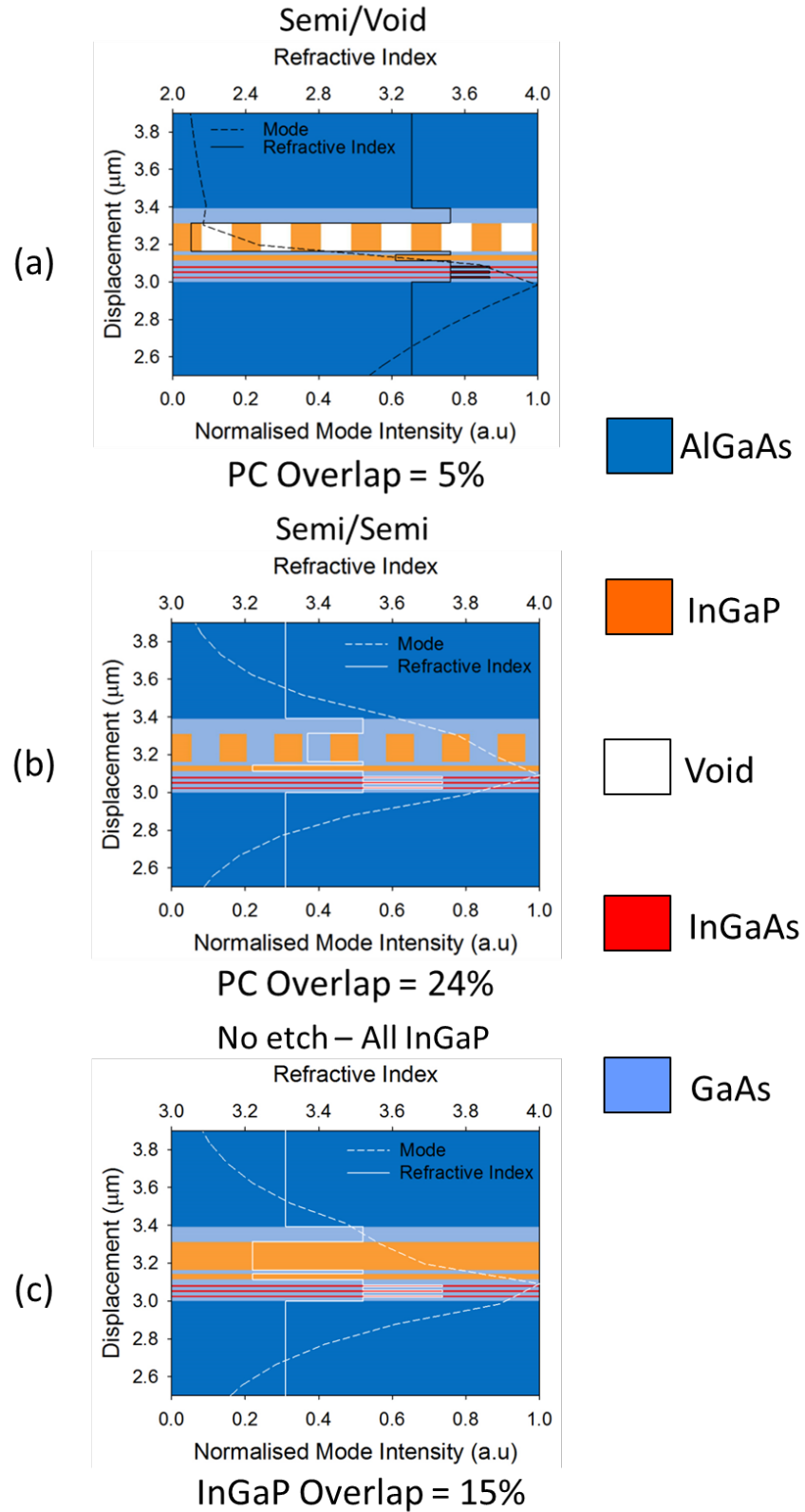


Figure 4.26: Optical mode plots of the void/semiconductor, all semiconductor and edge-emitting laser.

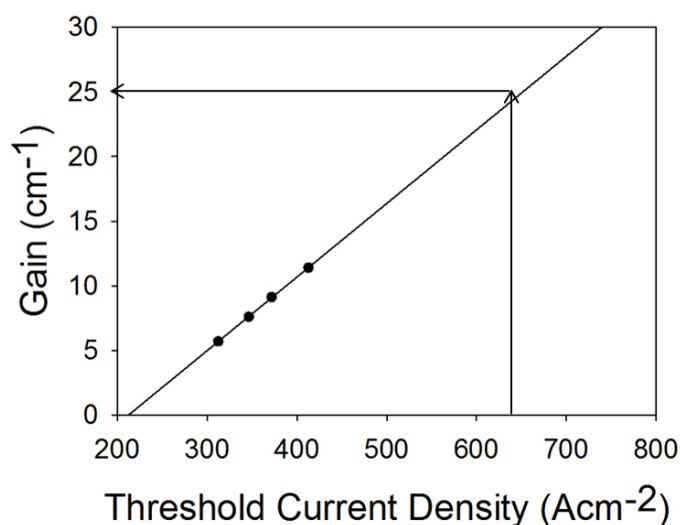


Figure 4.27: Threshold current density plot for multiple cavity lengths of the QW edge-emitting laser.

photonic crystal, which gives a higher average refractive index and hence a reduced difference between the active region and the photonic crystal, allowing the mode to penetrate more into the crystal. The threshold gain is calculated using the experimentally extracted material gain of the QWs. To extract the material gain, the photonic crystal region is replaced by 150 nm of $\text{In}_{0.48}\text{Ga}_{0.52}\text{P}$ and fabricated into broad area lasers with varying lengths. The mode plot of the edge-emitting laser is shown in figure 4.26 (c), where the mode overlap with the QWs is 13%. The material gain and threshold current densities of multiple edge-emitting lasers are plotted in in figure 4.27 for different cavity lengths. To extract the required material gain, previous PCSELS with the same active region were tested. The Threshold current density from this device can be used to extract the required gain by extrapolating the gain versus threshold current density plot. The threshold current density of the previous PCSEL is used to extract the material gain of the PCSEL. The threshold current density for the PCSEL is 650 A cm^{-2} and therefore, the material gain needed for the devices to work is 25 cm^{-1} . This value can be used to calculate the threshold gain (g_{th}) required by the QD-PCSELS to lase by using equation 4.4

$$g_{th} = \frac{g_{old}\Gamma_{QW}}{\Gamma_{PC}} \text{ eqn (4.4)}$$

where g_{old} is the threshold gain for the QW PCSELS devices, Γ_{QW} is the mode overlap with the photonic crystal for the original structure and Γ_{PC} is the mode overlap with the photonic crystal for the new structure.

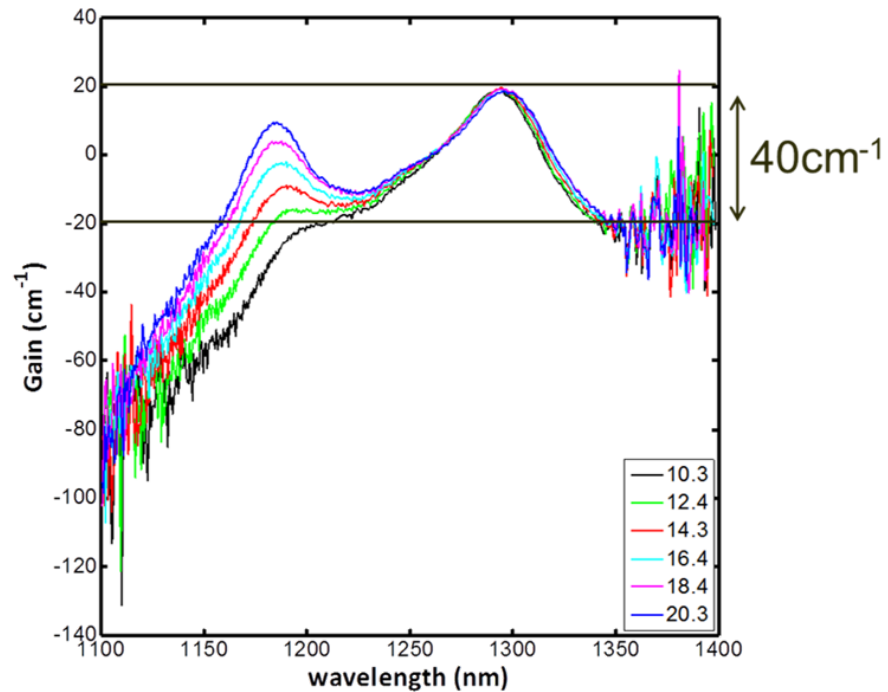


Figure 4.28: Gain plot for the QDs from QD laser Inc. for the development of the QD-PCSEL measured by Dr Negin Peyvast. Image courtesy of Dr. N. Peyvast, University of Sheffield Department of Electronic and Electrical Engineering.

To calculate the net modal gain for the QD PCSELS the material gain of the QD devices needs to be calculated. Figure 4.28 shows gain measurements for the QD material taken at multiple current densities by Dr Negin Peyvast. The material gain is measured to be 40 cm^{-1} at the target wavelength of 1300 nm. The calculated mode profile for an edge-emitting QD laser is shown in figure 4.29, where the mode overlap with the QD layers is calculated to be 11%. Using this value the net modal gain of the QD PCSEL can be calculated using equation 4.5

$$g_{net} = \frac{G_{QD}\Gamma_{QD}}{\Gamma_{active}} - \alpha_i \text{ eqn (4.5)}$$

where G_{QD} is the material gain of the QDs, Γ_{QD} is the mode overlap of the QDs in the PCSEL structure, and Γ_{active} is the mode overlap of the QDs in the laser structure shown in figure 4.29.

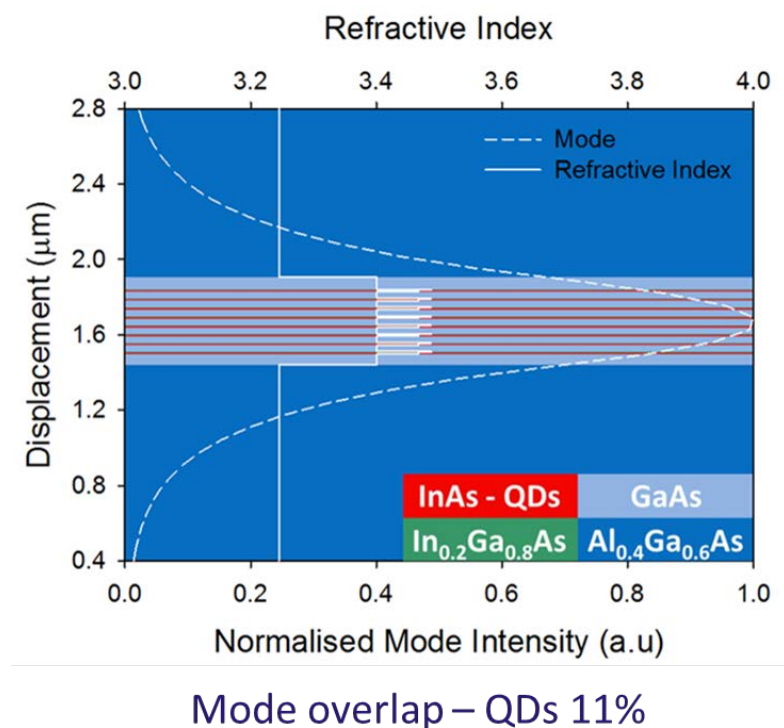


Figure 4.29: Optical mode plot of the QD edge-emitting laser.

FimmWave modelling is used to determine the mode overlap with both the photonic crystal and QD layers, which are then used to calculate the threshold gain and net modal gain. Obtaining a large mode overlap with the photonic crystal region will increase the optical feedback. However, this will affect the material gain produced by the active region due to the reduced mode overlap. Therefore, a trade-off is required, which will be determined for the different material systems. Three material systems have been modelled, void/GaAs (used in wafer fusion), InGaP/GaAs (used in previous all-semiconductor PCSELS) and a new material system AlAs/GaAs. Initially, the modelling focused on using a GaAs layer, called the ballast layer, above the photonic crystal layer, which will attract the optical mode, increasing the overlap with both the active and photonic crystal regions. All the structures use $\text{Al}_{0.42}\text{Ga}_{0.58}\text{As}$ cladding layers. The photonic crystal region is determined to be 388 nm thick from equation 4.3. Figure 4.30 shows how the net modal gain and threshold gain are affected by an increase in the thickness of the GaAs layer above the void/GaAs photonic crystal. The optical mode is forced away from photonic crystal and active region, due to the large change in refractive index between the voids and GaAs. With the optical mode further away from the active region, the modal gain

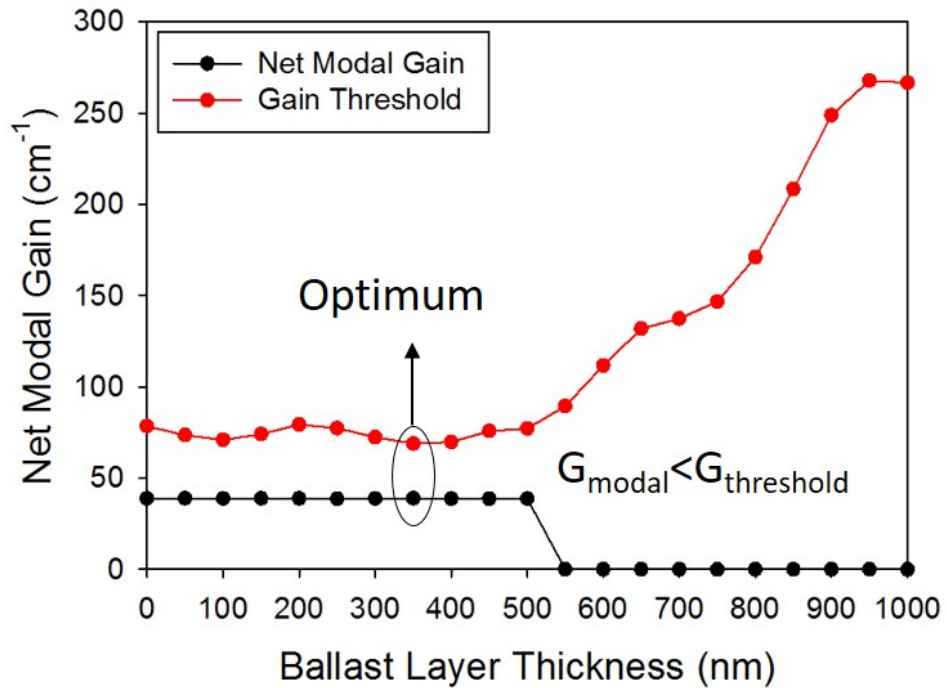


Figure 4.30: Net modal gain and required threshold gain plot for increasing the GaAs ballast layer thicknesses above the photonic crystal for the void/GaAs photonic crystal

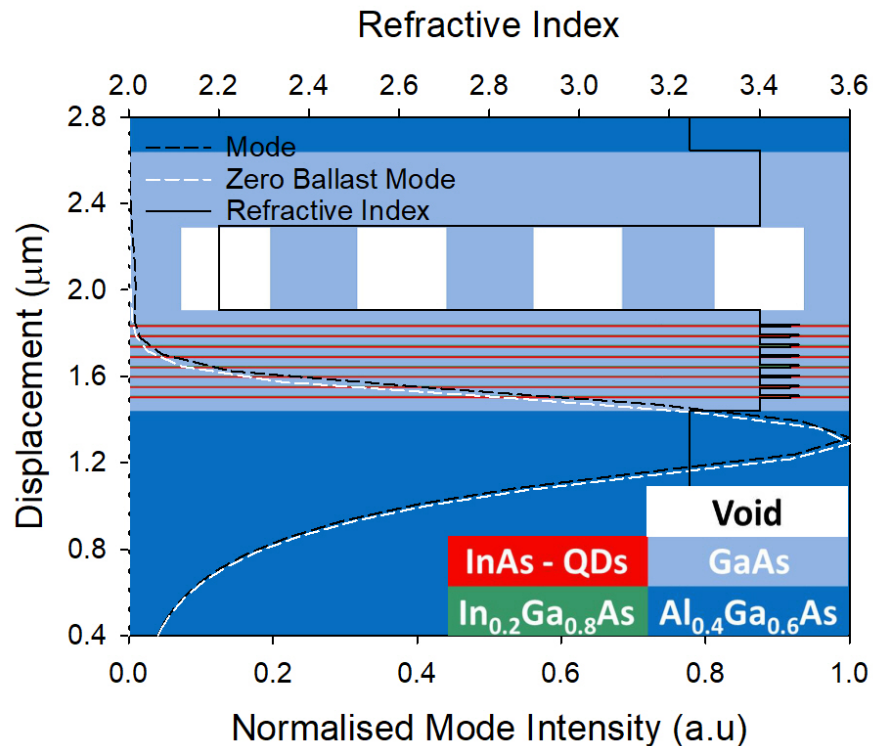


Figure 4.31: Two optical mode profiles plotted, the dotted black line is for a 350 nm thick GaAs ballast layer and the dotted white line is for the zero ballast, for the void/GaAs photonic crystal. The refractive index is plotted in solid black for the 350 nm thick GaAs ballast layer.

produced is lower. The mode profile and refractive index plot are shown in figure 4.31 for a ballast layer thickness of 350 nm and also for no ballast layer. The maximum of the optical mode for the 350 nm ballast layer is found to occur below the active region in the bottom cladding layer, having a small overlap with the photonic crystal of 1.5% and an active region overlap of 11.4%. Similarly, the maximum of the optical mode profile for the zero thickness ballast layer is also below the active region but a slightly smaller overlap of 1.2% is observed with the photonic crystal and 11.3% with the active region. The net modal gain drops to zero when the ballast layer thickness is increased above 550 nm, which is due to the optical mode shifting from being confined below the photonic crystal region to being confined in the ballast region. The optimum GaAs ballast layer thickness is calculated to be the largest difference between the required gain and the net modal gain. For the void/GaAs photonic crystal structure, the optimum is 350 nm of GaAs. Although this produces a mode overlap with the active region of 11%, the overlap with the photonic crystal is only 1.5%. As a result of this low confinement with the photonic crystal, the net modal gain never achieves the minimum threshold value.

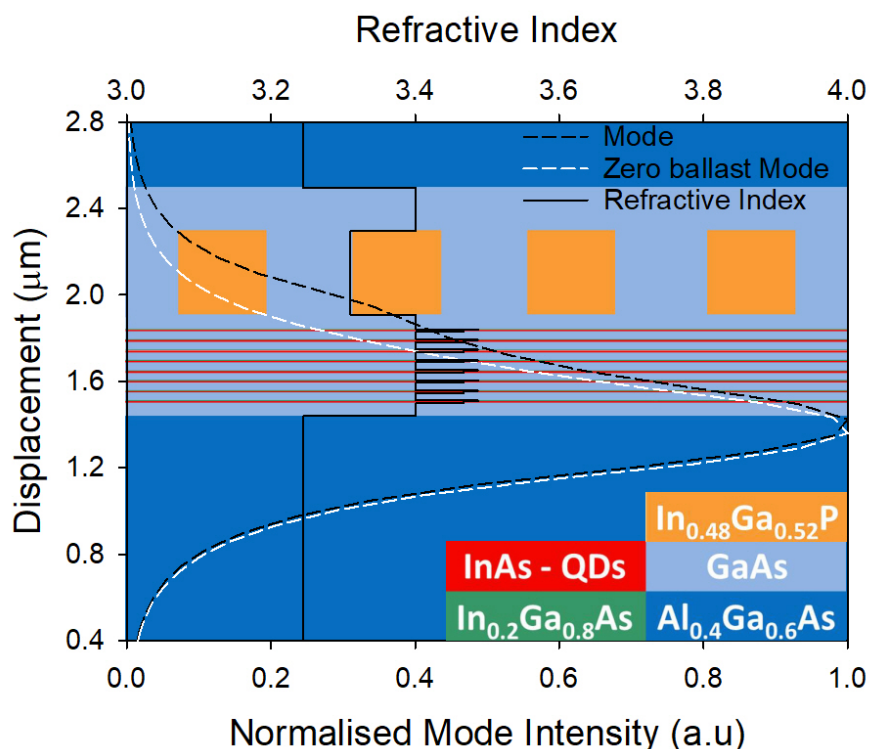


Figure 4.33: Two optical mode profiles plotted, the dotted black line is for a 200 nm thick GaAs ballast layer and the dotted white line is for the zero ballast, for the InGaP/GaAs photonic crystal. The refractive index is plotted in solid black for the 200 nm thick GaAs ballast layer.

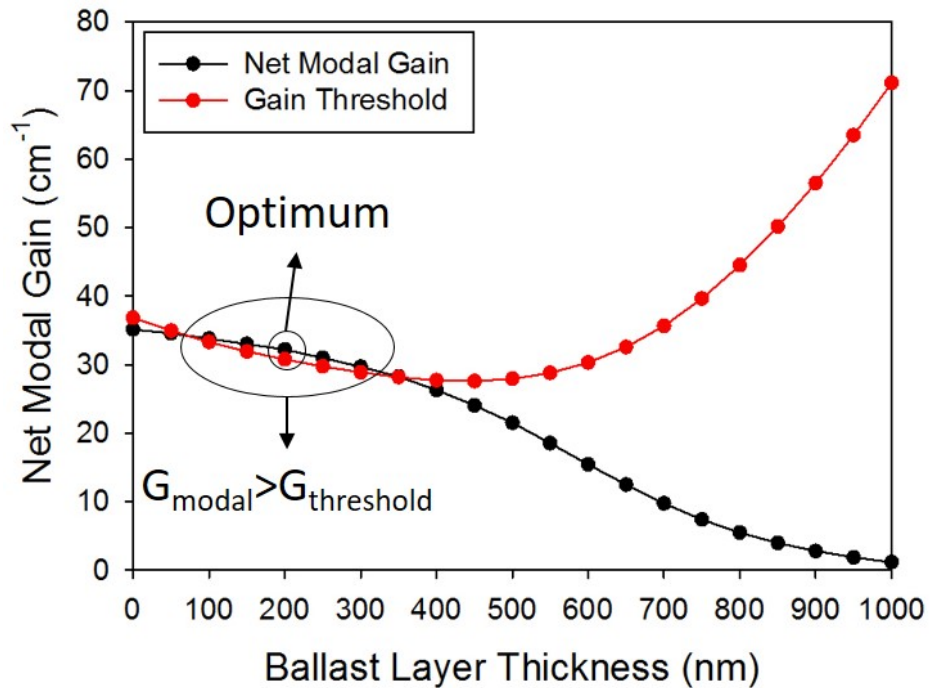


Figure 4.32: Net modal gain and required threshold gain as a function of the GaAs ballast layer thickness above the InGaP/GaAs photonic crystal.

Figure 4.32 shows how the net modal gain and threshold gain is affected by the thickness of the GaAs layer placed above the InGaP/GaAs photonic crystal structure. Similar to the void/GaAs photonic crystal the optical mode is forced away from photonic crystal and the active region, but in the present structure the refractive index change between the InGaP and GaAs is much smaller than the void/GaAs case, leading to a higher average refractive index and a larger overlap with the optical mode. The mode profile and refractive index plot are shown in figure 4.33 for a ballast layer thickness of 200 nm and also for no ballast layer. The maximum of the optical mode for the 200 nm ballast layer is found to occur below the active region in the bottom cladding layer, having an overlap with the photonic crystal of 21.6% and an active region overlap of 9.1%. Similarly, the maximum of the optical mode profile for the zero thickness ballast layer is also below the active region but a smaller overlap of 18% is observed with the photonic crystal and a slightly larger overlap of 10.3% with the active region. Due to the reduced refractive index contrast, the mode overlap with the active region is only 8% but this reduction in overlap with the active region is compensated by the huge increase in mode overlap with the photonic crystal, calculated to be 24%. The net modal gain is above the threshold value between

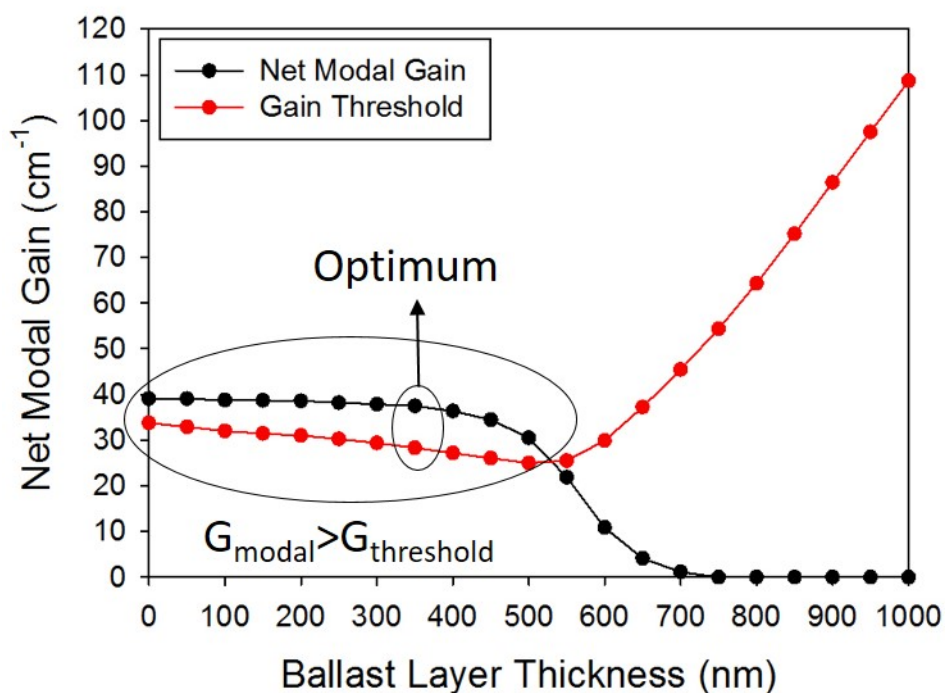


Figure 4.34: Net modal gain and required threshold gain as a function of the GaAs ballast layer thickness placed above an AlAs/GaAs photonic crystal

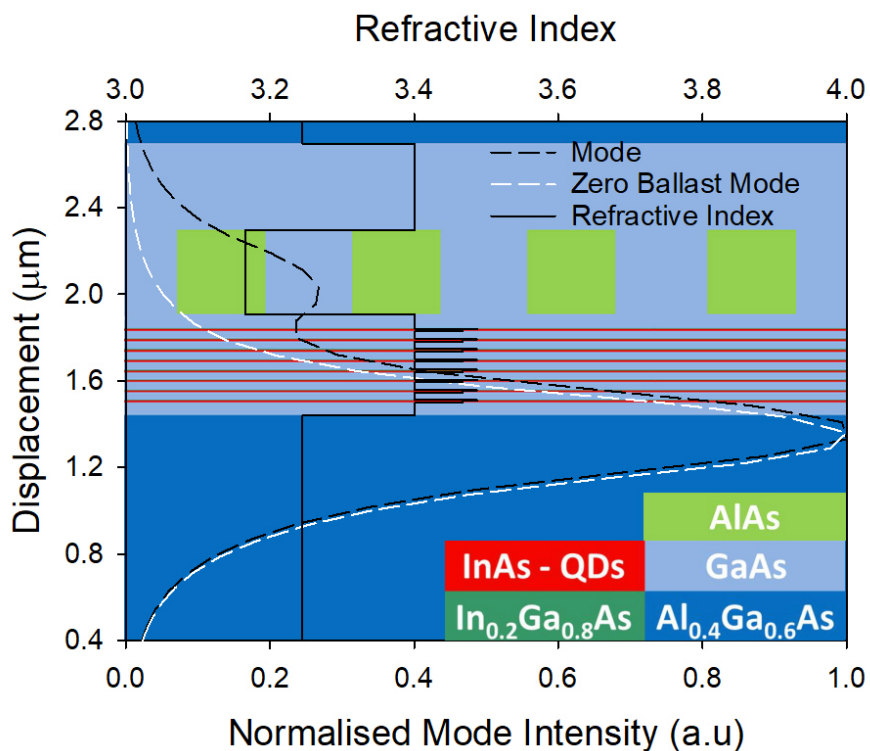


Figure 4.35: Two optical mode profiles plotted, the dotted black line is for a 400 nm thick GaAs ballast layer and the dotted white line is for the zero ballast, for the AlAs/GaAs photonic crystal. The refractive index is plotted in solid black for the 400 nm thick GaAs ballast layer.

ballast layer thicknesses of 150 to 300 nm. The optimum value is 200 nm but as this gives a modal gain of 34.2 cm^{-1} , which is only just above the required gain threshold value of 30.8 cm^{-1} , any issues with the overgrowth or fabrication would probably mean that devices would not lase from the ground state. Although the device may lase from an excited state this would mean a change in emission wavelength, which may not be matched to the reflectivity maximum of the photonic crystal. Therefore, it can be concluded that the InGaP/GaAs material system is not ideal for a QD PCSEL.

Figure 4.34 shows how the net modal gain and threshold gain are affected by the thickness of the GaAs ballast layer placed above an AlAs/GaAs photonic crystal. Similar to the void/GaAs and InGaP/GaAs photonic crystal structures the optical mode is forced away from photonic crystal and the active region, however whilst the refractive index contrast between AlAs and GaAs is smaller than in the void/GaAs case it is higher than for the InGaP/GaAs case. The mode profile and refractive index plot are shown in figure 4.35 for a ballast layer thickness of 400 nm and also for no ballast layer. The maximum of the optical mode for the 400 nm ballast layer is found to occur below the active region in the bottom cladding layer, having an overlap with the photonic crystal of 9.4% and an active region overlap of 10.6%. Similarly, the maximum of the optical mode profile for the zero thickness ballast layer is also below the active region but a smaller overlap of 7.6% is observed with the photonic crystal and a slightly larger overlap of 11.4% with the active region. The mode overlap with the active region is 10%, which is higher than for the InGaP/GaAs photonic crystal but slightly lower than for the void/GaAs photonic crystal. The mode overlap with the photonic crystal is 9%, which is lower than for InGaP/GaAs but much higher than for the void/GaAs photonic crystal. The net modal gain is above the threshold value for a ballast layer thickness between 0 and 500 nm. The optimum value is 350 nm where the net modal gain is 10 cm^{-1} greater than required for lasing. Hence, the AlAs/GaAs photonic crystal material system is likely to work, even if the losses in the structure are somewhat higher than expected. At large ballast layer thicknesses, a similar effect to the void system is observed, with the optical mode confined in the ballast layer instead of the active region. Three material systems for the photonic crystal have been

considered, void/GaAs, InGaP/GaAs and AlAs/GaAs. The GaAs ballast layer thickness has been optimised to obtain sufficient modal gain for a ground state QD-PCSEL device for both InGaP/GaAs and AlAs/GaAs photonic crystals, with the latter exhibiting a larger difference between the required gain and the calculated net modal gain. In contrast, the void/GaAs photonic crystal had insufficient net modal gain to be above the required threshold gain. For any practical system a relatively large difference between the required threshold gain and the net modal gain is required for a QD-PCSEL to compensate for any fabrication issues.

A potential approach to increase the net modal gain and reduce the threshold gain is by the introduction of an additional layer with a lower refractive index below the active region, called a repulsion layer. AlAs is a suitable material and the incorporation of such a layer is modelled to study its effects on the mode overlap with the QD layers and the photonic crystal for all three material systems as discussed previously. To study the effect of the repulsion layer the GaAs ballast layer is removed.

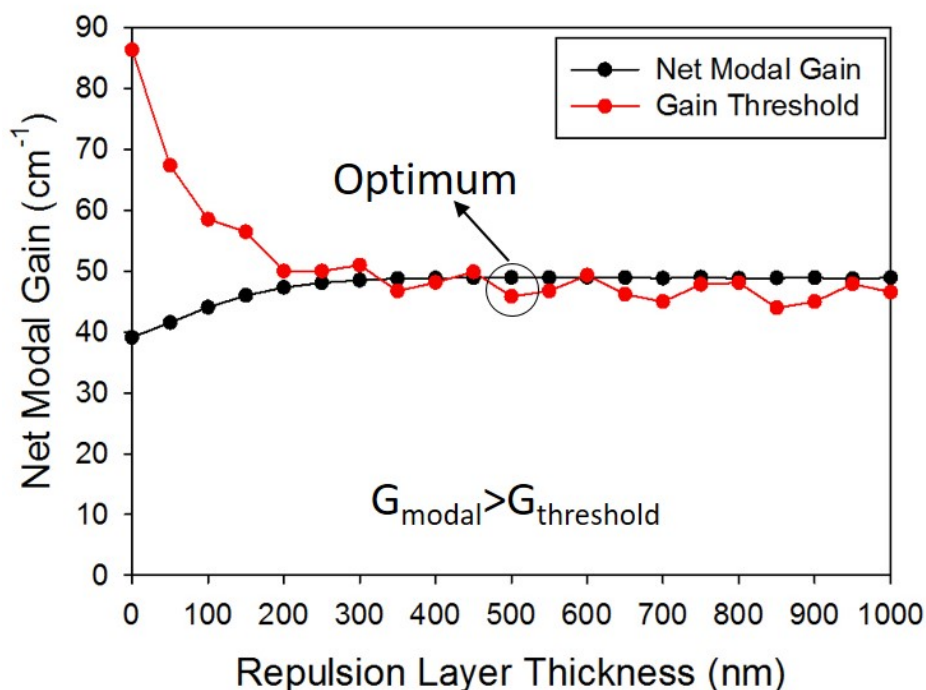


Figure 4.36: Net modal gain and required threshold gain as a function of the AlAs repulsion layer thickness placed below the active region for the void/GaAs photonic crystal.

Figure 4.36 shows how the net modal gain and threshold gain vary with the thickness of an AlAs repulsion layer placed below the active region of a

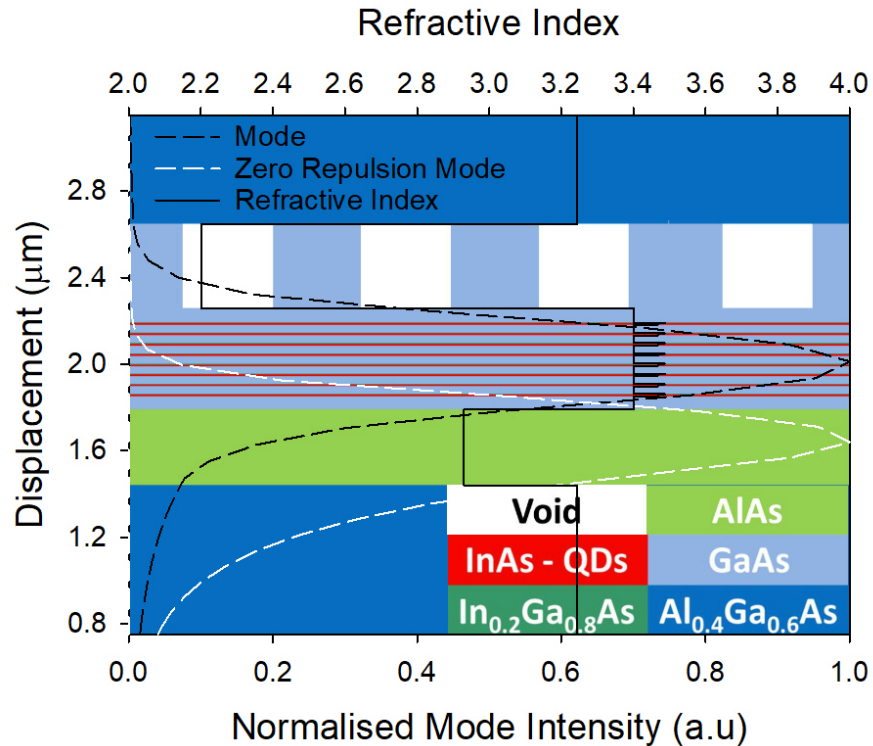


Figure 4.37: Two optical mode profiles plotted, the dotted black line is for a 500 nm thick AlAs repulsion layer and the dotted white line is for the zero ballast, for the void/GaAs photonic crystal. The refractive index is plotted in solid black for the 500 nm thick AlAs repulsion layer.

void/GaAs photonic crystal structure. The mode profile and refractive index variation are shown in figure 4.37, where the optical mode is seen to have a maximum in the middle of the active region. The mode overlap with the active region is 14%, which is higher than the 11% achieved with the ballast layer. The mode overlap with the photonic crystal is also higher at 2%, compared to 1.5% with the ballast layer. With both of these values increasing, the net modal gain for the structure is increased and the threshold gain is reduced. The optimum AlAs thickness is 850 nm, with the net modal gain being 5 cm^{-1} more than required for lasing.

Figure 4.38 shows how the net modal gain and threshold gain are affected by varying the thickness of an AlAs repulsion layer placed below the active region of an InGaP/GaAs photonic crystal structure. The mode profile and refractive index variation are shown in figure 4.39, where the optical mode is seen to have a maximum just above the middle of the active region. The mode overlap with the active region is 10%, which is higher than the 8% achieved using a ballast layer. The mode overlap with the photonic crystal remains the same at 24%. With the increase in the mode overlap with the QDs, the threshold gain is

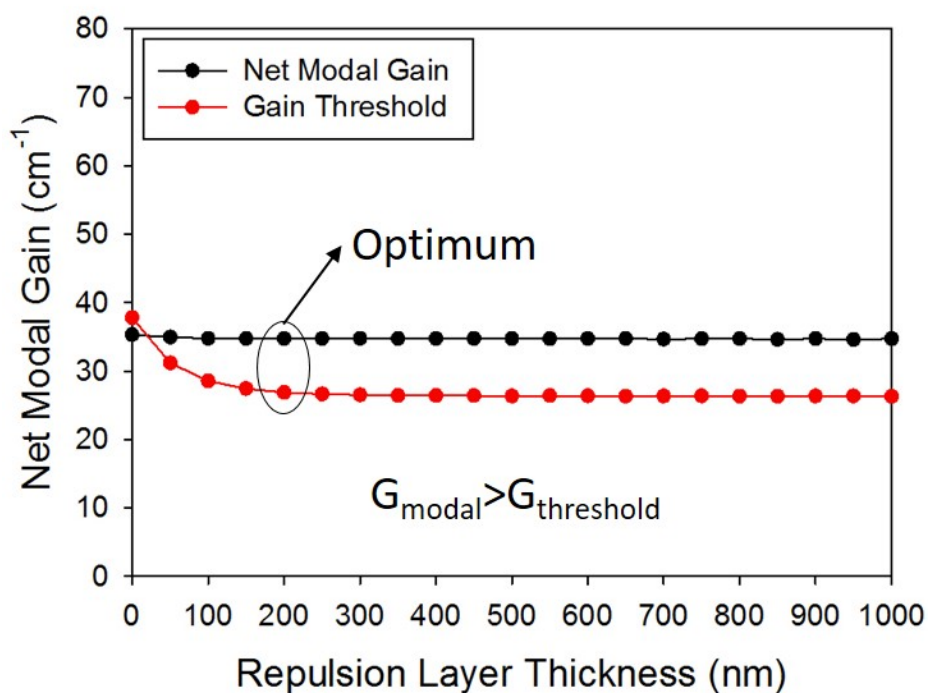


Figure 4.38: Net modal gain and required threshold gain as a function of the AIAs repulsion layer thickness placed below the active region for the InGaP/GaAs photonic crystal.

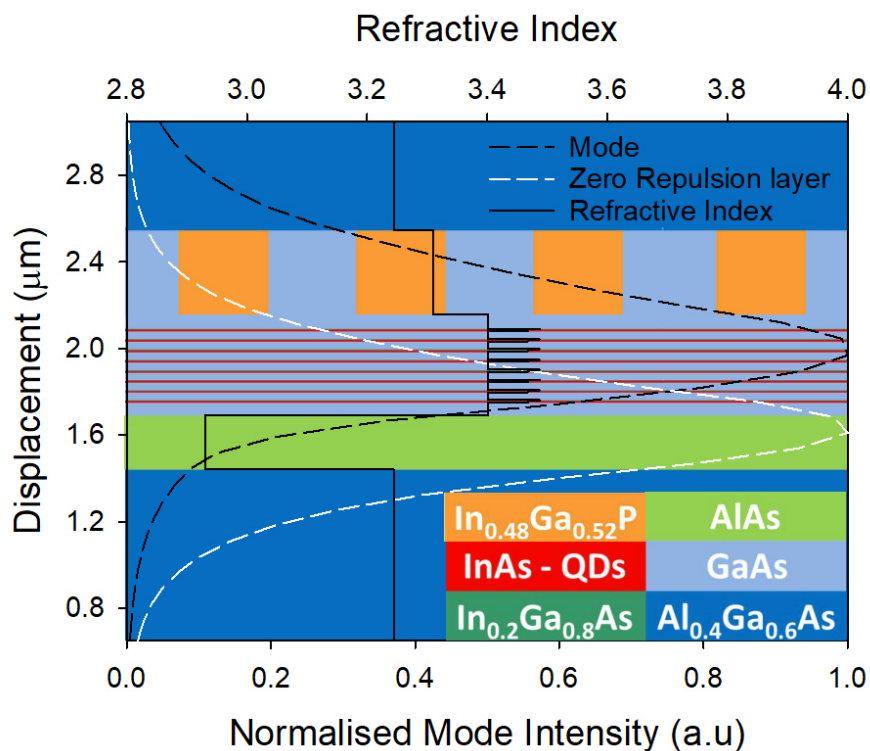


Figure 4.39: Two optical mode profiles plotted, the dotted black line is for a 200 nm thick AIAs repulsion layer and the dotted white line is for the zero ballast, for the InGaP/GaAs photonic crystal. The refractive index is plotted in solid black for the 200 nm thick AIAs repulsion layer.

reduced, increasing the likelihood for the devices to lase even with growth and processing defects. The optimum AIAs layer thickness is 200 nm with the net modal gain obtaining being 12 cm^{-1} more than required for lasing. Figure 4.40 shows how the net modal gain and threshold gain vary with the thickness of the AIAs repulsion layer placed below the active region of an AIAs/GaAs photonic crystal structure. The mode profile and refractive index variation is shown in figure 4.41 for a 200 nm thick AIAs layer, where the optical mode is seen to have a maximum at the centre of the active region. The mode overlap with the active region is 12%, which is higher than the 10% achieved using a ballast layer. The mode overlap with the photonic crystal is also higher at 11%, compared to 9% achieved with just the ballast layer. With both of these values increasing, the net modal gain for the structure is increased and the threshold gain is reduced, allowing more potential for the devices to work even with increased losses. The optimum AIAs thickness is 200 nm, with the net modal gain obtained being 20 cm^{-1} higher than required for lasing in an ideal structure.

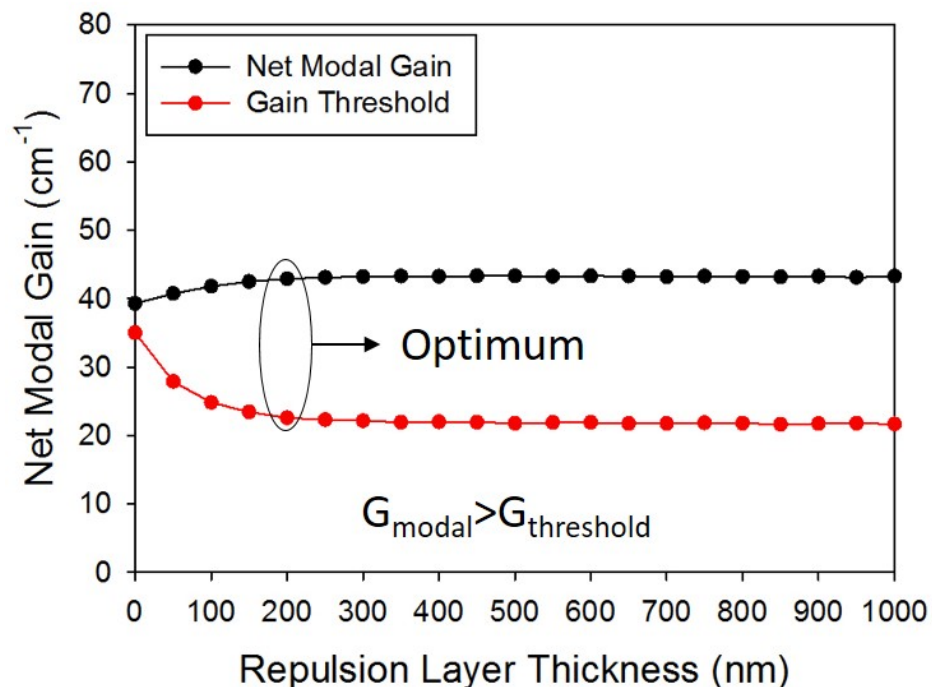


Figure 4.40: Net modal gain and required threshold gain as a function of the AIAs repulsion layer thickness placed below the active region for the AIAs/GaAs photonic crystal.

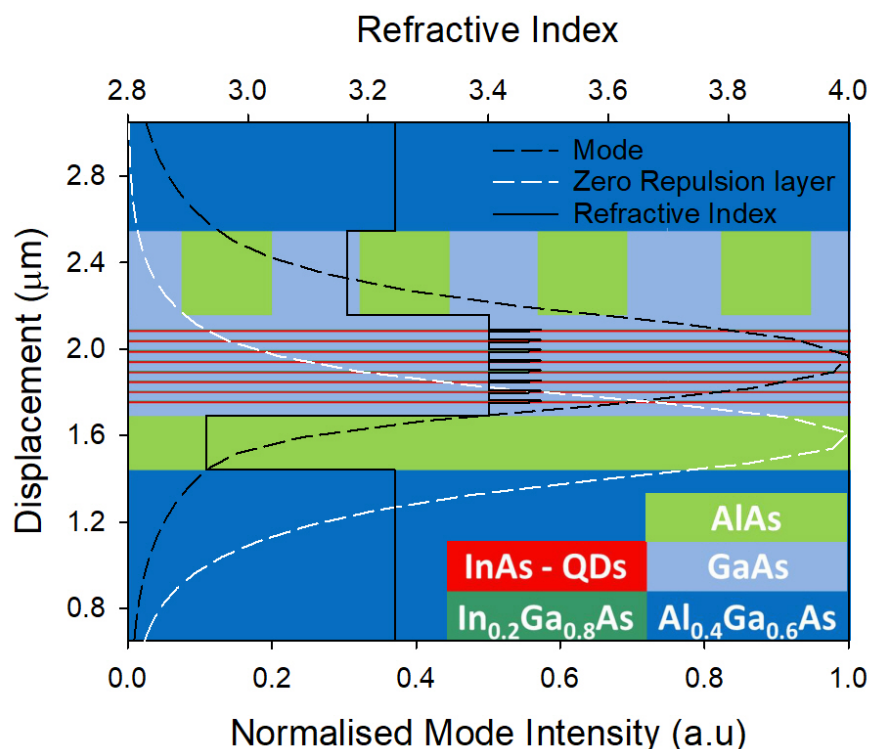


Figure 4.41: Two optical mode profiles plotted, the dotted black line is for a 200 nm thick AlAs repulsion layer and the dotted white line is for the zero ballast, for the AlAs/GaAs photonic crystal. The refractive index is plotted in solid black for the 200 nm thick AlAs repulsion layer.

This strongly suggests that the AlAs/GaAs photonic crystal material system with a 200 nm AlAs repulsion layer is likely to lase from the ground state.

Table 4.3 summarise the photonic material systems showing the required gain and the net modal gain of each and the maximum difference between these two quantities. With the void/GaAs photonic crystal there is a deficit in the net modal gain compared to the required gain for the zero ballast/repulsion layer and for the 350 nm ballast layer. However, an excess is achieved with the use of a repulsion layer, although this excess is relatively small. With the InGaP/GaAs photonic crystal, any thicknesses of AlAs repulsion layer shows a larger difference between the gain threshold and net modal gain compared to the zero repulsion layer and an excess in gain leading to the potential for a working laser. However, the excess is small and hence the effects of the fabrication process might result in devices having insufficient ground state gain, although the addition of the repulsion layer increases the excess suggesting the potential for a practical device. For the AlAs/GaAs photonic crystal, all three material systems, void/GaAs, InGaP/GaAs and AlAs/GaAs have an excess in

Photonic crystal	Required Gain (cm^{-1})	Net modal Gain (cm^{-1})	Difference (cm^{-1})
void/GaAs	78.5	40.8	-37.7
void/GaAs (350 nm ballast layer)	68.9	40.9	-28
void/GaAs (850 nm repulsion layer)	44	50.9	6.9
InGaP/GaAs	36.8	37.1	0.3
InGaP/GaAs (200 nm ballast layer)	30.8	34.2	3.4
InGaP/GaAs (200 nm repulsion layer)	26.9	36.7	9.8
AlAs/GaAs	33.8	41.1	7.3
AlAs/GaAs (200 nm ballast layer)	28.3	39.5	11.2
AlAs/GaAs (200 nm repulsion layer)	22.6	44.9	22.3

Table 4.3: Summary of the required gain, net modal gain and the difference for the three photonic crystal material systems and the optimum GaAs ballast thickness and the optimum AlAs repulsion thicknesses.

the net modal gain leading to the potential that these AlAs/GaAs photonic crystal structures will lase. However, the possibility of a working PCSELS is enhanced by the use of an AlAs repulsion layer with the AlAs/GaAs photonic crystal being the optimum structure. Therefore, the most promising structures for growth and study are AlAs/GaAs photonic crystals without either layer and with a ballast or repulsion layer and the InAsP/GaAs photonic crystal with a repulsion layer. In addition, the use of both a GaAs ballast layer and an AlAs repulsion layer may lead to further improvements in the difference between the required gain and the net modal gain.

4.8 Epitaxial Overgrowth of Planar Structures

The ultimate aim of this work was to fabricate QD PCSELs starting with wafers supplied by QD Laser Inc. containing eight QD layers separated by 39.2 nm of GaAs with a lower cladding layer of 1.4 μm of $\text{Al}_{0.40}\text{Ga}_{0.60}\text{As}$. Before a full QD PCSEL structure could be attempted, a large number of test and development steps are required. Initial overgrowth was used to investigate how the MOVPE growth temperature might affect the emission wavelength of the QDs. The growth temperature used was 580°C to minimise annealing of the QDs which would blue-shift their emission and potentially giving a mismatch with the reflectivity maximum of the photonic crystal. In addition, the effect of incorporating a highly doped AlAs layer above the active region was studied; this layer was designed to represent the photonic crystal region.

Before overgrowth of the QD wafers, doping calibrations of the carbon flow rates were performed to ensure the correct doping levels in the AlAs and $\text{Al}_{0.42}\text{Ga}_{0.58}\text{As}$ layers. The AlAs doping level is calibrated to $1 \times 10^{18} \text{ cm}^{-3}$ and the AlGaAs layer is calibrated to $5 \times 10^{17} \text{ cm}^{-3}$ and $1 \times 10^{18} \text{ cm}^{-3}$ using Hall

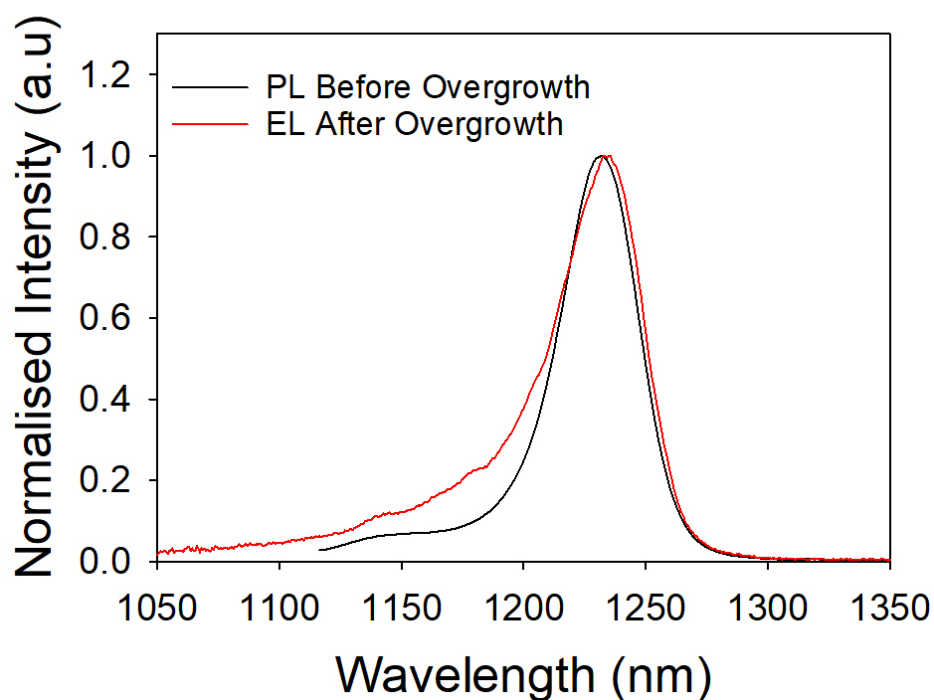


Figure 4.42: Emission spectra of the QDs before and after MOVPE overgrowth.

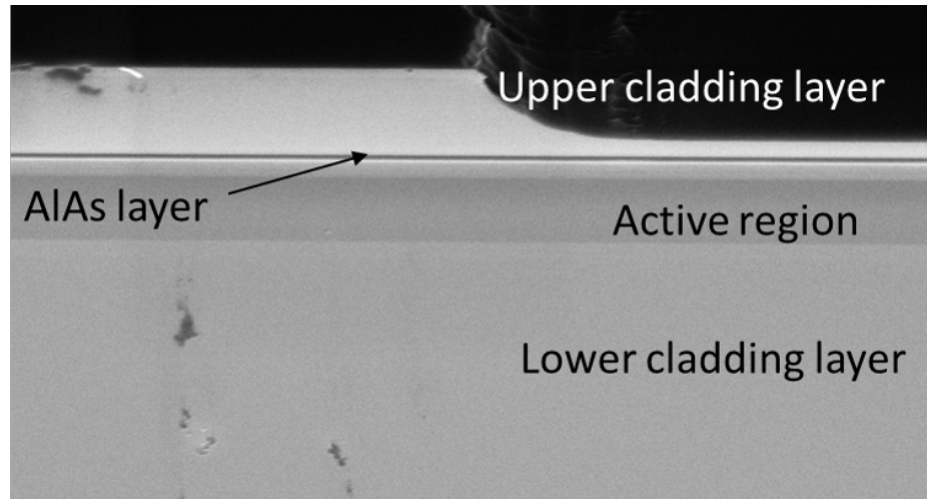


Figure 4.43: SEM image of the etch profile of the mesa diode.

measurements. Two doping levels are used to reduce internal losses associated with highly doped layers near the active region. A high doping layer is required to reduce the contact and internal resistance of the device. Before the QD Laser Inc. wafers were loaded into the MOVPE growth chamber, they were cleaved into quarters, cleaned using the three stage clean and oxygen asher described in section 4.3, and HF dipped for one minute to remove the surface oxide and any residual contaminants. Two overgrowths were attempted, the first was the growth of an upper cladding layer consisting of 750 nm of low doped $\text{Al}_{0.42}\text{Ga}_{0.58}\text{As}$ followed by 750 nm of high doped $\text{Al}_{0.42}\text{Ga}_{0.58}\text{As}$ and capped with 200 nm of highly doped ($1 \times 10^{19} \text{ cm}^{-3}$) GaAs which forms the contact layer. The second overgrowth had the same upper cladding and contact layer but an additional layer between the active and cladding regions consisting of 100 nm of highly doped ($1 \times 10^{18} \text{ cm}^{-3}$) AlAs, this is the position where the photonic crystal would be fabricated. Both overgrowth structures are temperature limited to 580°C to ensure that there are no adverse annealing of the QDs. Figure 4.42 shows the room temperature PL spectra before and EL spectra after overgrowth. No changes are observed in the wavelength of the QD emission, confirming that the overgrowth temperature is sufficiently low to prevent any significant annealing of the QDs, which would result in a blue shift of the emission.

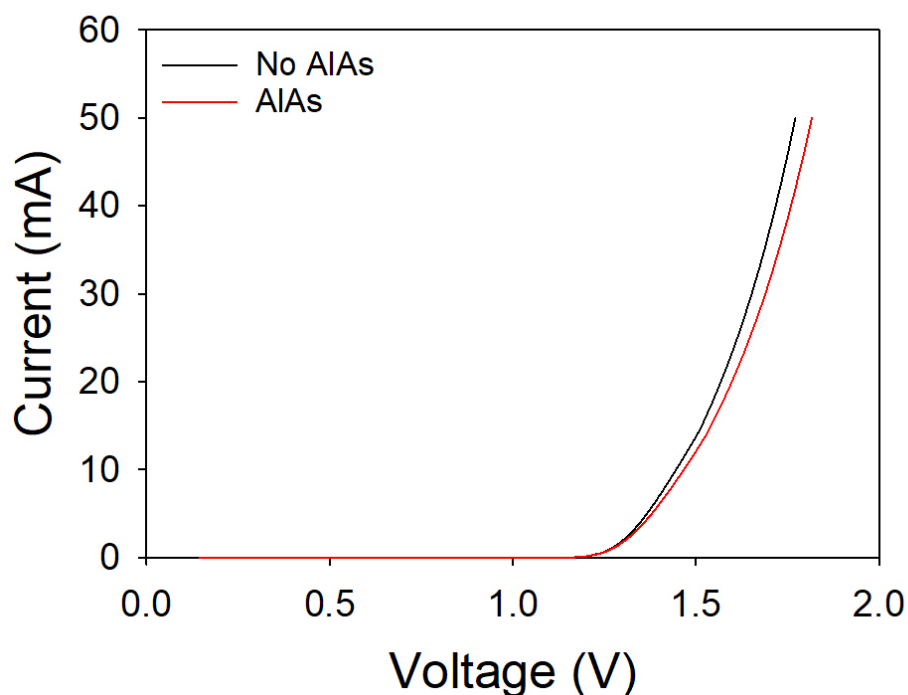


Figure 4.44: Room temperature IV for MOVPE overgrown QD structures fabricated into mesa diodes. Characteristics for structures both with and without a 100 nm AIAs layer placed above the active region are shown.

Both overgrowth structures were fabricated into mesa diodes, as described in section 4.3. To ensure that the AIAs layer does not oxidise, the isolation etch is limited to the upper cladding and contact layer. Figure 4.43 is a SEM image showing the isolation etch, where the AIAs layer is confirmed not to be exposed. Figure 4.44 shows the electrical characteristics of both overgrowth structures (with and without the AIAs layer). The IV characteristics of both samples are observed to be very similar, indicating that heavily doping the AIAs layer has prevented this wide bandgap material from creating an additional potential barrier, which impedes carrier transport in the device. These results show that it is possible to overgrow the supplied QD material using MOVPE without any significant change to the QD properties. In addition, adding an AIAs layer, which would be required, as the starting material for the photonic crystal, does not cause a noticeable degradation to the electrical characteristics of the diode.

4.9 Further work

Further work is required to improve the lasing performance of the edge emitting QD lasers. The initial studies detailed above show considerable promise, with an improved performance for the 30 nm strain balanced device in comparison to that of the 30 nm device without strain balancing. Further optimisation of the QD growth parameters have shown improvements towards obtaining long wavelength room temperature lasing based on a non-strain balanced structure with 50 nm layer separation, as discussed in section 4.5. Therefore, incorporating the QD growth parameters used in the room temperature QD laser with the strain balancing would allow 30 nm and potentially the 20 nm layer separations room temperature laser. As a consequence further development using larger numbers of QD layers within the active region could be attempted, which should reduce the threshold current density. The fabrication of multi-section devices and/or ridge laser with different cavity lengths would allow the gain produced by the QDs to be determined.

Continuation of the QD-PCSEL work would focus on the implementation of an AlAs/GaAs photonic crystal, with wafers provided by QD Laser Inc. need to be fabricated to define the photonic crystal, which will be infilled with AlAs during the overgrowth process to form an AlAs/GaAs photonic crystal. Additional growth studies are required to study the effect of the AlAs repulsion layer placed below the active region and also to investigate differences between the use of a ballast layer and a repulsion layer in AlAs/GaAs and InGaP/GaAs photonic crystals. Further modelling can be performed to study the effect of using both a ballast and repulsion layers within the same structure to increase the mode overlap with the photonic crystal and active region.

4.10 Conclusions

In this chapter the fabrication techniques used to successfully fabricate mesa diodes and broad area lasers has been presented. Low temperature EL measurements of the mesa diodes reveals issues with QD bimodality. It is shown that this bimodality can be reduced by increasing the InAs coverage, showing promise for future room temperature ground state lasing devices at 1300 nm and novel device applications. Laser devices were grown and fabricated with and without a strain-balancing layer. Incorporation of this layer is shown to improve the performance of a device with a 30 nm spacing between QD layers, although performance is still inferior to that of a 50 nm device without strain balancing. Both strain balanced and non-strain balanced lasers operate up to at least 200 K for 30 nm QD layer separation and 220 K for 50 nm QD layer separation, without any facet coating. A strong QD bimodality is shown to limit the ground state gain for QDs emitting close to 1.3 μm . Further growth optimisation has yielded room temperature lasing from an excited QD state by reducing the V/III ratio to 5 from 208 and reducing the reactor pressure to 50 from 100 Torr.

Modelling has been performed of QD-PCSEL devices with input parameters obtained from the experimental measurements of QD gain and previous QW-PCSEL devices. This modelling has been used to determine the minimum threshold current density and net modal gain. Three photonic crystal material systems have been modelled. The first is the void/GaAs system. Here results suggest difficulty in obtaining ground state laser without additional layers being added below the active region. An AlAs repulsion layer improves the potential performance but this would require additional growth steps. The second material system is InGaP/GaAs, which has been previously used in the fabrication of QW-PCSELS operating at 980 nm. Although lasing appears possible in the basic structure there is little tolerance to imperfections resulting from growth or fabrication. The addition of an AlAs repulsion layer significantly improves the tolerance to a less than ideal structure. The third material system is AlAs/GaAs where the net modal gain produced without any additional AlAs repulsion layer is

already significantly above that required, but is further improved with its addition. Initial test structures grown with a 100 nm AlAs layer above the active region show little or no degradation in the electrical characteristics if this layer is highly doped. In addition, no change to the QD emission properties resulted from the overgrowth. These initial growth studies suggest the viability of this approach to produce a QD-PCSEL operating at 1.3 μm .

4.11 References

- [1] G. S. May and C. J. Spanos, *Fundamentals of semiconductor manufacturing and process control*. IEEE, 2006.
- [2] S. S. Li, *Semiconductor physical electronics*. Springer, 2010.
- [3] Y. P. Varshni, "Temperature dependence of the energy gap in semiconductors," *Physica*, vol. 34, no. 1, pp. 149–154, Jan. 1967.
- [4] P. Blood, *Quantum confined laser devices: optical gain and recombination in semiconductors*, 1st ed. Oxford University Press, 2015.
- [5] Z. Y. Xu et al., "Carrier relaxation and thermal activation of localized excitons in self-organized InAs multilayers grown on GaAs substrates," *Phys. Rev. B*, vol. 54, no. 16, pp. 11528–11531, Oct. 1996.
- [6] D. Bimberg, N. Kirstaedter, N. N. Ledentsov, Z. I. Alferov, P. S. Kop'ev, and V. M. Ustinov, "InGaAs-GaAs quantum-dot lasers," *IEEE J. Sel. Top. Quantum Electron.*, vol. 3, no. 2, pp. 196–205, Apr. 1997.
- [7] L. Brusaferrri et al., "Thermally activated carrier transfer and luminescence line shape in self-organized InAs quantum dots," *Appl. Phys. Lett.* 69, 3354 (1996)
- [8] J. M. García et al., "Intermixing and shape changes during the formation of InAs self-assembled quantum dots," *Appl. Phys. Lett.*, vol. 71, no. 14, p. 2014, Oct. 1997.
- [9] Y. T. Dai, J. C. Fan, Y. F. Chen, R. M. Lin, S. C. Lee, and H. H. Lin, "Temperature dependence of photoluminescence spectra in InAs/GaAs quantum dot superlattices with large thicknesses," *Journal of Applied Physics* 82, 4489 (1997)
- [10] A. A. El-Emawy et al., "Formation trends in quantum dot growth using metalorganic chemical vapor deposition," *J. Appl. Phys.*, vol. 93, no. 6, p. 3529, 2003.
- [11] A. Passaseo et al., "Dependence of the emission wavelength on the internal electric field in quantum-dot laser structures grown by metal-organic chemical-vapor deposition," *Appl. Phys. Lett.*, vol. 79, no. 10, p.

- 1435, 2001.
- [12] A. Passaseo, G. Maruccio, M. De Vittorio, R. Rinaldi, R. Cingolani, and M. Lomascolo, "Wavelength control from 1.25 to 1.4 μm in $\text{In}_x\text{Ga}_{1-x}\text{As}$ quantum dot structures grown by metal organic chemical vapor deposition," *Appl. Phys. Lett.*, vol. 78, no. 10, p. 1382, 2001.
- [13] L. Finger et al., "Modification of energy relaxation of InGaAs quantum dots by postgrowth thermal annealing," in *Conference Proceedings. 1998 International Conference on Indium Phosphide and Related Materials (Cat. No.98CH36129)*, 1998, pp. 151–154.
- [14] D. Guimard et al., "Interface properties of InAs quantum dots produced by antimony surfactant-mediated growth: Etching of segregated antimony and its impact on the photoluminescence and lasing characteristics," *Appl. Phys. Lett.*, vol. 94, no. 10, p. 103116, 2009.
- [15] H. Z. Song, Y. Tanaka, T. Yamamoto, N. Yokoyama, M. Sugawara, and Y. Arakawa, "AlGaAs capping effect on InAs quantum dots self-assembled on GaAs," *Phys. Lett. A*, vol. 375, no. 40, pp. 3517–3520, Sep. 2011.
- [16] A. O. Kosogov et al., "Structural and optical properties of InAs–GaAs quantum dots subjected to high temperature annealing," *Appl. Phys. Lett.* 69, 3072 (1996)
- [17] K. Pötschke et al., "Ripening of self-organized InAs quantum dots," *Phys. E Low-dimensional Syst. Nanostructures*, vol. 21, no. 2–4, pp. 606–610, Mar. 2004.
- [18] S. Mokkalapati, J. Wong-Leung, H. H. Tan, C. Jagadish, K. E. McBean, and M. R. Phillips, "Tuning the bandgap of InAs quantum dots by selective-area MOCVD," *J. Phys. D. Appl. Phys.*, vol. 41, no. 8, p. 85104, Apr. 2008.
- [19] K. Sears, H. H. Tan, J. Wong-Leung, and C. Jagadish, "The role of arsine in the self-assembled growth of InAs/GaAs quantum dots by metal organic chemical vapor deposition," *J. Appl. Phys.*, vol. 99, no. 4, p. 44908, Feb. 2006.

- [20] S. Mokkaḡpati, H. H. Tan, and C. Jagadiḡ, “Multiple wavelength InGaAs quantum dot lasers using selective area epitaxy,” *Appl. Phys. Lett.*, vol. 90, no. 17, p. 171104, Apr. 2007.
- [21] K. Sears, H. Tan, M. Buda, J. Wong-Leung, and C. Jagadiḡ, “Growth and Characterization of InAs/GaAs Quantum Dots and Diode Lasers,” 2006 Int. Conf. Nanosci. Nanotechnol., pp. 505–508, 2006.
- [22] A. L. Schawlow and C. H. Townes, “Infrared and Optical Masers,” *Phys. Rev.*, vol. 112, no. 6, pp. 1940–1949, Dec. 1958.
- [23] T. H. MAIMAN, “Stimulated Optical Radiation in Ruby,” *Nature*, vol. 187, no. 4736, pp. 493–494, Aug. 1960.
- [24] A. Javan, W. R. Bennett, and D. R. Herriott, “Population Inversion and Continuous Optical Maser Oscillation in a Gas Discharge Containing a He-Ne Mixture,” *Phys. Rev. Lett.*, vol. 6, no. 3, pp. 106–110, Feb. 1961.
- [25] I. Hayashi, M. B. Panish, P. W. Foy, and S. Sumski, “JUNCTION LASERS WHICH OPERATE CONTINUOUSLY AT ROOM TEMPERATURE,” *Appl. Phys. Lett.*, vol. 17, no. 3, pp. 109–111, Aug. 1970.
- [26] A. Perot and C. Fabry, “On the Application of Interference Phenomena to the Solution of Various Problems of Spectroscopy and Metrology,” *Astrophys. J.*, vol. 9, p. 87, Feb. 1899.
- [27] K. Otsubo et al., “Temperature-Insensitive Eye-Opening under 10-Gb/s Modulation of 1.3- μm P-Doped Quantum-Dot Lasers without Current Adjustments,” *Jpn. J. Appl. Phys.*, vol. 43, no. No. 8B, pp. L1124–L1126, Jul. 2004.
- [28] M. Asada, Y. Miyamoto, and Y. Suematsu, “Gain and the threshold of three-dimensional quantum-box lasers,” *IEEE J. Quantum Electron.*, vol. 22, no. 9, pp. 1915–1921, Sep. 1986.
- [29] Y. Arakawa and H. Sakaki, “Multidimensional quantum well laser and temperature dependence of its threshold current,” *Appl. Phys. Lett.*, vol. 40, no. 11, p. 939, 1982.
- [30] G. W. Turner, H. K. Choi, and M. J. Manfra, “Ultralow-threshold

- (50 A/cm²) strained single-quantum-well GaInAsSb/AlGaAsSb lasers emitting at 2.05 μm,” *Appl. Phys. Lett.*, vol. 72, no. 8, p. 876, Jun. 1998.
- [31] P. G. Eliseev et al., “Transition dipole moment of InAs/InGaAs quantum dots from experiments on ultralow-threshold laser diodes,” *Appl. Phys. Lett.*, vol. 77, no. 2, p. 262, Jun. 2000.
- [32] P. G. Eliseev, H. Li, T. Liu, T. C. Newell, L. F. Lester, and K. J. Malloy, “Ground-state emission and gain in ultralow-threshold InAs-InGaAs quantum-dot lasers,” *IEEE J. Sel. Top. Quantum Electron.*, vol. 7, no. 2, pp. 135–142, 2001.
- [33] Xiaodong Huang, A. Stintz, C. P. Hains, G. T. Liu, J. Cheng, and K. J. Malloy, “Very low threshold current density room temperature continuous-wave lasing from a single-layer InAs quantum-dot laser,” *IEEE Photonics Technol. Lett.*, vol. 12, no. 3, pp. 227–229, Mar. 2000.
- [34] I. R. Sellers et al., “1.3 μm InAs/GaAs multilayer quantum-dot laser with extremely low room-temperature threshold current density,” *Electron. Lett.*, vol. 40, no. 22, p. 1412, 2004.
- [35] G. T. Liu, A. Stintz, H. Li, K. J. Malloy, and L. F. Lester, “Extremely low room-temperature threshold current density diode lasers using InAs dots in In_{0.15}Ga_{0.85}As quantum well,” *Electron. Lett.*, vol. 35, no. 14, p. 1163, 1999.
- [36] D. L. Huffaker, G. Park, Z. Zou, O. B. Shchekin, and D. G. Deppe, “Continuous-wave low-threshold performance of 1.3 μm InGaAs-GaAs quantum-dot lasers,” *IEEE J. Sel. Top. Quantum Electron.*, vol. 6, no. 3, pp. 452–461, May 2000.
- [37] M. Grundmann et al., “Low threshold, large To injection laser emission from (InGa)As quantum dots,” *Electron. Lett.*, vol. 30, no. 17, pp. 1416–1417, Aug. 1994.
- [38] A. Passaseo et al., “Comparison of radiative and structural properties of 1.3 μm In_xGa_{1-x}As quantum-dot laser structures grown by metalorganic chemical vapor deposition and molecular-beam epitaxy: Effect on the lasing properties,” *Appl. Phys. Lett.*, vol. 82, no. 21, p. 3632, May 2003.

- [39] J. Tatebayashi, N. Nuntawong, P. S. Wong, Y.-C. Xin, L. F. Lester, and D. L. Huffaker, "Strain compensation technique in self-assembled InAs/GaAs quantum dots for applications to photonic devices," *J. Phys. D. Appl. Phys.*, vol. 42, no. 7, p. 073002, Apr. 2009.
- [40] R. L. Sellin, C. Ribbat, M. Grundmann, N. N. Ledentsov, and D. Bimberg, "Close-to-ideal device characteristics of high-power InGaAs/GaAs quantum dot lasers," *Appl. Phys. Lett.*, vol. 78, no. 9, p. 1207, Feb. 2001.
- [41] R. L. Sellin et al., "High-reliability MOCVD-grown quantum dot laser," *Electron. Lett.*, vol. 38, no. 16, p. 883, 2002.
- [42] I. N. Kaiander et al., "1.24 μm InGaAs/GaAs quantum dot laser grown by metalorganic chemical vapor deposition using tertiarybutylarsine," *Appl. Phys. Lett.*, vol. 84, no. 16, p. 2992, 2004.
- [43] N. Nuntawong et al., "Quantum dot lasers based on a stacked and strain-compensated active region grown by metal-organic chemical vapor deposition," *Appl. Phys. Lett.*, vol. 86, no. 19, p. 193115, 2005.
- [44] D. Guimard et al., "Ground state lasing at 1.30 μm from InAs/GaAs quantum dot lasers grown by metal-organic chemical vapor deposition," *Nanotechnology*, vol. 21, no. 10, p. 105604, Mar. 2010.
- [45] J. Tatebayashi et al., "1.28 μm lasing from stacked InAs/GaAs quantum dots with low-temperature-grown AlGaAs cladding layer by metalorganic chemical vapor deposition," *Appl. Phys. Lett.*, vol. 86, no. 5, p. 53107, 2005.
- [46] J. Tatebayashi et al., "Low threshold current operation of self-assembled InAs/GaAs quantum dot lasers by metal organic chemical vapour deposition," *Electron. Lett.*, vol. 39, no. 15, p. 1130, 2003.
- [47] M. S. Skolnick and D. J. Mowbray, "SELF-ASSEMBLED SEMICONDUCTOR QUANTUM DOTS: Fundamental Physics and Device Applications," *Annu. Rev. Mater. Res.*, vol. 34, no. 1, pp. 181–218, Aug. 2004.
- [48] D. J. Mowbray and M. S. Skolnick, "New physics and devices based on

- self-assembled semiconductor quantum dots,” *J. Phys. D. Appl. Phys.*, vol. 38, no. 13, pp. 2059–2076, Jul. 2005.
- [49] O. B. Shchekin and D. G. Deppe, “Low-threshold high- T_0 1.3 μm InAs quantum-dot lasers due to p-type modulation doping of the active region,” *IEEE Photonics Technol. Lett.*, vol. 14, no. 9, pp. 1231–1233, Sep. 2002.
- [50] O. B. Shchekin and D. G. Deppe, “1.3 μm InAs quantum dot laser with $T_0=161$ K from 0 to 80°C,” *Appl. Phys. Lett.*, vol. 80, no. 18, pp. 3277–3279, May 2002.
- [51] E. Yablonovitch, “Inhibited Spontaneous Emission in Solid-State Physics and Electronics,” *Phys. Rev. Lett.*, vol. 58, no. 20, pp. 2059–2062, May 1987.
- [52] W. Streifer, R. Burnham, and D. Scifres, “Effect of external reflectors on longitudinal modes of distributed feedback lasers,” *IEEE J. Quantum Electron.*, vol. 11, no. 4, pp. 154–161, Apr. 1975.
- [53] H. Kogelnik and C. V. Shank, “Coupled-Wave Theory of Distributed Feedback Lasers,” *J. Appl. Phys.*, vol. 43, no. 5, pp. 2327–2335, May 1972.
- [54] H. C. Casey, S. Somekh, and M. Ilegems, “Room-temperature operation of low-threshold separate-confinement heterostructure injection laser with distributed feedback,” *Appl. Phys. Lett.*, vol. 27, no. 3, pp. 142–144, Aug. 1975.
- [55] R. Burnham, D. Scifres, and W. Streifer, “Single-heterostructure distributed-feedback GaAs-diode lasers,” *IEEE J. Quantum Electron.*, vol. 11, no. 7, pp. 439–449, Jul. 1975.
- [56] K. Iga, “Surface-emitting laser-its birth and generation of new optoelectronics field,” *IEEE J. Sel. Top. Quantum Electron.*, vol. 6, no. 6, pp. 1201–1215, Nov. 2000.
- [57] H. Soda, K. Iga, C. Kitahara, and Y. Suematsu, “GaInAsP/InP Surface Emitting Injection Lasers,” *Jpn. J. Appl. Phys.*, vol. 18, no. 12, pp. 2329–2330, Dec. 1979.

- [58] K. Iga, F. Koyama, and S. Kinoshita, "Surface emitting semiconductor lasers," *IEEE J. Quantum Electron.*, vol. 24, no. 9, pp. 1845–1855, Sep. 1988.
- [59] J. D. Joannopoulos, S. G. Johnson, J. N. Winn, and R. D. Meade, *Photonic Crystals: Molding the Flow of Light (Second Edition)*. Princeton University Press, 2008.
- [60] M. Berggren, A. Dodabalapur, R. E. Slusher, Z. Bao, A. Timko, and O. Nalamasu, "Organic lasers based on lithographically defined photonic-bandgap resonators," *Electron. Lett.*, vol. 34, no. 1, p. 90, 1998.
- [61] M. Imada, S. Noda, A. Chutinan, T. Tokuda, M. Murata, and G. Sasaki, "Coherent two-dimensional lasing action in surface-emitting laser with triangular-lattice photonic crystal structure," *Appl. Phys. Lett.*, vol. 75, no. 3, p. 316, Jul. 1999.
- [62] D. Ohnishi, T. Okano, M. Imada, and S. Noda, "Room temperature continuous wave operation of a surface-emitting two-dimensional photonic crystal diode laser," *Opt. Express*, vol. 12, no. 8, p. 1562, Apr. 2004.
- [63] E. Miyai, K. Sakai, T. Okano, W. Kunishi, D. Ohnishi, and S. Noda, "Lasers producing tailored beams," *Nature*, vol. 441, no. 7096, pp. 946–946, Jun. 2006.
- [64] K. Sakai, E. Miyai, T. Sakaguchi, D. Ohnishi, T. Okano, and S. Noda, "Lasing band-edge identification for a surface-emitting photonic crystal laser," *IEEE J. Sel. Areas Commun.*, vol. 23, no. 7, pp. 1335–1340, Jul. 2005.
- [65] M. Imada, A. Chutinan, S. Noda, and M. Mochizuki, "Multidirectionally distributed feedback photonic crystal lasers," *Phys. Rev. B*, vol. 65, no. 19, p. 195306, Apr. 2002.
- [66] K. Hirose, Y. Liang, Y. Kurosaka, A. Watanabe, T. Sugiyama, and S. Noda, "Watt-class high-power, high-beam-quality photonic-crystal lasers," *Nat. Photonics*, vol. 8, no. 5, pp. 406–411, May 2014.
- [67] M. Imada, S. Noda, A. Chutinan, M. Murata, and G. Sasaki,

- “Semiconductor lasers with one- and two-dimensional air/semiconductor gratings embedded by wafer fusion technique,” *IEEE J. Sel. Top. Quantum Electron.*, vol. 5, no. 3, pp. 658–663, 1999.
- [68] R. J. E. Taylor, D. M. Williams, J. R. Orchard, D. T. D. Childs, S. Khamas, and R. A. Hogg, “Band structure and waveguide modelling of epitaxially regrown photonic crystal surface-emitting lasers,” *J. Phys. D. Appl. Phys.*, vol. 46, no. 26, p. 264005, Jul. 2013.
- [69] D. M. Williams et al., “Epitaxially Regrown GaAs-Based Photonic Crystal Surface-Emitting Laser,” *IEEE Photonics Technol. Lett.*, vol. 24, no. 11, pp. 966–968, Jun. 2012.
- [70] D. M. Williams et al., “Optimisation of Coupling between Photonic Crystal and Active Elements in an Epitaxially Regrown GaAs Based Photonic Crystal Surface Emitting Laser,” *Jpn. J. Appl. Phys.*, vol. 51, no. 2, p. 02-05, Feb. 2012.
- [71] R. J. E. Taylor et al., “Coherently Coupled Photonic-Crystal Surface-Emitting Laser Array,” *IEEE J. Sel. Top. Quantum Electron.*, vol. 21, no. 6, pp. 493–499, Nov. 2015.
- [72] R. J. E. Taylor et al., “Electronic control of coherence in a two-dimensional array of photonic crystal surface emitting lasers,” *Sci. Rep.*, vol. 5, no. 1, p. 13203, Oct. 2015.
- [73] R. J. E. Taylor et al., “Mode Control in Photonic Crystal Surface Emitting Lasers Through External Reflection,” *IEEE J. Sel. Top. Quantum Electron.*, vol. 23, no. 6, pp. 1–8, Nov. 2017.
- [74] R. J. E. Taylor et al., “All-Semiconductor Photonic Crystal Surface-Emitting Lasers Based on Epitaxial Regrowth,” *IEEE J. Sel. Top. Quantum Electron.*, vol. 19, no. 4, pp. 4900407–4900407, Jul. 2013.
- [75] R. J. E. Taylor et al., “Mode Control in Photonic Crystal Surface Emitting Lasers Through External Reflection,” *IEEE J. Sel. Top. Quantum Electron.*, vol. 23, no. 6, pp. 1–8, Nov. 2017.
- [76] I. O’Driscoll, P. Blood, and P. M. Smowton, “Random Population of Quantum Dots in InAs–GaAs Laser Structures,” *IEEE J. Quantum*

- Electron., vol. 46, no. 4, pp. 525–532, Apr. 2010.
- [77] M. Grundmann and D. Bimberg, “Theory of random population for quantum dots,” *Phys. Rev. B*, vol. 55, no. 15, pp. 9740–9745, Apr. 1997.
- [78] H. . Wang, D. Ning, and S. . Feng, “Temperature dependence of the optical properties of InAs/GaAs self-organized quantum dots with bimodal size distribution,” *J. Cryst. Growth*, vol. 209, no. 4, pp. 630–636, 2000.
- [79] F. Franchello, L. D. de Souza, E. Laureto, A. A. Quivy, I. F. L. Dias, and J. L. Duarte, “Influence of bimodal distribution and excited state emission on photoluminescence spectra of InAs self-assembled quantum dots,” *J. Lumin.*, vol. 137, pp. 22–27, 2013.
- [80] D. Zhou et al., “Lateral wavelength control of InAs/InGaAsP/InP (100) quantum dots in the 1.55 μm region by selective-area metal organic vapor-phase epitaxy,” *J. Appl. Phys.*, vol. 100, no. 11, p. 113512, Dec. 2006.
- [81] T. Shioda et al., “Simulation and design of the emission wavelength of multiple quantum well structures fabricated by selective area metalorganic chemical vapor deposition,” *Thin Solid Films*, vol. 498, no. 1–2, pp. 174–178, Mar. 2006.
- [82] G. Park, D. L. Huffaker, Z. Zou, O. B. Shchekin, and D. G. Deppe, “Temperature dependence of lasing characteristics for long-wavelength (1.3- μm) GaAs-based quantum-dot lasers,” *IEEE Photonics Technol. Lett.*, vol. 11, no. 3, pp. 301–303, Mar. 1999.
- [83] K. Sears, J. Wong-leung, M. Buda, H. H. Tan, and C. Jagadish, “Growth and characterisation of InAs/GaAs quantum dots grown by MOCVD,” *IEEE*, pp. 6–9, 2005.
- [84] K. Sears, H. H. Tan, J. Wong-Leung, and C. Jagadish, “The role of arsine in the self-assembled growth of InAs/GaAs quantum dots by metal organic chemical vapor deposition,” *J. Appl. Phys.*, vol. 99, no. 4, p. 44908, 2006.
- [85] G. B. Stringfellow, *Organometallic Vapor-Phase Epitaxy: Theory and*

Practice. Academic Press, 1999.

- [86] “Bragg reflector.” http://www.batop.com/information/r_Bragg.html.
- [87] E. Yablonovitch, T. Gmitter, and K. Leung, “Photonic band structure: The face-centered-cubic case employing nonspherical atoms,” *Phys. Rev. Lett.*, vol. 67, no. 17, pp. 2295–2298, Oct. 1991.
- [88] S. Noda, N. Yamamoto, H. Kobayashi, M. Okano, and K. Tomoda, “Optical properties of three-dimensional photonic crystals based on III–V semiconductors at infrared to near-infrared wavelengths,” *Appl. Phys. Lett.*, vol. 75, no. 7, p. 905, Aug. 1999.
- [89] S. Y. Lin et al., “A three-dimensional photonic crystal operating at infrared wavelengths,” *Nature*, vol. 394, no. 6690, pp. 251–253, Jul. 1998.
- [90] D. M. Williams et al., “Epitaxially Regrown GaAs-Based Photonic Crystal Surface-Emitting Laser,” *IEEE Photonics Technol. Lett.*, vol. 24, no. 11, pp. 966–968, Jun. 2012.

Chapter 5:

Conclusions and Further Work

This chapter will discuss further work and provide brief conclusions of chapters two, three and four. The aim of this thesis was to establish InAs/GaAs self-assembled quantum dot (QD) growth by metal-organic vapour phase epitaxy (MOVPE) at the University of Sheffield. An additional aim was the development of a suitable strain-balancing layer to reduce the overall strain in the structure close to zero and hence allow a reduction in the QD layer separation. This reduction gives a higher volumetric QD density and allows a greater number of QD layers to be placed close to the maximum of a laser cavity mode. In addition to increasing the maximum available gain this should reduce the threshold current density and permit new and novel devices. Following the optimisation of the QD growth and the development of a suitable strain-balancing layer, the QDs were incorporated in a simple Fabry-Perot laser structure to compare the performance of devices with and without strain balancing layers. In addition the first steps in the development of a QD photonic crystal surface emitting laser (PCSEL) were performed.

In chapter two, the optimisation process for the quantum dot (QD) growth was discussed. The growth parameters: InAs coverage, growth rate, V/III ratio during the QD growth and capping layer growth were all optimised. For the QD growth the optimum parameters for the InAs coverage was 2 ML, the growth rate was 0.18 ML/s, the V/III ratio during the QD growth was 208 and the V/III ratio during the capping layer growth was 12. However, the V/III ratio for QD growth was subsequently to be substantially higher than values given in the literature. A later study investigated lowering the V/III ratio during QD growth. This was found to increase the QD optical efficiency but also gave a blue-shift of the emission which is problematic for devices aiming for emission at 1.3 μm . During the growth optimisation, transmission electron microscopy (TEM) images showed an unintentional indium diffusion layer above the QDs.

Chapter 5: Conclusions and Further Work

Attempts were made to remove this layer by increasing the initial cap layer thickness and increasing the capping layer growth temperature. Neither method was found to be successful in removing the indium diffusion layer but the surface morphology was observed to improved with an increase to 580°C of the capping layer growth temperature.

Further work is required to remove the indium diffusion layer and to investigate the presence of this layer on the properties of the QDs, including their wavelength, carrier capture and optical efficiency. In addition, the only growth parameter not changed in this study was the growth temperature, due to the limitations of the EpiTT. The stated growth temperature is relative to a reference temperature of 525°C, the QDs were grown 40°C below this as indicated by a thermocouple. Therefore, a comprehensive study of the effect of growth temperature on the QD properties is required.

In chapter three, the concept of strain balancing of QD layers with $\text{GaAs}_z\text{P}_{1-z}$ was discussed as a method to allow a reduction in layer the separation. Initially, LaserMod modelling of the possible effects of different phosphorous concentrations in a 5 nm $\text{GaAs}_z\text{P}_{1-z}$ layer on the electrical and optoelectronic characteristics was performed. From this modelling it was concluded that the use of a 5 nm $\text{GaAs}_{0.8}\text{P}_{0.2}$ strain balancing layer would not significantly affect either the IV turn-on behaviour or the lasing threshold current. Leptos modelling was used to study the effects of varying different structural parameters, including layer compositions, thicknesses and periodicity, on the X-Ray diffraction (XRD) spectra Simulations of a QW structure designed to replicate the strain in a QD device showed that a 4 nm $\text{GaAs}_{0.8}\text{P}_{0.2}$ layer should fully strain balance a layer of QDs. This value was used to estimate the required thickness of GaAsP calculated from the average indium composition in the repeat. However, this was not expected to produce the same thickness for the strain balancing of the QD layer, as there is an expected difference in average indium composition but will provide an estimate of what was required.

Following the modelling, six QD structures with three different QD layer separations of 50, 30 and 20 nm were grown with and without a 5 nm $\text{GaAs}_{0.8}\text{P}_{0.2}$ strain-balancing layer. The required thickness of $\text{GaAs}_{0.8}\text{P}_{0.2}$ was

calculated from the XRD spectra of the 50 nm device without strain balancing to be 5.6 nm; however, a value of 5 nm was used to ensure the structure was not overcompensated. Optical access mesa devices were fabricated to study the effectiveness of the strain balancing. All devices showed similar electrical characteristics and the 50 nm devices showed similar optical characteristics. The addition of the strain-balancing layer to devices with QD layer separations of 30 nm and 20 nm, showed some evidence of improvement in the overall optical intensity.

Further modelling is required to study the effect of a thinner barrier with a higher phosphorus concentration as the current work only considered a barrier thickness of 5 nm. In addition, understanding the mechanism by which carriers are transported through the barrier is desirable. The effectiveness of these two transport processes is expected to depend on both the height and width of the barrier for quantum mechanical tunnelling and the height for thermal excitation. Hence, a study of different combinations of width and composition may allow these two processes to be separately studied and the composition that allows the most efficient carrier transport to be identified. Growth of different strain-balanced samples will provide experimental confirmation of the modelling. In addition, studies of the positioning of the GaAsP layer could be performed. For example, this layer could be placed before the QD layers or split into two separate layers placed before and after each QD layer. Finally, a QD layer separation intermediate between 30 and 20 nm should be grown to determine the lower limit for non-coupled QD layers.

In chapter four, mesa diode and Fabry-Perot laser devices are fabricated from the strain balanced and non-strain balanced wafers and characterised. In addition, the first steps in developing a novel photonic crystal surface emitting laser using QDs are described. Low temperature electroluminescence (EL) reveals an issue with QD bimodality; however, this can be reduced with an increase in the InAs coverage although the optical efficiency starts to fall off, possibly due to the presence of dislocations. Broad area Fabry-Perot laser devices with QD layer separations of 50 and 30 nm and with and without a strain-balancing layer were fabricated. Both strain balanced and non-strain

balanced lasers operate up to 220 K for 50 nm separation and 200 K for 30 nm separation, but with excited state lasing. However, incorporation of the strain-balancing layer is shown to improve the performance of a device with 30 nm spacing between QD layers, as the threshold current density was always lower for the strain-balanced device with a 30 nm separation over a range of temperatures, although performance is still inferior to that of a 50 nm device without strain balancing. Further growth optimisation has yielded room temperature lasing from an excited QD state by reducing the V/III ratio to 5 from 208 and reducing the reactor pressure to 50 from 100 Torr.

Fimmwave modelling has been performed to optimise the waveguide of a QD-PCSEL, using input parameters from experimental measurements of QD gain and previous QW-PCSELS to determine the minimum threshold gain and the net modal gain. Three photonic crystal material systems were compared: void/GaAs, InGaP/GaAs and AlAs/GaAs. The addition of a GaAs ballast layer above the photonic crystal or an AlAs repulsion layer below the active region were modelled. From the modelling, the optimum material system for a QD-PCSEL was found to be AlAs/GaAs. However, all three material systems showed potential improvement from an AlAs repulsion layer placed below the active region. Initial test structures, grown with a highly doped 100 nm AlAs layer above the active region, show little or no degradation in their electrical characteristics. In addition, no change to the QD emission properties resulted from an overgrowth step. These initial growth studies suggest the viability of this approach to produce a QD-PCSEL operating at 1.3 μm .

Further work is required to improve the lasing performance of the edge emitting QD lasers. The initial studies detailed above show considerable promise, with improved performance for the 30 nm strain balanced device in comparison to that of the 30 nm device without strain balancing. Further optimisation of the QD growth parameters have shown promise for obtaining longer wavelength room temperature lasing based on a non-strain balanced structure with 50 nm layer separation. Therefore, incorporating the QD growth parameters used in the room temperature QD laser with the strain balancing would allow 30 nm and potentially the 20 nm layer separations room temperature laser. As a

consequence, further development using larger numbers of QD layers within the active region could be attempted, which should reduce the threshold current density and allow ground state lasing close to 1.3 μm . The fabrication of multi-section devices and/or ridge laser with different cavity lengths would allow the gain produced by the QDs to be determined.

Continuation of the QD-PCSEL work would focus on the implementation of an AlAs/GaAs photonic crystal. QD containing wafers, provided by QD Laser Inc., would be fabricated to define the photonic crystal, which would then be infilled with AlAs during the overgrowth process to form an AlAs/GaAs photonic crystal. Additional growth studies are required to study the effect of the AlAs repulsion layer placed below the active region and also to investigate differences between the use of a ballast layer and a repulsion layer in both AlAs/GaAs and InGaP/GaAs photonic crystals. Further modelling can be performed to study the effect of using both a ballast and repulsion layer within the same structure to increase the mode overlap with the photonic crystal and active region.